Using multi-modal MRI techniques to measure glymphatic function in-vivo

Balázs Örzsik

Thesis submitted to University of Sussex for the degree of Doctorate of Philosophy

October 2021

Declaration of authorship

I declare that the research contained in this thesis, unless otherwise formally indicated in the text, is the original work of the author. I hereby declare that this thesis has not been and will not be, submitted in whole or in part to another University for the award of any other degree

Signed:

Date: 12/10/2021

University of Sussex

Balázs Örzsik

Thesis submitted for the degree of Doctorate of Philosophy

Using multi-modal MRI techniques to measure glymphatic function in-vivo

Abstract

Background

The brain lacks conventional lymphatic vessels, however it has its own macroscopic waste clearance system, which is called the glymphatic system. It utilizes perivascular tunnels surrounded by astroglia cells and promote cerebrospinal-interstitial fluid exchange. Rodent studies have suggested that glymphatic system is active during sleep. Imaging the glymphatic system without a contrast agent is a challenging task.

Aims

I propose that glymphatic system related changes can be detected with non-invasive MRI techniques sensitive to fluid motion (diffusion weighted MRI) and changes in intra-, extracellular volume fraction (sodium MRI) by comparing acquisitions obtained during wake and sleep.

Methods

21 healthy young participants (6 females, 22.3 ± 3.2 years) were scanned in two separate sessions, after a night of normal sleep and after a full night of sleep deprivation. In the sleep deprivation session participants also received 10mg of Zolpidem to increase the chance of falling asleep in the scanner. Multiple MRI modalities were acquired: sodium, high resolution anatomical, diffusion weighted and arterial spin labelling (ASL) images.

Results and discussion

Physiological recordings and questionnaires indicated that participants were able to achieve sleep in the scanner. ASL indicated reduced cerebral blood flow (CBF) during sleep session, which was in line published literature. Sodium MRI indicated increased sodium signal during sleep, which might be due to glymphatic system related expansion in extracellular space. Although, sodium data is likely to be compromised by technical issues. Significant changes in diffusion were observed during sleep (decrease in diffusion kurtosis), which was in line with the hypothesized increase glymphatic function during sleep.

Conclusion

My study highlighted the issues with acquiring and quantifying sodium MRI data during sleep. In future studies one should acquire higher order diffusion weighted data and measure diffusion kurtosis as it shows better sensitivity to glymphatic system related changes than classical diffusion measures.

Table of Contents

Table of table

Table of Tables

ix

Table of Figures

Acknowledgements

This thesis is dedicated to two of my dear friends Lara Nosiru and Alex Elsmore, who are no longer with us. Lara thank you for helping me with the application process for this PhD, I was thinking a lot about you while writing this thesis. Alex, I will never forget our science/physics conversation over a bottle of wine (or two). I hope you both found peace.

I would like to thank my supervisors:

Professor Mara Cercignani- for introducing me to the field of neuroimaging.

Professor Neil Harrison- for teaching me how to “get out of the weeds and get on to that helicopter”.

Dr Iris Asllani- for the time and help with the ASL data and all the little projects that we worked on alongside this PhD.

Thank you all for all your time and effort that went into this project!

I would like to thank Professor Derk-Jan Dijk for seeing us at the University of Surrey and discussing sleep with us.

I would like to thank the radiographers at the Clinical Imaging Science Centre.

Finally, I would like to thank my family and friends, who are always there to support me.

Definitions and Abbreviations

^{18}FDG..... ^{18}F-fluoro-2-deoxyglucose

^{1}H ..... Hydrogen/proton

^{23}Na MRI ..... Sodium MRI

A/D..... Analog to digital

aal3v1 ..... Automated anatomical labelling

AAN..... Ascending arousal network

ABDM..... Active blur detection method

aCSF ..... Artificial CSF

AD ..... Axial diffusivity

ADC ..... Apparent diffusion coefficient

AK..... Axial kurtosis

ANOVA..... Analysis of variance

AQ4..... Aquaporin 4

ASL ..... Arterial spin labelling

b-value ..... Diffusion weighting

BOLD ..... Blood oxygen level dependent

CAG ..... cytosine adenine guanin

CASL ..... Continuous ASL

CBF..... Cerebral blood flow

CBV ..... Cerebral blood volume

CNS ..... Central nervous system

CSF ..... Cerebrospinal fluid

D ..... Diffusion coefficient

DARTEL ..... Diffeomorphic Anatomical Registration Through Exponential Lie Algebra

DKI ..... Diffusion Kurtosis Imaging

DKTI ..... Diffusion Kurtosis Tensor Imaging

DTI ..... Diffusion tensor imaging

DW MRS..... Diffusion-weighted magnetic resonance spectroscopy

dwMRI ..... Diffusion weighted MRI

ECG ..... Electrocardiography

ECoG ..... Electrocorticography

EEG ..... Electroencephalography

EMG ..... Electromyography

f..... Extracellular volume fraction

FA..... Fractional anisotropy

FDR ..... False discovery rate

FLORET..... Fermat Looped Orthogonally Encoded Trajectories

fMRI ..... functional MRI

FOV ..... Field of view

FWHM..... Full-width at half maximum

GABA..... Gamma-aminobutyric acid

GM ..... Grey matter

h..... Hours

HF..... High frequency

HRV ..... Heart rate variability

ICBM ..... International Consortium of Brain Mapping

IR..... Inversion recovery

ISF ..... Interstitial fluid

K..... Kurtosis

KFA..... Kurtosis fractional anisotropy

KSS ..... Karolinska Sleepiness Scale

LF ..... Low frequency

m ..... Minutes

MD ..... Mean diffusivity

MK ..... Mean kurtosis

MKT ..... Mean kurtosis tensor

MNI ..... Montreal neurological institute

MPRAGE ..... Magnetisation prepared rapid gradient echo

MQF ..... Multiple quantum filtering

MRI ..... Magnetic Resonance Imaging

N1 sleep ..... Stage 1 sleep

N2 sleep ..... Stage 2 sleep

N3 sleep ..... Stage 3 and 4 sleep

NMR ..... Nuclear magnetic resonance

NODDI ..... Neurite Orientation and Dispersion Density Imaging

NREM ..... Non-rapid eye movement

PASL ..... Pulsed ASL

pCASL ..... Pseudo continuous ASL

PET ..... Positron emission tomography

PLD ..... Post labelling delay

PSF ..... Point spread function

PSQI ..... Pittsburgh Sleep Quality Index

PVEs ..... Partial volume effects

RD ..... Radial diffusivity

REM ..... Rapid eye movement

RIESLING ..... Radial Interstices Enable Speedy Low-Volume imaging

RK ..... Radial kurtosis

ROI ..... Region of interest

RR interval ..... Inter beat interval

RSA ..... Respiratory sinus arrythmia

s ..... Seconds

SD..... Standard deviation

SEM..... Standard error of mean

SQ ..... Single quantum

SWA ..... Slow wave activity

SWS..... Slow wave sleep

T ..... Tesla

T_1..... Longitudinal relaxation time

T_2..... Transverse relaxation time

TE ..... Echo time

TMA ..... Tetramethyl- ammonium

TOD ..... Time of day

TPM ..... Tissue probability map

TR..... Repetition time

TSC ..... Total sodium concentration

VBM ..... Voxel based morphometry

VLF ..... Very low frequency

WASO..... Wake after sleep onset

Water PET ..... $H_2{}^{15}O$ PET

WM ..... White matter

Chapter 1 Background

1.1 Introduction

Nothing made me more aware of the joy and importance of a good night sleep than missing out on it while writing this thesis. But why do we need to sleep? One of the recent theories suggests that our need for sleep might be related to the brain's waste clearance system (known as the glymphatic system). In this thesis I investigate a range of novel approaches to imaging and quantifying the glymphatic system using multimodal Magnetic Resonance Imaging (MRI) techniques. Data from rodents indicates that this system becomes particularly activated during sleep and has provided a compelling alternative hypothesis for why sleep is such an essential physiological process. Therefore, I always found it grotesque when I could not sleep because of thinking too much of importance and the processes that happen during sleep.

In this introductory chapter, I will first discuss the importance and characteristics of sleep and highlight some of the leading hypotheses regarding its control and function. I will then describe the relatively novel hypothesis that activation of the brain's waste clearance system may underpin the necessity of sleep, why we should be interested in studying this system and why it is so challenging to do so in humans. Finally, I present my study aims, describing how we proposed to measure changes associated with the brain's waste clearance system during sleep in humans using non-invasive MRI techniques.

1.2 Need for sleep

Sleep deprivation even in the most modest or acute form can have serious negative impact on physical and cognitive performance, as well as on emotion regulation (Wickens et al., 2015). Chronic sleep deprivation is associated with increased levels of stress hormones, blood pressure and impairments in immune function, which increase the risk somatic and mental health disorders (Luyster et al., 2012). Animal studies have demonstrated that sleep is a necessity, rats prevented from sleeping lost weight (despite their increased food intake), appeared weak, developed ulcers on their paws and died within 4-6 weeks (Rechtschaffen and Bergmann, 2002). The need for sleep appears to be universal across the animal kingdom, as prolonged sleep deprivation also leads to

death in invertebrates such as fruit flies (Shaw et al., 2002) and cockroaches (Stephenson, Chu and Lee, 2007). In humans, individuals diagnosed with fatal familial insomnia die relatively shortly after the diagnosis, in 5-10 months (Tabernero, 2000).

Recently the American Academy of Sleep Medicine released a statement emphasizing that sleep is an essential biological necessity, sleep related problems are detrimental for well-being and pose a public health risk, as well as emphasizing the importance of sleep research (Ramar et al., 2021). However, despite the primacy of sleep to health and survival, the underlying mechanisms of sleep and even its fundamental functions remain largely unresolved (Cirelli and Tononi, 2008).

1.3 Sleep characterization

Sleep can be characterized on many different levels, spanning from the level of behaviour down to the level of gene expression (Cirelli, Gutierrez and Tononi, 2004). Before the emergence of electroencephalography (EEG), sleep was solely determined and classified based on behavioural aspects such as reduced sensitivity to external stimuli, body posture, increased arousal threshold and state reversibility by stimulation (Flanigan, 1972). Until the early 1950s, sleep was considered to be a uniform phenomenon. However, Nathaniel Kleitman and Eugene Aserinksy's seminal experiment in 1953 revealed that when measured at a systems level using EEG, sleep could be shown to consist of several stages that evolve in a characteristic sequential manner (Aserinsky and Kleitman, 1953). Subsequently, EEG became the gold standard for identifying and grouping sleep stages in humans that can distinguish between wake and 4 (or according to the more recent nomenclature 3) stages of sleep as depicted on Figure 1.

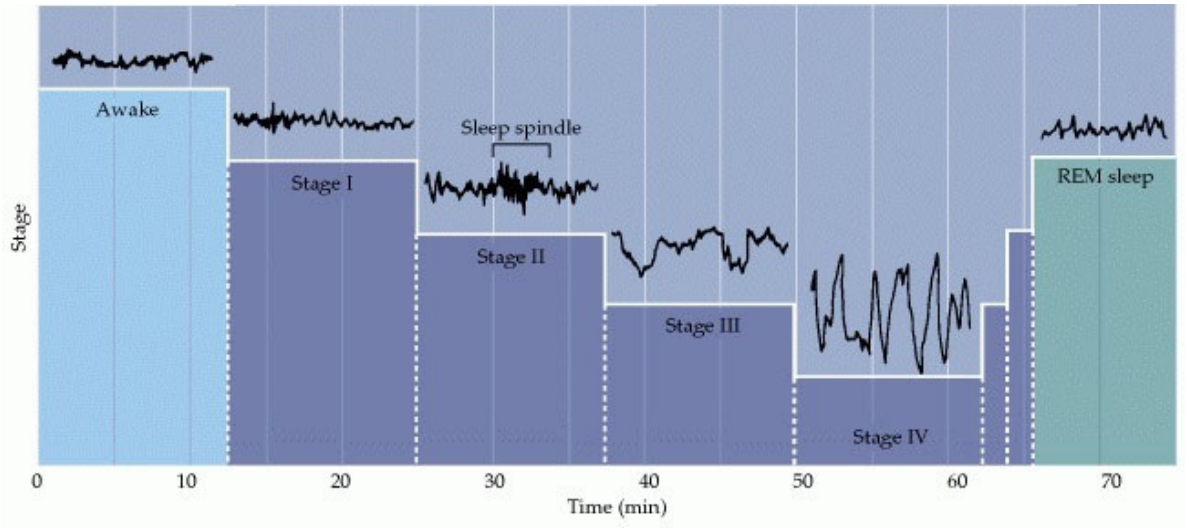

Figure 1: Schematic illustration of sleep stages and their corresponding EEG pattern.

Wakefulness is characterized by high frequency (15-60 Hz), low amplitude (~30 μV) beta oscillations. Stage 1 (or N1), the first stage of non-rapid eye movement (NREM) sleep is characterized by lower frequency (4- 8Hz) and higher amplitude (50- 100 μV) theta waves. In stage 2 (N2) so-called sleep spindles are observed, which are high frequency (10- 15Hz) and high amplitude (50- 150 μV) oscillations which appear periodically and last for several seconds. Stage 3 and 4(N3) are characterized by a further decrease in EEG frequency (1- 4Hz) and increase in amplitude (100- 150 μV) called delta waves. Deep (N3) sleep is followed by a period of rapid eye movement (REM) sleep, which is characterized by as its name says, by fast movements of the eyes (but paralysis of other voluntary muscles) and high frequency, low amplitude EEG waves that are more similar to the awake stage than to any other sleep stages (source: Hobson, 1989)

Sleep initiation (Stage 1) is characterized by the disappearance of high frequency beta waves, slow rolling of the eyes and a moderate decrease in heart rate (Burgess, Kleiman and Trinder, 1999). Sleep onset is further associated with changes in respiratory control that becomes unstable during transition from wake to sleep (Trinder et al., 1992). In healthy individuals, this stage lasts only a few minutes and is characterized by a low arousal threshold (Kryger, Roth and Dement, 2016).

The slowing of the brain (in terms of a reduction in EEG frequency and increase in amplitude) continues in Stage 2, which is further characterized by sleep spindles and K-complexes that are the stereotypical EEG signatures of stage 2 sleep (Kryger, Roth and Dement, 2016). It usually lasts 10-25 minutes and is marked by a further reduction in heart rate and respiration (Burgess, Kleiman and

Trinder, 1999; Colrain et al. 1987) and a higher arousal threshold, i.e., the same stimulus that leads to awakening in stage 1 would only evoke K-complexes in Stage 2 sleep (Wennberg, 2010).

Sleep stage 3 only last for few minutes in the first sleep cycle and there is a rapid transition to stage 4 sleep. Stage 3 and 4 (or N3 according to the newer nomenclature in sleep medicine) is often called deep sleep, delta sleep or slow wave sleep (SWS) and is marked by delta waves in the 1-4Hz range, often referred to as slow wave activity (SWA). In this stage, there are further reductions in heart and respiration rate (Kryger, Roth and Dement, 2016; Kirby and Verrier, 1989; Penzel et al., 2003). It lasts for about 20-40 minutes and is associated with highest arousal threshold, i.e., it is the most difficult to wake someone at this stage.

At the end of stage 4 sleep, one ascends back to lighter NREM sleep for a short period of time (1-2 minutes in stage 3 and ~10 minutes is stage 2), which is often accompanied by body movement, before entering rapid eye movement (REM) sleep. In REM sleep both brain activity and cardio-pulmonary physiology is closer to the awake state. This stage of sleep is typically linked to dreaming and in REM sleep one is completely paralyzed (only the muscles essential for breathing and for eye movement are active) (Kryger, Roth and Dement, 2016). Kleitman et al. in their original experiment found that there was a ~20% increase in respiration rate and ~10% increase in pulse rate in REM than the period of sleep preceding it (Aserinsky and Kleitman, 1953). REM sleep is either followed by a short period of wake or a return to stage 2 of NREM sleep where the cycle then repeats.

One full sleep cycle takes approximately 90 minutes and during a typical 8 hours sleep one goes through ~6 cycles. Figure 5 illustrates a normal hypnogram in a young and an older individual. One typical characteristic of these sleep cycles is that deep sleep (Stage 3 and Stage 4) proportionally decreases as one progresses through the cycles, while the proportion of REM sleep increases. During a good night's sleep, one spends around 50- 60% of time in light sleep, 15-20% in deep sleep, 20- 25% in REM sleep and about 5% or less is spent awake between sleep stages (Kryger, Roth and Dement, 2016).

1.4 Homeostatic control of sleep

According to a leading paradigm in sleep theory, sleep regulation can be divided into two interacting processes: 1. Homeostatic process (sleep debt that increases with the time awake) and 2. Processes controlled by circadian pacemakers (~24h self-sustained oscillator) (Borbély et al., 2016). Here, I

review studies pointing towards a homeostatic control of sleep and will present the leading hypothesis explaining the compensatory increase in sleep depth and duration after sleep deprivation.

1.4.1 Global

Sleep pressure or sleep debt increases with time being awake, meaning that being deprived of sleep will lead to a build up of sleep pressure, which has a direct effect on the subsequent sleep architecture. One study investigating the effect of daytime naps on sleep architecture showed an associated increase in sleep latency, a reduction in REM latency and a significant reduction in SWS (reduced delta and theta power) (Werth, Achermann and Borbély, 1996a). Additional evidence supporting the homeostatic model of sleep comes from total sleep deprivation studies, where participants are asked to stay awake for prolonged periods of time (e.g., for 24 hours). Studies have shown that during recovery sleep after total sleep deprivation SWA is highest during the first two sleep cycles and that stage 3 and 4 (N3) gets exponentially shorter as one proceeds through the cycles (Dijk et al., 1990). During recovery sleep participants tend to have elevated arousal thresholds, i.e., they are less likely to be awakened by external stimuli. It is important to mention here that REM sleep gets longer as one progress through the sleep cycles, suggesting different functions for NREM and REM sleep. The function of REM sleep remains an open question in neuroscience, it has been associated with brain development (as infants spend a considerably longer time in REM sleep) and with memory consolidation (Peever and Fuller, 2017). Sleep homeostasis is present in both mammalian and non-mammalian species including Drosophila and roundworms (Caenorhabditis elegans), however there is no single explanation that fully and convincingly explains the function of sleep (Zimmerman et al., 2008; Cirelli and Tononi, 2008).

1.4.2 Local sleep

For a long time, it was believed that sleep is a purely global phenomenon. However, local control of slow wave generation has been observed in both isolated cortices as well is in vivo. (Kristiansen and Courtois, 1949; Pigarev, Nothdurft and Kastner, 1997). In one study, the authors measured extracellular and single neuron activity in the visual cortex in monkey (Macaca fascicularis) while it was continuously caring out a visual task (Pigarev, Nothdurft and Kastner, 1997). When the monkey became tired, the response to visual stimulation was reduced and the background activity was more similar to that seen during sleep (short bursts followed by hyperpolarization). They also recorded

sleep-like activity in visual cortex V4, while the animal was awake. Furthermore, it suggested that SWA develops locally in areas that have been extensively used.

The most extreme cases of local sleep can be observed in animals that live in the water but need air to breath such as seals and dolphins that both show uni-hemispheric sleep (Mukhametov, Supin and Polyakova, 1977; Lyamin et al., 2012). Cortical sleep asymmetries can also be observed in humans, SWA is more dominant in the anterior parts of the brain, and it is the most apparent during the first sleep cycle, while REM frequency band is more prominent in posterior regions (Werth, Achermann and Borbély, 1996b).

Sleep deprivation leads to asymmetries in EEG power-spectra in the subsequent recovery sleep (Achermann, Finelli and Borbély, 2001). After 40h of total sleep deprivation, enhanced delta activity in anterior areas of the dominant hemisphere were observed. This suggests that brain areas that have been extensively used during wakefulness require more SWA to return to homeostasis. Further evidence for local sleep in humans has also come from a study, where prolonged tactile hand stimulation was delivered to one area only (Kattler, Dijk and Borbély, 1994). When the right arm was simulated prior sleep, there was a shift in interhemispheric asymmetry to the left hemisphere. This shift in asymmetry was mainly driven by an increase in delta power in the left hemisphere. The effect was small but significant, suggesting that neural populations active during sleep "need" more slow wave sleep in the subsequent sleep.

SWS appears to be locally controlled, further stressing the importance of sleep in areas with increased activity during the awake state. Despite the vast evidence indicating the importance of SWS to health and even survival, there is no single explanation that fully and convincingly explains its function (Cirelli and Tononi, 2008). Next, I will present some of the leading hypotheses for the role of SWS.

1.5 Sleep hypotheses

1.5.1 Restorative hypothesis

Benington and Heller proposed that sleep is driven by metabolic processes, specifically the depletion of glial (astrocytic) glycogen stores that in turn lead to increased extracellular adenosine levels that induce sleepiness and increase SWA (Benington and Heller, 1995). This theory of sleep fits nicely with the homeostatic sleep control hypothesis, where increased daytime activity causes an increase in metabolic need hence longer SWS is required to restore function (Borbély et al.,

2016). There are several lines of evidence that suggest that the key function of sleep is restorative. For example, increases in the expression of genes associated with lipid transport, maintenance of vesicle pools, antioxidant production and regulation of energy expenditure have been shown during sleep in mouse cortex and hypothalamus (Mackiewicz et al., 2007). Others have suggested that sleep is involved in the reduction in free radicals (hence reduced oxidative stress), arguing for sleep being an innate antioxidant of the brain. (Reimund, 1994).

Benington and Heller's hypothesis has been a good starting point for researchers to uncover the relationship between metabolic challenge during wakefulness and the compensatory mechanism during sleep. However, the full story is more complex than just glycogen and adenosine, as there are several different processes that are energetically demanding during the wake state that might drive/contribute to the homeostatic control of sleep (Scharf et al., 2008). Even though the metabolic regulation of sleep has good face validity, it still fails to explain why these processes cannot happen during wakefulness and why orchestrated neural activity (as observed during SWS) is necessary for restoration (Vyazovskiy and Harris, 2013).

1.5.2 Synaptic homeostasis, plasticity and memory consolidation

The synaptic homeostasis hypothesis proposes that during wakefulness, synaptic strengthening occurs due to learning and experience, which is associated with increased synaptic activity and metabolic need. In contrast, in SWS synaptic downscaling occurs with spontaneous neural activity serving to restore cellular homeostasis (Cirelli and Tononi, 2014). According to this hypothesis synaptic downscaling during SWS is necessary to renormalize synaptic connections by decreasing overall synaptic strength, which in turn maintains plasticity and the ability to form new connections.

Others have suggested that the key function of sleep is memory consolidation (Buzsáki, 1998). The central tenet of this hypothesis is that delta oscillations (or SWA) act as carrier waves from the hippocampus (associated with short term/episodic memory formation) to the neocortex where long-term memories are ultimately encoded (Buzsáki, 1998; Fujisawa and Buzsáki, 2011). This theory provides a framework for how memories travel and become encoded in the cortex. The memory consolidation theory of sleep is supported by evidence showing that brain areas active during learning are re-activated during sleep (Ji and Wilson, 2006). Although, others have also pointed out that sleep is not just critical for consolidating memories *after* learning, as sleep *before* learning also affects memory retrieval (Yoo et al., 2007). This might suggest that the primary function of sleep is not memory consolidation, but something more fundamental.

Despite numerous studies supporting the role of sleep in learning and memory, these theories still fail to explain why sleep deprivation has an umbrella effect on many cognitive/emotional processing and not just on memory (Frank, 2012).

1.5.3 Energy conservation

Chronic sleep deprivation in vertebrates and invertebrates has been associated with an increase in metabolism, as indicated by increased food intake and weight loss in rats and increased oxygen consumption (Rechtschaffen and Bergmann, 2002; Stephenson, Chu and Lee, 2007). Sleep has also been associated with reduced metabolism in humans. Next, I will review metabolic changes associated with SWS, particularly focusing on cerebral blood flow changes (CBF).

At the neural population level, the slow 1-4Hz oscillations of SWA are attributed to the alternation of short bursting ("on") periods with long silent lapses of hyperpolarization ("off") (Achermann and Borbely 1997; Amzica and Steriade 1997). This type of firing appears to reduce neurons' metabolic demands which are manifested as reductions in CBF and glucose metabolism in humans (Dang-Vu et al. 2005, Dang-Vu et al. 2007, Hofle et al 1997; Maquet et al. 1990).

To date, positron emission tomography (PET; ^{18}F-fluoro-2-deoxyglucose: ^{18}FDG and particularly water: $H_2{}^{15}O$) and to a lesser extent functional MRI (fMRI) have been the principal functional neuroimaging modalities used to study sleep-related changes in CBF and glucose metabolism during sleep (Braun et al. 1997; Hofle et al. 1997; Maquet et al. 1997; Andersson et al. 1998; Kajimura et al. 1999; Maquet et al. 1990; Buchsbaum et al., 2001; Nofzinger et al., 2002; Tushaus et al., 2017).

Table 1 summarizes the findings of $H_2{}^{15}O$ PET (water PET) studies investigating the effects of slow wave sleep on CBF (SWS vs awake). Compared to wakefulness (after sleep deprivation), SWS was characterized by a global reduction in CBF of 26% (Braun et al. 1997). Interestingly these studies highlighted that the areas exhibiting the greatest and most consistent reductions in CBF during SWS are the ones that are also involved in sleep generation such as the thalamus (Steriade et al., 2003), prefrontal cortex (Sterman and Clemente 1962; Massimini et al., 2004), basal ganglia (Lazarus et al., 2013), brainstem (Moruzzi and Magoun, 1949) or exhibit high activity during wakefulness e.g., frontoparietal association cortices and brain areas that form parts of the default mode network (Raichle et al., 2001), such as posterior cingulate cortex and precuneus (Braun et al. 1997; Hofle et al. 1997; Maquet et al. 1997; Andersson et al. 1998; Kajimura et al. 1999).

	Maquet et al. (1997)	*Braun et al. (1997)*	*Andersson et al. (1998)*	*Kajimura et al. (1999)*		*Hofle et al. (1997)*
Quantification	–	+	+	+		–
Global activity Adjustment	+	+	+	–	+	+
Brainstem	↓	↓		↓	↓	↓
Thalami	↓	↓	↓	↓	↓	↓
Basal forebrain	↓	↓		↓		
Basal ganglia	↓	↓		↓	↓	
Prefrontal cortex	Orbital ↓	DLPFC ↓ Orbital ↓	DLPFC ↓ Orbital ↓	↓		Orbital ↓
Parietal cortex	↓	↓	↓	↓	↓	
Precunes/posterior cingulate cortex	↓	↓	↓	↓	↓	
Anterior cingulate cortex	↓	↓	↓	↓		↓
Mesio-temporal cortex	↓	↓		↓		
Insula-temporal cortex		↓		↓		
Cerebellum		↓		↓	↓	↓
Remarks	CBF [(W + REMS)/2] – SWS	CBF W – SWS	CBF W – SWS	CBF W – SWS*	CBF W – SWS	CBF†

Table 1: Summary of $H_2{}^{15}O$ PET studies investigating the effects of slow wave sleep on CBF.

(Source: Maquet, 2000)

Negative correlations between SWA and CBF has been observed in the thalamus, brainstem, cerebellum, anterior/medial cingulate, prefrontal cortex, basal ganglia, insula and precuneus (Hofle et al., 1997; Tüshaus et al., 2017; Dang-Vu et al., 2005). Although, it should be remarked that Dang-Vu et al. did not find significant correlations between thalamic CBF and delta activity, though this study did not include any sleep deprivation or wake scans. This highlights the importance of study design when interpreting findings. Whereas significant positive correlation has been observed in visual and auditory cortices (Hofle et al., 1997; Tüshaus et al., 2017). Positive correlation was only present in regions that also showed increased CBF during SWS compared to wake, which might reflect activation associated with dreaming during SWS (Cavallero et al., 1992).

These studies show a link between SWA and reduced CBF during sleep suggesting that deep sleep helps to conserve energy. In contrast, the build-up of sleep pressure has been associated with the opposite finding, as CBF has been shown to increase from morning to evening; a finding which has been shown to be further augmented by sleep deprivation (Elvsåshagen et al., 2019). Despite the negative relationship between brain metabolism and SWS, the energy conservation theory of sleep remains an incomplete theory, as it fails to explain the increased metabolism during REM (Hofle et al 1997).

1.6 Interim summary 1

So far, I have highlighted the importance of sleep and described its homeostatic regulation - that links sleep pressure to slow wave activity. Furthermore, I have presented some of the leading theories for slow wave sleep and their limitations. While these theories all hold some face validity, they are not absolute, i.e., no one theory gives a full explanation for why we sleep. On the other hand, they highlight the importance and multifaced role of sleep. Next, I will present another question that similarly to sleep, has puzzled scientist for decades, if not for centuries: “How does the brain clear itself without a lymphatic system?”. Moreover, I will present evidence that suggests a molecular/mechanistic link between SWS and brain’s waste clearance system.

1.7 Glymphatic system

1.7.1 Overview

The clearance of cellular metabolites and other solutes such as soluble proteins, and excessive interstitial fluid (ISF), is critical to the maintenance of cell homeostasis. In peripheral tissue, these solutes are filtered and returned to the general circulation by lymph vessels that form the lymphatic system (Liao and Padera, 2013). Here, the density of lymph vessels correlates well with tissue metabolic need, raising the important question: How does a highly metabolically active organ such as brain clear itself of cellular metabolites and excess interstitial fluid without a conventional lymphatic system (Liao and Padera, 2013)? The brain is an exceptional organ in many ways, including the fact that synaptic transmission is exquisitely sensitive to the chemical composition of the extracellular fluid suggesting the “need” for a unique macroscopic waste clearance system (Holz and Fisher 1999). Recently, Iliff and Nedergaard *et al.* have proposed that the brain utilizes convective influx of cerebrospinal fluid (CSF) through the periarterial space as a mechanism to achieve this. Here, inflowing CSF exchanges with parenchymal ISF and consequently clears solutes from the interstitial space (Iliff et al., 2012; Iliff and Nedergaard, 2013). They named this macroscopic waste clearance system the ‘Glymphatic system’, G for glia because astrocytes initiate the exchange between CSF and ISF, and lymphatic for functional similarities with the conventional lymphatic system. Before considering current knowledge on the function and mechanisms of the glymphatic system in more detail, I will first review the anatomy and driving forces that are believed to enable the exchange of CSF and ISF.

1.7.2 CSF circulation

CSF is continuously produced by the choroid plexus. Importantly, the whole CSF volume (125-150 ml in a healthy young brain) is completely re-circulated around four times per day (Johanson et al., 2008), resulting in the constant production and removal of CSF. Until recently, it was believed that the main route of CSF uptake was through the arachnoid granulations (Pollay, 2010). However, current evidence suggests that the bulk of CSF flow is in fact drained via the glymphatic system. Concurrent discovery of dural lymphatic vessels, suggests that at least part of the exchanged CSF-ISF and macromolecules cleared via the glymphatic system is taken up by rudimental dural lymphatic vessels that are upstream of the cervical lymphatic nodes (Aspelund et al., 2015; Louveau et al., 2015). Unlike peripheral tissues, the brain parenchyma completely lacks conventional lymph vessels that would allow the removal of ISF. However, CSF bathes the whole of the brain parenchyma entering deep tissue along perivascular spaces that surround penetrating arteries that descent into the brain from the pial surface (Ahn and Prince, 2013). These perivascular spaces have long been recognized and are known as Virchow-Robin spaces. As illustrated in Figure 2, this peri-vascular space is bordered by a leptomeningeal cell layer on the inner wall adjacent to the vessel, and an outer wall facing the perivascular astrocytic end feet. A unique characteristic of the brain's vasculature is that it is surrounded by astrocytic end-feet throughout the whole parenchyma, which contain high density of aquaporin 4 (AQ4) water channels (Ahn and Prince, 2013).

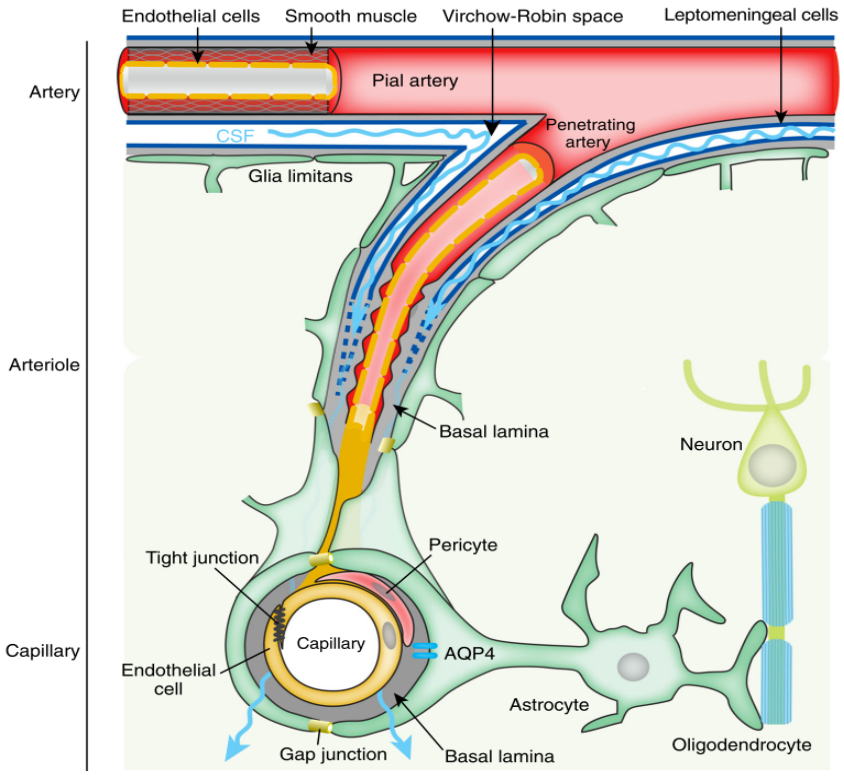

Figure 2: Schematic diagram of the neurovascular unit.
The neurovascular unit consists of endothelial, smooth muscle, leptomeningeal cells, astrocytes, and neurons. (source: Nedergaard et al. 2015.)

As the pial artery branches into a penetrating artery and dives deep into the parenchyma it drags with it a meningeal layer giving rise to the Virchow-Robin space. Consequently, this space is surrounded by a leptomeningeal cell layer on both its inner and outer walls. However, as the penetrating artery dives deeper and branches into arterioles the leptomeningeal cell layer begins to disappear and become continuous with the basal lamina. The neurovascular unit is linked to the loose structure of extracellular matrix proteins of the basal lamina that allows CSF influx into the parenchyma with minimal resistance (Barakat and Redzic, 2015).

1.7.3 Basic mechanism

Iliff et al (2012) used in vivo 2-photon imaging to visualize the temporal distribution of fluorescent dye after subarachnoid and intra-cisternal injections in mice. Using this technique, they showed that CSF within the subarachnoid space first passes through the Virchow-Robin space then moves

along the perivascular space into the brain parenchyma acting like a drainage system for interstitial solutes. Both low (TR-dr, 3kD) and high molecular weight molecules (FITC-d2000, 2000kD) rapidly moved into the perivascular space. However only the low molecular weight TR-d3 entered the interstitial space (FITC-d2000 was restricted to the perivascular space) (Iliff et al., 2012). Due to the depth imaging limitations of 2-photon microscopy they dissected the brains to analyze the distribution of the dye at various time points. This technique showed that dye moved rapidly into the parenchyma along the penetrating arteries then arterioles to reach the capillary bed. At early time points the dye was not detected around veins. However, an hour after injection, the dye started to accumulate around the capillaries, reached the parenchymal venules and exited through perivenous routes. Importantly, this group also showed that tracer injected directly into the cortex, striatum, or thalamic parenchyma was cleared along the same pathways (Iliff et al., 2012). In order to investigate the significance of AQ4 channels in this exchange of CSF and ISF, they next deleted the Aqp4-gene. In these AQ4 KO mice the rate of clearance of [^{3}H]mannitol from the interstitium was reduced by 70% (interestingly this matches the clearance rate of [3H]dextran-10 that has 55 times greater molecular size in wild type mice). Furthermore, clearance of radio-labelled soluble amyloid beta (^{125}I-amyloid β1–40) was reduced ~55% in AQ4 KO mice. Together, these studies suggest a central role of AQ4 in the bulk movement of CSF through the brain parenchyma. They also highlight a role for the glymphatic system in clearing amyloid-beta from the brain, with implications for the development and progression of Alzheimer's disease (Iliff et al., 2012).

Further support for the "classical glymphatic"[1] clearance mechanism has come from Aspelund et al. and Louveau et al., two independent groups who recently showed the existence of rudimental dural lymphatic vessels that are downstream from the glymphatic system (Aspelund et al., 2015; Louveau et al., 2015). One group injected fluorescent dye into the parenchyma of mice, then showed that 2 hours later this dye exited along the perivenous space to the CSF (Aspelund et al., 2015). Lymphatic clearance of the exchanged ISF was confirmed by presence of an intense fluorescent signal in the deep cervical lymphatic nodes. Furthermore, transgenic mice completely lacking dural lymphatic vessels showed reduced macromolecule clearance from subarachnoid space into cervical lymph

[1] By classical glymphatic clearance, I mean influx of CSF along the periarterial and exit along the perivenous space; others have suggested that the injected CSF leave along a periarterial basement membrane (Albargothy et al., 2018)

nodes, though glymphatic clearance of the tracer was not affected (indicated by detectable perivascular outflow of the tracer in the subendothelial and perivascular spaces). Together, these findings suggest that the glymphatic system communicates with the systemic lymphatic system through rudimentary dural lymphatic vessels (Aspelund et al., 2015). High resolution contrast enhanced MRI also supports the existence of similar dural lymphatic vessels in humans (Absinta et al., 2017).

1.7.4 Driving forces of the Glymphatic system

Glymphatic filtration is driven by several forces. First, transport of CSF along the periarterial spaces is driven by a combination of a CSF pressure gradient (established by the constant production of CSF), and second by respiratory and arterial pulsations (Yamada et al., 2013). The pulse wave generated by endothelial smooth muscles travels along the whole length of the pial arteries through to the penetrating arterioles. The importance of arterial pulsatility is supported by studies using dobutamine (an adrenergic agonist) that increases both CSF influx to the parenchyma and pulsatility of the pial arteries. Furthermore, ligation of the carotid artery results in a reduction in pulse waves and influx of CSF into the brain parenchyma, consequently decreasing CSF - ISF exchange (Iliff et al., 2013b).

1.8 The glymphatic system is active during sleep

Recent studies have proposed that glymphatic clearance might contribute to or perhaps be the primary reason for the need for sleep across species. In support of the relationship between sleep and glymphatic clearance, Xie et al. found that during natural sleep (in mice) there is a rapid increase in the appearance of fluorescent dye along the periarterial spaces and bulk flow to the parenchyma after its injection into the cisterna magna in mice. The same effect is observed in anesthetized mice (Xie et al., 2013, Iliff et al., 2012). Furthermore, they found a ~95% decrease in periarterial and parenchymal dye influx in awake compared to sleep using 2-photon microscopic imaging (Figure 3). Interestingly, there was no significant difference between the distribution of the fluorescent dye (FITC-dextran, which is a low molecular weight tracer, 3 kD) between naturally sleeping and anesthetized mice with ketamine/xylazine mixture (Figure 3**,** C and D), suggesting that parenchymal CSF influx is state- rather than circadian rhythm-dependent (Xie et al., 2013). The increase in dye distribution was accompanied by an increase in cortical delta activity measured by Electrocorticography (ECoG). As previously mentioned, CSF influx along the periarterial space is

partly driven by arterial pulse waves and positively correlated with noradrenergic function (Iliff et al., 2012). However, it is unlikely that suppression of arterial pulsatility underlies this reduction of CSF movement to the parenchyma during wakefulness because the noradrenergic system that promotes arousal is more active during wake.

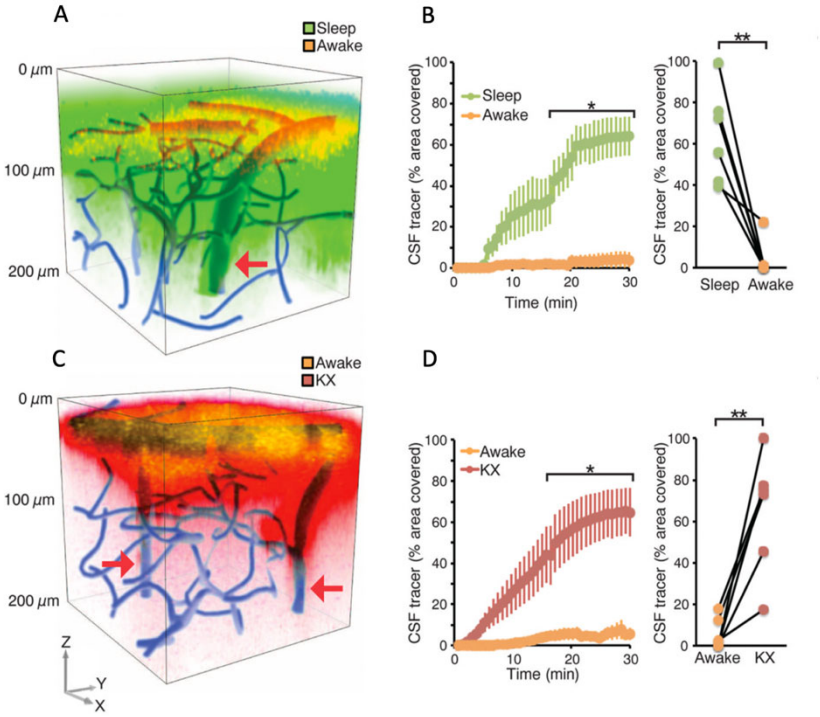

Figure 3: Glymphatic activity during sleep in mice.

A: Schematic illustration of the area covered by the CSF tracer during natural sleep (green) and during wakefulness (yellow); **B**: Distribution of dye with time in the imaged volume during natural sleep (green) and awake (yellow), right- volume covered at 30minute time point : **C**: Schematic illustration of the area covered by the CSF tracer during anaesthesia (red) and during wakefulness (yellow); **B**: Distribution of dye with time in the imaged volume during anaesthesia (green) and awake (yellow), right- volume covered at 30minute time point (source: Xie et al., 2013).

Real time iontophoretic tetramethyl- ammonium (TMA) technique has been used to assess changes in interstitial volume fraction. Using this technique, sleep was associated with a 60% increase in interstitial volume fraction (expanding from ~15% to ~24%). It has been proposed that this expansion of the interstitial space during sleep and anaesthesia facilitates exchange of CSF with ISF

with less resistance (Xie et al. 2013). This change in interstitial volume can be (at least partly) attributed to the change in noradrenergic system that is the major driver for arousal (Xie et al., 2013, Berridge and Waterhouse, 2003). Xie et al. have confirmed this in mice by applying a noradrenaline antagonist locally, which resulted in an increase in interstitial volume comparable to that observed during natural sleep and anaesthesia. Moreover, it resulted in increased delta power indicated by ECoG.

It has been shown that noradrenaline application increases astrocyte volume that in turn reduces the interstitial space volume (Sherpa et al., 2016), hence the reduced noradrenergic tone during SWS is a likely driver of the volumetric changes associated with sleep (I will further discuss this relationship in the next section).

Moreover, blocking noradrenaline signalling in the choroid plexus leads to increased CSF production (Nilsson, Lindvall-Axelsson and Owman, 1992). Consequently, it is believed that the reduction of noradrenaline signalling that occurs during sleep leads to an increase in CSF pressure and a decrease in resistance within the interstitial spaces, facilitating increased exchange between CSF and ISF (through AQ4 channels) and increasing removal of extracellular waste products. In support of this, rats receiving an agent that blocks noradrenaline release from the locus coeruleus (dexmedetomidine) in combination with low-dose isoflurane show a 30% increase in glymphatic transport function compared to rats receiving isoflurane alone (Benveniste et al., 2017). The inverse relationship between glymphatic filtration and the adrenergic activity in rodent models suggest that arousal is an important factor in glymphatic function. On the other hand, delta activity during SWS and anaesthesia seem to facilitate glymphatic clearance.

Next, I will review some experiments linking neuromodulation, changes in interstitial fluid composition/volume and SWA.

1.8.1 What is the link between slow wave sleep and the Glymphatic system?

Arousal and wakefulness are characterized by increased activity of brainstem nuclei (the ascending arousal network) that release several neuromodulators that promote arousal including noradrenaline, acetylcholine, histamine, dopamine and hypocretin (orexin) (Lee and Dan, 2012). These neuromodulators have several distinct effects on both neuronal and non-neuronal cells (glia cells) including membrane properties such as permeability to certain ions, electrical activity (neuronal spiking), intracellular signalling and morphology (O'Donnell et al., 2012; Sherpa et al., 2016). However, the effect of neuromodulation on EEG activity is still not very well understood.

One study looked at how neuromodulation affects cortical electrical (recorded from both neurons and glia cells) activity, K^+ concentration and CBF during SWS (induced by ketamine-xylazine in cats) – wake transition (Seigneur et al., 2005). When cholinergic neurons in brainstem and basal forebrain were electrically activated (pedunculopontine tegmental nucleus and nucleus basalis) during natural sleep there was an increase in CBF, decrease in extracellular K^+, glial hyperpolarization and neural depolarization. The net effect of acetylcholine release to the cortex was a shift in neuronal oscillation form delta activity (1-4Hz) to fast rhythms (20-40Hz). However, it is not entirely clear whether the change in extracellular ion composition during the sleep-wake cycle is a direct effect or secondary to the change in electrical activity.

Another study aiming to elucidate this question, used a cocktail of wake promoting neuromodulators (noradrenaline, acetylcholine, histamine, dopamine, and hypocretin/orexin) and observed a rapid increase in K^+ (0.43 ± 0.07mM) independent of synaptic activity (Ding et al., 2016). Next, they investigated extracellular ion composition in naturally sleeping mice and found that arousal (transition from SWS to awake by external stimulation) was characterized by a rapid increase in K^+ (0.40 ± 0.05mM; which is ~10% change) that quickly returned to baseline when the mice fell back to sleep. These changes were comparable with those observed with isoflurane anaesthesia, i.e. a sharp decrease of K^+ (0.37± 0.06mM). Sleep and anaesthesia were further characterized by an increase in Ca^{2+}, Mg^{2+}, H^+ and expansion of the extracellular space. This group prepared two artificial CSF solutions (aCSF) based on the ionic concentrations measured from samples from awake and asleep mice, respectively. The hypothesis was that either preparation would tend to induce wakefulness or sleep. First, they delivered the wake-inducing aCSF to the left hemisphere of sleeping mice, which resulted in a significant decrease in delta activity (34± 5%) in the ipsilateral but not in contralateral hemisphere. In contrast, when they applied the sleep inducing aCSF to awake mice, they observed a 43± 13% increase in delta activity. Furthermore, the TMA+ method indicated that changing the sleep aCSF to an awake aCSF resulted in 21.7 ± 1.2% decrease, while changing from awake aCSF to sleep aCSF resulted in 32.2 ± 2.9% increase in local extracellular space. This is comparable with Xie et al. findings in naturally sleeping mice (Xie et al., 2013). Nevertheless, the most interesting finding of the study was that altering the extracellular ion content can override behavioural states—i.e. when awake mice were infused with sleep inducing aCSF there was an increase in SWA and a decrease in electromyography (EMG) activity, while awake inducing aCSF lead to reduced delta activity and increased EMG in sleeping mice. This study showed that there is state dependent regulation of extracellular ion concentrations of K^+, $Mg^{2+,}$ Ca^{2+} and H^+ and these concentrations can maintain sleep related changes in neuronal and glial cell population.

A recent study suggests that astrocytes actively participate in SWS, showing that a distinct variation in astrocytic Ca^{2+} signalling occur across sleep-wake cycles in naturally sleeping mice. SWS is associated with a decrease in astrocytic Ca^{2+} signalling. Interestingly, there is also an increase in Ca^{2+} before transitioning between sleep stages (SWS- to REM) and SWS to wakefulness. During the SWS to wake transition, the peak in astrocytic Ca^{2+} precedes the change of electrical activity measured via ECoG, suggesting that astrocytes might play a direct role in sleep-wake transitioning. Furthermore, knocking out a gene involved in astrocytic Ca^{2+} signalling resulted in impaired SWS with increased levels of awakenings and abnormal brain rhythms (Bojarskaite et al., 2020).

These studies suggest a functional link between neurotransmission, extracellular ion composition, CBF, glymphatic system (as it is tightly linked to interstitial volume) and SWS with astrocytes being an integral part of this link.

1.9 Why should we be interested in the Glymphatic system? - Pathology of the glymphatic system

There is considerable evidence that many of the proteins associated with neurodegeneration are cleared via the glymphatic system. A hallmark of neurodegenerative disorders is protein aggregation, formation of fibrillary tangles of hyperphosphorylated/misfolded proteins (Soto and Pritzkow, 2018). Once an oligomer forms it attracts and initiates oligomerization of other protein monomers in a prion like fashion (Soto and Pritzkow, 2018). Neurodegeneration and dementia affect 1 in 14 people aged over 65 and 1 in 6 in over 80 years old (Prince, M et al., 2014). The global population as well as the average life expectancy are both increasing and so are dementia cases. Global dementia cases are projected to triple in the next 30 years (Dementia fact sheet December 2017; World Health Organisation). This puts immense pressure not just on patients and their families, but also on health and social care, which comes with significant financial burden. Currently there is no effective treatment for dementia. Costs associated with dementia in the UK is £25billion pounds each year which is predicted to increase to £55 billion pounds in the next 25 years (Prince, M et al., 2014). Thus, understanding the glymphatic system and its role in protein waste clearance in neurodegenerative disorders is potentially of extreme importance, as it may open new doors for finding effective treatments. In this section, I will present animal and human studies highlighting the importance of glymphatic system function in neurodegenerative conditions and its relationship with sleep.

Figure 4C illustrates a simplified model that links changes in glymphatic system with protein aggregation in neurodegenerative disorders. According to this model, reduced glymphatic clearance leads to increased protein aggregation that in turn leads to impaired glymphatic clearance (essentially forming a positive feedback loop) (Nedergaard and Goldman, 2020). Next, I will list some of the key studies that demonstrate a link between vascular pathology/neuroinflammation/aging and sleep and impaired glymphatic function.

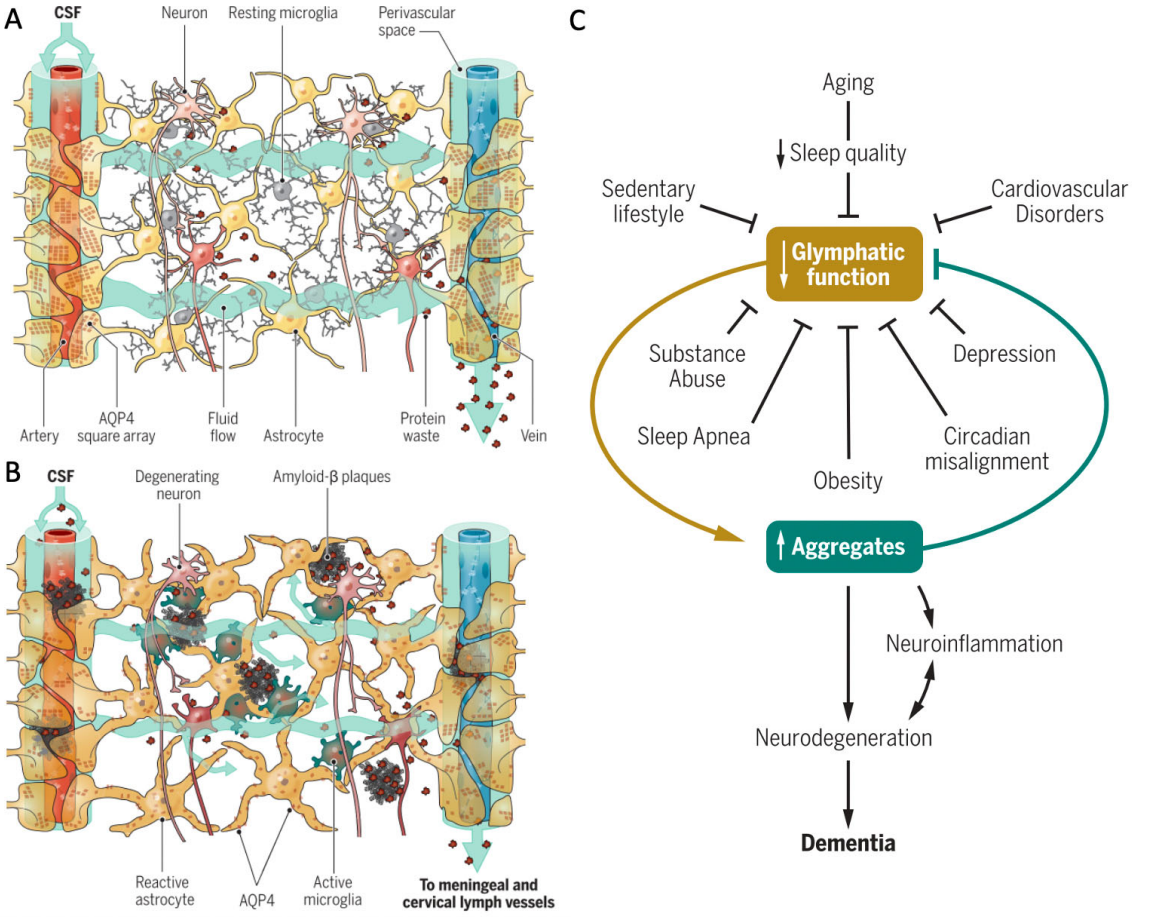

Figure 4: Glymphatic system in health and disease

A: Schematic illustration of healthy perivascular spaces and the interstitium. CSF arrives to the parenchyma along the periarterial space and enters the interstitial space via AQ4 channels that are highly polarized at the astrocytic end feet. Fluid flows through the interstitium clearing protein waste and exits to the perivenous space. **B:** Illustration of pathological perivascular space and interstitium in Alzheimer's disease. CSF entry to the periarterial space is compromised by amyloid

beta plaques, by swelling of astrocytic end feet and displacement of AQ4 channels form the end feet. Fluid flow through the interstitium is impaired due to a drop in fluid pressure and increased resistance due to increases in astrocyte (astrogliosis) and microglia volume, thus reducing protein waste clearance. Exit to the perivenous space is further compromised by amyloid beta plaques and displacement of AQ4 channels from the end feet. **C:** A simplified model showing hypothetical/established connections between factors reducing glymphatic function and increase protein aggregation linked to neuroinflammation and neurodegeneration. (source: Nedergaard and Goldman, 2020)

1.9.1 Traumatic brain injury

In mice model of traumatic brain injury glymphatic clearance was reduced by ~60% after 1 month of injury, which was further augmented by AQ4 knockout (Iliff et al., 2014). Post traumatic brain injury was associated with reactive astrogliosis, as shown in Figure 4B, and displacement of AQ4 channels from astrocytic end feet. The increase in astrocyte volume associated with astrogliosis increases the resistance to fluid flow through the tissue, reducing glymphatic clearance. This results in reduced phosphorylated tau clearance and increased neuroinflammation. In a separate study, it was shown that the glymphatic system transports biomarkers of traumatic brain injury to the blood via the cervical lymphatic system, which was reduced/or completely abolished with suppression of the glymphatic system, i.e., with sleep deprivation and cisternotomy in mice (Plog et al., 2015).

1.9.2 Vascular pathology

Amyloid beta deposition was found in vascular walls that impaired ISF drainage, furthermore ischaemic stroke further reduced ISF drainage, suggesting that vascular pathology affects glymphatic clearance (Peng et al., 2016; Arbel-Ornath et al., 2013).

1.9.3 Role in neuro-inflammation

Dural lymphatic vessels seem to be involved in both CSF drainage from perivascular space and immune cell response. Abolition of dural lymphatic vessels resulted in reduced inflammatory response in animal model of multiple sclerosis (induced by brain reactive T cells) (Louveau et al., 2018). Neuroinflammation leads to astrogliosis and activation of microglia that reduces interstitial volume, thus increasing resistance to fluid flow, as illustrated on (Figure 4B) (Webers, Heneka and Gleeson, 2019).

1.9.4 Aging and sleep

Age is the most prominent risk factor for developing neurodegenerative disorders linked to protein aggregation (Hoyer, 1994). Impairment of dural lymphatic vessels have been observed in aged mice, and associated with reduced glymphatic clearance and cognitive decline (Da Mesquita et al., 2018). On the other hand, when this group recovered the function of these vessels it also recovered improved learning and memory in aged mice. In addition, they found that in mice model of Alzheimer's disease there was deposition of amyloid beta in the meningeal lymphatic vessels that may contribute to the reduced clearance. Human studies with intrathecal administration of contrast agent showed reduced glymphatic as well meningeal lymphatic clearance with aging, suggesting a similar mechanism to that observed in aging mice (Zhou et al., 2020).

There is a significant change in sleep architecture with age; episodes of insomnia become more common, sleep onset latency becomes longer, wake after sleep onset (WASO) increases, there is more stage 1 sleep and there is a substantial reduction in NREM sleep especially stage 3 and 4 sleep (Landolt and Borbély, 2001) as shown in Figure 5. In mice, glymphatic clearance positively correlated with delta power (or SWA) and negatively with beta power and heart rate during anaesthesia (Hablitz et al., 2019), emphasizing the importance of SWA for glymphatic clearance. There is substantial evidence for the importance of SWS for effective glymphatic clearance in both mice and humans.

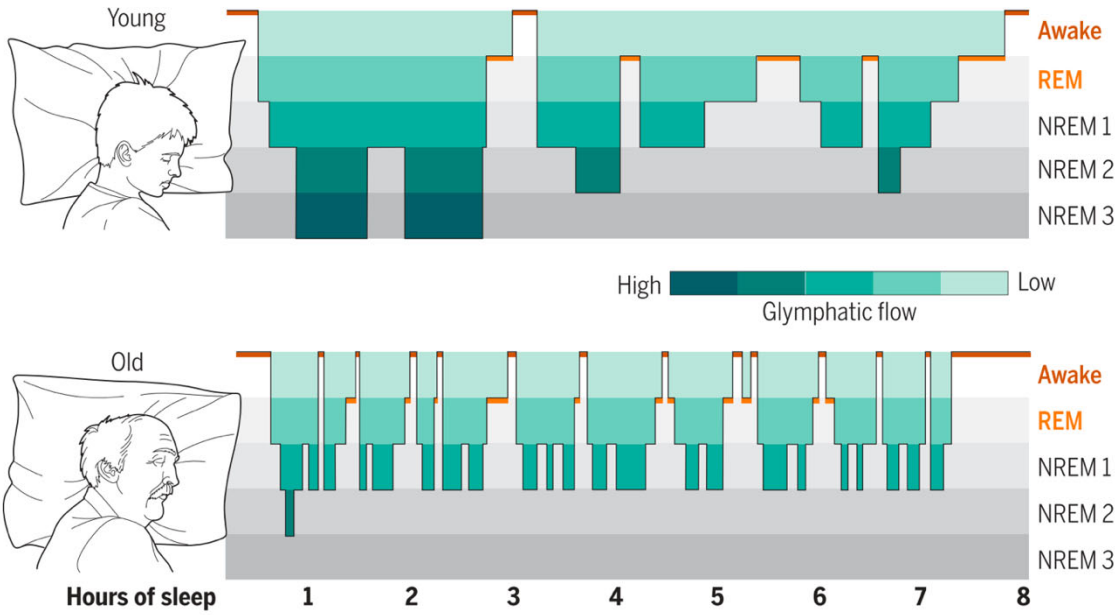

Figure 5: Illustration of typical hypnogram of young and old individuals.

(source: Nedergaard and Goldman, 2020)

Extracellular amyloid beta and tau tend to fluctuate with the sleep wake cycle in mice and in humans. Disturbed sleep has also been linked to increases in amyloid beta and tau production and reduced clearance (Lim, Gerstner and Holtzman, 2014; Holth et al., 2019; Wang and Holtzman, 2019). Increases in amyloid beta aggregation and deposition have also been shown in chronic sleep deprivation in animal models of Alzheimer's disease (Wang and Holtzman, 2019). A single night of sleep deprivation in humans has been shown to significantly reduce amyloid beta clearance, suggesting a similar mechanism in humans (Shokri-Kojori et al., 2018). Human studies have also demonstrated a link between reduced SWA during amyloid beta deposition (Mander et al., 2013; Mander et al., 2015). Furthermore, disruption in SWA was associated with an increase CSF amyloid beta. This effect was specific to amyloid beta and SWA, as there was no significant correlation with total protein, hypocretin or tau concentration in CSF and total sleep time/ sleep efficiency (Ju et al., 2017). On the other hand, tau concentration in CSF was associated with sleep quality over several days. A longitudinal study investigating the relationship between cognitive performance, brain imaging and CSF Alzheimer's biomarkers showed an inverse relationship between cognitive decline and reduced SWA that was linked to tau pathology. The authors suggested that reduced SWA activity could serve as an early marker for tau pathology in Alzheimer diseases (Lucey et al., 2019).

1.10 Interim summary 2

In the previous sections I described the proposition of a novel mechanism for brain waste clearance, the Glymphatic system, which utilizes the influx of CSF in the periarterial space, where it exchanges with interstitial fluid. The exchanged fluid passes through the tissue clearing protein waste and exists via the perivenous space. This system has been shown to be mostly active during sleep, which has been associated with reduced noradrenergic tone during slow wave sleep. The main driver of increased glymphatic clearance during SWS has been associated with expansion of interstitial volume fraction, i.e., reduction in glial cell volume. Moreover, I showed evidence for glymphatic system clearance of proteins associated with neurodegeneration and dementia, showing an association between aging related decline in SWS and reduced glymphatic clearance.

1.11 Imaging the Glymphatic system in human

The glymphatic system is an extremely exciting area to study to improve our understanding of basic central nervous system (CNS) physiology, clearance of misfolded proteins, understanding the need for sleep, how systemic and CNS immune systems communicate and their implication for neurological/psychiatric conditions. To further our understanding of the glymphatic system as well as to evaluate treatment targeting the glymphatic system, we need ways to measure it in a non-invasive manner. The importance of imaging the glymphatic system is further emphasized by a recently published article, that showed that the outcome of antibody treatment against amyloid beta in mice model of Alzheimer's disease was dependent on functional meningeal lymphatic vessels that are linked to the glymphatic system (Da Mesquita et al., 2021; Aspelund et al., 2015). However, imaging the glymphatic system in vivo in a non-invasive manner is not a mundane task. Here, I will briefly review key imaging studies investigating the glymphatic system in humans. Finally, I will discuss the multi-modal MRI experiment I developed and used in this thesis to attempt to investigate the glymphatic system in a non-invasive manner in humans.

1.11.1 Injection studies

Since the formulation of the glymphatic system hypothesis, several pre-clinical and human studies have attempted to describe the brain's fluid dynamics. A wide range of techniques have been tested and proposed to show potential sensitivity to glymphatic system related changes. The earliest and most direct techniques involved injection of labelled tracers such as fluorescent dyes, radio-labelled isotopes, or gadolinium directly in the CSF spaces and then measuring the spatio-temporal

distribution of the dye (Iliff et al., 2012; Gaberel et al., 2014; Eide and Ringstad, 2015). Due to the invasive nature of injection studies, there have only been a handful of human clinical studies (for CSF leakage detection, or in idiopathic normal pressure hydrocephalus) where they administered gadolinium intrathecally and observed a brain-wide parenchymal distribution (Eide and Ringstad, 2015; Ringstad, Vatnehol and Eide, 2017; Eide et al., 2018).

In a case study, a patient diagnosed with a CSF leakage was administered gadolinium (gadobutrol) intrathecally and this was shown to be widely distributed across the whole CNS between 1 and 4.5 hours after injection, suggesting that contrast agent is moving from the CSF and reaching perivascular spaces in the parenchyma (Eide and Ringstad, 2015).

In another study, 15 idiopathic normal pressure hydrocephalus patients and 8 controls with suspected CSF leakage were intrathecally injected with Gadobturol and T_1-weighted MRI images captured at various time points (1–2 h, 2–4 h, 4–6 h, 6–9 h, and 24 h after injection) over the subsequent 24 hours. In this study, T_1 enhancement by gadobutrol peaked overnight in both groups suggesting that this might be due to enhanced glymphatic flow during sleep (Ringstad, Vatnehol and Eide, 2017). Furthermore, in a separate study intrathecal administration of contrast agent in 19 individuals revealed that cervical lymph node enhancement coincides in time with peak glymphatic enhancement. CSF enhancement peaks before glymphatic enhancement (defined as parenchyma enhancement) 4-6h after the injection. The glymphatic and cervical lymph node enhancement peaked 24h after the injection. Although it is important to note here that they acquired images 2–4h, 4–6h, 6–9h, 24h, and 48h after injection. So, a peak 24h after injection does not mean that the contrast agent took 24h to reach the cervical lymph node. This observation that cervical lymph node enhancement coincides with glymphatic rather than with CSF enhancement suggests that there might be an anatomical link between the perivascular compartment and lymphatic pathways (Eide et al., 2018).

One of the obvious limitations of these studies is the potential risks associated with gadolinium, as intrathecal injection may cause gadolinium encephalopathy (Reeves et al., 2017; Provenzano, Pellis and DeRiggi, 2019). Furthermore, these types of studies take a long time as images must be acquired at multiple time points and cannot give information about microstructural changes that are necessary to gain deeper understanding of the glymphatic system.

Consequently, non-invasive MRI techniques have been proposed with potential sensitivity to glymphatic system related changes in humans. As the glymphatic flow is expected to modulate the relative sizes of intracellular, interstitial and CSF fluid compartment, studies have focussed on MRI

techniques sensitive to water compartmentalization, such as diffusion weighted MRI (dwMRI), volumetry and CSF flow quantification. Here, I will briefly review studies looking at diffusion as well volumetric/flow changes associated with time of day (TOD) and sleep.

1.11.2 Time of day studies

TOD studies revealed that parenchymal volume seems to decrease from morning to evening (Nakamura et al., 2015). This decrease seems to be more prominent in the frontal and temporal lobes than in other areas. Unsurprisingly this decrease in grey matter (GM) and white matter (WM) volume from morning to evening has been associated with an increase in CSF (Trefler et al., 2016). Thomas et al. 2018 also observed an increase in GM mean diffusivity (MD) (derived from diffusion tensor imaging (DTI)) along major fissures and sulci from morning to evening (Thomas et al., 2018). Application of a dual compartment model that accounted for an isotropic (free water) compartment revealed that the increase in GM MD was due to an increase in free water volume fraction.

Consistent with the previous findings, a recent study showed an overnight increase in GM and WM volumes (non-significant) and a converse decrease in CSF (Tuura et al., 2021). Different from the other studies, here they recorded overnight EEG and correlated this with brain tissue volume changes as well as with diffusion measures obtained from DTI. They observed overnight increase in MD in cingulate gyrus, basal ganglia, thalamus, cerebellum, brainstem and bilateral white matter regions. Overnight decrease in MD was only observed in CSF areas and there was significant positive correlation with the change in MD and CSF. Interestingly, the increase in MD in the parenchyma correlated with the proportion of total time spent in REM sleep and negatively with NREM. The unexpected positive correlation between MD and REM may suggest that diffusion in the brain is affected by more complex interactions of sleep stages than just by the sheer amount of SWA. However, it should be noted that diffusion and EEG were not recorded simultaneously, and brain diffusivity was not measured during sleep.

All these studies consistently show reduced CSF from evening to morning, which is particularly interesting because CSF production peaks between 11pm and 2am (42 ± 2ml/h) and is lowest between 4pm and 6pm, so one would expect to have the largest CSF volume in the morning (Nilsson et al., 1992). The fact that these studies consistently show the opposite trend suggests that there might be a higher re-absorption during sleep than during wake arguing for glymphatic clearance during sleep. Although, it should be remarked that TOD studies cannot uncover the dynamic changes happening during sleep (e.g., changes specific to sleep stage, such as expansion of

interstitial space in response to SWA), as they only measure the "after effect" of sleep. When talking about imaging the glymphatic system, it is worth distinguishing which part of the glymphatic system is being measured, the external i.e., CSF movement in perivascular spaces/meningeal lymphatic vessels or the internal, i.e., fluid flow through the tissue. To investigate changes associated with the glymphatic system in a more direct manner, one must acquire images sensitive to water compartmentalization (internal waste clearance related change in interstitial volume change) or CSF flow (external waste clearance) during sleep.

1.11.3 Sleep studies

To date, there are only 2 published human studies that have investigated the glymphatic system during sleep with MRI.

One study focusing on the external glymphatic system, simultaneously measured BOLD fMRI dynamics, EEG and CSF dynamics (Fultz et al., 2019). They measured occipital EEG waves to determine sleep/wake state, grey matter blood oxygen level dependent (BOLD) signal to assess haemodynamic oscillations in addition to measuring CSF dynamics in the fourth ventricle. NREM sleep was associated with high amplitude low frequency (0.05Hz or one wave every 20 seconds) CSF waves that were anticorrelated with GM haemodynamic oscillations. Their model was based on haemodynamic coupling linked EEG, cerebral blood flow, cerebral blood volume (CBV) and CSF oscillations. Increased delta activity was linked to a reduction in CBF and CBV and an increase in CSF flow suggesting that reduced CBV leads to relative expansion of the Virchow-Robin space, which in turn allows CSF flow with less resistance during SWS.

The second study focused on the internal glymphatic system by measuring apparent diffusion coefficient (ADC, which is the same as MD from DTI) and brain tissue volume in sleeping participants after 24h of sleep deprivation (Demiral et al., 2019). They acquired images with a range of diffusion weighting and based on the weighting divided the data into "slow" and "fast" diffusion components. Doing so, they found an increase in slow diffusion in the cerebellum and the temporal lobe during sleep. Furthermore, they observed reductions in fast diffusion within the thalamus, insula, parahippocampus and striatal regions. Furthermore, sleep was associated with a significant increase in CSF volume (and no significant change in GM, WM volume) which was further associated with an increase in slow ADC in the dorsal cerebellar cluster. They suggested that the observed increase in slow ADC is related to an increase in interstitial volume fraction and that the decrease in fast ADC is likely to reflect reduced perfusion during sleep. Although, the physiological

significance of these changes is rather ambiguous, as all tissue compartments contribute to the ADC. Using slow ADC change as an approximation for interstitial volume change is also very simplistic and might be a biased approach.

1.12 Study aims and primary hypotheses

Here I present an overview of the multimodal MRI study that I used in my thesis. It aimed to complement previous glymphatic system related changes during sleep by aiming to measure changes in interstitial volume in a more direct manner.

Measuring glymphatic flow in perivascular spaces (external waste clearance) without the use of a contrast agent is extremely difficult, if not impossible with current techniques available. Here, we aimed to investigate the internal waste clearance mechanism, i.e., fluid flow through the tissue, which has been associated with an increase in interstitial volume fraction. Thus, we proposed that changes in glymphatic system activity can be detected with MRI techniques sensitive to the relative sizes of the intra- and extracellular fluid compartments by comparing images obtained during wake and sleep in healthy young participants.

To maximize the chance of falling and staying asleep in the scanner we used a full night of sleep deprivation in combination with a sleep drug (10mg of Zolpidem), more details about experiment design in Chapter 3.

1.12.1 Sodium (^{23}Na) MRI

One promising technique for measuring the relative sizes of water compartments in biological tissue is ^{23}Na MRI. Sodium is one of the most tightly regulated ions in cells and is present at ~12 times higher concentrations in extracellular compared to intra-cellular fluid (Rose and Valdes, 1994). Thus, even a small increase in extracellular fluid volume fraction would be associated with a relatively large increase in sodium signal providing a potentially sensitive measure of extracellular (or interstitial fluid) volume fraction. ^{23}Na MRI can provide measures of total sodium concentration (TSC) and by assuming that the inter- and extracellular sodium concentration are constant (e.g., intracellular sodium concentration $[Na_i]$=12mM; extracellular sodium concentration $[Na_e]$=140mM) and that the voxel consists of only intra- and extracellular fluid (no solid compartment) one can model the compartment sizes using the following formula (Thulborn et al., 2016):

Equation 1

$$TSC = f * ([Na_e]) + (1 - f) * ([Na_i]),$$

where f represents and (1- f) represent the extra- and intra cellular volume fractions respectively. We can rearrange this equation to calculate the extracellular volume fraction:

Equation 2

$$f = \frac{TSC - [Na_i]}{[Na_e] - [Na_i]}$$

and by assuming fixed $[Na_i]$ and $[Na_e]$ all we need to estimate the extracellular volume fraction is TSC:

Equation 3

$$f = \frac{TSC - 12}{128}$$

We hypothesized that ^{23}Na MRI will be sensitive to the SWS related expansion of interstitial space, which will result in an increase in TSC reflecting an increase in *f*.

1.12.2 Diffusion MRI (dwMRI)

The other technique that we hypothesized to be sensitive to changes in relative fluid compartment changes is diffusion MRI (dwMRI). Diffusion MRI is sensitive to the motion of water molecules within tissue and can provide specific information about Gaussian/hindered and non-Gaussian/restricted diffusion (Assaf and Basser, 2005). We hypothesized that there will be increase in free diffusion and a decrease in hindered diffusion during sleep scans.

1.12.3 Arterial Spin Labelling (ASL)

Moreover, we decided to use arterial spin labelling (ASL) to measure CBF during wake and sleep, as changes associated with sleep are well characterized, while changes in sodium and diffusion are not. Thus, we intended to use CBF change as a positive control for achieving sleep in the scanner because reduction in CBF is expected during sleep.

1.12.4 Voxel-based morphometry (VBM)

Finally, we used voxel-based morphometry (VBM) that is sensitive to changes in brain tissue volume after sleep deprivation and overnight sleep, to investigate the changes in tissue volume corresponding to sleep, with no prior hypothesis.

Chapter 2 MRI techniques

In this chapter I describe the basic physical principles of the MRI techniques used in our study. Furthermore, I discuss their strength and limitations. A detailed explanation of the physics behind these techniques are beyond the scope of this thesis, relevant references are provided.

2.1 ^{23}Na MRI

2.1.1 Overview

Although hydrogen (^{1}H) is by far the main nucleus imaged using MRI, other nuclei that are present in biological tissues exhibit nuclear magnetic resonance, and one of them is ^{23}Na. The chemical reactions that make up the complex biology of the brain are organized and coordinated through compartmentalization of biochemical pathways. Transport mechanism evolved to source substrates, release products, eliminate toxins, regulate ion/metabolite concentrations and to regulate intra- and extracellular volumes. Despite the multifaced nature of these processes, they are all linked to chemical gradients established by the Na^+/K^+ ATPase that pumps two K^+ in and three Na^+ out of the cell against their concentration gradient, shown in Figure 6. This process requires energy that is provided by breaking the high energy phosphate bonds of ATP (Jorgensen, Håkansson and Karlish, 2003). The Na^+/K^+ ATPase uses ~70% of all neuronal ATP further highlighting the importance of sodium ion homeostasis (Rose and Valdes, 1994). The intracellular volume fraction of neural cells is ~80% of total brain volume with sodium concentration of ~12mM, while extracellular fluid compartment is ~20% with 140mM (Madelin and Regatte, 2013).

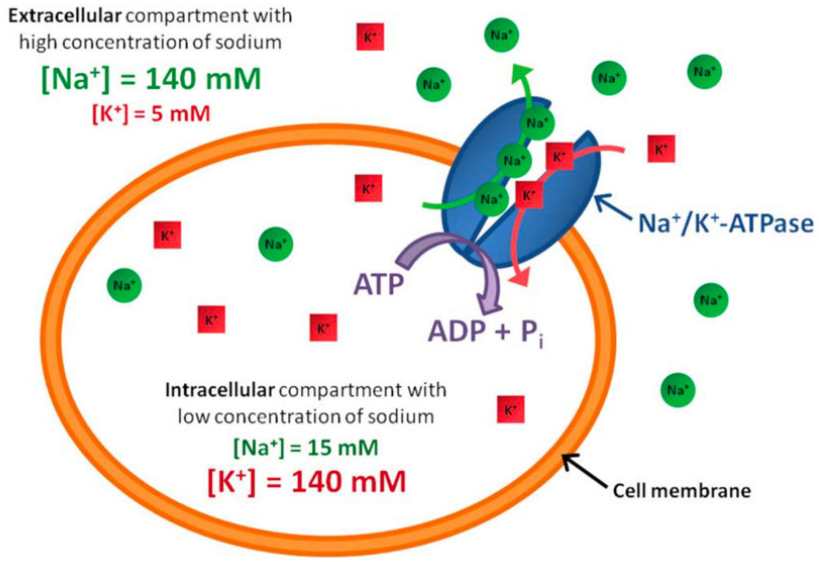

Figure 6: Schematic illustration of the Na^+/K^+ ATPase.

(source: Madelin and Regatte, 2013)

The potential to directly measure metabolic changes in the brain was one of the early driving forces to develop ^{23}Na MRI. While many proton MRI techniques used in medicine are based on finding anatomical/hemodynamical correlates (biomarkers) with pathological conditions, which often emerge late during disease progression, ^{23}Na MRI offers a novel way measure metabolic parameter with biochemical dimensions such as concentration (millimoles per volume of tissue), reaction rate (millimoles/unit time/volume or mass of tissue) and intra-, extracellular volume fractions – often referred to as bioscales (Faro et al., 2013). Although, the potential benefits that sodium MRI can offer do not come without serious technological hurdles.

Despite having the second most sensitive biologically relevant MR signal, ^{23}Na MRI must overcome two intertwined critical limitations: low signal to noise ratio (SNR) and low spatial resolution. These limitations arise from a number of biophysical constraints. First, tissue concentrations and the gyromagnetic ratio of ^{23}Na are substantially lower than those of ^{1}H making ^{23}Na MRI intrinsically less sensitive than ^{1}H MRI. Body sodium concentration (~35mM) is ~2000 times lower than that of ^{1}H (80M) and its gyromagnetic ratio ~4 times lower than that of ^{1}H (Thulborn, 2018). Second, the ^{23}Na nucleus has a spin of 3/2 and possesses a quadrupolar moment that interacts with the electrical field gradients from its molecular environment. Consequently, ^{23}Na spins will have

different relaxation properties based on the molecular environment around them—for example in CSF, where sodium ions can move freely, the static quadrupolar interaction is averaged to zero (type d relaxation on Figure 7), while in solids the spins experience quadrupolar interactions (type a relaxation of Figure 7) (Thulborn, 2018). In complex environments, where sodium ions exist in both solid and liquid state, such as in biological tissue, this behaviour results in biexponential transverse relaxation (T_2-short on the order 0.5–5 ms and T_2-long on the order 15–30 ms). Figure 7 summarizes the energy levels of the corresponding energy spectra of sodium nuclei from single pulse/ single quantum (SQ) nuclear magnetic resonance (NMR) experiments. The relaxation of the spins and the corresponding NMR peaks in the SQ ^{23}Na spectra are sensitive to the motional regime of system, as depicted in Figure 7 (Thulborn, 2018). Depending on the spin dynamics and the molecular environment three motional regimes and four types of spectra are possible (Kemp-Harper et al., 1997). In the brain, sodium spectra are most likely to be of type d (fluid with isotropic diffusion such as CSF) and of type c, while in other tissue the most likely spectrum is type c, although depending on the local degree of anisotropy type b spectra also possible (Rooney and Springer, 1991).

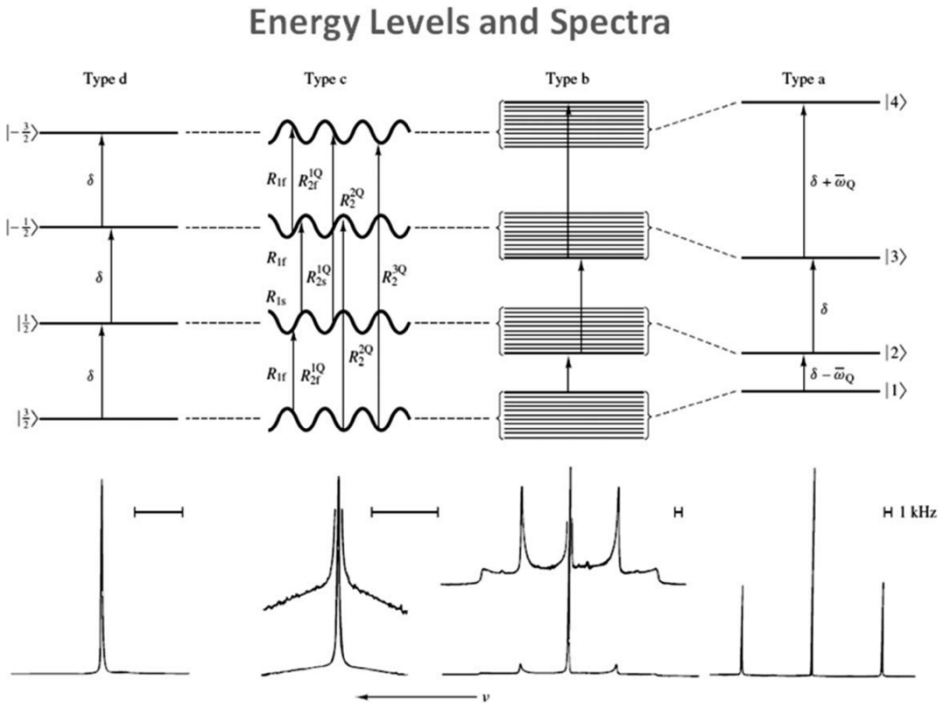

Figure 7: Schematic illustration of typical energy levels and NMR spectra in various molecular environments.

Four types of SQ spectra are possible (Type-d, c, b and a). Type-d: NaCl dissolved in water; Type-c: Na^+ in aqueous solution with high concentration of micelle-solubilised gramicidin channels; Type-b: powder like environment of unoriented dodecyl sulphate micelles in aqueous solution; Type-a: crystal like environment of oriented dodecyl sulphate micelles in aqueous solution. (source Rooney and Springer, 1991)

2.1.2 ^{23}Na pulse sequence

The T_2-short component of ^{23}Na is more than an order of magnitude shorter than the T_2 of ^{1}H, making Cartesian sampling of k-space not possible, if not at the price of losing half of the signal. In order to minimize the effect of rapid signal decay, ^{23}Na MRI sequences typically combine ultrashort echo times with center-out radial or spiral sampling of the k-space (Thulborn, 2018). Several alternative k-space trajectories have been proposed (Thulborn, 2018), and the one that we used in our study is called FLORET, which stands for Fermat Looped Orthogonally Encoded Trajectories (Pipe et al., 2011). The k-space sampling trajectory of this sequency is based on single Fermat spiral waveform like those shown in Figure 8a. Each single waveform undersamples the centre of the k-space; multiple Fermat spiral trajectories are combined in a so-called stacked cone (Figure 8b) that give uniform sampling around a hub (Figure 8c) and multiple hubs are combined orthogonally (Figure 9) in order to fully sample k-space.

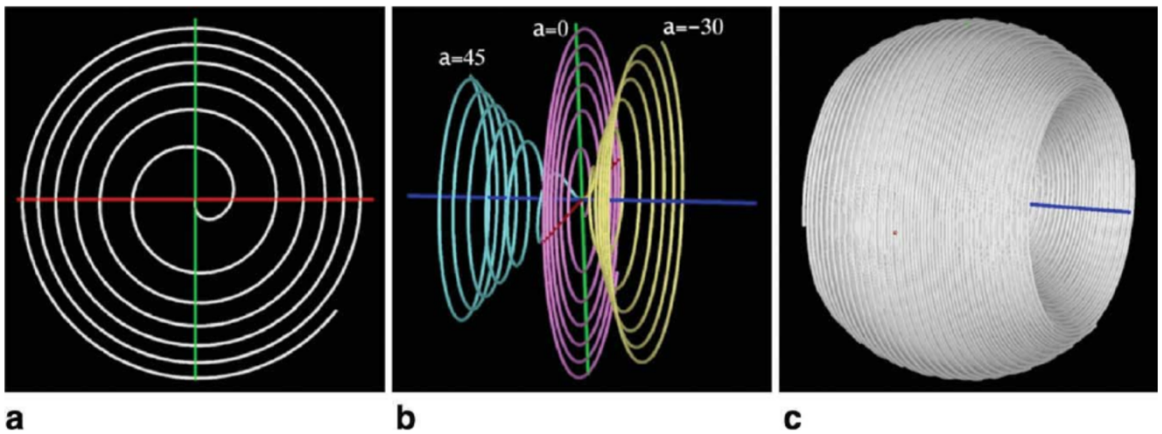

Figure 8: Schematic representation of how the z- axis hub is formed.

a) 2D Fermat spiral trajectory, **b**) 3D cone with angle α about the k_z axis, **c**) Multiple trajectories are rotated by the golden angle about k_z axis as α varies from $-\alpha_0$ to $+\alpha_0$ giving rise to the z-axis hub. (source: Pipe et al., 2011)

Full sampling of the k-space can be achieved in many ways by different orthogonal combination of the 3D hubs, as shown in Figure 9. By this type of sampling the centre of the k-space is oversampled, while there are missing data points at the corners of the k-space.

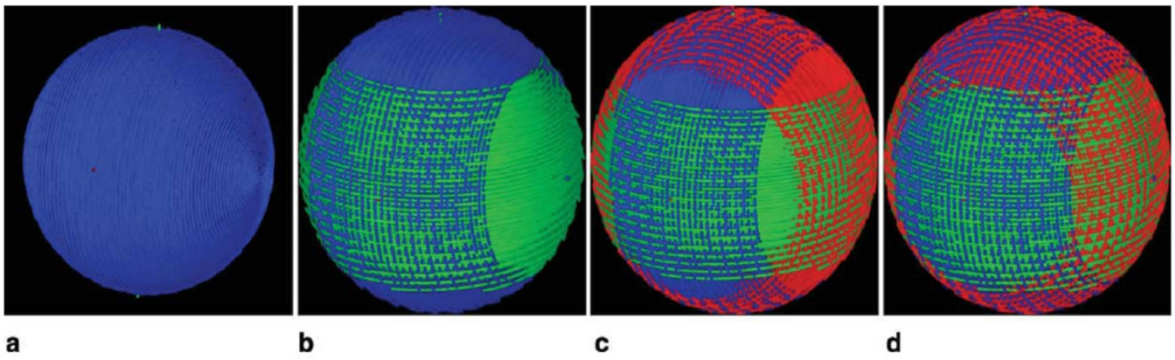

Figure 9: Schematic diagram of four examples how full sampling with FLORET can be

a) 1 hub, α_0= 90°, b) 2 orthogonal hubs α_0= 45°, c) 3 orthogonal hunbs α_0= 36° d) 3 orthogonal hubs α_0= 45° (source: Pipe et al., 2011)

One advantage of FLORET sequence that the data is oversampled and a single hub contains a high percentage of the desired sphere in k-space (E.g., with α_0= 45°, it contains 71%). This allows several possible reconstruction approaches with the sliding window method depicted on Figure 10, which allows reconstruction of an image from a single hub by sharing 29% of the data with hubs before and after.

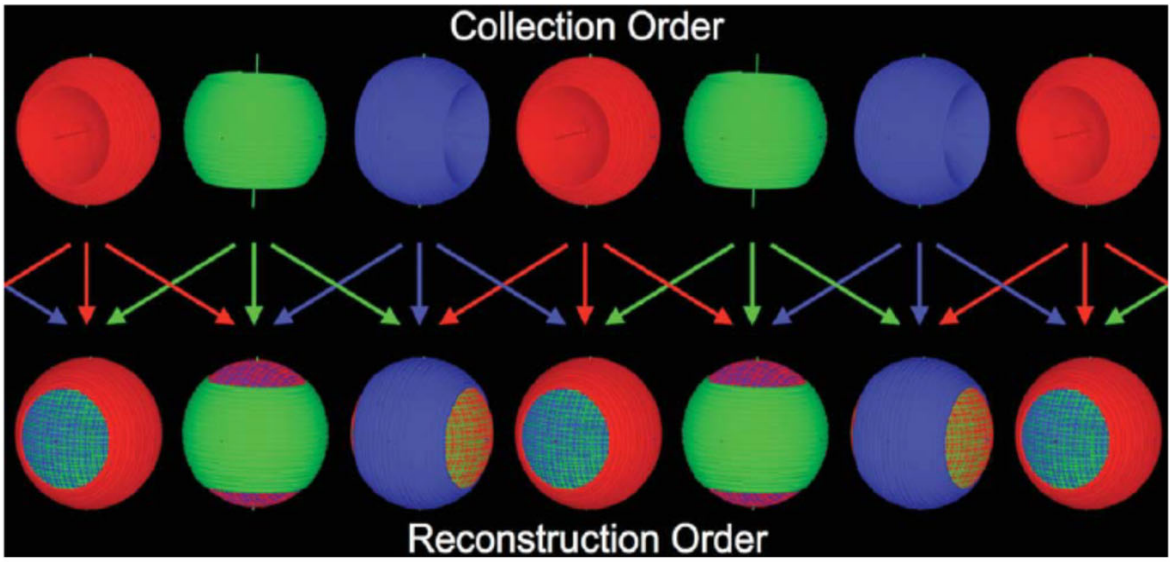

Figure 10: Schematic illustration of sliding window approach of image reconstruction by essentially a single hub.

(source: Pipe et al., 2011)

2.1.3 Benefits and limitations

One of the main benefits of ^{23}Na imaging is that the signal can be quantified in physiologically relevant units, such as concentration which can give unique information about brain physiology and pathology. The quantification of ^{23}Na signal is often done by placing known concentration of phantoms made of agar gel (mimicking the viscosity of brain tissue as it affects sodium spin relaxation properties) around the head and using linear regression to transform the signal image to concentration units (Madelin et al., 2015). The bi-exponential transverse relaxation can be utilized to gain specific information about the intra-, extracellular and CSF environments. There are 2 techniques that are suitable for human studies, one using the fact that the three fluid compartments have different T_1 relaxation times which inversion recovery (IR) pulses can be applied to suppress e.g., interstitial/CSF signal weighting the signal toward intracellular compartment (Konstandin and Nagel, 2013). This allows one to estimate the pseudo intra- and extracellular volumes fraction, though this technique has several limitations (Madelin et al., 2015). For example, in order to get compartment specific signal with IR, the specific relaxation must be estimated from pre-clinical studies as it cannot be measured directly in humans.

Consequently, the compartment specific signal is susceptible to confounds, which is further complicated by the fact that the relaxation times in pathological tissues are unknown (Madelin et al., 2015). The second technique relies on using multiple excitation pulses with multiple quantum filtering (MQF) that is based on the fact that sodium has different transverse relaxation properties based on the surrounding macromolecular environment, as discussed previously (Fleysher et al., 2012). However, this technique comes with multiple hurdles, such as artifacts caused by magnetic field inhomogeneity, low SNR, long acquisition time, the need for high field scanner and indirect estimation of compartmentalized ^{23}Na as the signal cannot be completely separated (Gast et al., 2018). The reason why the signal from intra- and extracellular fluid cannot be completely separated by these techniques is that both techniques work around the assumption that only sodium ions in intracellular compartment are restricted in their motion (hence the different T_1 that IR method utilizes and different T_2 relaxation that MQF utilizes), however there is evidence that sodium ions in the extracellular space can also interact with macromolecules, membranes that would be wrongly detected as intracellular signal (Thulborn, 2018). Even without measuring signal separately from intra- and extracellular compartments we can gain valuable information about the relative compartment sizes by assuming that the sodium ion concentration in the compartments is constant (Thulborn et al., 2016), although we need to be careful with this assumption because this may not be true in pathological conditions.

The clinical potential of ^{23}Na MRI has been shown for several diseases such as for detecting TSC elevation after acute stroke that likely arises from defective Na^+/K^+ ATPase due to hypoxic cell death and perifocal oedema and could serve as a marker for hypoxic tissue at risk (Thulborn et al., 1999; Hussain et al., 2009). Its potential has also been shown in Huntington's disease where TSC increase in caudate correlate with grey matter atrophy and CAG length (Reetz et al., 2012). Furthermore, in Alzheimer's disease there was a 7.5% increase in TSC that negatively correlated with hippocampal volume (Mellon et al., 2009). One study used ultra-high field (9.4T) sodium MRI and calculated cell volume fraction (by assuming that Na^+ concentration inside and outside the cells are constant) and showed that normal aging is associated with an increase in TSC, but no change in cell volume fraction suggesting that the increase in TSC is due to an expansion of CSF spaces (normal process with aging) and not due to cell loss—offering a way to distinguish normal aging from neurodegeneration that is associated with cell loss (Thulborn et al., 2016).

^{23}Na MRI still faces many obstacles before it can reach commercial use. The biggest obstacle comes from the low SNR and high field strength scanners that are needed to obtain “good” quality images. Figure 11 illustrates sodium image quality at different field strengths, the SNR increases approximately linearly with magnetic field strength (Huhn et al., 2019). In addition, special hardware that is not typically included as standard for clinical scanners is required.

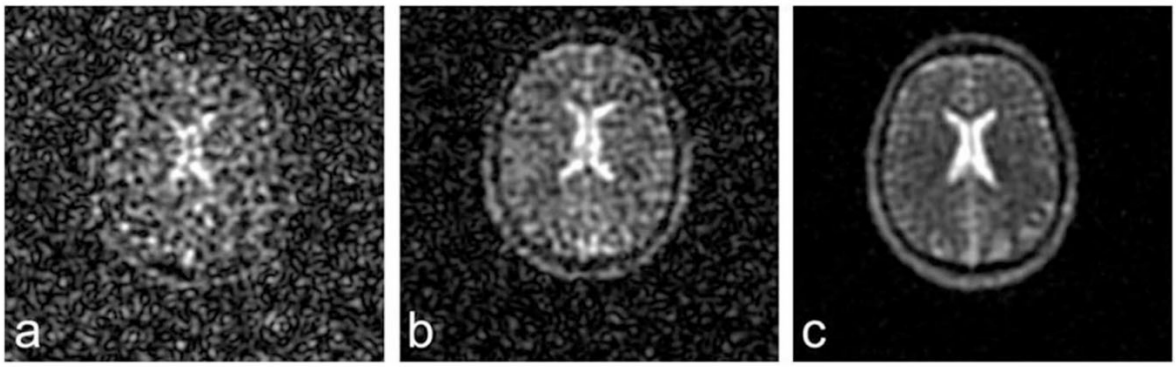

Figure 11: Schematic illustration of sodium image quality at different magnetic field strengths. All images were acquired with nominal spatial resolution of 4 mm^3. a) 1.5T b) 3T c) 7T (source: Huhn et al., 2019)

The nominal resolution of our images (acquired on 3T scanner) is isotropic 4mm. At this kind of resolution, it is very likely that a single voxel will include mixtures of grey, white matter and CSF. Sodium concentration in GM and WM are ~40mM and ~30mM respectively, while in CSF is ~140mM, consequently overflow form signal from other compartments (even if they are small) can influence the measured signal. For example, a “mainly” GM voxel will contain substantial signal from CSF and WM compartments as well. The mixing of different tissue signal values within a single voxel is often referred to as partial volume effects (PVEs). This does not only affect sodium MRI but any MRI modality with large voxel dimensions. In ^{23}Na MRI PVEs are further complicated by how the image is sampled. Non-Cartesian trajectories, with variable densities of points and lack of data in some parts of the k-space (corners of the Cartesian space), will unavoidably broaden the point spread function (PSF), which can cause a ~40% discrepancy between effective and nominal spatial resolution (Boada et al., 1997; Lu et al., 2010). This discrepancy exacerbates the PVEs, thus deteriorating the ability of ^{23}Na MRI to measure sodium concentration in discrete tissue types. Even in the absence of the above mentioned "spill-over" effect of PSF, the nominal spatial resolution of ^{23}Na MRI is still relatively low due to the need for increased SNR and speedy acquisition.

2.2 Diffusion weighted MRI

2.2.1 Overview

In addition to ^{23}Na MRI that aims to provide information about microstructural (as well as metabolic) changes such as change in the relative sizes of intra- and extracellular fluid compartments, dwMRI also aims to provide information about processes that occur on the microscopic scale. Here, I would like to emphasize that neither sodium nor diffusion imaging can provide even sub millimetre spatial resolution, but rather they use clever signal acquisition and/or signal modelling that allows us to see the "invisible".

dwMRI utilizes protons from highly abundant water as an exogenous tracer to gain information about the microstructural environment of brain tissue via measuring water diffusion. Diffusion is the random displacement of molecules resulting from the thermal energy that these molecules carry, often referred to as Brownian motion (Einstein, 1905). The displacement of a molecule in a free medium after a given time interval can be described by a three-dimensional Gaussian distribution. The random motion of a molecule over a distance can be statistically described by the diffusion coefficient (D) that is dependent on the size of the molecule, the temperature and a viscosity of the medium (Einstein, 1905). Diffusion in 3-dimension space can be defined as:

Equation 4

$$< r^2 >= 6Dt \, ,$$

where D is the diffusion coefficient and $<r^2>$ is the average mean square displacement along 3 dimensions during diffusion time t.

In theory any MRI acquisition can be made sensitive to diffusion by adding diffusion sensitizing gradients (also known as motion probing gradients). Diffusion sensitization works by applying a gradient pulse along a single direction to de-phase the spins and then a second one, after a given delay, with equivalent area but opposite sign (or separated by a 180° pulse) to the first one, as shown in Figure 12 (Arab et al., 2018). Only the spins that stay stationary will be re-phased completely by the second pulse, randomly moving proton spins do not perfectly rephase at the time

of signal sampling, resulting in signal attenuation that is dependent on the diffusion coefficient D. Thus, the signal loss due to diffusion can be described by the following equation:

Equation 5

$$S = S_0 e^{-bD}$$

therefore:

Equation 6

$$ln\frac{S}{S_0} = -bD,$$

where S_0 is the signal intensity without the application diffusion sensitizing gradient, S is the signal intensity in the presence of diffusion sensitizing gradient and b is the b-factor or b-value, a coefficient proportional to shape, duration and amplitude of the diffusion gradients, which expresses the amount of diffusion weighting of a given acquisition.

For rectangular gradients, the b value is given by:

Equation 7

$$b = \gamma^2\delta^2|G|^2\left(\Delta - \frac{\delta}{3}\right),$$

where γ is the gyromagnetic ratio (in this case of proton), δ is the duration of diffusion sensitizing pulse, $|G|$ is the amplitude of diffusion sensitizing pulse and Δ is the time delay between the two diffusion sensitizing pulses. By altering the b value we can make the diffusion weighted images more or less sensitive to molecular motion. For example, low b values will be less sensitive to diffusion hence the signal loss will be attributed to fast moving protons (e.g. at b=100 s/mm^2 most signal loss can be attributed to capillary perfusion), while at high b values (above b= 1500 s/mm^2) the signal will represent non-gaussian hindered or restricted diffusion (Le Bihan, 2019).

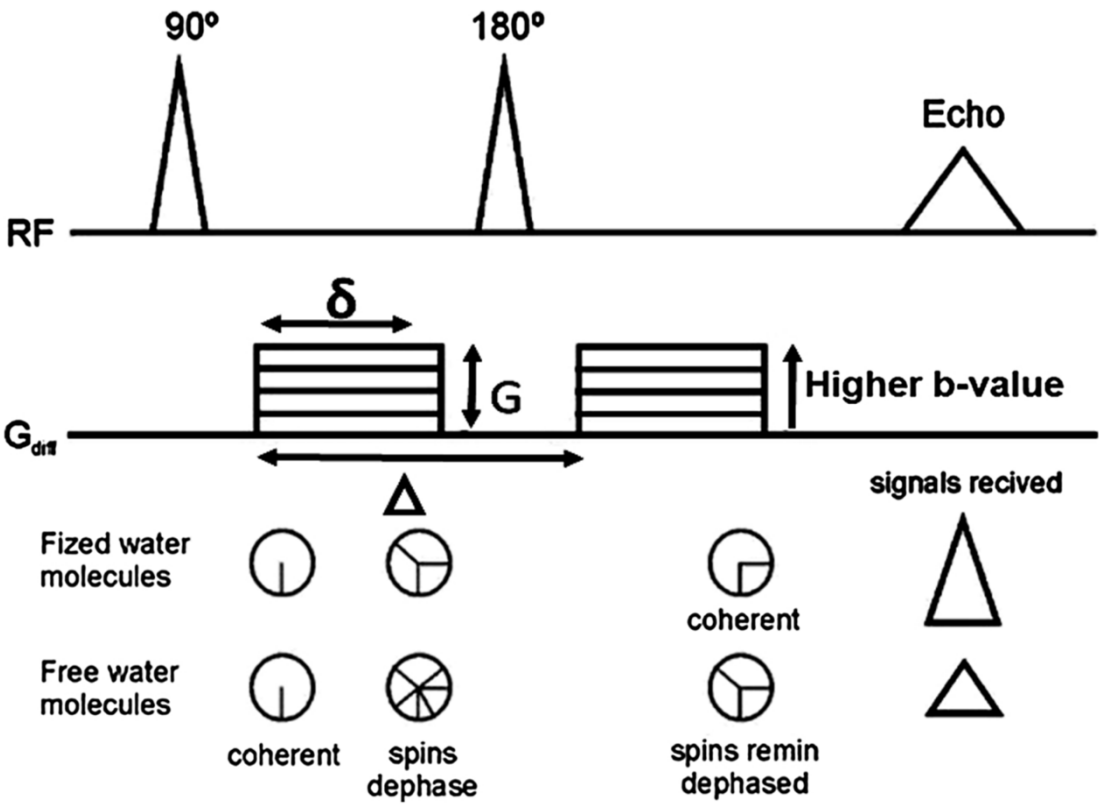

Figure 12: Schematic representation of two diffusion sensitizing gradient pulses added to a T2 weighted spin-echo sequence.

The first gradient pulse is added after the 90° RF pulse to de-phase the water molecules (both fixed and free) and a second one after 180° pulse (hence both the de- and re-phasing pulses are in the same direction). δ is the duration, G is the amplitude, Δ is the time delay between the two diffusion sensitizing pulses. As G increases so does the b-value. After the second gradient pulse water in freely moving molecules will be more de-phased and hence there will be more signal loss than in the freely moving molecules. (source: Arab et al., 2018)

2.2.2 Apparent Diffusion Coefficient

In the previous section I showed how dwMRI is based on Einstein's equation describing diffusion in free media. The assumption of Gaussian diffusion results in a mono-exponential decay of the MRI signal as function of b- value (Equation 5), as illustrated on Figure 13. With this assumption the

diffusion coefficient can be easily estimated by acquiring image with just 2 b-values, as D is the slope of Figure 13. Although in biology diffusion is rarely Gaussian, the initial attempts to measure diffusion via MRI were based on this simplistic assumption, and the concept of apparent diffusion coefficient (ADC) - directly obtained by applying Einstein's equation to non-Gaussian systems (Le Bihan et al., 1986) – was introduced. It should also be remarked that in the early days of dwMRI, due to hardware limitation, it was very difficult to achieve b-values higher than 1000 s/mm^{-2}, and therefore the assumption of Gaussian diffusion was justifiable. The ADC concept has been very successful, and many diffusion models still use its assumption, including one of the most used one: Diffusion Tensor Imaging (DTI) (Le Bihan, 2013, Basser, Mattiello and Lebihan, 1994). The ADC is affected by the local water environment, so, for example, in CSF it will closely match the free diffusion coefficient of water, while in white matter where cells are closely packed is much lower.

DTI model fit represented by the dashed line assumes Gaussian diffusion and hence mono-exponential decay of diffusion weighted signal (this is the same assumption as for ADC). This assumption is only valid at low b-values (0- 1000 s/mm^2). Diffusion Kurtosis Imaging (DKI) – an extension of DTI that accounts for the non-Gaussian components of the signal - fits the measured data better than the DTI model.

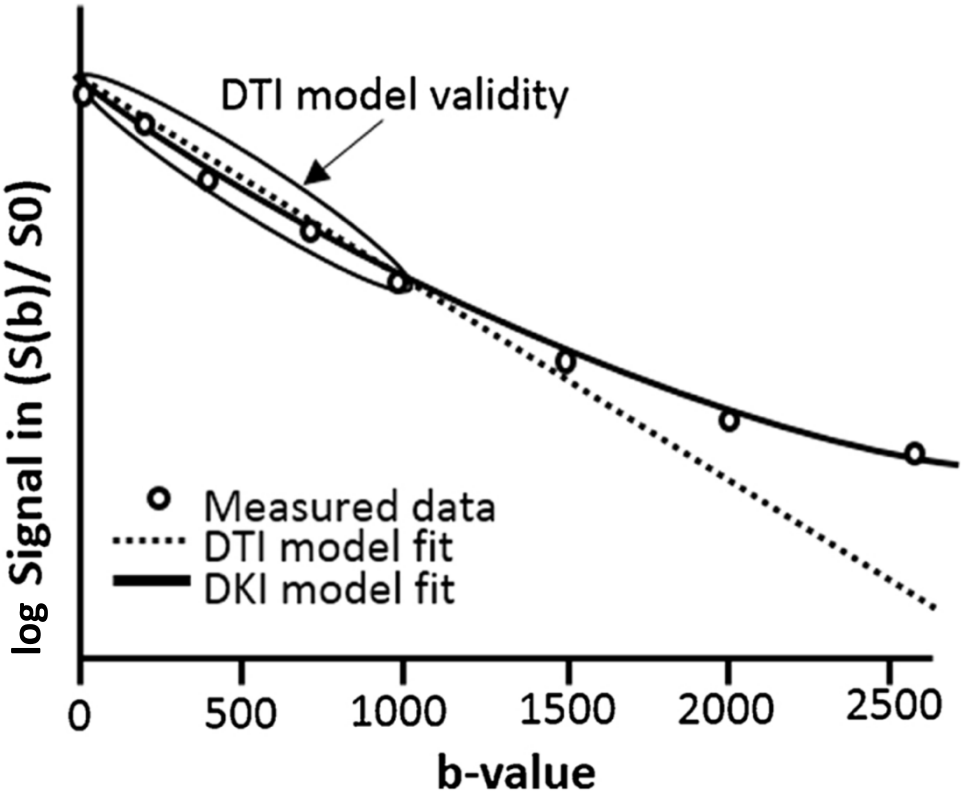

Figure 13: Schematic illustration of the relationship between signal loss due to diffusion weighting (b-value) in the brain.

(source: Arab et al., 2018)

2.2.3 Diffusion Tensor Imaging

Soon after dwMRI was introduced, it was observed that the actual signal was dependent upon the specific direction along which the diffusion gradients were applied, i.e., it became apparent that diffusion in the white matter is anisotropic (Moseley et al., 1991). DTI is an extension to ADC that measures diffusion in many directions, this technique became especially useful to gain valuable information of white matter tracts (Basser, Mattiello and Lebihan, 1994; Basser and Pierpaoli, 1996). The origin of diffusion anisotropy in the brain is still a subject of debate, but it is likely to arise from restrictions to water molecule's motion by tissue microstructure. The DTI model assumes that both isotropic and anisotropic diffusion can be described by a 2nd order diffusion tensor:

Equation 8

$$\mathbf{D} = \begin{pmatrix} D_{xx} D_{xy} D_{xz} \\ D_{yx} D_{yy} D_{yz} \\ D_{zx} D_{zy} D_{zz} \end{pmatrix}$$

, where D_{xx}, D_{xy} … D_{zz} represent diffusion in different directions. The assumption of the tensor is that D is positive definite, symmetric and diffusion in each direction is Gaussian. Geometrically, a tensor can be represented by an ellipsoid. Figure 14 illustrates diffusion tensor as triaxle ellipsoid in the reference frame of eigenvectors (Basser, Mattiello and Lebihan, 1994).

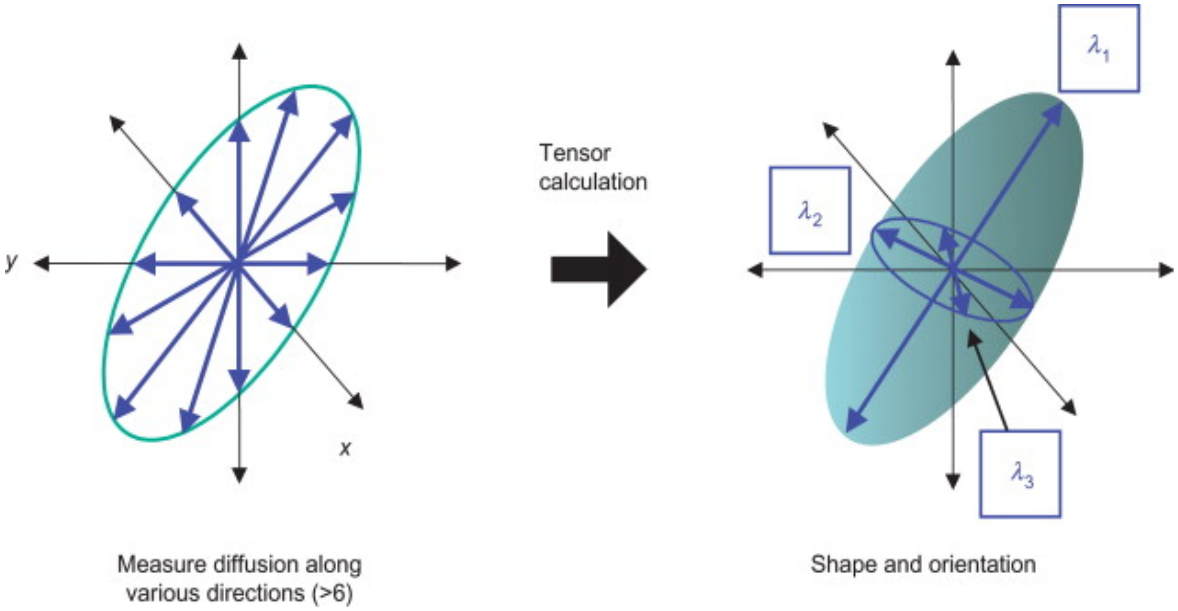

Figure 14: Schematic representation of a diffusion ellipsoid

Diffusion ellipsoid/tensor can be fully characterized by measurements along 6 orthogonal axes with at least two b-values; DTI represented by 3 eigenvalues: longest (λ_1), middle (λ_2), and shortest (λ_3) axes. (source: Mori and Tournier, 2014)

DTI represents isotropic diffusion (e.g., in CSF) when the off-diagonal elements are 0, and the on-diagonal elements are all the same, so $D = D_{xx} + D_{yy} + D_{zz} = 3Dxx$.

This model is particularly useful to determine white matter fibre tract orientation, as water molecules are more likely to diffuse along the fibres than across the closely packed fibres. DTI gives information about water movement in 3 dimensions, thus can give information about the preferred diffusion direction. The most used scalar measures derived from DTI are the following: Mean Diffusivity (MD), Axial Diffusivity (AD), Radial Diffusivity (RD) and Fractional Anisotropy (FA). These measures are represented by the following equations:

Equation 9

$$MD = \frac{D_{xx} + D_{yy} + D_{zz}}{3}$$

, giving information about tissue integrity (e.g., cell density) $MD_{CSF} > MD_{GM} > MD_{WM}$;

Equation 10

$$AD = D_{xx}\,, \qquad RD = \frac{D_{yy} + D_{zz}}{2}$$

, AD and RD can give relevant information about axonal injury, premature axon/myelin development (Feldman et al., 2010);

Equation 11

$$FA = \sqrt{\frac{3}{2}\frac{(D_{xx} - MD)^2 + (D_{yy} - MD)^2 + (D_{zz} - MD)^2}{D_{xx}^2 + D_{yy}^2 + D_{zz}^2}}$$

, which essentially normalizes the variance in diffusion vectors by the magnitude of the tensor. In simple terms it is a measure of anisotropy (or directionality) that varies between 0 (isotropic diffusion) and 1 (diffusion in a single direction only), showing in Figure 15.

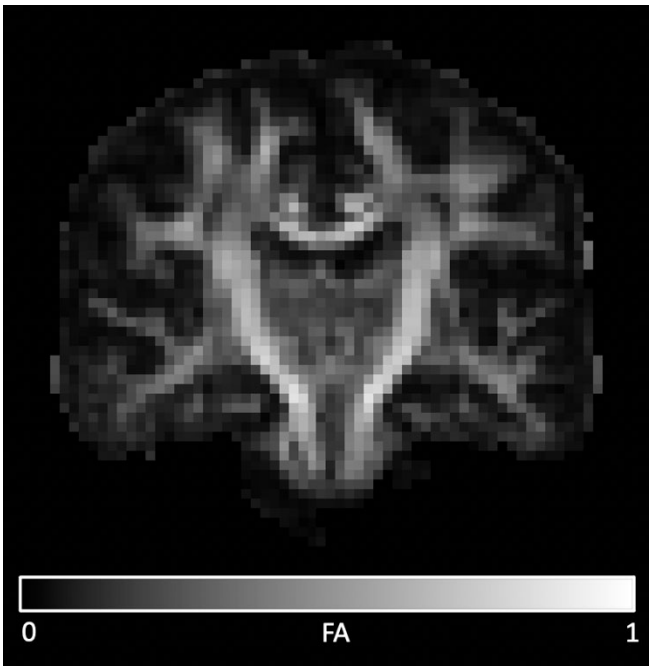

Figure 15: Coronal slice of a FA image.

Light areas represent high anisotropy, these are the areas where white matter fibres run.

Among these measures FA is the most used, as it gives a measure of white matter fibre integrity that is compromised during various pathological conditions such as multiple sclerosis and schizophrenia (Sbardella et al., 2013; Alba-Ferrara and de Erausquin, 2013). Despite broad clinical use and application of DTI, it is known to be systematically biased (Jones, Knösche and Turner, 2013). While the assumption for Gaussian diffusion can be adequate for describing diffusion for water molecules in the same compartment experiencing the same degree of hindrance, it does not represent well the complexity of biological tissue (where multiple compartments exist in a single voxel) (Frank, 2001). In addition to microstructural properties DTI measures are also affected by confounding variables such as orientation and dispersion of tissue components (Wheeler-Kingshott and Cercignani, 2009) and parameters of dwMRI acquisition (Jones and Basser, 2004), as shown in Figure 13 at high b-values (over 1000 s/mm^2). There have been attempts to improve the modelling of non-Gaussian diffusion in the brain, and some models attempt to directly relate diffusion properties to microstructural features. These are called mechanistic models, one example is the Neurite Orientation and Dispersion Density Imaging (NODDI) that is 3 compartment model composed of restricted diffusion (intracellular), hindered diffusion (extracellular, neural soma and

glia cells) and isotropic (CSF) compartment (Zhang, Schneider, Wheeler-Kingshott and Alexander, 2012). From this model, neurite density and orientation density as well as relative compartment size can be estimated, however it works with many assumptions (e.g., intracellular diffusion is modelled by stick with zero radius) that are not always valid or the model is not applicable to certain tissue (e.g., to grey matter) (Huber et al., 2019). In parallel to mechanistic models, methods that deal with non-Gaussian diffusion without strict assumption of the different compartments have evolved—these are called phenomenological models or signal representation techniques (Novikov et al., 2018).

2.2.4 Diffusion Kurtosis Imaging (DKI) and Diffusion Kurtosis Tensor Imaging (DKTI)

One of the early examples of a signal representation technique was DKI, that in addition to estimating diffusivity also estimates the degree of deviation from a single Gaussian component, also known as kurtosis (Jensen et al., 2005). DKI describes diffusion in a voxel as an infinite mixture of Gaussians, as opposed to single Gaussian and the measured kurtosis (K) can be directly linked to the variation in ADCs between compartments, Figure 13 highlights that the DKI model provides a better fit than DTI (Jensen et al., 2005; Jensen and Helpern, 2010). In addition to the DTI parameters, DKI also provides kurtosis measures such as mean kurtosis (MK), axial and radial kurtosis (AK and RK respectively). Kurtosis is a dimensionless measure that reflects the deviation from a Gaussian distribution. A process with a purely Gaussian distribution has 0 kurtosis, while absolute K values larger than zero relate to more deviation from the Gaussian, as shown in Figure 16. In biology, kurtosis is non-negative and higher kurtosis means a higher degree of tissue complexity and microstructural heterogeneity (Szczepankiewicz et al., 2016). As mentioned before, to solve DTI one must obtain images with at least 6 diffusion encoding direction and two b-values, while for DKI one must obtain 15 independent diffusion encoding gradients and at least 3 b-values (Jensen et al., 2005).

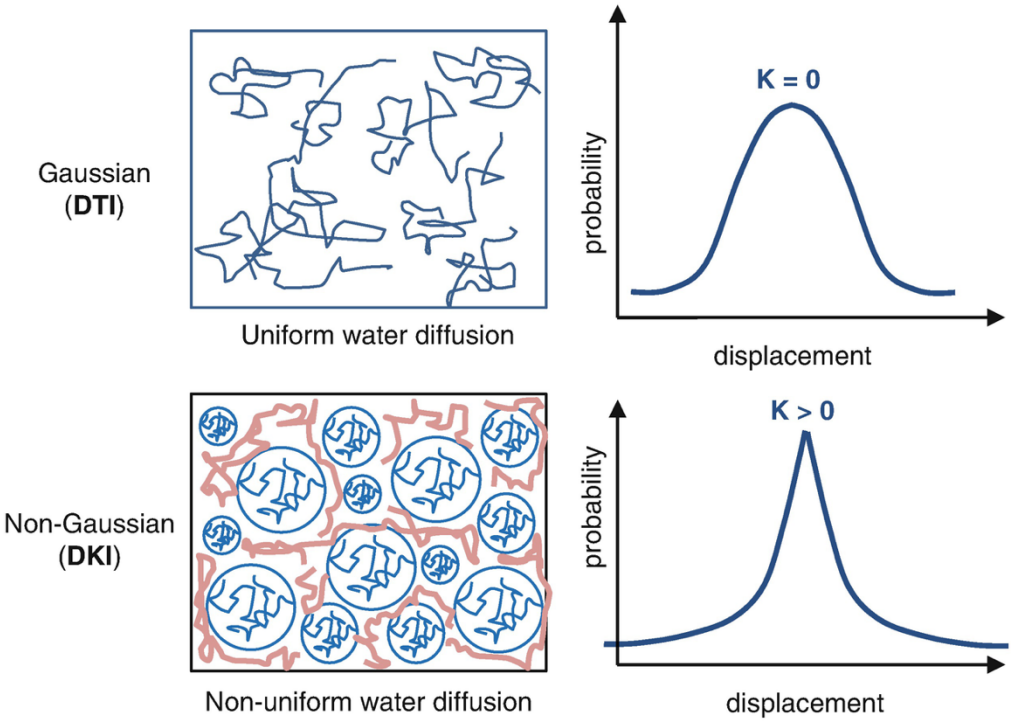

Figure 16: Schematic illustration of Gaussian and non-Gaussian diffusion.

Gaussian diffusion in free media where kurtosis (K) is 0 and non-Gaussian diffusion in complex biological tissue where K>0. Kurtosis can be considered as the “peakedness” of a probability density function. (source: Zhuo and Gullapalli, 2020)

In DKI, kurtosis and diffusion tensors are inherently linked, however independent (from diffusion) kurtosis measures such as mean kurtosis tensor (MKT) and Kurtosis Fractional Anisotropy (KFA) measures can be obtained by the technique often referred to as DKTI (Hansen et al., 2013; Glenn et al., 2015). MKT and MK have similar contrast in neural tissue, as displayed on Figure 17, but MKT is independent from the diffusion tensor. KFA is analogous to FA, but here the anisotropy of kurtosis is measured, a comparison between the two is shown in Figure 17.

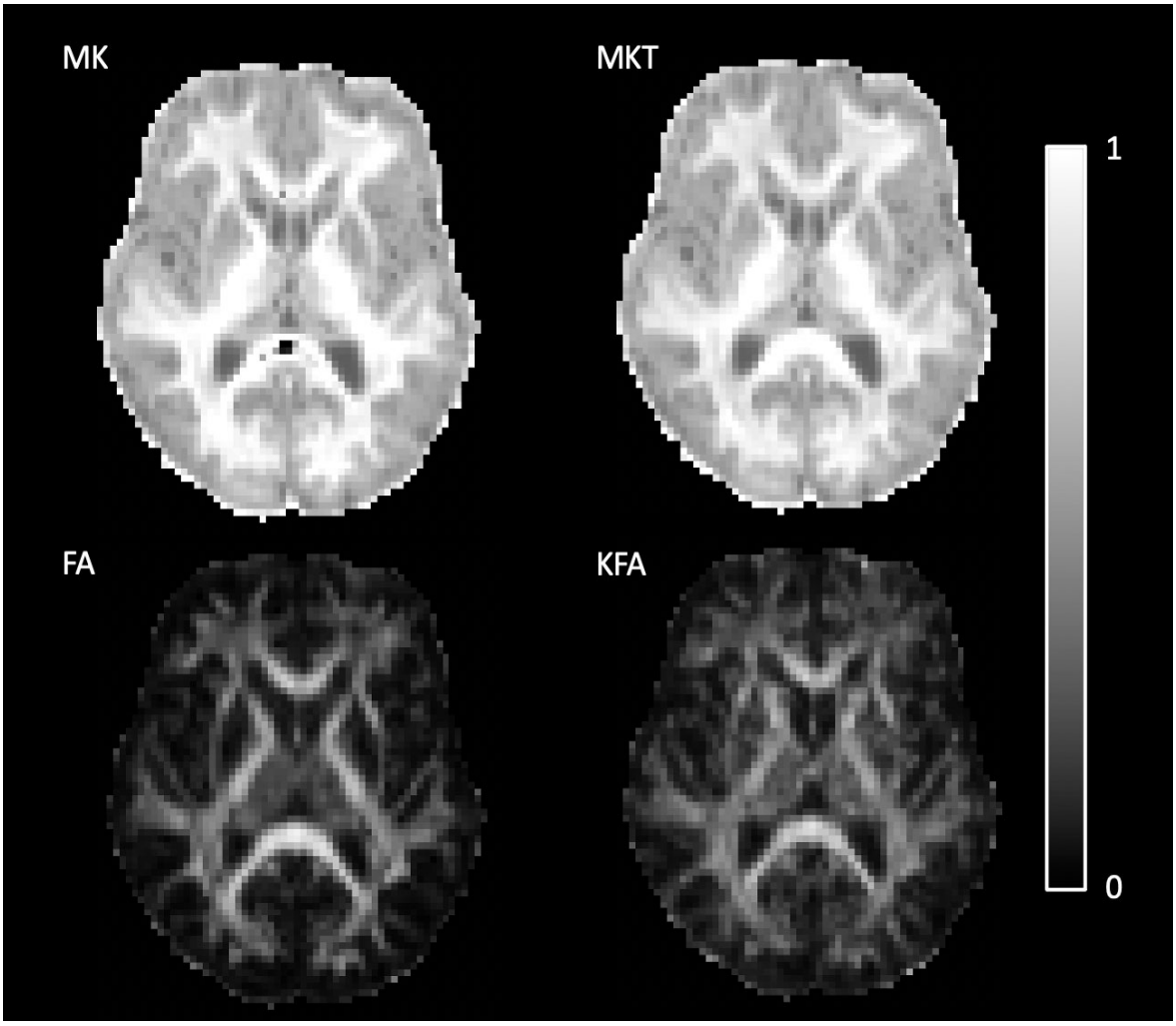

Figure 17: Examples of Diffusion Kurtosis Measures.

Mean Kurtosis (MK), Mean Kurtosis Tensor Images (MKT), Fractional Anisotropy (FA) and Kurtosis Fraction Anisotropy (KFA) images in native space. Note that MK and KFA show very similar contrast, while KFA shows enhancement in deep nuclei (basal ganglia and thalamus) compared to FA, suggesting that KFA is more sensitive to tissue heterogeneity.

Kurtosis measures can give extra valuable information about tissue complexity and integrity, for example MK provided better visualization of ischemic lesions in animal models than MD, which was in line with human stroke patient findings showing MK's potential to predict tissue outcome (Grinberg et al., 2012; Jensen et al., 2011; Hui et al., 2012). DKI derived MD and MK have also been shown to be more sensitive to microstructural changes in patients with epilepsy than the DTI derived parameters when compared to control population (Gao et al., 2012). Furthermore, KFA

might offer new ways of studying complex biological tissue such as deep cerebral grey matter, as it provides better enhancement in deep structures (such as thalamus) than FA (Glenn et al., 2015). KFA has been suggested to be a valuable measure for studies where miniscule microstructural remodelling is expected in grey matter regions, such as in our study (Hansen, 2019). A recent study compared DKTI measures such KFA and MKT with aged matched post-mortem histological samples and found that: KFA measure in deep grey matter is similar to that of white matter, which is due to the small white matter fibres running through these structures (Maiter et al., 2021). Furthermore, they showed that MKT positively correlated with histological tissue kurtosis, suggesting that DKTI measures are suitable for studying regional structural variations in cerebral tissue microenvironment and microstructural changes.

2.3 Arterial Spin Labelling

2.3.1 Overview

ASL offers a non-invasive way of measuring cerebral blood flow, which is an important physiological correlate to brain activity as it delivers glucose and oxygen. In contrast to more established PET methods sensitive to brain metabolism ($H_2{}^{15}O$ and ^{18}FDG-PET), ASL is completely non-invasive as it does not rely on the injection of exogenous radiotracers. ASL utilizes arterial water as an endogenous tracer, proton spins in arterial water are being magnetically “labelled” (i.e. their spin is inverted) while travelling along the carotid arteries and after a time delay an image is acquired (Alsop and Detre, 1996). The time delay allows the labelled protons from arterial water to exchange with the tissue, thus causing signal attenuation. Moreover, a so-called control image is acquired in which arterial water proton spins were not altered, meaning that both the arterial and static tissue spins are in the same orientation (Borogovac and Asllani, 2012). The difference between the 2 scans removes the signal from the static tissue, highlighting local perfusion. Figure 18 illustrates a schematic representation of labelled and control images, where static tissue is represented by +1 value and labelled water with -1.

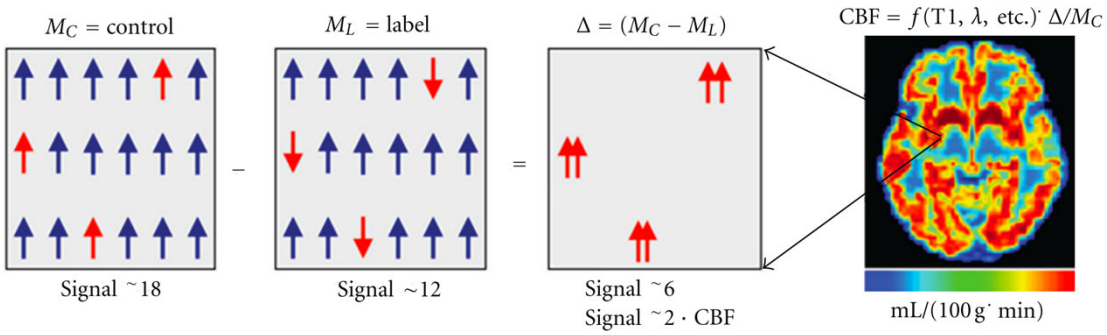

Figure 18: Illustration of the theoretical framework of ASL.

The first three panel shows the control (left) and labelled (centre) signal obtained from a single voxel and their difference (right). The fourth panel represents the CBF image that was calculated from the differences between control and labelled by applying a function that considered various MR parameters and blood tissue water partition coefficient (source: Borogovac and Asllani, 2012).

ASL signal is often obtained by the following equation (Williams et al., 1992):

Equation 12

$$\mathrm{ASL_{signal}} = \frac{(\mathrm{M_C} - \mathrm{M_L})}{\mathrm{M_C}}$$

,where $\mathrm{M_C}$ is control and $\mathrm{M_L}$is labelled image.

2.3.2 ASL pulse sequences

ASL signal images can be obtained by several different pulse sequence protocols, based on how the labelling is achieved. Historically there were two major categories: continuous ASL (CASL) where labelling duration is on the seconds scale and pulsed ASL (PASL) where labelling happens on the millisecond scale (Golay, Hendrikse and Lim, 2004). More recently other ASL techniques have been developed, one of them is pseudo continuous ASL (pCASL), which can be considered as intermediate between CASL and PASL (Dai, Garcia, de Bazelaire and Alsop, 2008). pCASL was developed to take the advantage of CASL and PASL, such as the superior signal to noise ratio of CASL and the high labelling efficiency of PASL (Wong, Buxton and Frank, 1998; Wu et al., 2007). Furthermore, it was designed to reduce the associated limitations of the two techniques, such signal loss due to magnetization transfer (CASL) and reduced SNR (PASL) (Wolff and Balaban, 1989; Wong, Buxton

and Frank, 1998). pCASL offers 50% higher SNR than PASL and 18% higher labelling efficiency than CASL at 3T (Wu et al., 2007), consequently we decided to use pCASL in our study.

In pCASL the radio frequency pulses are applied across the axial plane as shown in Figure 19A to magnetize the blood in the carotid arteries. The time delay between labelling and image acquisition is called post labelling delay (PLD) (shown in Figure 19B), which should be selected to match arterial transit time (the time for the labelled blood to reach the microvasculature) and tissue transit time (time to exchange the labelled blood with the tissue) (Alsop and Detre, 1996). Some compromises must be made when selecting PLD, because if it is too long there will be too much signal loss at regions with long transit times and if it is too short then there won't be enough time for the labelled spins to reach the tissue (Alsop and Detre, 1996).

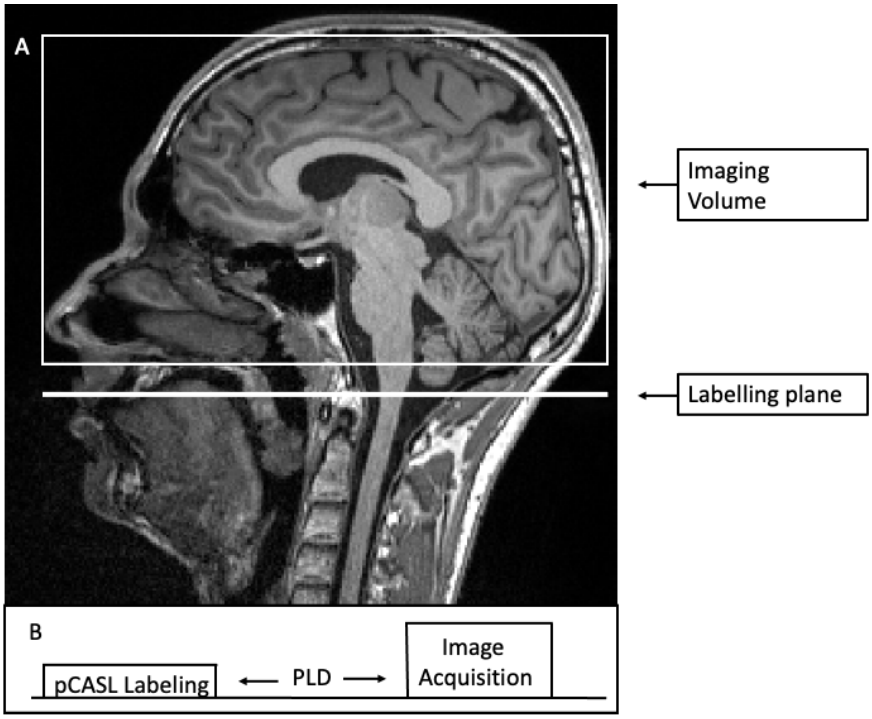

Figure 19: pCASL labelling

A: Schematic diagram illustrating pCASL labelling plane and the corresponding imaging volume. B: Timing diagram for pCASL.

2.3.3 Advantages and limitations of ASL

In addition to the non-invasive nature of ASL that makes it ideal for longitudinal studies where data is collected at multiple time points, quantitative ASL can give reliable measures of CBF (Ye et al., 2000). A relatively simple model has been proposed to quantify CBF from single PLD pCASL, which works with three assumptions: 1. PLD is longer than the arterial transit time, meaning that all labelled spins are delivered to the tissue; 2. There is no outflow of blood water, meaning that all labelled spins are exchanged with the tissue; 3. Relaxation of labelled spins are governed by the T_1 of blood and not tissue T_1 (Alsop et al., 2014). The formula to calculate CBF from pCASL images is the following:

Equation 13

$$\mathrm{CBF} = \frac{6000 * \lambda * (\mathrm{M_c} - \mathrm{M_l}) * e^{\frac{\mathrm{PLD}}{\mathrm{T_{1,blood}}}}}{2 * \alpha * \mathrm{T_{1,blood}} * \mathrm{M_0} * (1 - e^{-\frac{\tau}{\mathrm{T_{1,blood}}}})} \ [\mathrm{ml/100g/min}]$$

,where λ is the brain/blood partition coefficient in ml/g; $\mathrm{M_c}/\mathrm{M_l}$ are the time-averaged signal intensities in the control and label images respectively, $T_{1,\,blood}$ is the longitudinal relaxation time of blood in seconds, α is the labelling efficiency, $\mathrm{M_0}$ is the signal intensity of a proton density weighted image, and τ is the label duration. The recommended parameter values are the following: λ= 0.9 ml/g; $T_{1,\,blood}$ (at 3T)= 1650ms; α= 0.85 (Alsop et al., 2014).

Although the spatial resolution of ASL is superior compared to water PET, it is still rather poor. The relatively poor resolution is due to the fast image acquisition that is required to capture the signal from labelled blood before it relaxes to its equilibrium state. For example, the images that we have acquired with pCASL sequences (shown in Figure 20) had an in-plane resolution of 3.4mm and slice thickness of 6mm.

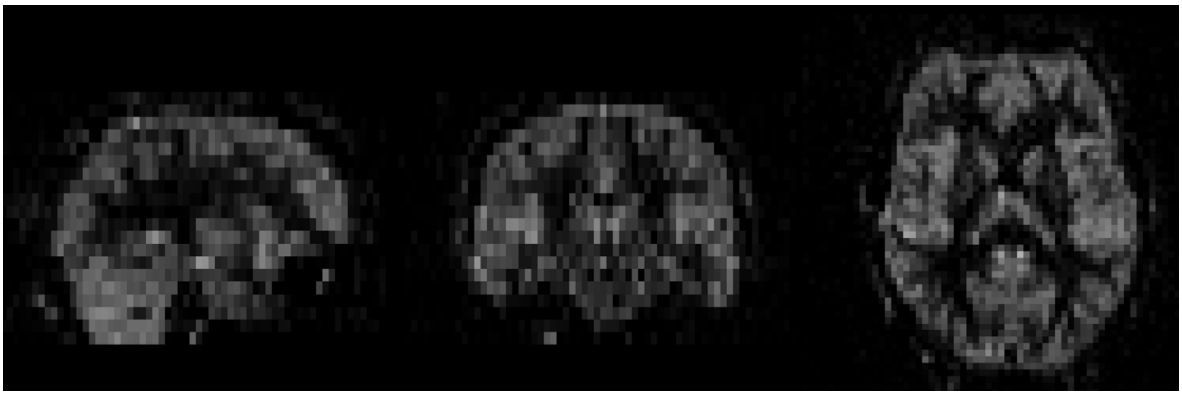

Figure 20: Example of perfusion weighted image acquired with pCASL

Image was acquired with in-plane resolution of 3.4mm and slice thickness of 6.6mm.

PVEs are compromising the signal within a voxel as at this kind of resolution flow values represent a mixture of values from GM, WM and CSF, it should be remarked that flow values are very different in these tissues, where GM exhibiting higher CBF than WM (Asllani, Borogovac and Brown, 2008). There have been attempts to reduce and correct for PVEs via post processing algorithms (Asllani, Borogovac and Brown, 2008; Chappell et al., 2011). One of these algorithms assumes that at any given voxel, perfusion of a given tissue is constant over a region ('kernel') surrounding the voxel, which allows for a set of linear equations to be constructed with tissue perfusions as unknown variables and the tissue segmentation probabilities (obtained from high resolution anatomical images) as weighting factor for linear regression (Asllani, Borogovac and Brown, 2008).

2.4 Voxel based morphometry

VBM is an automated technique that typically uses T_1-weighted volumetric MRI scans, (in our case high-resolution anatomical image acquired with magnetisation prepared rapid gradient echo (MPRAGE) (Brant-Zawadzki, Gillan and Nitz, 1992) sequence and uses statistics to identify changes in brain anatomy such as grey, white and CSF volume between groups (Whitwell, 2009). It has been particularly useful in furthering our understanding of how the brain changes in neurological/psychiatric disorders and to make statistical association between clinical and anatomic features (Whitwell, 2009). In simple terms VBM involves segmentation and normalization of high resolution T_1-weighted images to the same space with minimal distortion of the individual's main anatomical features (Ashburner, 2007). The normalized images can then be used for voxel-wise

analysis within and between different groups. One of the methods for VBM analysis is called Diffeomorphic Anatomical Registration Through Exponential Lie Algebra (DARTEL) that utilizes non-linear deformations. A detailed description of DARTEL is beyond the scope of this thesis, details on the method can be found in Ashburner, 2007.

Chapter 3 Study design

3.1 Funding and Ethical Approval

This study was funded by Sussex Neuroscience and by University of Sussex Research and Development Fund. Ethical approval was obtained from the Brighton and Sussex Medical School Research and Governance Ethics Committee (ER/BO80/1). All participants gave written informed consent prior enrolment in accord with the Declaration of Helsinki and were financially compensated for their time and effort.

3.2 Recruitment

Twenty-one healthy individuals were recruited for the study (15 males and 6 females, 22.3 ± 3.2 years). Originally, we were aiming to recruit 40 participants. This number was based on a previous sleep experiment that utilized a similar experimental protocol to investigate the effect of sleep on the apparent diffusion coefficients (Demiral et al., 2019). In this study the authors recruited 30 participants and scanned them twice in a repeated measures fashion, showing that this number is sufficient for showing changes in ADC during sleep. As this is the first study looking a sodium change during sleep, we did not have an estimate of the effect size. Nevertheless, it is reasonable to expect it to be larger than the ADC changes, based on the 60% increase in extracellular volume during sleep in rodents (Xie et al., 2013, Dinge et al., 2016). Unfortunately, recruitment to this study was significantly impacted by the COVID19 pandemic and only half of the planned participants were recruited. However, we are confident that 21 participants scanned twice is suitable to detect sleep related changes in higher order diffusion coefficients, as 30 participants were enough to detect changes with a less sensitive diffusion technique (Demiral et al., 2019). Moreover, significant changes in CBF were shown with ASL using similar number of participants (N=19) (Tüshaus et al., 2017).

Participants were recruited by advertisements placed on the University of Sussex and University of Brighton message boards and by word-of-mouth by our research team. Information sheets were available to any participants who expressed interest in the study and were sent via e-mail. Before study inclusion, all participants were screened for current and previous somatic and psychiatric

illness, the medical questionnaire used in this study specially focused on contraindications to the sleep drug administered in this study (10mg of Zolpidem).

3.3 Inclusion criteria

- Age between 18 and 35
- Able and willing to give informed consent
- Committed to 3 visits, 2 visits involving ~70 minutes of scanning each
- Willing to commit to a single night of full sleep deprivation and taking 10mg of Zolpidem
- Regular sleep wake cycle
- Self-reported sleep efficiency higher than 80%

3.4 Exclusion criteria

- Standard MRI exclusion criteria
- Any contradiction to Zolpidem
- History of sleep disorders
- Current or chronic somatic illness
- History of serious psychiatric conditions
- History of alcohol or illegal substance abuse

3.5 Study design overview

The study utilized a within-subject cross-over design in which all participants underwent two scanning sessions separated by 3-7 days (average 4 days). In one session (awake session) participants were instructed to arrive at the imaging centre well rested after a full night sleep. In the other, they were required to remain awake (at home) the night before the scan (sleep session) and were given 10mg Zolpidem half an hour before the scheduled MRI scan to maximize sleep during the scanning session. Participants were asked to avoid caffeinated beverages and nicotine for 12h prior to each scan.

In Chapter 1, I presented evidence that the glymphatic system is associated with slow wave sleep (Xie et al., 2013; Ding et al. 2016; Fultz et al., 2019) and that sleep deprivation increases sleep pressure that in turn leads to increased slow wave activity in the subsequent recovery sleep (Dijk et al., 1990). Consequently, to measure glymphatic system related changes we wanted to maximize the chance of SWS in the scanner, hence we used sleep deprivation. However, sleep deprivation on its own proved not to be very efficacious in inducing sleep in our pilot study and we decided to use it in combination with Zolpidem to increase the chance of falling asleep.

All MRI scanning took place at Clinical Imaging Science Centre (University of Sussex) using a Siemens Prisma 3T scanner with a maximum gradient strength of 80 mT/m.

3.6 Zolpidem

Zolpidem is one of the most widely prescribed short-acting hypnotic drug that has been shown to be efficacious in inducing and maintaining sleep with minimal dependence liability and toxicity (Priest et al., 1997; Langtry and Benfield, 1990). It is a non-benzodiazepine positive allosteric modulator of the gamma-aminobutyric acid (GABA) A receptor, meaning that it has a different chemical backbone than benzodiazepines and it increases the affinity of the endogenous chemical (GABA) for GABA A receptor binding (Goetz et al., 2007). GABA A is an ion channel receptor, which when activated allows the influx of Cl^- to the cells and hyperpolarizes/inhibits them (Goetz et al., 2007). Pharmacological agents that potentiate GABA A have been shown to reduce delta power and increase sleep spindles during slow wave sleep (Borbély et al., 1985; Dijk et al., 1989; Brunner et al., 1991). Although, increased delta activity was also reported in young individuals with self-reported chronic insomnia (Benoit et al., 1994). Decreased SWA associated with Zolpidem is not ideal for our study, but we decided the benefits of using Zolpidem outweighs the drawbacks. As, Zolpidem has been shown to reduce both the time to fall asleep and time spent in stage 1 sleep, furthermore in one study where it was used in combination it reduced the time to fall asleep after being woken up, which is particularly important for our study (Landolt et al. ,2000). The effects of Zolpidem on imaging data are discussed in Chapter 9.1.4.

3.7 Scanning time of the day

In Chapter 1.11.2 I reviewed studies looking at changes associated with time-of-day effects. To minimise circadian variations both wake and sleep session took place at the same time of the day, at 9h44min ± 22min and 9h47min ± 26min respectively (paired t-test, t= 0.34, df= 20, two-tailed p=0.737).

3.8 Session order

As the aim of our study was to investigate the effect of sleep on the glymphatic system, it was crucial that the participants felt comfortable sleeping in the MRI scanner. Thus, we offered them the choice of choosing the order of sessions. Most of our participants had never had a MRI scan before and choose to start with the wake session, so they could acclimatize to the environment. Fourteen participants started with wake scan first, while 7 participants started with the sleep scan.

3.9 Study timeline and data collection

Figure 21 summarizes the timeline and all the data collected during our study. During the first visit informed consent was obtained and the participants were asked to complete the medical questionnaire, as well as the Pittsburgh Sleep Quality Index (PSQI), as shown in Figure 21A. The PSQI assesses sleep quality over the past month and gives a self-reported measure for sleep efficiency, which was assessed prior to inclusion. Actigraphy watch (Actiwatch Spectrum Plus, Phillips Respironics) that estimates wake/sleep status from motion was used to determine total sleep time and sleep quality prior to the awake scan and to check compliance with sleep deprivation before the sleep scan. An example of an actogram (data collected over many nights) is shown in Figure 21B, where the blue areas represent sleep. 10mg of Zolpidem was orally delivered 30minutes before scan start, Figure 21C. Sleepiness immediately prior to each scanning session was assessed using the Karolinska Sleepiness Scale (KSS) (Akerstedt and Gillberg, 1990), which is a Likert type scale ranging from 1 (“Extremely alert”) to 9 (“Extremely sleepy, can’t keep awake”), Figure 21D. During scanning, participants were also required to maintain light pressure on a button box which served to detect muscle relaxation that occurs at the onset of sleep. Button box responses were

recorded and plotted in real time using a custom Matlab script (MathWorks, Natick, Massachusetts, United States). The output was displayed in real time, example shown on Figure 21E1. During scanning, respiration and pulse were continuously monitored (Figure 21E2) using a respiration belt (Biopac) and pulse oxymeter (Nonin 8600FO) respectively and data was recorded with Biopac AcqKnowledge 5 software (Biopac).

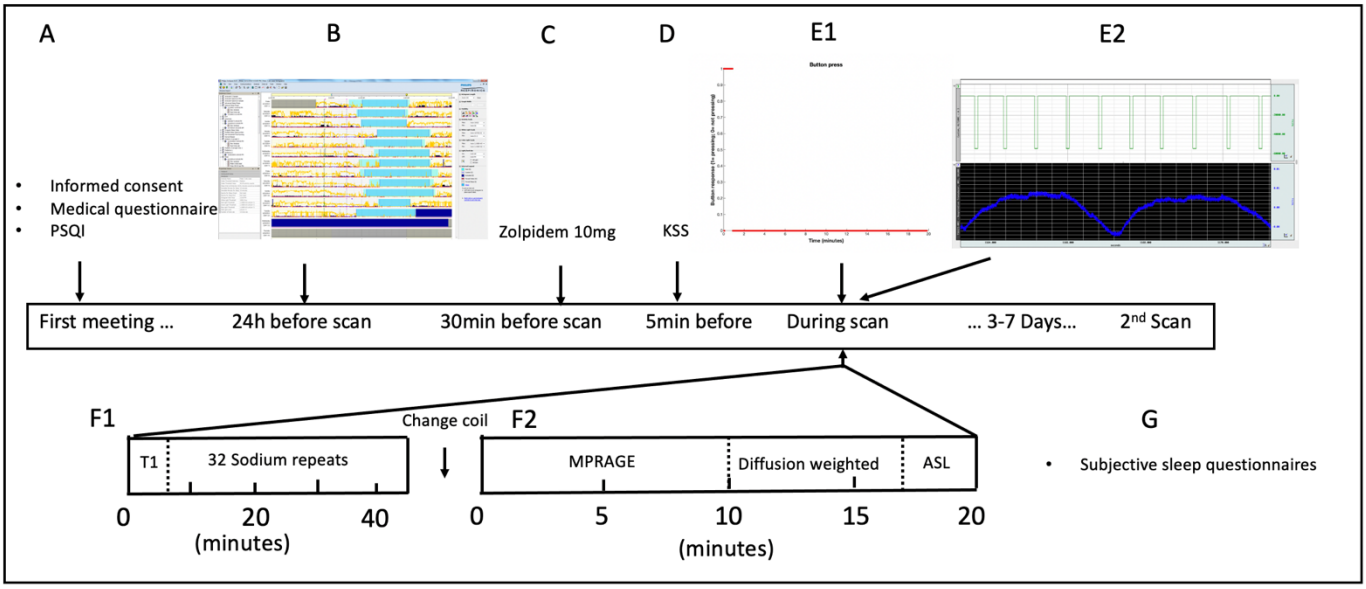

Figure 21: Schematic illustration of study timeline and data collection

Example of study starting with sleeps session first. **A**: first meeting with the participant; **B**: Actigraphy 24h before the scan to assess compliance with sleep deprivation; **C:** Delivering zolpidem 30 minutes before the scan; **D:** KSS 5 minutes before the scan; **E:** recordings during scanning, **1**- button press response, **2**- pulse events from pulse oximetry (top) and respiration signal (bottom); **F**: the order of MRI pulse sequences, **1**- sodium acquisition, **2**- order of proton coil acquisitions; **G**: subjective sleep

Figure 21F1 and 2 summarizes the order and length of the scans. Each scanning session started with the sodium acquisition, low resolution T_1 weighted images matching sodium resolution were acquired with the sodium coil at the beginning of the sodium acquisition (taking ~5 minutes). During the awake scan 16 Sodium MRI scan repeats were acquired. During the sleep scan this was doubled to investigate the temporal evolution of sodium signal during sleep Figure 21F1. To further increase the chance of falling asleep, we provided the participants with a leg cushion (to prevent back pain),

a blanket for comfort and the lights were off for the entire duration of the sleep scan. Participants were still provided leg cushion and blanket (if requested) in the wake scan as well, however the lights were on, and participants were asked to keep their eyes open. After the sodium acquisition, participants were awakened (if it was a sleep scan) and asked to sit up, while the head coil was changed that is because the sodium and proton scans required different head coils. During this procedure both the pulse oximeter and respiration belt stayed on the participant and was done very quickly, not taking more than 2 minutes. In the case of sleep scan the coil was changed in pitch dark to maximize the chance of falling back asleep. The proton scans included a high resolution anatomical T_1-weighted image (MPRAGE), diffusion weighted MRI and ASL, as displayed on Figure 21F2. After the end of proton scan participants were presented with "subjective sleep questionaries" (Figure 21G) details provided in Chapter 5.2.5. The second scanning session took place in the 3-7 days after the first one, allowing enough time to fully recover from sleep deprivation when the study started with sleep session.

3.10 Rational behind pulse-sequence order

To make sure that the participant can fall asleep in the scanner we started with the sodium acquisition first. It would have been more difficult to capture any sleep starting with proton scan first for two reasons: 1. Proton scans were shorter (20 mins vs 45 mins), so there would be less time to fall asleep before waking to change the coil for the sodium scans 2. Proton scans are much louder (especially diffusion and ASL) and more irregular sounding than sodium scans; the sodium scan are relatively quiet and very regular (almost soothing as described by some participants) because it is the same sequence repeated for 40 minutes. Based on these reasons, we decided to start with sodium scan first to let the participants accommodate to sleep while being scanned and anticipated that they were fall back asleep more easily after sleeping some time in noisy, confined environment of the scanner.

Chapter 4 Development and optimization of sodium analysis pipelines

4.1 Overview

In this chapter I describe the sodium image processing pipelines that I developed to pre-process and quantify the ^{23}Na MRI data. I include a discussion of the challenges associated with the processing and how I optimized the pipelines to address them.

Before I start describing the processing steps, I would like to recap some of the key features of sodium MRI that I described in detail in Chapter 2.1. Although sodium exhibits nuclear magnetic resonance, its intrinsic sensitivity is 4 time less than hydrogen. This combined with its lower abundance in the human body makes its measurement by MRI challenging. In addition, the sodium MR signal in tissue has biexponential relaxation behaviour with the fast component being lost within a few milliseconds. For these reasons, special pulse sequences, with ultra-short echo times (TE) and non-Cartesian sampling of k-space are necessary to sample sodium signal (Thulborn, 2018). Consequently, sodium MRI has a low SNR and wide point spread function that influences image quality and resolution.

Ignoring relaxation, the sodium MRI signal is proportional to sodium concentration, albeit on an arbitrary scale. Although in theory there should be direct proportionality between the signal intensity and total sodium concentration (TSC), in practice a small offset is always present due to noise and magnitude extraction. Quantification is often done by placing phantoms (e.g., test tubes with known concentration of NaCl) around the head from which refence signal is measured and used for linear regression to determine the transformation for signal to TSC conversion (Madelin et al., 2015). To do so we used four calibration phantoms[2], made from 3% Agar gel with known concentrations of sodium: 30, 50, 75 and 120mM NaCl, as displayed on Figure 22. Please note that we did not attempt to correct for T_1 saturation, as the chosen TR= 100ms should ensure minimal attenuation even in the CSF.

[2] Many thanks for Daire Cattilon for preparing the phantoms for Frank Riemer for providing the recipe

Figure 22: Custom-made head band holding the sodium phantoms.

4.2 Imaging parameters

^{23}Na MR images were acquired using a dual-tuned, 2-channel (one channel for sodium and one for proton) birdcage ^{23}Na/^{1}H coil developed by RAPID Biomedical GmbH (Rimpar, Germany). Sodium images were acquired using the FLORET sequence (Pipe et al., 2011), kindly provided by Dr Guillaume Madelin from NYU.

- Repetition time (TR)= 120ms
- Echo time (TE) = 0.2ms
- Flip angle= 80°
- 3 hubs at 22°
- 200 interleaves
- Pulse duration= 0.5ms
- Dwell time= 0.01ms
- Field of view (FOV) = 256 x 256 x 256mm^3
- Resolution= 4mm^3 (isotropic)

The k-space data were transferred offline and image reconstruction performed in Matlab (MathWorks, Natick, MA, USA) using 3D re-gridding (Pipe et al., 2011) with density compensation (Zwart, Johnson and Pipe, 2011). The reconstruction code was provided by Dr Madelin.

A low-resolution ^{1}H T_1-weighted image (T_1-4mm^3), matching the resolution of the Na image was acquired using the dual-tuned sodium coil as well as a higher resolution ^{1}H T_1-weighted image (T_1-2mm^3). These images were used for co-registration and processing purposes.

4.3 Pipeline 1- TSC estimation

It is extremely important to set up a reliable algorithm for signal estimation, as due to the low resolution of the sodium MRI scan and the presence of Gibbs ringing (Czervionke et al., 1988), the signal within the phantoms (which have a radius of 15mm) is typically non-uniform, particularly near the edges. For these reasons, manual region of interest (ROI) selection can bias the TSC estimation. Consequently, I developed a pipeline in Matlab that automatically draws the phantom ROIs, removing the potential bias from manual ROI selection. Next, I will describe each step from reconstruction to TSC estimation and will discuss some of the limitations of this pipeline and will offer an alternative solution to it.

1. The final sodium MRI protocol takes approximately 40 minutes to acquire yielding 32 volumes (sleep scan; wake scan: 16 volumes) that are averaged to achieve sufficient SNR. During this time, it is very likely that participants move, particularly while asleep. It is therefore necessary to realign each single volume before averaging. Realignment can be performed either in K-space or in image space. Although realignment in K-space is possible, there are no off-the-shelf algorithms, and therefore we chose to perform the realignment in image space. The downside of this choice is that typically only the magnitude of the signal is displayed, and the noise in magnitude images follows a Rician distribution (Gudbjartsson and Patz, 1995). For low SNR data (like sodium MRI) the bias introduced by the Rician distribution is substantial. Therefore, a complex (real and imaginary parts) image was reconstructed for each volume. The corresponding magnitude images were computed as sqrt(real^2+imag^2) and were realigned using SPM12 (http://www.fil.ion.ucl.ac.uk/spm/software/spm12/; Friston et al. 1996). The realignment parameters were then separately applied to the real and imaginary part of the images. This was done to be able to average the complex signal as opposed to the magnitude signal, and thus to avoid amplifying the noise due to its Rician distribution in magnitude images Figure 23 shows the effect of averaging the real and complex part before calculating the average magnitude image.

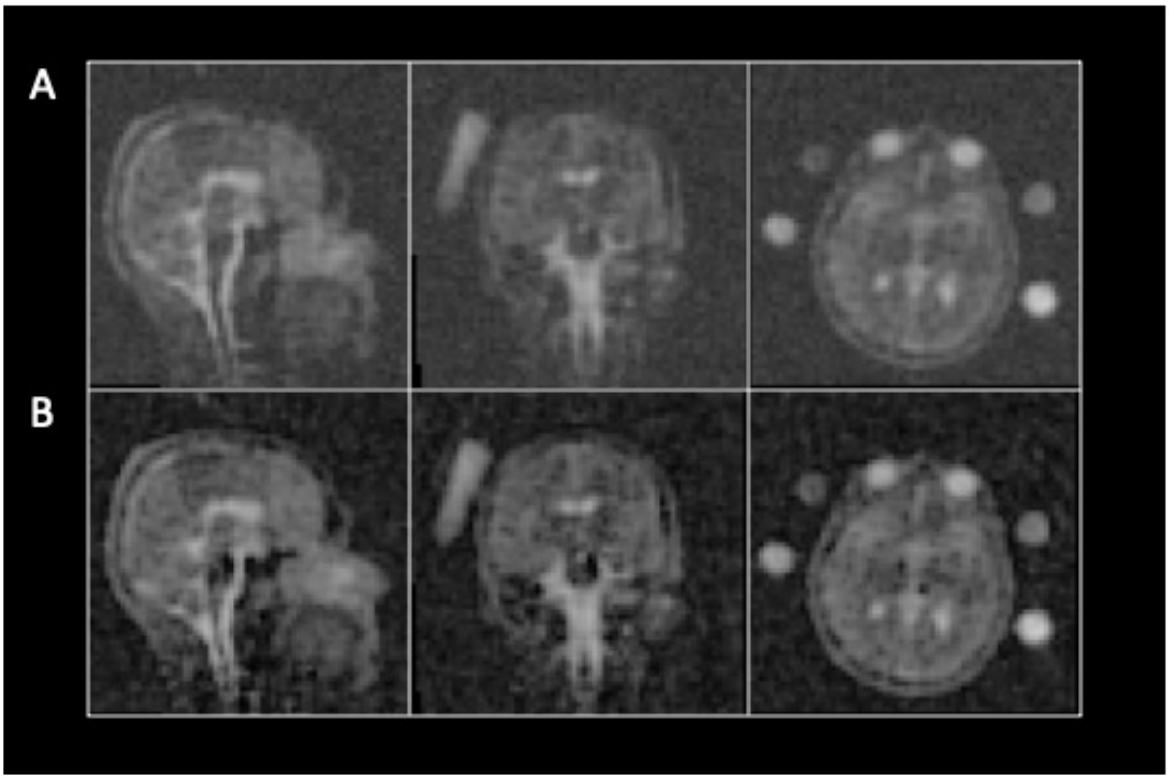

Figure 23: The effect of averaging complex images before calculating magnitude image

A: Average of 8 realigned magnitude images **B**: Magnitude image calculated as the average of 8 realigned imaginary and complex parts of the image. Note that when the magnitude images are averaged (A), the noise is amplified which is the most noticeable in the background.

2. 8 realigned complex images were averaged together before calculating the mean signal image (example shown in Figure 23B) to increase SNR. This gave 2 averages for the awake scan and 4 averages for the sleep scan.

3. The averaged signal images were then registered to the T_1 image with matching resolution (4 mm isotropic resolution). T_1 image with matching resolution was used as a source image to register the sodium averages to the higher resolution (2mm isotropic) T_1 image (which was also acquired with the dual-tuned sodium coil). Example of 4mm and 2mm resolution

images are shown in Figure 24A and B. Registering the sodium images to higher resolution space, makes it easier and more precise to create automated phantom region of interests (ROIs), which is described in the next step.

4. Automated phantom ROI creation and phantom sodium signal estimation: A bespoke Matlab algorithm was developed to automatically segment the phantoms and create ROIs to measure the mean signal in each phantom. The algorithm relies on the fact that the phantoms have a relatively high intensity and consistent signal on the T_1-2mm images (as the gel concentration is the same, only the sodium concentration, which does not affect 1H signal, varies), which makes it easy to set a threshold to create 4 independent non-touching objects as shown in Figure 24C. The inbuilt Matlab function “bwconncomp” was used to identify the phantom regions and binary masks were then created for them. These binary masks were then used as “seed masks” for an active contour algorithm that can identify the whole phantom from the background in the T_1-2mm image (Chan and Vese, 2001). The benefit of using the active contour algorithm over using a simple threshold method is that the former can more robustly distinguish edges and it is not reliant on an arbitrary threshold, shown in Figure 24D. In the next step the 4 phantom ROI binary images were separately co-registered to the sodium (2mm) mean images— this step is important because the phantoms might have moved during the acquisition (especially considering that the sleep scan lasted for 45minutes, the participant is less aware and might move more—this will be discussed later in more detail). The mean sodium signal was then estimated from each phantom ROI.

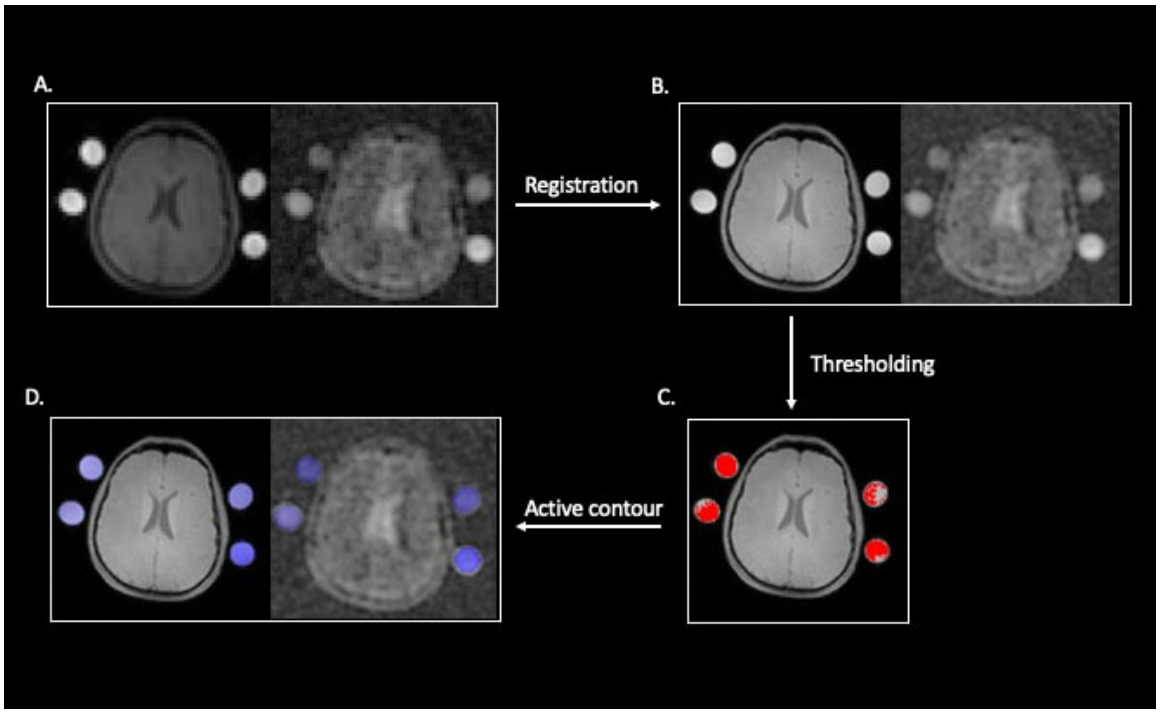

Figure 24: Sodium pipeline 1 processing steps

A: Left: T_1-weighted image acquired with the sodium coil, matching the resolution of the native (4mm^3 resolution) sodium image (on the right). **B:** The native sodium image was registered to the 2mm^3 resolution T_1 weighted image (Left), which was also acquired with the sodium coil. The registered (now 2mm^3 resolution) sodium is on the right. **C:** An arbitrary threshold was applied to the T_1 weighted (2mm^3) images to binarize the image and make 4 non touching object (red), which was overlaid on top of the non-thresholded T_1 image. Note that the binary mask is not completely covering the phantoms in the original image (e.g. the phantoms on the right). **D:** The binary masks from **C** were then used as seed masks for the active contour algorithm. On the left we can see that the phantom masks (blue) are perfectly matching phantoms (even the edges). The phantom masks (blue) are overlapping the sodium image phantoms well, on the left.

5. Linear regression was then applied to the known concentration phantoms and their mean sodium signal value to find the equation to convert the signal image to a sodium concentration image, as described in Figure 25**.**

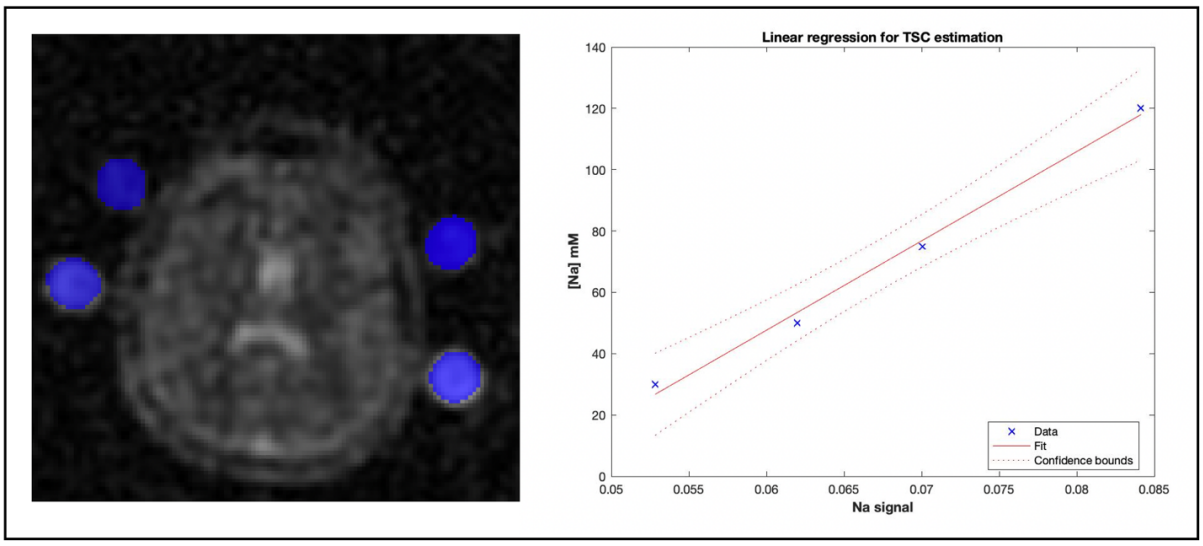

Figure 25: Estimation of Total Sodium Concentration

A: The blue areas show the four phantom masks on an axial sodium signal image that are used to estimate the mean phantom signals **B**: Linear regression of reference phantom signal that provides the conversion from signal to concentration: TSC= m*Sodium Signal+ c, in this case TSC= 2913.7*Sodium signal – 127.2. The coefficient of determination (R^2) is also calculated, for this line R^2= 0.99 indicating that the model explains 99% of variability in sodium concentration.

4.4 Motion during acquisition

As mentioned previously, phantom ROI selection can potentially bias the signal to TSC conversion. Next, I planned to investigate how motion of the phantoms affect the estimated signal and how it could be objectively detected/quantified. Finally, I went on to investigate the efficacy of realignment by using 2 examples acquired during sleep scans.

4.4.1 Motion simulation

To investigate the effects of motion during scanning, we acquired 8 phantom images (sodium phantoms were placed around a water cylinder) and calculated the average signal image by keeping 4 stationary and rotated (artificially in Matlab) the other 4 by 0°, 2°, 4°, 6°, 8° along the longitudinal

axis. Figure 26A shows the average image when all volumes were kept stationary before averaging. Rotating half of the volumes by 6° led to prominent image blur, as displayed on Figure 26B.

To complement visual evaluation, I developed an objective way to measure image blur, which I called the Active Blur Detection Method (ABDM) that served as quality control for the realignment (in analysis pipeline 1). This method is conceptually the same as making phantom ROIs in step 4 of processing pipeline 1, but here the 120mM phantom mask (obtained from T_1-weighted image) is used as the seed mask and applied to the sodium image. The assumption behind this approach is that the blurriness would lead to an overestimation of the size of the phantom because the edges are ill-defined. Therefore, once we have the mask for the phantom from T_1 and the mask for sodium, we can compare the volume of the two masks Figure 26C shows the relationship between change in estimated phantom volume and the estimated signal loss. Signal loss increases with more rotation, and this can be detected by ABDM, as the volume of the phantom mask increases as hypothesized.

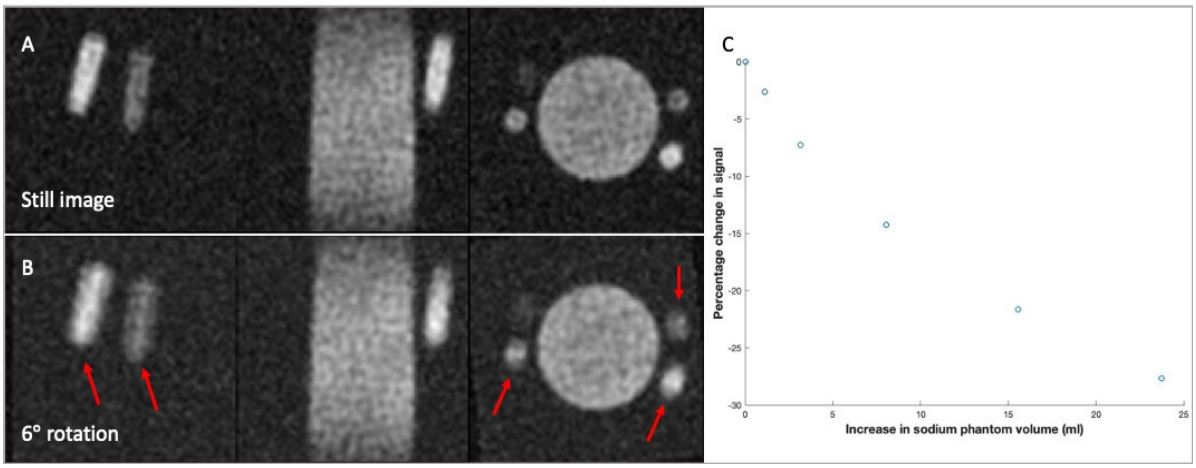

Figure 26: Simulated phantom motion and estimated signal loss

A: Average of 8 sodium acquisitions with sodium phantoms wrapped around a water cylinder. **B**: Average of 8 sodium acquisition with 4 acquisitions kept stationary and 4 rotated by 6°. The red arrows represent the blurry areas. **C**: Relationship between change in mean signal (in 120mM phantom) and change in phantom volume (for reference size phantom volume estimated from T1 image is ~45ml). The points represent 0°, 2°, 4°, 6°, 8° rotation respectively.

4.4.2 Testing efficacy of realignment with ABDM

Figure 27 shows mean sodium signal images acquired during the sleep session, without motion correction (Figure 27A and B) and with motion correction (Figure 27C). Figure 27A is the average of 8 images where the participant stayed relatively still, while Figure 27B is the next average compromised by motion, as highlighted by the red arrows. Figure 27C illustrates the effectiveness of realignment, as previously compromised/blurred regions now look sharper (as indicated by the white arrows).

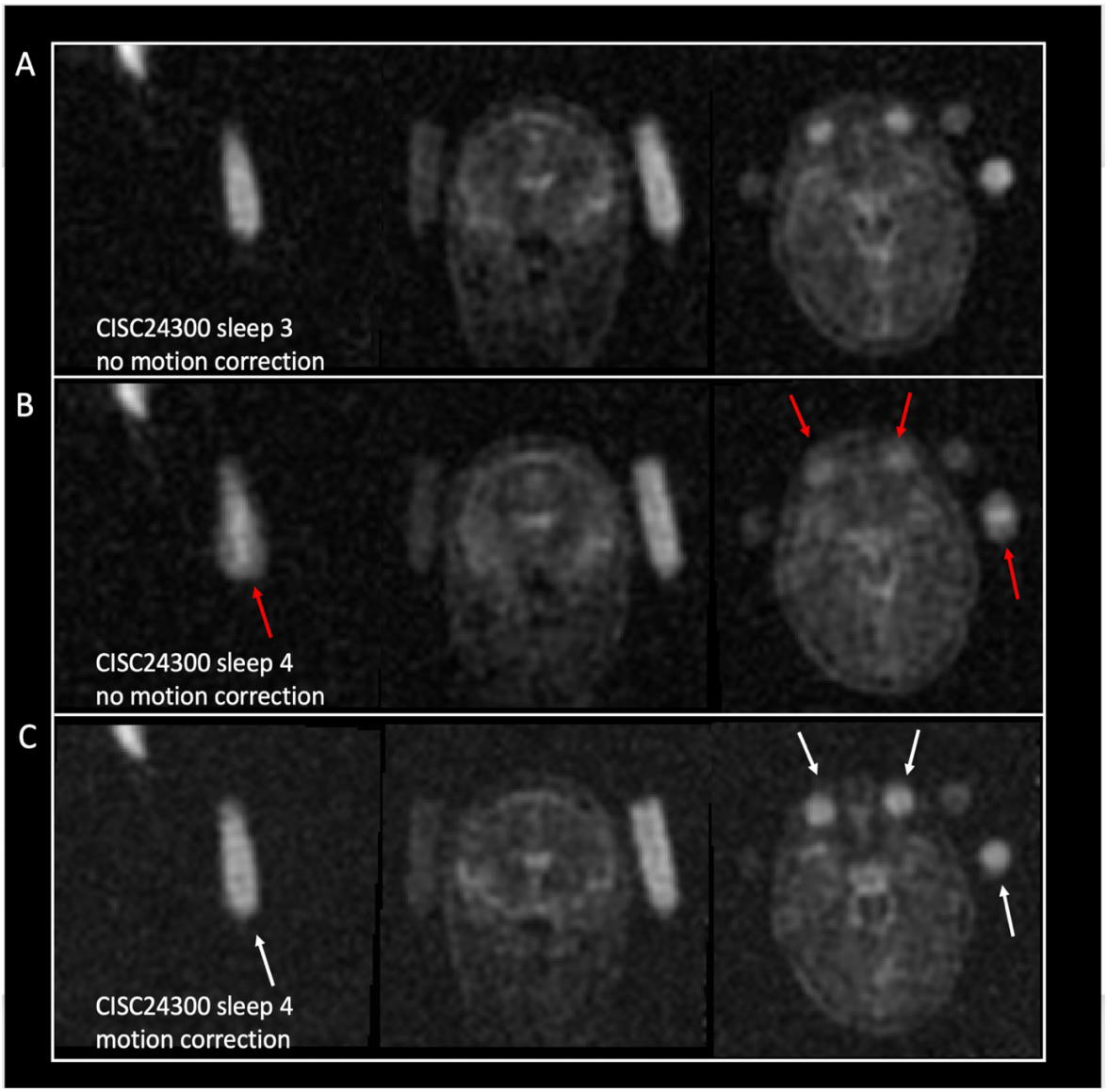

Figure 27: Effect of motion during image acquisition

A: Average of 8 sodium acquisitions without motion correction (realignment), when the participant stayed relatively stable. **B**: Average of 8 sodium acquisitions of the same participant without motion correction. In this instance the participant has moved during the scan and hence there is image blur indicated by the red arrows. **C**: Shows the same acquisition as **B**, however now the individual images were realigned (motion corrected) before the mean was calculated. The white arrows indicate the previously compromised/blurry areas that now become sharper.

Next, I evaluated the efficacy of realignment with ABDM. In Figure 28C, I measured the volume of the ^{1}H T_1 phantom mask (Figure 28B red), which serves as the ground truth for the phantom volume

and compared it to the volume of the masks obtained with ABDM. Note that these are averages obtained without motion correction. Figure 28C summarizes the sodium mask volumes and the T_1 mask volume (only one T_1 image was acquired, it is only displayed multiple times to enable better comparisons). In the first 3 averages the difference in sodium phantom volume is negligible (sleep 1: 47.0ml; sleep 2: 48.1ml; sleep 3: 47.5ml) and slightly higher than T_1 phantom volume (45.3ml), which is expected because of the wider point spread function of sodium MRI. On the other hand, the sodium phantom volume in the last average is noticeable higher (54.0ml), indicating that this average is considerably affected by motion-induced blur. In Figure 28C, it is apparent that motion correction dealt well with image blur, which is also reflected in the phantom volume measure that went from 54.0ml to 48.9ml.

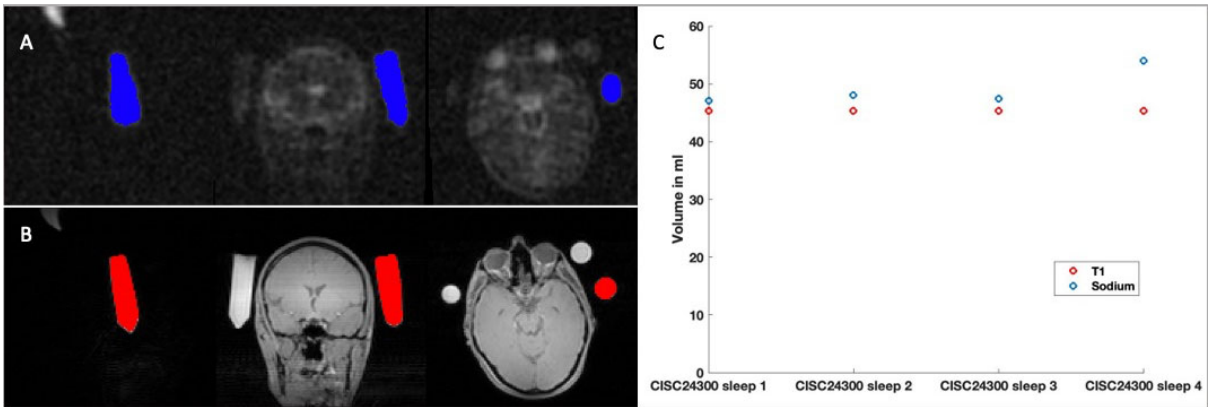

Figure 28: Efficacy of motion correction determined by active blur detection method

A: Blue shows the active contour 120mM phantom mask created from the un-realigned blurry sodium image (CISC24300 sleep 4). **B**: Shows the active contour mask 120mM phantom mask created from the T_1 weighted image. **C**: Shows the volume of the 120mM phantom mask estimated from the T_1 weighted image and the volume estimated form the (un-realigned) sodium averages.

Figure 29 shows the rigid body motion during the last 8 acquisition of the sleep scan example previously presented (Figure 27 and Figure 28).

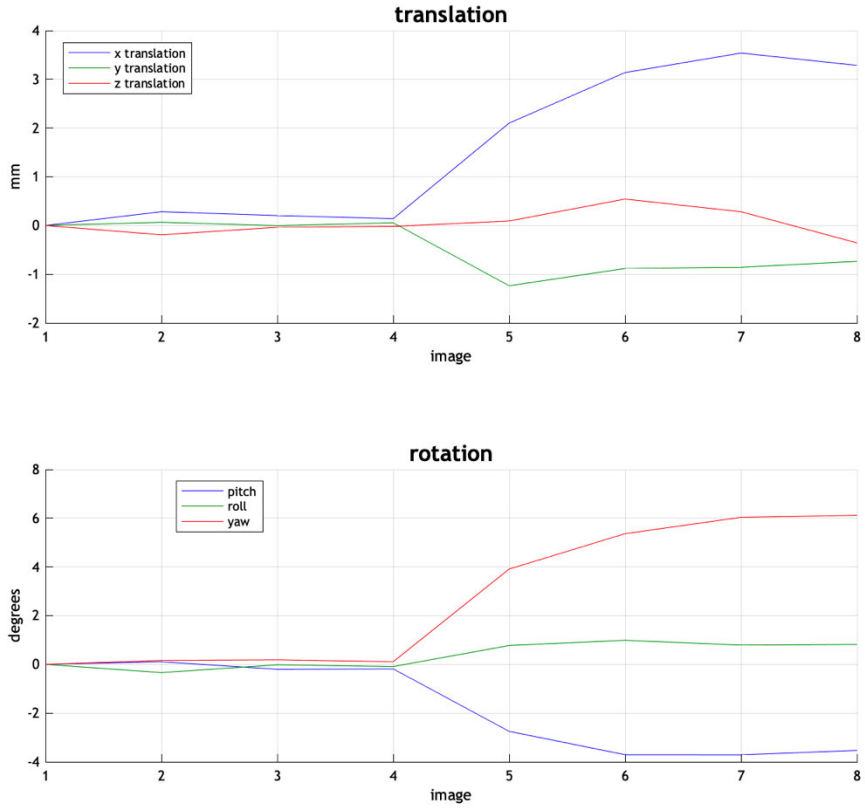

Figure 29: Example of motion during sleep

Translation and rotation of the 8 images during one of the sleep scans (CISC24300 sleep 4). During the first 4 acquisition the participant stayed relatively stable but moved after.

4.4.3 Importance of motion correction

Image blur leads to an underestimation of the mean phantom signal, consequently overestimating TSC estimation. For example, before motion correction (CISC24300 sleep 4) the mean TSC in 99% grey matter was estimated at 56mM, while after motion correction it was estimated at 49mM.

So far, I showed that motion during sodium acquisition leads to image blur that can be quantified with ABDM in both simulated and real data. Moreover, I showed that blur in the phantoms can lead to signal underestimation (in simulated data) that in turn leads to overestimation in brain TSC. Furthermore, I showed that rigid body motion correction (realignment) can deal with the motion related image blur (at least in the presented example). The fact that motion correction removed the blur from both the eyes and the phantom (as shown in Figure 27C) means that the phantoms moved with the head, which is the “ideal” kind of motion because we can correct for it. Although

motion correction did improve image quality in general, I became aware of cases where motion correction seemed not to improve image blur in the phantoms, an example shown in Figure 30. This kind of image blur is likely to originate from independent (from head) movement of the phantoms, which is due to the slipping of the head band (that hold the phantoms) during the scan.

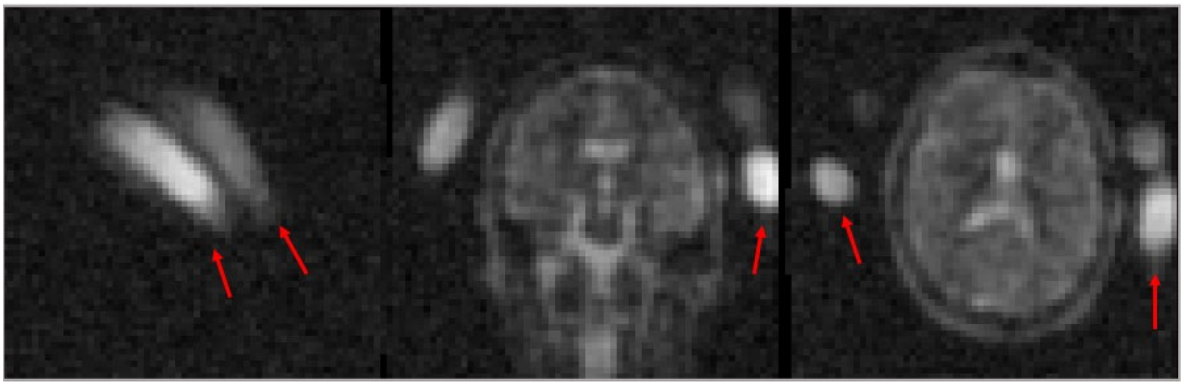

Figure 30: Failure of motion correction

An example where the motion correction failed to correct for phantom displacement during the scan, resulting in blurred phantoms as indicated by the red arrows.

4.5 Pipeline 2- Signal normalization to the eyes' signal

Despite best efforts to minimize and correct the effects of motion, some datasets remained impacted by motion where the phantoms and head moved independently, leading to overestimation of TSC in the brain. Because the TSC estimation is highly sensitive to phantom blur (and the COVID19 pandemic prohibited further data collection) I decided to use a different approach to normalize the sodium images. Sodium signal in the eyes seemed like an ideal candidate for normalization. Firstly, the eyes move synchronously with the head so the motion correction for head movement would simultaneously correct for the eyeball movement, which is not always true for the phantoms as they can slip and move independently from the head. Secondly, the vitreous body of the eyes is highly homogenous, consists of 99% water, collagen and hyaluronic acid, and it is large enough (16mm in length and almost completely spherical) to place an ROI in it with little partial volume effects (Sebag, 1989). There are no reliable published data on vitreous fluid sodium concentration in living humans, however different animal studies have consistently shown that the

sodium concentration is ~95% of those in blood (McLaughlin, and McLaughlin, 1987; Wilkie and Bellamy 1982). The high sodium concentration in vitreous fluid (~140mM) and the relatively large size gives decent SNR. Furthermore, the vitreous fluid can be considered as an isolated fluid that is less vulnerable to ionic fluctuations than blood (Coe, 1969), therefore we assumed that sodium concentration will be the same across the two sessions and the eye signal gives a stable normalization coefficient. The disadvantage of this approach is that it does not provide quantitative concentrations and extracellular volume fraction cannot be estimated but, in this study, as we were primarily interested in between-session changes, it provides a good enough benchmark.

1. The reconstruction step was almost the same as in the first pipeline, however here we utilized FLORET sequence's oversampling property and used a sliding window approach for reconstruction (as described in Chapter 2.1.2, Figure 10). This led to a 3-fold increase in the number of magnitude images available for estimating realignment parameters to further reduce movement related image blur. Although, we need to note that these images have very low SNR, consequently high signal areas can bias the realignment (I discussed this in Chapter 7.6.5).
2. The mean signal image along with all the individual images were then registered to the high resolution T_1 weighted proton image (MPRAGE). The T_1-weighted image was segmented with SPM12 to obtain GM, WM and CSF tissue probability masks. These masks were then used to compute global sodium change.
3. Eye masks were created by applying active contour (Chan and Vese, 2001) to both the sodium (high resolution space – $1mm^3$) and T_1 weighted anatomical image with the seeds manually positioned at the centre of right and left eyes. The final eye mask was created by the conjunction of the masks created from the sodium and anatomical image. The masks were further eroded to ensure that they do not include any other tissue, as shown in Figure 31.

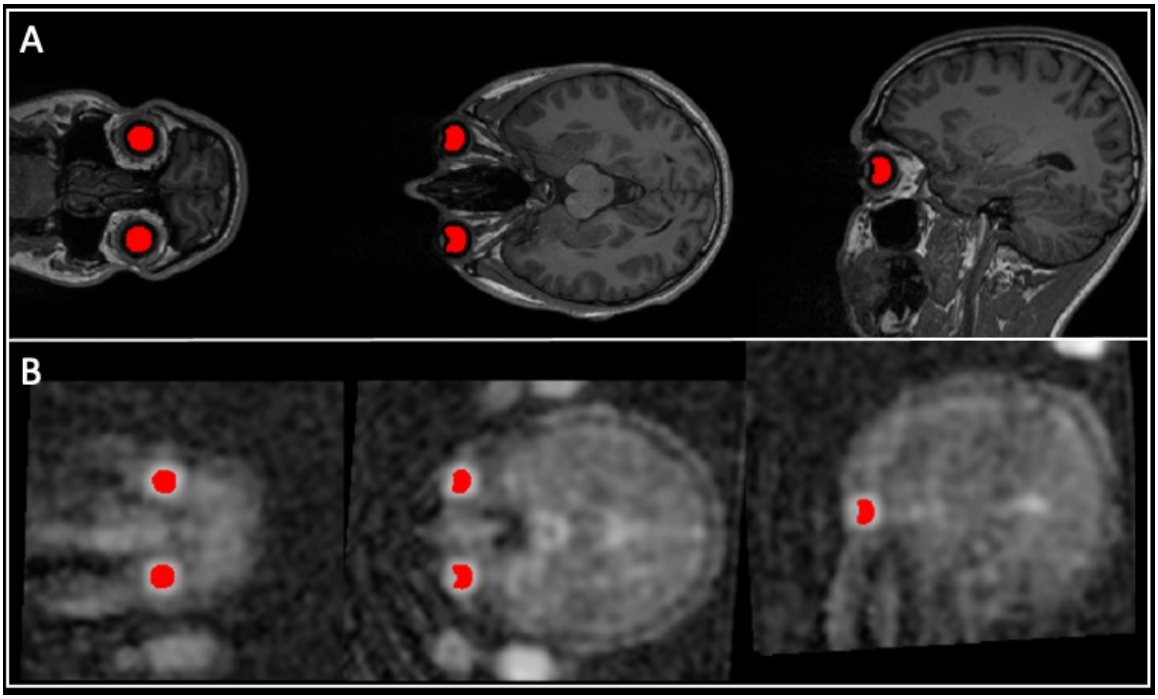

Figure 31: Eye masks for signal estimation

A: Eye masks used for signal estimation overlaid on the high resolution T_1-weighted image **B**: Eye masks overlaid on the (co-registered) sodium image. The mean sodium signal from both eyes were then used to determine the signal normalization parameter.

4. The signal normalization parameter was applied to all individual sodium images in high resolution (1mm^3 MPRAGE space) and mean images were calculated for every 5 minutes of acquisition—these images were then used to investigate the temporal evolution of the sodium signal in GM, WM and CSF during wake and sleep scans.
5. All sodium images (high resolution space) were normalized to Montreal Neurological Institute (MNI) space and resliced to 2x2x2mm^3 isomorphic voxels using the normalization parameters obtained from the segmentation of high resolution T_1-weighted image.
6. Mean images for every 20 minutes of acquisition were calculated (1 image for awake and 2 images for sleep). The images were masked with participant specific brain masks and smoothed with a 6 mm full-width at half maximum (FWHM) Gaussian Kernel with SPM12.

Chapter 5 Behavioural and physiological recordings

5.1 Introduction

This chapter focuses on all the non-MRI measures that were used to assess sleep quality before and during the scans. In particular, this includes, questionnaire assessing sleep quality during the month preceding the scans, actigraphy assessing sleep the night before scans, and metrics assessing the effectiveness of sleep deprivation combined with 10 mg of Zolpidem in inducing sleep. Moreover, we recorded some physiological parameters during scanning used as indicators of sleep in the scanner. The gold standard for detecting sleep is EEG, which could not be used in this study because even MR-compatible EEGs are MR conditional, i.e., can only be used with some pulse sequences (for safety reasons), and burns have been reported when using them in combination with, e.g., diffusion MRI (Demiral et al., 2019).

Sleep is associated with various physiological changes, which I briefly touched upon in Chapter 1.3. Here, I will review some of the measures that show sensitivity for sleep onset and potentially for sleep depth during scanning.

5.1.1 Muscle tone

One of the earliest observations showed a relationship between muscle tone and EEG activity, a handheld spool was dropped shortly after (1-25 seconds) after the disappearance of alpha waves, indicating the transition from wakeful relaxation to light sleep (Blake, Gerard and Kleitman, 1939). Others have also used a reduction in muscle tone as an approximation for sleep onset, by asking their participants to hold down lightly a microswitch continuously, pressing indicated awake and the passive release indicated the onset of sleep (Ogilvie, 2001). This method showed good correlation between sleep onset and stage 2 sleep measured by polysomnography (Viens et al., 1988).

5.1.2 Heart and respiration rate

Transition from wake to NREM sleep is associated with a decrease in heart and respiration rate (Burgess, Kleiman and Trinder, 1999). Slow wave sleep is associated with a moderate but significant decrease in heart rate (Kirby and Verrier, 1989; Penzel et al., 2003).

Respiration rate becomes unstable during sleep onset as chemosensitivity becomes the main driving force for ventilation. It is worth noting that chemosensitivity is supressed at sleep onset, where there is a higher threshold for hypercapnia, which leads to fluctuations in breathing (Trinder et al., 1992). These changes can vary a lot between individuals. On the other hand, SWS is associated with reduced minute ventilation (tidal volume x respiration rate), however there seems to be disagreement about whether this is due to reduced tidal volume and/or respiration rate (Douglas et al., 1982; Krieger et al., 1990; Gutierrez et al., 2016).

5.1.3 Heart rate variability (HRV)

The cardiovascular system is coordinated by the autonomic nervous system (sympathetic and parasympathetic) that controls heart rate, blood pressure, peripheral blood flow on a beat-by-beat basis. Precise control is needed to match cardiac output to the current needs of the body which is affected by behavioural, environmental, and emotional factors. Due to these constant adjustments variability in the inter-beat intervals (RR intervals—usually obtained from electro-cardiography (ECG)) can be observed (Akselrod et al., 1981). The inter-beat interval tends to oscillate with 0-0.5Hz and is influenced by the autonomic nervous system as well as respiratory changes. One of the most common ways to investigate HRV is by spectral analysis, which shows how power is distributed across different frequency bands for a given time period (e.g. in 5 minutes of recording). The variability in inter-beat intervals can be described by three frequency bands: very low frequency (VLF) (0.003- 0.039Hz), low frequency (LF) band (0.04- 0.1Hz) and high frequency (HF) bands (>0.15Hz). HF and LF power have been shown to be promising measures for approximating sleep state (Shaffer and Ginsberg, 2017). LF band has been associated with several physiological factors including sympathetic influence on the heart, however it is also influenced by irregular breathing patterns. The HF power band has mainly been associated with respiration driven modulation of sinus arrythmia (RSA- respiratory sinus arrythmia) and have been used as an approximation for vagal influence on the heart and has been associated with relaxation. Reduced HF power in healthy participants is associated with psychological stress (Allen and Crowell, 1989) and exercise (Hatfield

et al., 1998), while increased HF power is associated with psychological relaxation (Sakakibara, TakeuchI and Hayano, 1994).

Heart rate variability changes as one progresses through sleep stages. As one proceeds from light to deeper NREM sleep the vagal tone increases and there is an increase in inter-beat intervals and HF power (Žemaityte, 1986). HF-power tend to increase as sleep deepens, suggesting increased vagal tone, while LF tend to decrease as sympathetic tone is suppressed (Žemaityte, 1986). Although, it should be remarked that HRV measures can only give reliable measures of sleep stage under controlled circumstances, as there are many factors that can influence these measures e.g., respiration, time of day; and their reflection on autonomic control has been questioned (Hayano and Yuda, 2019).

5.2 Methods

5.2.1 Assessment of sleep quality over the past month

Participants' sleep quality over the past month was assessed with the Pittsburgh Sleep Quality Index (PSQI) (Buysse et al. 1989). PSQI is a self-reported questionnaire that assesses subjective sleep quality in the past month. It consists of 19 individual items that evaluates 7 components of sleep: subjective sleep quality, sleep latency, sleep duration, sleep efficiency, sleep disturbance, use of sleep medication and daytime dysfunction. Each of the 7 components are scored on 0-3 scale and then summed to get a global PSQI score, where 0 is the best sleep quality and 21 is the worst. A copy of the PSQI with the scoring sheet is provided in the Appendix A- PSQI.

5.2.2 Actigraphy the night before scanning sessions

Participants were required to wear an actigraphy watch (Actiwatch Spectrum Plus, Phillips Respironics) for 24 hours prior to each scan. The actigraphy data was analysed using Actiware 6 software (Phillips Respironics). To carry out sleep analysis, epoch length must be one minute or less, for this study the finest epoch length was selected (15 seconds), meaning that the watch measures activity in 15 second intervals before saving it. Active, rest (where the subject may have been resting for 3 hours or more) and sleep intervals were automatically calculated using the Actiware default

settings and the automatically generated "Clinician's report" was used to determine sleep parameters. Examples of the output of the Clinician's report are shown in

Appendix B- Actigraphy clinicians report example.

5.2.3 Assessment of sleep deprivation

Actigraphy before sleep scan was used to assess compliance with sleep deprivation. Moreover, the Karolinska Sleepiness Scale (Appendix C- KSS)was used to assess sleepiness before the scans, which can be considered as an approximation for sleep deprivation/Zolpidem efficacy.

5.2.4 Physiological measures during MRI acquisition

Button press response

Participants were instructed to continuously hold down a trigger button with their right index finger during scanning. Responses were sampled every second (either press- 1 or no press 0). Button press fraction was calculated for 5 minutes epochs as the sum of responses divided by the number of samples *100. Significant effect/interaction between time and conditions (awake vs sleep session) was assessed with repeated measures ANOVA. Statistical test was done in SPSS 27, $p<0.05$ was considered as significant.

Heart rate and HRV

Pulse oximetry was used to record pulse events. Pulse oxymeter (Nonin 8600FO) was connected to DA100C advanced transducer amplifier via A/D (analog to digital) converter and connected to MP160 (Biopac) data acquisition system (sampled at 2000samples/second). AcqKnowledge 5 software (Biopac) was used to find the time of pulse events. Pulse events are representation of RR peaks, which were loaded in the Kubios software and analysed. Heart rate and HRV was estimated for contiguous 5-minute epochs and the software's inbuilt artifact correction was applied (threshold=medium). Significant effect/interaction between time and conditions (awake vs sleep

session) was assessed with repeated measures ANOVA. Statistical test was done in SPSS 27, $p<0.05$ was considered as significant.

Respiration rate

Respiration was measured with a respiration belt (Biopac) connected to DA100C advanced transducer amplifier (Biopac) via TSD-221-MRI- respiration transducer (Biopac) and connected to MP160 (Biopac) data acquisition system (sampled at 2000 samples/second). Amplifier specifications: gain= 50; low pass filter on 10Hz and high pass filter on 0.05Hz. Respiration data was pre-processed in AcqKnowledge 5 (Biopac), first it was resampled at 50 samples/second and a bandpass finite impulse response (FIR) filter between 0.05Hz and 1Hz was applied. The "find cycles" function was used to detect peaks of inspiration. A custom written Matlab code was then used to determine the mean respiration rate in 5-minute contiguous epochs (from the inspiration peak time intervals). Significant effect/interaction between time and conditions (awake vs sleep session) was assessed with repeated measures ANOVA. Statistical test was done in SPSS 27, $p<0.05$ was considered as significant.

Data visualization (heart rate, respiration rate and HF power)

For data visualization percentage change of baseline was calculated for each epoch (per participant), wake mean (0- 25 minutes awake scan, sodium and proton separately) was considered as baseline. For example mean heart rate (for 5 min epoch) minus the wake mean (calculated from whole sodium/proton scan) divided by the mean wake heart rate (calculated from whole sodium/proton scan)* 100.

5.2.5 Subjective sleep questionnaires

After scanning, participants were presented with a subjective sleep questionnaire that included questions about their sleep quality in the scanner. The questionnaires separately asked about their sleep during the sodium and proton acquisitions. Participants were asked whether they fell asleep at any point of the scan, whether they woke up after falling asleep. They were also presented several Likert scales asking about how sleepy they felt during the scan (if they did not sleep); when

they fell asleep; how long they think they slept for and how deep they felt they were sleeping. All of these scales were quantified on a 1-10 scale, e.g. very light sleep is 1 and very deep sleep is 10. Furthermore, they were asked whether they dreamt during the sleep scan. The subjective sleep questionnaire is included in Appendix D- Subjective sleep questionnaires.

5.2.6 Exclusion

It should be remarked that sleep measures exclusively related to sodium scans included measures from all 21 participants, while for proton only 18 participants. The reason for this discrepancy is that 3 participants were not included in any of the proton image analysis (2 for not sleeping at all during the proton scan and 1 for excessive motion).

Two participants were removed from the respiration rate analysis, because the data was too noisy, likely due to poor fit of the respiration belt.

5.3 Results and Discussion

5.3.1 PSQI

All participants reported a regular sleep-wake cycle in the preceding month with 7.6h ± 1.4h sleep per night on average. Participants reported an average PSQI score of 3.9 ± 2.2. Self-reported sleep times, sleep onset and efficiency are summarized in Table 2.

Parameters	Mean ± Standard deviation
Total sleep time (hours)	7.6 ± 1.4
Onset latency (minutes)	19.8 ± 11.8
Sleep efficiency (%)	95.8 ± 2.4
Total PSQI score	3.9 ± 2.2

Table 2: Summary of Pittsburgh Sleep Quality Index

5.3.2 Actigraphy the night before wake scan

On average participants went to bed at 23:43 ± 1h 57min and woke up at 08:02 ± 1h 29 min. The average total sleep time before the wake scan was 6h30min ± 1h23min. Figure 32 summarizes actigraphy results from the night before wake scan, including sleep efficiency estimation (Figure 32A), sleep onset latency (Figure 32B), wake after sleep onset (WASO) (Figure 32C) and number of awakenings (Figure 32D).

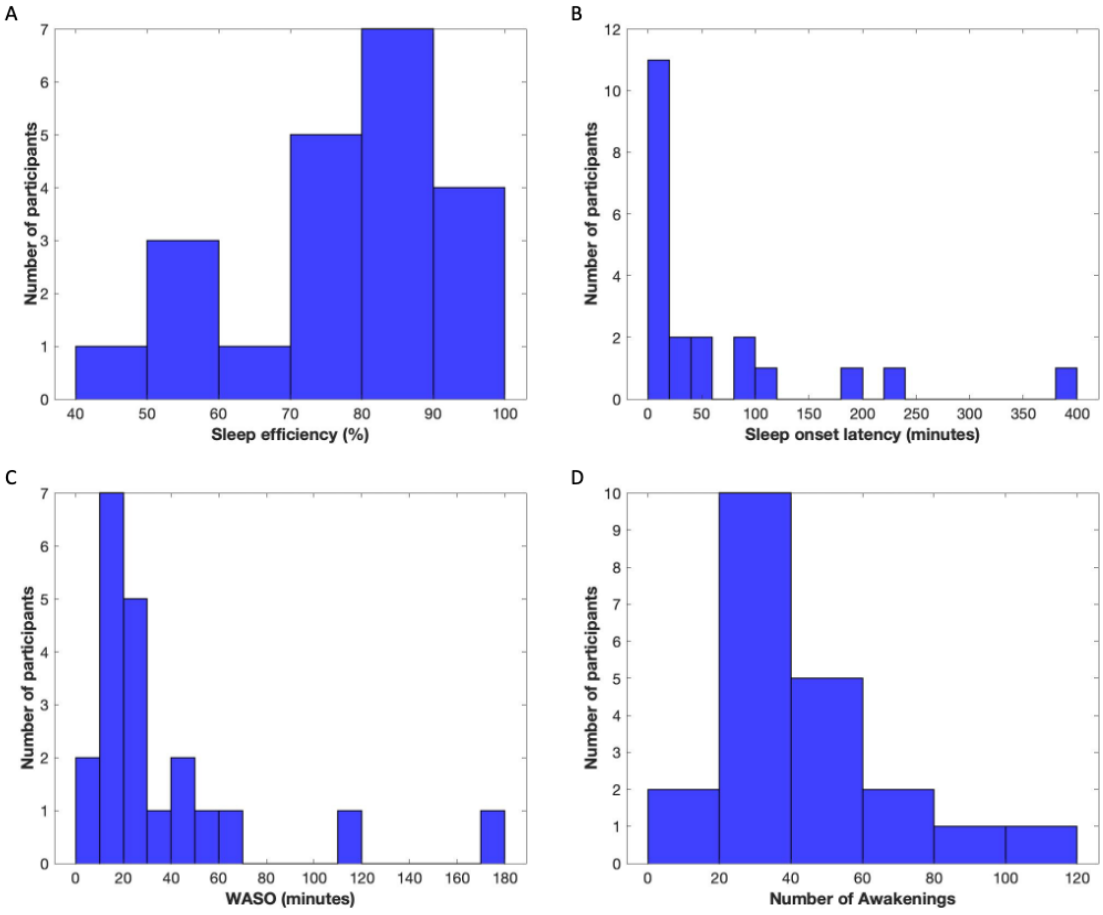

Figure 32: Actimetry results obtained the night before the wake scan.

A: Sleep efficiency; **B**: Sleep onset latency; **C**: Wake after sleep onset; **D**: Number of Awakenings

All participants reported a regular sleep wake cycle with mean sleep efficiency over 95%. The mean PSQI score (3.9± 2.2) reflected that the participants could be considered as good sleepers. More detailed information can be gained from the actigraphy measures obtained the night before the wake scan. Figure 32A illustrates that most of the participants' sleep efficiency the night before the

wake scan was above 70% (N=16), while some participants displayed extremely poor sleep efficiency (~50%). Figure 32B shows a strongly positively skewed onset latency distribution, meaning that while most participants fell asleep in a relatively short period of time (~30 minutes; in agreement with PSQI) there were several participants who took a very long (over 60 minutes; N=6) to fall asleep. Figure 32C and D shows positively skewed WASO and number of awakening prior the wake scan, suggesting that not all participants got the same quality of sleep and that they are not actually as good sleepers as suggested by PSQI score.

One explanation for the low sleep efficiency and long sleep onset latency is that participants bed behaviour was not controlled. We did not give participants clear instructions to maintain regular sleep and waking times days prior to the experiment. Furthermore, we did not specify to go to bed only with the intention to sleep. It is possible that participants with extremely low sleep efficiency watched TV or engaged in other activities for a prolonged time before actually trying to fall asleep. To overcome these problems in any future study, we should give clear instructions to maintain a regular sleep regime prior to the experiment, analyse actigraphy measures before the scans and only continue with the scanning if the participants complied with the instructions and sleep quality was sufficient (e.g., sleep efficiency >80%; and WASO and number of awakenings do not exceed a set limit).

5.3.3 Assessment of sleep deprivation

The wearable sleep sensor demonstrated that most participants complied with sleep deprivation, 18 out 21 participants did not sleep at all before the sleep scan, though three participants did not comply with the sleep deprivation and slept on average 5h42min ± 1h22min. Before the wake scan participants slept on average 6h30min ± 1h23min that is significantly higher (Wilcoxon signed-rank, $T= 231$, $z= 4.0145$, $p<0.0001$) than the total sleep time before the sleep scan 52min+ 2h05min as show in Figure 33A. Evidence for the effectiveness of sleep deprivation was also indicated by the KSS scores Figure 33B), which is a measure for sleepiness. Participants were significantly sleepier (paired t-test, $t= 8.243$, $df=20$, $p<0.0001$) before the sleep scan (mean KSS= 7.6 ± 1) than before the awake scan (KSS= 4.0±1.6).

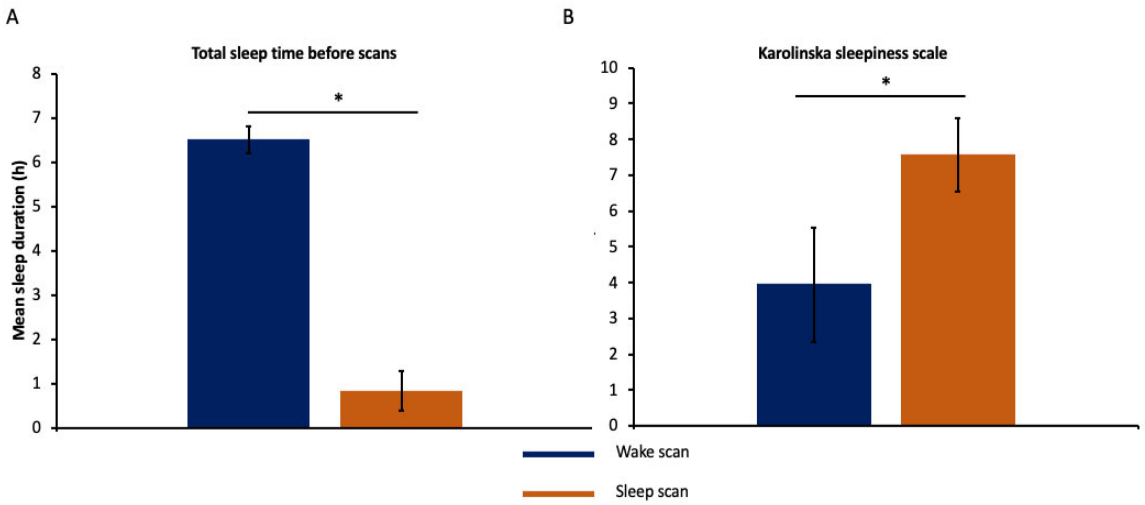

Figure 33: Assessment of sleep deprivation

A: Bar plot illustrating the mean total sleep time before the wake and sleep sessions. Error bar represents standard error of the mean (SEM). **B**: Bar plot illustrating the mean KSS before the wake and sleep sessions. Error bar represents standard deviation (SD). * represents $p<0.0001$

Evidence for the effectiveness of the combined sleep deprivation and sleep medication intervention was confirmed by the Karolinska Sleepiness Score, as participants were significantly sleepier before the sleep scan than the wake scan. All but 3 participants complied with full sleep deprivation, as reflected by the actigraphy the night before sleep scan. We decided not to exclude these participants from the final analysis as they were able to fall asleep during the sleep scan. However, we need to keep in mind that any sleep during the 24h before the sleep scan might have influenced the MRI measures, as these participants experienced less sleep pressure than the others, which is likely to influence sleep in the scanner (e.g., onset latency might be higher, arousal threshold lower, lighter sleep, more awakenings).

5.3.4 Physiological measures during MRI acquisition

Button press response

Figure 34 illustrates the button press response during sodium (Figure 34A) acquisitions and proton (Figure 34B) scans. During both sodium and proton acquisition participants were less responsive during the sleep session and showed similar decreasing responsiveness with time.

Repeated measures ANOVA comparing button response of the first 25 minutes of sleep sodium scan with the awake scan showed a significant time session x time interaction ($F_{(1.934, 38.674)} = 17.885$, $p<0.001$). Note, Mauchley's test indicated violation of sphericity $\chi^2(9) = 39.4$, $p < 0.001$, therefore Greenhouse- Geisser (Epsilon= 0.483) correction was used.

There was a significant time x session interaction in button press responses between wake and sleep scans ($F_{(2.016, 34.271)} = 13.171$, $p<0.001$) during proton acquisitions as well. Again, Mauchley's test indicated violation of sphericity $\chi^2(5) = 14.0$, $p= 0.016$ and Greenhouse- Geisser (Epsilon= 0.672) correction was used.

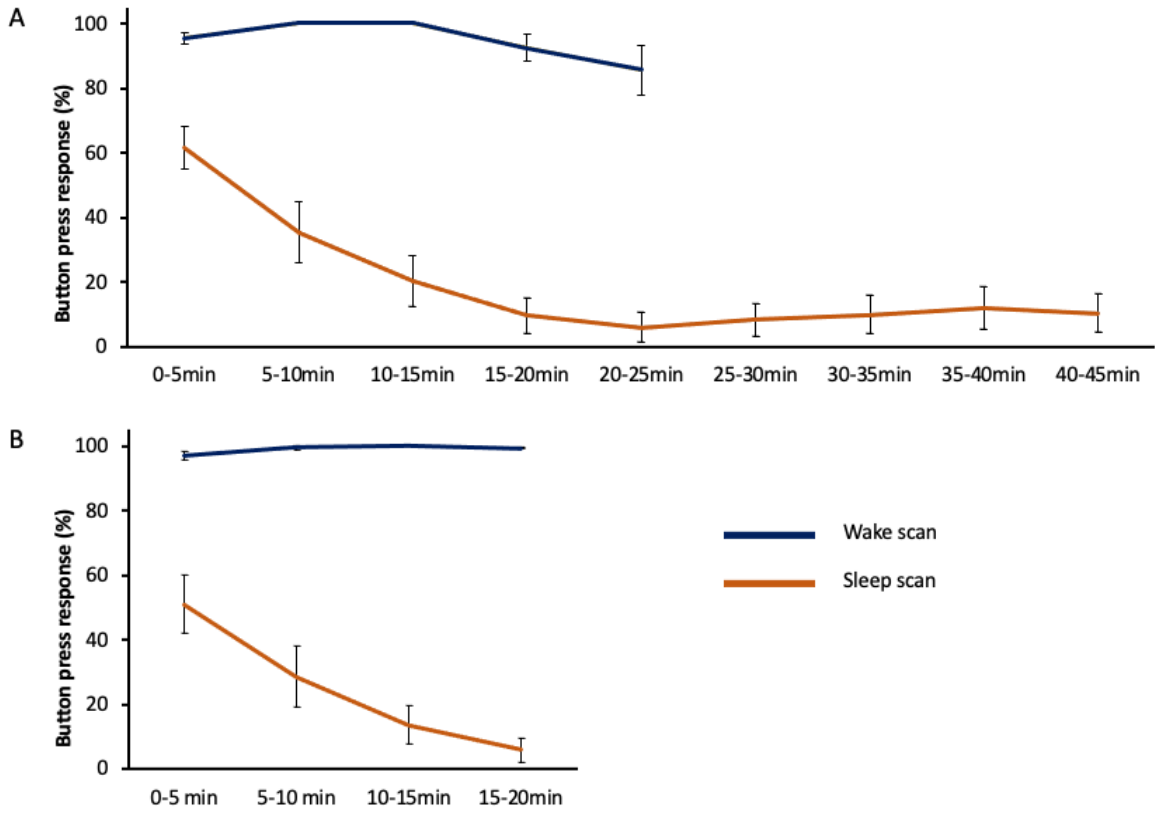

Figure 34: Button press response

A: Button press response during sodium image acquisition. Note, T_1 weighted images with the sodium coil are acquired in the first 5 minutes. **B**: Button press response during proton image acquisition. Images were acquired in the following order: High resolution anatomical image (0-10 min), Diffusion (10-17 min), ASL (17-20min). Error bars represent SEM.

During both sodium and proton scans participants continuously pressed the button for the entire duration of the awake scan, while in the sleep scan they become increasingly less responsive with time, confirming that most participant were asleep. The last 20 minutes of sodium scan was not statistically compared to wake, but Figure 34 clearly indicated that participants continued to be less responsive at later time intervals as well. It should also be remarked that sodium and proton sleep showed similar decrease in responsiveness indicating that participants were able to fall back asleep after being woken for changing the coils.

Heart rate

There was a decreasing trend in heart rate in both awake and sleep session during sodium acquisition, as depicted on Figure 35A. Repeated measures ANOVA comparing heart rate in the first 25 minutes of sleep with wake during sodium scan indicated a significant effect of time $F_{(2.166, 43.324)} = 29.632$, $p<0.001$. Mauchley's test indicated violation of sphericity $\chi^2(9) = 37.67$, $p < 0.001$ and Greenhouse- Geisser (Epsilon= 0.542) correction was used and $F_{(2.166, 43.324)} = 29.632$, $p<0.001$.

Figure 35B shows little difference in heart rate during proton acquisition between the two sessions. There was no significant effect of time or session.

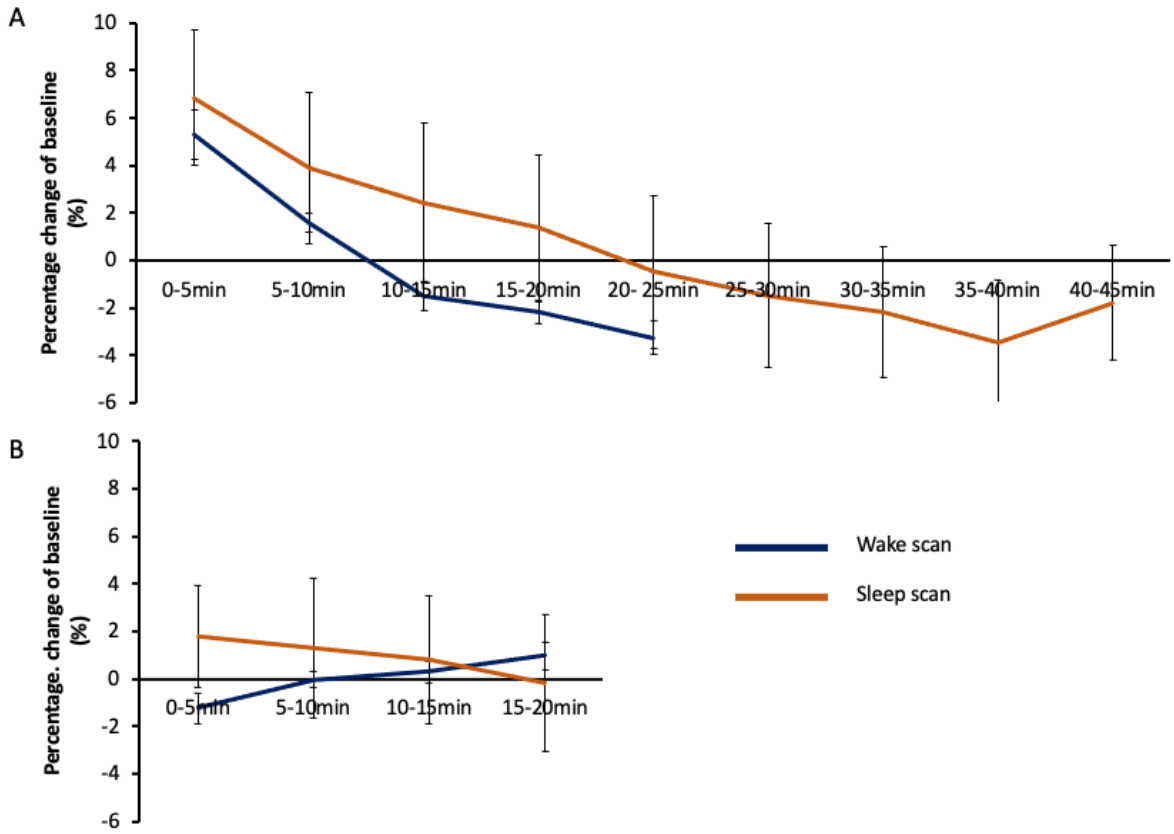

Figure 35: Heart rate change

A: Heart rate during sodium image acquisition. **B**: Heart rate during proton image acquisition. Error bars represent SEM.

There was a significant trend for a reduction in heart rate over time in both the sleep and wake sessions during sodium acquisition, as displayed on Figure 35. No effect of session was observed suggesting that the reduction of heart rate was not a simple effect of sleep. An alternative explanation is that participants' heart rate might be higher at the beginning of the scan because it is an unfamiliar environment and, as they get used to it, they start to feel more relaxed. The absence of a significant effect of time during the proton acquisitions supports this, as during proton acquisition participants had already had a chance to familiarize themselves with the environment.

Respiration rate

Figure 36A shows a decreasing trend in respiration rate in both the awake and the sleep session during sodium acquisition. Repeated measure ANOVA comparing the first 25 minutes of sleep

respiration rate with wake indicated a significant effect time ($F_{(2.563,\ 51.255)}$ = 5.485, p=0.004). Mauchley's test indicated violation of sphericity $\chi^2(9) = 35.62$, $p < 0.001$ and Greenhouse- Geisser (Epsilon= 0.641) correction was used.

Figure 36B shows a decreasing trend in respiration rate in both awake and sleep session during proton acquisition. Repeated measures ANOVA revealed a significant effect of time ($F_{(3, 45)} = 9.361$, p<0.001) and session ($F_{(1, 15)} = 6.101$, p=0.026).

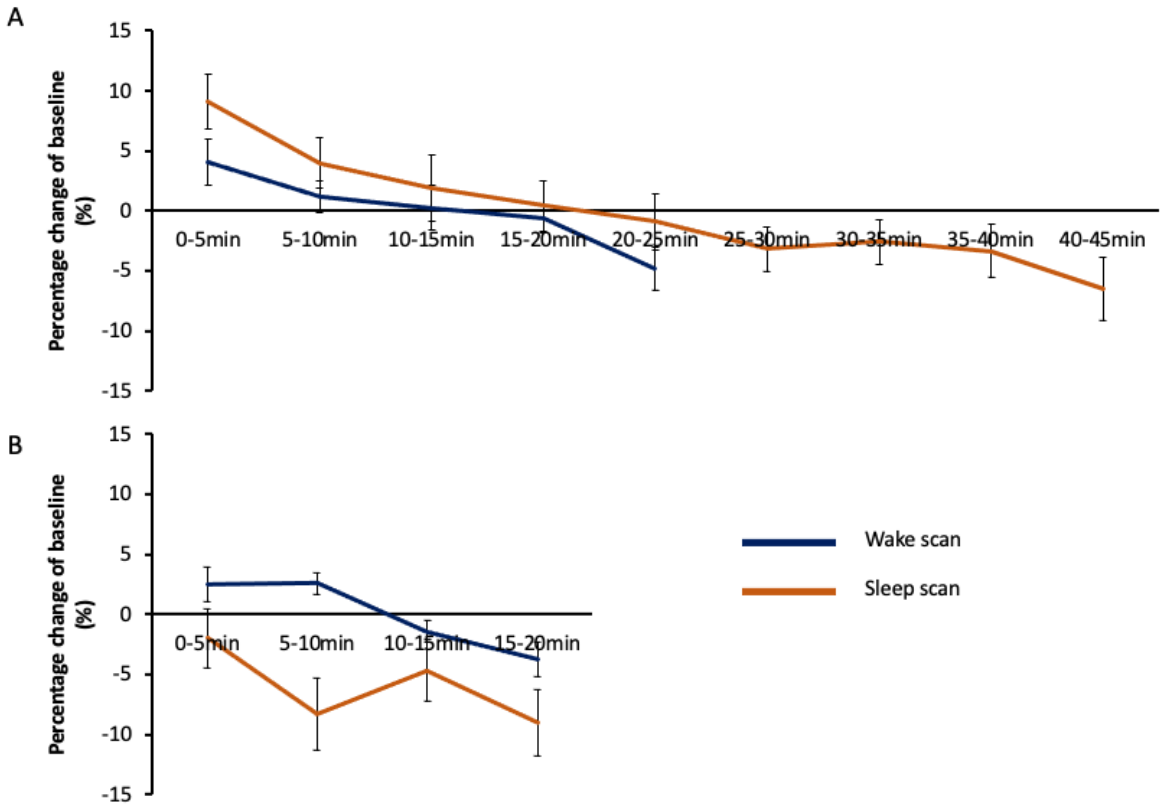

Figure 36: Respiration rate change

A: Respiration rate during sodium image acquisition. **B**: Respiration rate during proton image acquisition. Error bars represent SEM.

The significant decreasing trend in respiration rate during sodium scan (Figure 36A) in both wake and sleep sessions, suggests that it might be linked to relaxation. There was a significant effect of both time and session in the proton scan (Figure 36B), which suggests that the lower respiration rate during the proton acquisition might be an effect of sleep. Deep sleep is associated with

reduction in minute ventilation, which can reflect either reduction in tidal volume and/or reduction in respiration (Douglas et al., 1982; Krieger et al., 1990; Gutierrez et al., 2016).

HRV

Figure 37A shows that there was an increasing trend in high frequency (HF) power in both the awake and sleep conditions, however this increase seems to be more prominent in the sleep session. Repeated measure ANOVA comparing the first 25 minutes of sleep HF power with wake showed a significant effect of time $F_{(1.776,\ 35.510)} = 4.818$, p=0.017. Mauchley's test indicated violation of sphericity $\chi^2(9) = 43.1$, $p < 0.001$ and Greenhouse- Geisser (Epsilon= 0.444) correction was used. Figure 37A also shows that the increasing trend seems to continue at later time points. When the last 20minutes of sleep was compared with wake there was a significant effect of session $F_{(1,\ 20)} = 7.085$, p=0.015 that can be attributed to an increase in HF power in sleep.

Figure 37B shows an increasing trend in HF power in during sleep scan that is not present in the wake scan during proton acquisition. Repeated measures ANOVA indicated a significant time x session interaction in HF power during proton scan ($F_{(1.758,\ 29.891)} = 4.892$, p=0.018). Greenhouse-Geisser correction (Epsilon= 0.648) since Mauchley's test indicated violation of sphericity $\chi^2(5) = 16.801$, p= 0.005

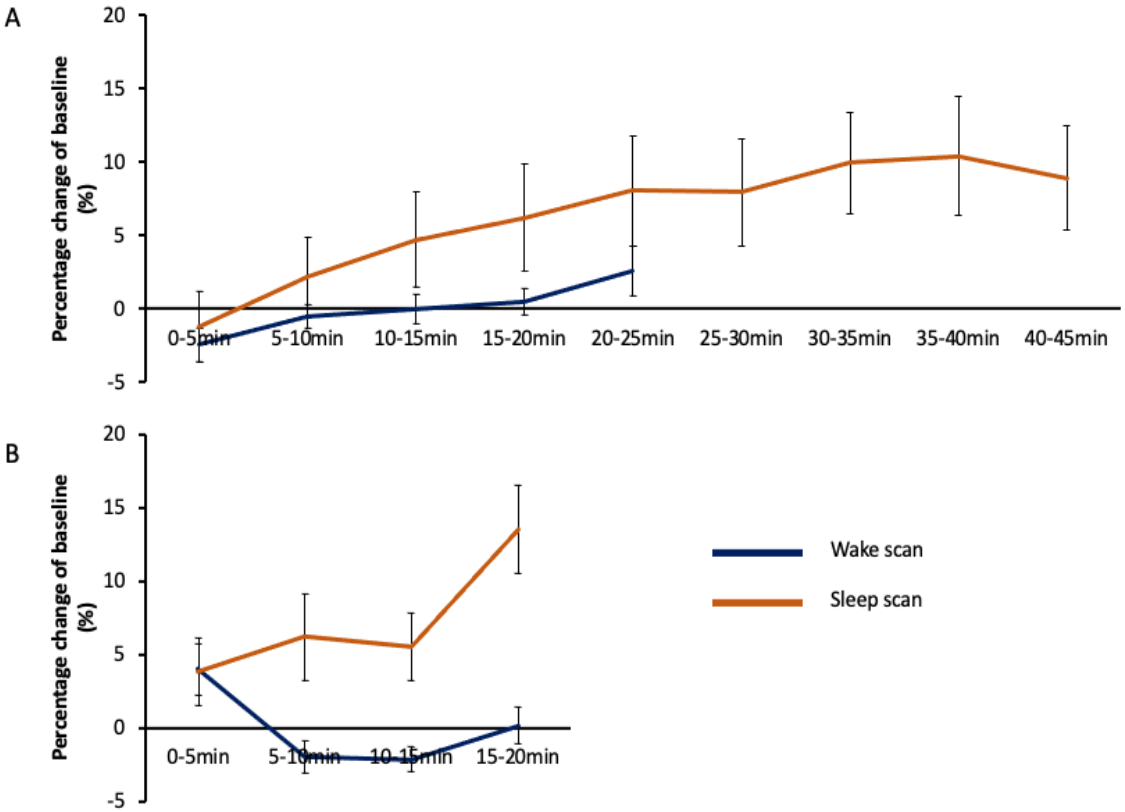

Figure 37: High frequency power change

A: High Frequency power of heart rate variability during sodium image acquisition. **B**: High Frequency power of heart rate variability during proton image acquisition. Error bars represent SEM.

Spectral analysis of heart rate variability revealed interesting significant changes in HF power between scanning sessions in both sodium and proton scans, as shown in Figure 37. HF power showed a significant increasing trend in both awake and sleep session, however the effect of session was not significant. As HF power showed a further increase after 25 minutes during sodium scan (Figure 37A), I decided to compare the last 20 minutes of sleep with the first 20 minutes of wake. While this may not be entirely rigorous from a statistical point of view, in the absence of data from the wake scan at later time points, I thought it could still provide some valuable information (but we should be cautious with the interpretation). There was a significant effect of session in the last

20 minutes of sleep that could be a result of sleep. Although, we cannot assume that HF power would not have increased in the wake session too if we had recorded for longer.

A significant time-by-session interaction was observed in HF power during the proton acquisition, which can be attributed to the increasing trend in HF power during sleep. A reduction in HF power has been associated with stress, while an increase is associated with psychological relaxation (Sakakibara, TakeuchI and Hayano, 1994). Moreover, a 20% increase in HF power has been reported during the wake to NREM sleep transition (Vanoli et al., 1995). Others have reported that HF power varies with the circadian clock and is not affected by sleep (Burgess et al., 1997). In our study all scans took place at the same time of the day, thus circadian variation should be negligible.

5.3.5 Subjective sleep questionnaires

Sleep during wake scan

3 participants reported that they fell asleep at some point during the wake sodium scan. They all reported very light sleep (on 1 to 10 scale, where 1 is very light sleep and 10 very deep sleep) with a mean value of 2 and SD of 1. The button response indicated that 2 of them were pressing throughout most of the scan (~70%), however stopped pressing for the last ~7 minutes. Furthermore, these participants reported that they kept waking up and falling asleep towards the end of the scan. The third participant who reported sleeping during data acquisition was pressing throughout the whole scan and reported that he/she fell asleep once and woke up shortly after.

The same 2 participants who reported sleeping during the wake sodium scan, also reported sleeping during the awake proton scan. The questionnaire indicated that the sleep was very light (1- 2 on the scale), falling asleep and waking up for a short period of time. In contrast to the subjective reports, the button press data did not indicate muscle relaxation at any point of the scan.

Despite some participants reporting some sleep during the wake scan, I decided to include them in the final analysis, for the following reasons: 1. The reported sleep was not confirmed by the button press response—the participants are likely to have experienced microsleep. 2. I did not want to throw away valuable data because only few participants reported sleep, I could not split the data into subgroups (e.g., wake, wake+ microsleep and sleep groups) 3. Our experimental intervention was sleep deprivation and Zolpidem (chosen to increase sleep pressure and likelihood of sleep in the scanner), which in theory should give good enough contrast between sessions even when the

awake scan is infiltrated with some episodes of microsleep (which would bias towards the null hypothesis).

In a future study, we should use eye-tracker that would detect microsleep episodes (defined as prolonged eye closure e.g., longer than 4s) with higher sensitivity and temporal accuracy than button press paradigm.

Sleep during sleep scan

In the sodium scan all participants but one reported that they fell asleep at some point during the sleep scan. In contrast with the sleep questionnaire, the participant who reported no sleep was not pressing for 20 minutes (~50%) in the middle of the scan.

All participants that were included in the final analysis reported sleeping during the proton scan. Note that two participants did not report any sleep during the proton scan, and in these cases, it was confirmed by the button press response. Consequently, we decided to remove these participants from the final analysis.

Self-reported sleep kind

Participants were asked what kind of sleep they experienced during the sleep scan. They could choose from 4 options, displayed on Figure 38. Figure 38A summarizes the distribution of different sleep types that participants reported during sodium scan and Figure 38B during proton scan.

Figure 38: Self-reported sleep kind

A: Self-reported sleep kind during sodium sleep session (N=21). **B**: Self-reported sleep kind during proton sleep session (N=18).

During the sodium scan most of participants (N=10 out of a total of 21) reported that once they fell asleep, they did not wake up until they were woken up; a similar number (N=8) reported that they keep falling asleep and waking up; 2 participants reported that they could not go back to sleep once they woke up during the scan, while only one participant reported that he/she could not sleep at all during the scan. Similarly, as during sodium scan, during proton scan most people reported that once they fell asleep, they did not wake up until we woke them up (11 out of 18).

Self-reported sleep start

Figure 39 summarizes participant responses to the question: When did you fell asleep? In both sodium (Figure 39A) and proton (Figure 39B) scans most of participants indicated that they felt like they fell asleep at the beginning of the scan.

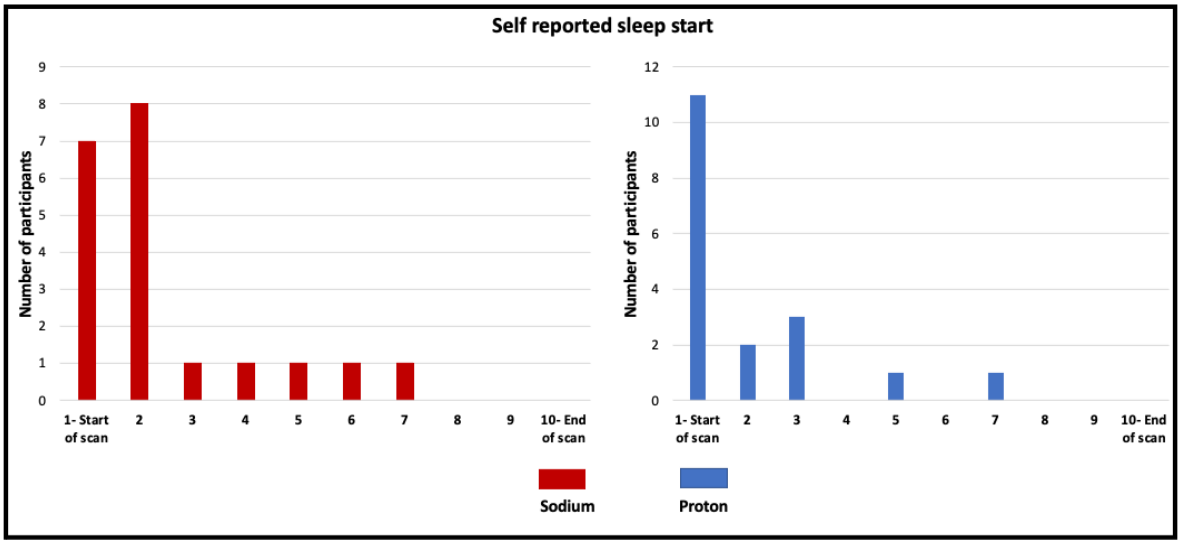

Figure 39: Self-reported sleep start

A: Self-reported sleep start during sodium sleep session (N=21). **B**: Self-reported sleep start during proton sleep session (N=18).

During sodium scan 16 participants (out of 20, one reported no sleep) indicated that they fell asleep at the beginning of the scan (defined as 1-3 on the scale), while during proton scan 16 out 18 indicated that they fell asleep at the beginning. Suggesting that most participants thought they managed to fall asleep at the beginning of both sleep scans.

Self-reported sleep length

Figure 40 summarizes how long participants felt like they were sleeping for on 1 (no sleep at all) to 10 (slept through the whole scan) during sodium (Figure 40A) and proton scans (Figure 40B).

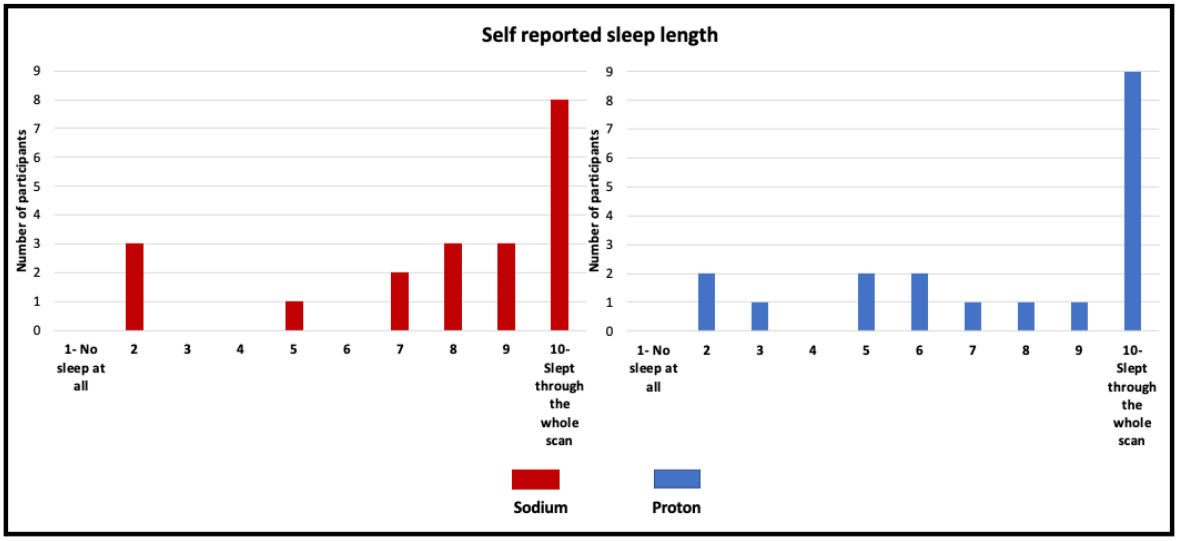

Figure 40: Self-reported sleep length

A: Self-reported sleep length during sodium sleep session (N=21). **B**: Self-reported sleep length during proton sleep session (N=18).

Most participants reported that they slept through most of the scan during both acquisitions. Although, 3 participants reported little sleep (less then 4 on the scale) in both sodium and proton scans.

Self-reported sleep depth

Figure 41 summarizes how deep participants thought they had slept on a 1 (very light sleep) to 10 (very deep sleep) scale during sodium (Figure 41A) and proton (Figure 41B) scans.

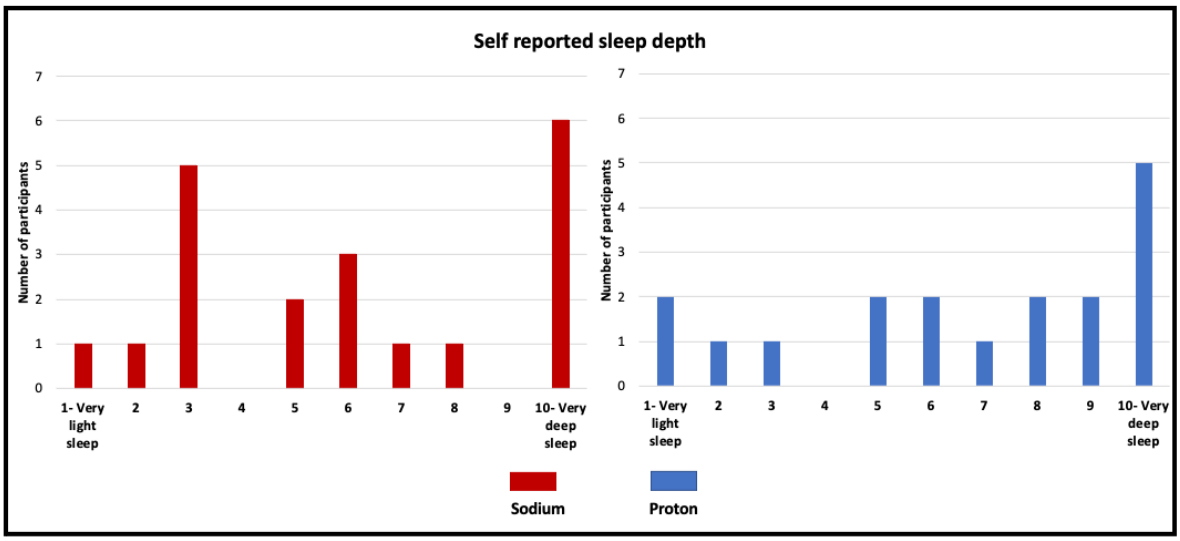

Figure 41: Self-reported sleep depth

A: Self-reported sleep depth during sodium sleep session (N=21). **B**: Self-reported sleep depth during proton sleep session (N=18).

There is more variability in the reported sleep depth compared to the other measures, where responses seem to be more skewed. Although, during both sodium and proton scans there were more participants that reported deep sleep (defined as above or equal to score 5) than light sleep. During sodium scan 13 (out of 21), while during proton scan 14 (out of 18) participants indicated deep sleep.

Dreaming

Out of the 20 participants who reported sleep during the sodium scan, 9 also reported that they dreamt during the scan. Out of the 18 participant who were included in the final analysis of proton scans, 7 reported that they dreamt during the scan.

Dreaming during the sleep scan may reflect that these participants entered REM as dreams are most commonly associated with REM sleep (Dement and Kleitman, 1957). However, there is substantial evidence that dreams can also occur during SWS, but with lower likelihood than in REM sleep (Foulkes, 1962; Tracy and Tracy, 1974; Cavallero et al., 1992). Alternatively, dreams during scans could reflect the effect of Zolpidem as dream-like hallucinations have been previously reported (Ansseau et al., 1992; Singh and Loona, 2013; Inagaki et al., 2010).

Zolpidem can also have a significant effect on memory retrieval, consequently the accuracy of self-reported sleep measures is likely to be affected. Thus, we should only treat these measures as rough approximations.

5.4 Conclusion

Decreased responsivity, increased HF power during sleep scans in addition to subjective sleep reports suggest that sleep deprivation and Zolpidem combination was sufficient to induce sleep in the scanner. Moreover, the significant effect of session in respiration rate change during the proton scan (which was not present during sodium scan) might suggest that participants achieved deeper sleep during the proton scan. It should be remarked that there was substantial variability in sleep quality the night before the wake scan, which may have affected the MRI measures. Validation of these measures by polysomnography is necessary to elucidate how these measures might reflect sleep state- discussed in Chapter9.2.2. Validation is particularly important, as there is great variability in reported physiological changes in sleep stages, which might reflect differences in study design and analysis.

Chapter 6 Cerebral blood flow changes during sleep

6.1 Introduction

Studies investigating cerebral blood flow during sleep have suggested that CBF increases with sleep pressure, which is reversed by the subsequent sleep (Elvsåshagen et al., 2019). Reduced CBF during SWS has been associated with reduced metabolic need during the long hyperpolarizing lapses ("off") periods in between bursts ("on" periods) of activity that is stereotypical of SWA. Brain areas that either actively participate in slow wave generation or are particularly active during wake, show more prominent reduction in CBF during SWS (Braun et al. 1997; Hofle et al. 1997; Maquet et al. 1997; Andersson et al. 1998; Kajimura et al. 1999, Tüshaus et al., 2017). Moreover, studies simultaneously monitoring EEG activity and CBF changes showed negative correlation between SWA and CBF, which were more pronounced in frontal brain areas, thalamus, brainstem although there some discrepancies between studies, which may be due to differences in study designs (Hofle et al., 1997; Tüshaus et al., 2017; Dang-Vu et al., 2005). For a more in-depth review of blood flow changes please see Chapter 1.5.3.

6.2 Aims

Increased glymphatic function during sleep has been linked to SWA and reduced arousal inducing neurotransmission. As we were unable to use EEG concurrently with our MRI modalities, we used CBF measurements as a positive control for achieving sleep in the scanner, because reductions in CBF during SWS have been widely reported.

6.3 Hypotheses

H1: There will be a reduction in total grey matter CBF during sleep compared to wakefulness.

H2: The spatial distribution of CBF reduction during sleep will be comparable to that reported during slow wave sleep by others (in studies in which SWS was confirmed by EEG).

H3: CBF will be reduced during sleep in areas involved in slow wave generation e.g. prefrontal cortex, thalamus, basal ganglia and brain regions that promote arousal e.g. brainstem nuclei, basal ganglia.

6.4 Methods

6.4.1 Imaging parameters

20 control/label images were acquired with pseudo-continuous ASL (pCASL) sequence with a 32-channel head coil. Furthermore, for quantification purposes a proton density, M_0, image was obtained using the same readout and TR as for the control/label images.

- TR= 5000ms
- TE= 14ms
- Labelling duration= 1800ms
- Post labelling delay= 2200ms
- Flip angle= 90°
- FOV= 220 x 220mm^2
- Matrix size= 64 x 64
- Number of slices= 20
- Slice thickness= 6mm

6.4.2 Image processing

SPM12 (www.fil.ion.ucl.ac.uk/spm/software/spm12) and customised Matlab scripts were used for image processing and statistics. Rigid-body motion correction was used to realign labelled and control images (20 pairs per session). Motion between images were estimated and removed from analysis if consecutive volumes moved by more than 2mm (in x, y or z direction). Perfusion weighted images were calculated for each control-labelled pair by subtracting the labelled image from the control. The median of the perfusion weighted images (awake and sleep) was co-registered to the same high resolution T1-weighted anatomical image. Anatomical images were segmented to obtain probabilistic maps of grey and white matter and a partial volume correction algorithm (Asllani, Borogovac and Brown, 2008) was then used to obtain grey and white matter maps of perfusion weighted images. The normalization parameters obtained from the segmentation were then used to warp these maps into MNI space.

6.4.3 Global CBF analysis

The normalized partial volume corrected GM and WM perfusion maps were converted to absolute CBF according to the consensus paper (Alsop et al., 2014), Equation 13.

Individual GM and WM tissue probability maps (TPMs) were obtained by segmentation of the T_1 weighted anatomical image (MPRAGE). Normalization parameters obtained from the segmentation were applied to the individual TPMs to wrap the images to MNI space. A group mean GM and WM TPM were calculated and were thresholded at TPM>0.7 to create GM and WM binary masks. A whole brain mask was created by combining the two binary masks. Binary masks were individually applied to the normalized CBF images and mean GM and whole brain values were obtained. Paired t-test in Matlab was used compare global averages between wake and sleep sessions, $p<0.05$ was considered as significant.

6.4.4 Whole brain voxel-wise perfusion analysis

The normalized (MNI) GM perfusion weighted images were compared between session (wake vs sleep) using a voxel wise paired-sample t-test (SPM12). The statistical significance was determined using cluster size inference with an initial cluster forming threshold of $p< 0.001$, where clusters with False Discovery Rate (FDR)- corrected $p<0.05$ were considered significant (Benjamini and Hochberg, 1995).

6.4.5 Brainstem ROI analysis

Paired t-test analysis was carried out to compare mean perfusion signal in Harvard Ascending Arousal Network (AAN) Atlas ROIs (Edlow et al., 2012). The AAN atlas includes the following nuclei: Dorsal Raphé, Locus Coeruleus, Median Raphé, Medial Reticular Formation, Periaqueductal grey, Parabrachial complex, Pontis Oralis, Pendunculopontine nucleus and Ventral Tegmental Area. Significance was determined at alpha= 0.05 after FDR correction. Note: that here not the PVE corrected images were used, because the segmentation of anatomical images does not perform well on the brainstem nuclei and is often wrongfully classifies them as white matter.

6.4.6 Thalamus nuclei ROI exploratory analysis

After reviewing voxel-wise analysis, symmetry around the midline of the thalamus was apparent. To investigate the symmetry and the distribution, the significant thalamus cluster was overlaid over a MNI atlas of human thalamic nuclei (Najdenovska et al., 2018).

6.5 Results

6.5.1 Exclusions

Two participants were excluded from the final analysis because they did not fall asleep. One participant was excluded due to excessive head motion.

6.5.2 Visual inspection of regional CBF

Figure 42 depicts mean regional CBF values during the awake and sleep conditions: simple visual inspection suggests a clear reduction in CBF during sleep session. The decrease in CBF during sleep seems to be global phenomenon, it is lower across the whole cortex. Nevertheless, some areas such as the anterior and posterior cingulate, orbitofrontal cortex, precuneus, insula, caudate nucleus, hippocampus and thalamus seem to be particularly less active during the sleep scan. The change in absolute CBF across the whole brain between the two conditions is illustrated on Figure 43.

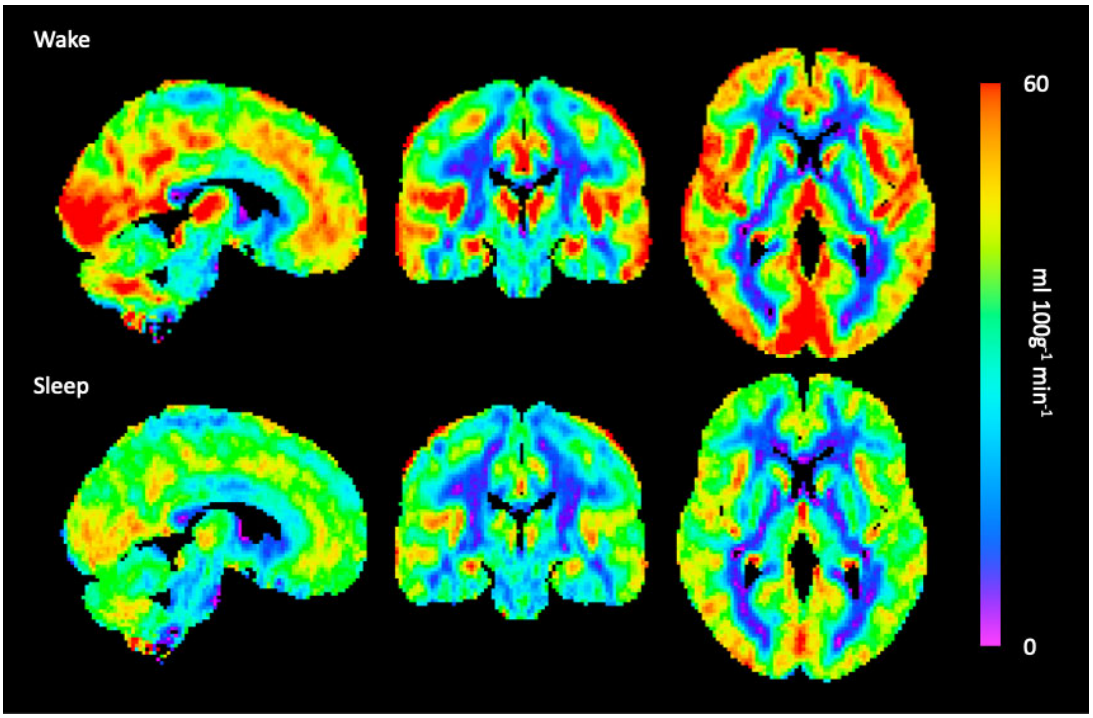

Figure 42: Mean Cerebral Blood Flow during wake and sleep

Illustration of mean cerebral blood flow (N=18) during wake and sleep scans. The regional CBF value changes from cold (low blood flow) to warm (high blood flow) colours. Slices were positioned at MNI: x= 6 y= -22 z= 4.

6.5.3 Global CBF changes

Figure 43 shows mean CBF values in grey matter and whole brain. In grey matter the mean CBF value was 46.7 ± 5.7 ml $100g^{-1}$ min^{-1} during wake session, while this was significantly reduced during the sleep scan to 39.8 ± 6.0 ml $100g^{-1}$ min^{-1} (paired t-test, t= 5.714, df= 17, p<0.0001). This a 17.3% reduction in grey matter CBF between the two sessions. Whole brain mean CBF was 35.3 ± 4.6 ml $100g^{-1}$ min^{-1} during the awake session, which was significantly reduced to 30.2 ± 4.8 ml $100g^{-1}$ min^{-1} during sleep session (paired t-test, t= 5.322, df= 17, p<0.0001).

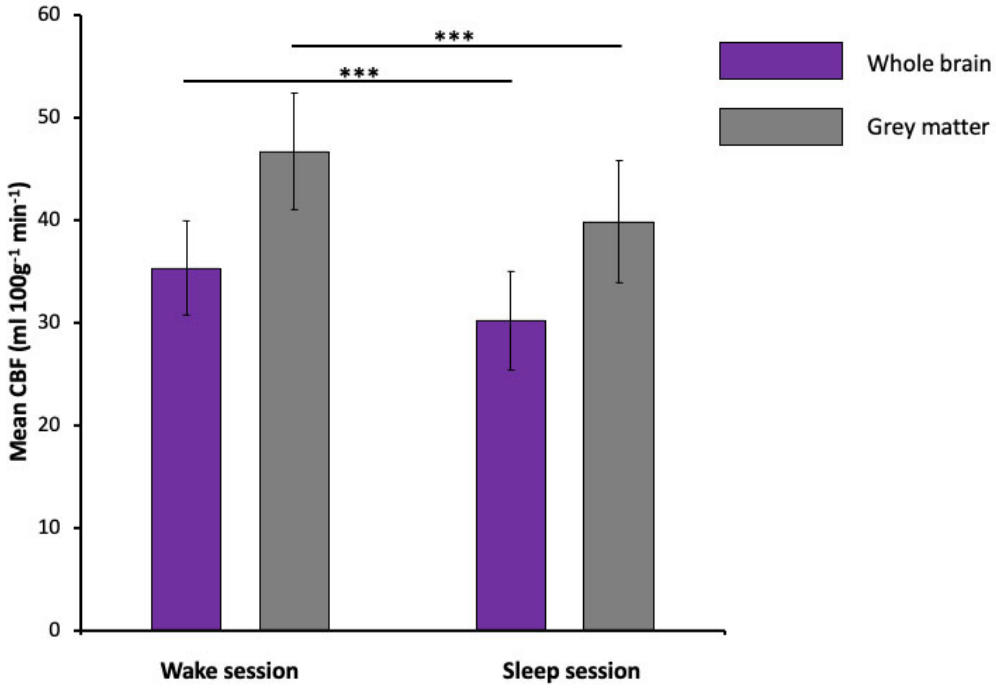

Figure 43: Bar graph of mean global CBF values during wake and sleep

Bar graph illustrating mean CBF values between the wake and sleep scan in grey matter (grey) and whole brain (purple). Bars represent absolute CBF values (mean ± SD in units of ml $100g^{-1}$ min^{-1}). *** paired t-test p<0.001.

6.5.4 Whole brain voxel-wise perfusion analysis

Voxel-wise comparison between the two conditions revealed areas that show significantly reduced perfusion during sleep that are illustrated on Figure 44. The location of the clusters is in good agreement with the visual observations from Figure 42, with the addition of temporal and parietal

cortices and the exception of hippocampus where change in perfusion was not statistically significant at the voxel level. The location, statistics and percentage change in blood flow between the two conditions of the significant clusters are summarized in Table 3.

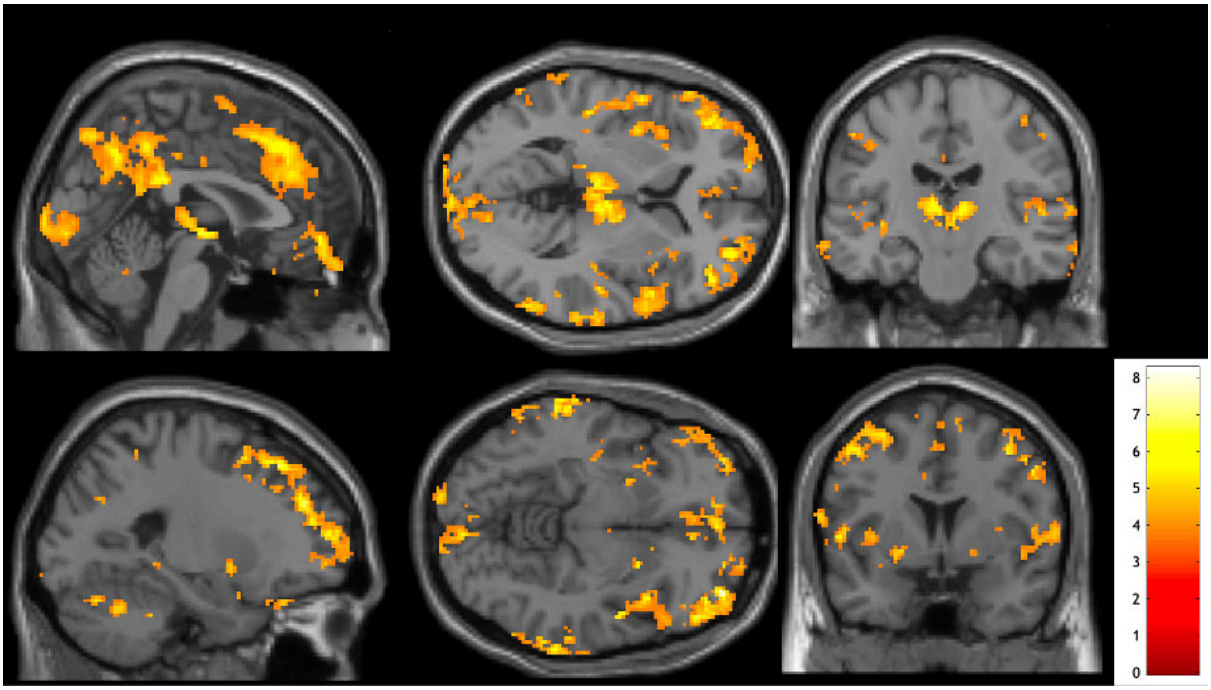

Figure 44: Whole brain voxel-wise comparison of perfusion between wake and sleep

Brain regions with significantly reduced CBF during sleep (compared to the wake condition). Top row MNI coordinates: x= 2 y= -18 z= 4; bottom row: x= -23 y= 4 z= -8. The statistical significance was determined using cluster size inference with an initial cluster forming threshold of $p < 0.001$, where clusters with a corrected FDR of $p < 0.05$ were considered significant.

Brain regions	MNI [x y z]	Cluster	L/R	T value	p (FDR-corr) cluster	Perfusion % change
SupraMarginal_R (aal3v1)	[62 -38 40]	911	R	8.27	0.000	-22.0
SupraMarginal_R (aal3v1)	[56 -44 40]		R	6.45		
Parietal_Inf_R (aal3v1)	[46 -44 40]		R	6.02		

Frontal_Mid_2_R (aal3v1)	[38 54 -8]	5324	R	8.08	0.000	-20.4
OFClat_R (aal3v1)	[44 38 -20]		R	8.06		
Frontal_Mid_2_R (aal3v1)	[38 46 22]		R	7.59		
OFCpost_L (aal3v1)	[-30 26 -24]	4355	L	7.7033	0.000	-22.1
Frontal_Mid_2_L (aal3v1)	[-28 54 16]		L	7.5121		
Frontal_Mid_2_L (aal3v1)	[-26 42 30]		L	7.0227		
Rectus_R (aal3v1)	[6 54 -16]	1858	R	7.0913	0.000	-19.3
Supp_Motor_Area_R (aal3v1)	[4 22 48]		R	6.9128		
ACC_sup_R (aal3v1)	[4 34 28]		R	6.2677		
Temporal_Mid_L (aal3v1)	[-70 -32 -12]	314	L	6.9869	0.000	-27.1
Temporal_Mid_L (aal3v1)	[-66 -38 -4]		L	6.2956		
Temporal_Mid_L (aal3v1)	[-64 -46 0]		L	5.6329		
Parietal_Inf_L (aal3v1)	[-54 -54 42]	1530	L	6.8301	0.000	-25.3
SupraMarginal_L (aal3v1)	[-60 -40 30]		L	6.4729		
Prarietal Inferior (outside)	[-60 -50 46]		L	6.2262		
Calcarine_L (aal3v1)	[4 -88 -4]	841	L	6.7013	0.000	-24.9
Cuneus R	[10 -102 -4]		R	5.7573		
Calcarine_R	[10 -92 10]		R	5.4054		
Thal_MDm_L (aal3v1)	[-6 -20 8]	645	L	6.6657	0.000	-24.9
Thal_PuA_R (aal3v1)	[10 -20 10]		R	6.5641		
Midbrain	[2 -14 -4]			6.5607		
Insula_L (aal3v1)	[-36 14 -14]	269	L	6.5287	0.000	-21.0
Insula L	[-30 18 0]		L	5.4247		

Insula L	[-32 6 -12]		L	5.163		
Temporal_Mid_R (aal3v1)	[72 -32 -12]	691	R	6.2773	0.000	-23.5
Temporal_Mid_R (aal3v1)	[70 -40 -8]		R	5.6506		
Temporal_Mid_R (aal3v1)	[72 -24 -14]		R	5.6492		
Cingulate_Mid_R (aal3v1)	[6 -22 40]	1999	R	6.2415	0.000	-23.2
Precuneus_R (aal3v1)	[4 -76 52]		R	6.2202		
Precuneus_R (aal3v1)	[2 -62 40]		R	6.0886		
Temporal_Sup_R (aal3v1)	[50 -22 6]	118	R	6.1865	0.000	-22.6
Heschl_R (aal3v1)	[46 -16 10]		R	4.5545		
Insula R	[40 -22 4]		R	4.5234		
Rolandic_Oper_L (aal3v1)	[-52 2 8]	452	L	5.6759	0.000	-23.5
Postcentral_L (aal3v1)	[-62 0 14]		L	5.5879		
Temporal_Sup_L (aal3v1)	[-46 -26 4]		L	5.5306		
Cerebellum_6_L (aal3v1)	[-22 -56 -30]	96	L	5.6435	0.000	-22.4
Cerebellum_6_L (aal3v1)	[-32 -48 -26]		L	5.0921		
Cerebellum_6_L (aal3v1)	[-30 -56 -28]		L	4.1973		
Supp_Motor_Area_R (aal3v1)	[10 -10 74]	98	R	5.3626	0.000	-22.9
Supp_Motor_Area_R (aal3v1)	[4 -2 68]		R	5.2951		
Supp_Motor_Area_R (aal3v1)	[16 0 66]		R	4.4676		
Precentral_R (aal3v1)	[42 -12 54]	62	R	5.0038	0.003	-15.5
Precentral_R (aal3v1)	[40 -22 56]		R	4.6351		
Temporal_Inf_R (aal3v1)	[34 -28 62]		R	4.2466		
Cerebellum_Crus1_R (aal3v1)	[14 -82 -22	283	R	4.9306	0.000	-21.5

Cerebellum_6_R (aal3v1)	[36 -72 -24]		R	4.7241		
Cerebellum_6_R (aal3v1)	[28 -72 -26]		R	4.5069		
Pallidum_L (aal3v1)	[-22 2 -4]	34	L	5.74	0.039	-22.7
Precuneus_R (aal3v1)	[8 -52 62]	42	R	5.6625	0.02	-21.3
Parietal_Sup_R (aal3v1)	[16 -52 56]		R	3.7288		
Cerebellum_6_L (aal3v1)	[-22 -70 -24]	40	L	5.419	0.024	-22.6
Temporal_Inf_L (aal3v1)	[-56 -8 -34]	36	L	5.2298	0.034	-21.9
Cingulate_Mid_L (aal3v1)	[0 -14 38]	35	L	4.9283	0.036	-26.2
Temporal_Inf_R (aal3v1)	[64 -12 -30]	39	R	4.4214	0.025	-19.8
Temporal_Mid_R (aal3v1)	[64 -10 -22]		R	4.185		

Table 3: Clusters showing significant reduction in perfusion during sleep

Brain regions showing significant clusters with reduced perfusion during sleep (compared to the wake condition). Perfusion percentage change was determined for each participant before averaging in the following way: ((mean cluster sleep perfusion- mean cluster wake perfusion)/mean cluster wake perfusion) *100. The statistical significance was determined using cluster size inference with an initial cluster forming threshold of $p< 0.001$, where clusters with FDR- corrected $p<0.05$ were considered significant. Anatomical information was derived using the xjView toolbox (http://www.alivelearn.net/xjview; based on the WFU_PickAtlas, http://fmri.wfubmc.edu/software/PickAtlas). In the table “aal3v1” denotes Automated Anatomical Labelling.

Note that some of these clusters are rather large and include several different brain regions, which is not well represented by just 3 local maxima in Table 3: Clusters showing significant reduction in perfusion during sleep. For example, cluster with sizes 5324 and 4355 include orbitofrontal, frontal gyrus as well as precentral gyrus and parts of the temporal gyrus-- this becomes more obvious on the 3D render image on Figure 45.

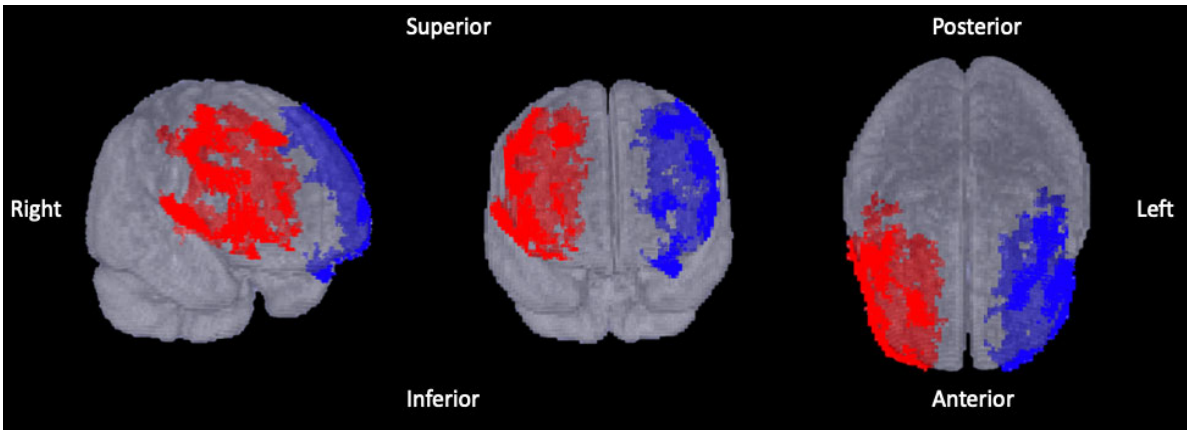

Figure 45: 3D render of the two largest significant clusters

These clusters cover a large area, spanning from the prefrontal cortex to the parietal lobe.

Perfusion percentage change across significant clusters ranges from -15.5% to -27.1%, with a mean of -22.5 ± 2.4% (inter cluster standard deviation). Significant clusters include thalamus, basal ganglia (putamen and *caudate*), prefrontal cortex, parietal cortex, anterior cingulate, posterior cingulate/precuneus, insula, temporal lobe and cerebellum. When looking at all significant clusters as whole the mean perfusion percentage change was -22.3% ± 13.1% (inter subject standard deviation).

6.5.5 Brainstem ROI analysis

Figure 46 illustrates the distribution of perfusion percentage change values between the two sessions. Significant reduction in CBF was observed in Locus Coeruleus, Median Raphe, Medial Reticular Formation and in Pontis Oralis nucleus. The distributions of mean percentage change of significant brainstem nuclei are all positively skewed, consequently the mean is not a correct representation of the change. Median percentage change in Locus Coeruleus was -23.7%; in Median Raphe was -22.2%; in Medial Reticular Formation was -14.2% and in Pontis Oralis was -21.2%.

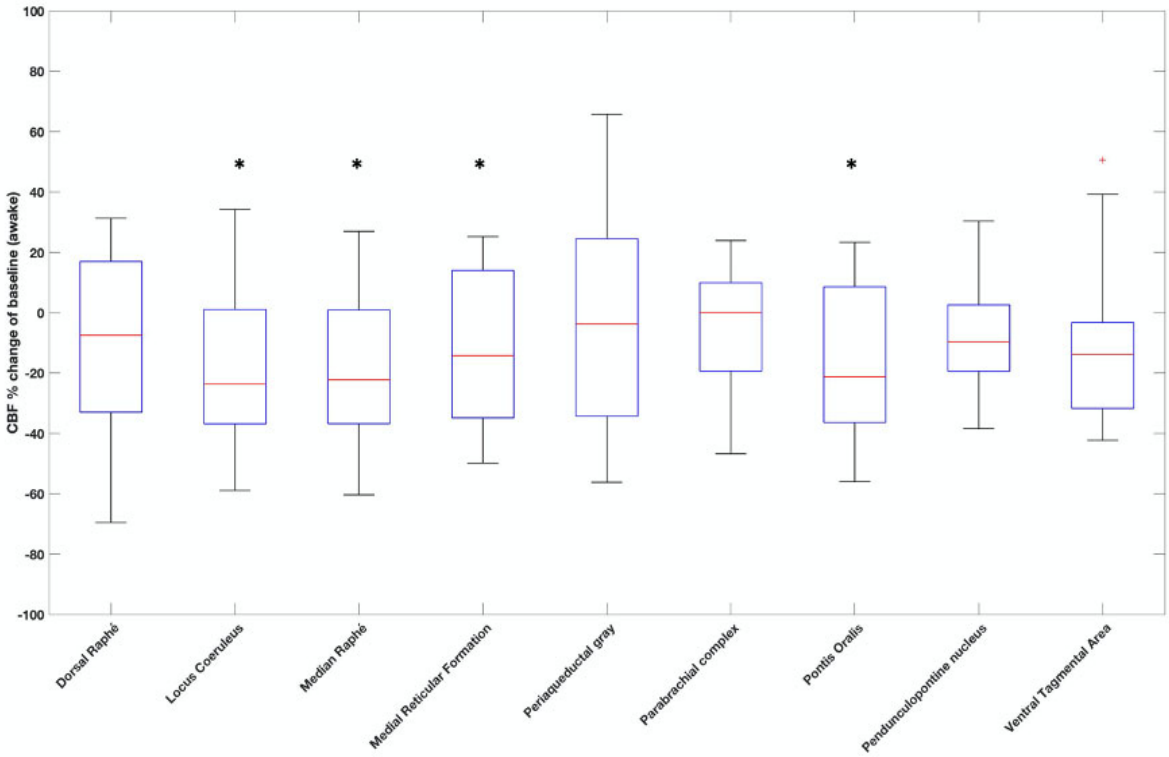

Figure 46: Boxplot of perfusion change in Ascending Arousal Network ROIs

Perfusion percentage change during sleep; red line represents the median % change; blue box indicates the 25th and 75th percentiles; whiskers show 5th and 95th percentiles; red plus signs show the outliers; stars represent the significant ROIs after correction for multiple comparison with FDR.

6.5.6 Thalamus nuclei ROI exploratory analysis

On the top right coronal slice on Figure 44 we can see that the thalamic cluster is passing through the midline of the thalamus. To investigate the distribution of significant voxels passing through the thalamus, the thalamic cluster was overlaid on a MNI thalamic atlas (Najdenovska et al., 2018). Figure 47 illustrates the distribution of the significant cluster passing through the thalamus and shows left-right symmetry around the midline. Over 50% of the Medio-Dorsal nuclei show reduced CBF during sleep (Left- 54%; Right- 56%).

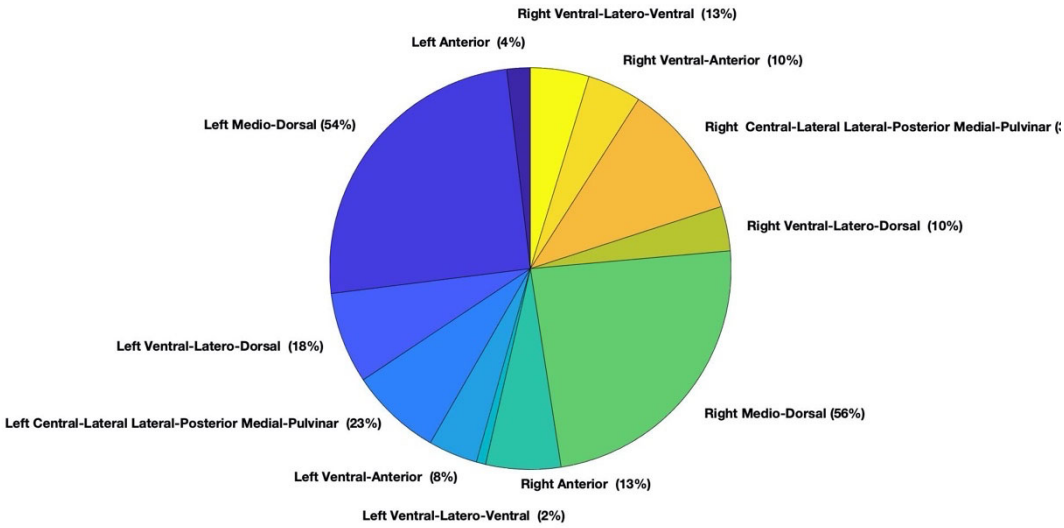

Figure 47: Pie chart representing the distribution of significant voxels in thalamic nuclei

The percentage in the brackets shows how much of the nucleus is occupied by the significant cluster.

6.6 Discussion

6.6.1 Key results

ASL results indicated a brain wide reduction in perfusion. Brain regions showing significant reduction in perfusion during sleep in our study are in good agreement with the literature showing reductions in CBF during slow wave sleep. Moreover, the regional CBF values reported in our study are comparable with previously reported values during SWS (Hofle et al., 1997). This further suggests that participants were able to achieve slow wave sleep in the scanner.

6.6.2 Global CBF

Simple visual inspection of the mean wake and sleep CBF images (Figure 42) revealed a global decrease in CBF with some regional variations. This was confirmed statistically, where global CBF measures were significantly lower during sleep scan than wake in both whole brain and in grey matter. In agreement with the sleep measures (Chapter 5), decrease in CBF during the sleep session suggests that our experimental protocol was sufficient to induce sleep.

6.6.3 Voxel-wise analysis

Voxel-wise analysis shed light on regional variation in perfusion, significant decrease was observed in anterior and posterior cingulate, orbitofrontal/prefrontal cortex, precuneus, insula, caudate nucleus, temporal, parietal cortices, and thalamus. These areas are in good agreement with the areas that have previously been shown to have significantly reduced CBF during SWS (Braun et al. 1997; Hofle et al. 1997; Maquet et al. 1997; Andersson et al. 1998; Kajimura et al. 1999; Tushaus et al., 2017). Some of these areas, such as the orbitofrontal cortex (Sterman and Clemente 1962; Massimini et al., 2004), thalamus (Steriade and Amzica 1998), basal ganglia (Lazarus et al., 2013) have previously been associated with slow wave generation. While other areas e.g. the medial prefrontal cortex, posterior cingulate cortex, precuneus, angular gyrus which form parts of the default mode are associated with high waking metabolic activity at rest (Raichle et al., 2001). Interestingly, these areas might in fact lead to increased slow wave activity during sleep (based on the local sleep hypothesis). We did not find any significant increase in CBF with sleep, whereas Tushaus et al. (ASL study) and Braun et al. both found increase in occipital areas, but here I need to emphasize that our experimental protocol was not identical and differences between studies are expected (Braun et al. 1997; Tushaus et al., 2017).

6.6.4 Brainstem ROI analysis

ROI analysis of brainstem nuclei revealed significant CBF reduction in the Locus Coeruleus, Median Raphe, Medial Reticular Formation and in Pontis Oralis nucleus. Brainstem nuclei form extensive connections with thalamus and are believed in wake-sleep state switching (Saper et al., 2010).

The Locus Coeruleus is the primary source of noradrenaline, a key neurotransmitter for attention and arousal. Furthermore, noradrenaline has been shown to be a key regulator of the glymphatic system (regulates extracellular space volume and CSF production) (Aston-Jones and Waterhouse, 2016; Xie et al., 2013; Berridge and Waterhouse, 2003; O'Donnell et al., 2012; Benveniste et al., 2017; Nilsson, Lindvall-Axelsson and Owman, 1992). The Median Raphe contains serotoninergic neurons. Inhibition of these neurons is associated with anxiolysis (reduced levels of stress and sedation) in rats (Andrade, Zangrossi and Graeff, 2013). Reticular formation (including medial reticular formation and pontis oralis nuclei) plays a modulatory role in many functions including cardiovascular, motor control, pain, learning (Saladin, 2018). Furthermore, via connections with the

thalamus it modulates conscious attention and sleep (Saladin, 2018). However, need to be cautious with the interpretation of these findings, as these nuclei are rather small (only a few ASL voxels in native space) and the ASL sequence was not optimized for measuring brainstem perfusion.

6.6.5 Thalamus nuclei ROIs

Thalamus is involved in slow wave generation, and the midline nuclei seem to be particularly important is sleep-wake control (Baker et al., 2014; Gent et al., 2018). The thalamic cluster we identified (coronal slice, top right on Figure 44) passes through the medial/midline of the thalamus. Figure 47 highlights that the thalamic cluster shows high left-right symmetry, and the cluster is centred around the dorsomedial nuclei which is adjacent of the midline intralaminar nuclei (not actually part of the Thalamic Atlas used here). Here, I wanted to highlight that the significant cluster is likely to include the central medial thalamus nucleus, although from the present data we cannot draw any definite conclusion on its role in human sleep.

6.6.6 Comparison of our data with the literature

We observed a 17.3% reduction in grey matter CBF during sleep compared to wake, which is considerably lower than that reported by Braun et al. (26% reduction in CBF) when they compared pre-sleep wake (wake after sleep deprivation) and SWS (Braun et al. 1997).

Braun et al. compared SWS with post sleep wakefulness (wake after recovery sleep) and found a 11.4% decrease between the two conditions. As we have compared wake after a night sleep with sleep after sleep deprivation (+ Zolpidem) the sleep pressure difference was likely lower than between measuring CBF during wake (after sleep deprivation) and sleep after sleep deprivation—consequently this could explain why Braun et al. reported a higher change between pre-sleep wake and SWS. On the other hand, when compared with post-sleep wake immediately after waking (low sleep pressure) with SWS the sleep pressure contrast is lower than in our study where we scanned "post sleep" a few hours after the participants woke up. This could explain why our global change in CBF (17.3%) is somewhere in between pre sleep wake vs SWS (26%) and post sleep wake vs SWS (11.4%) reported by Braun et al.

However, there are additional factors that might have led to differences between the two studies: 1. Sleep deprivation in our study was considerably shorter (24h) vs 24-54h of total sleep deprivation; 2. In our sleep session participants took a sleep drug (Zolpidem) that might have affected sleep state and hence CBF (effect of Zolpidem is discussed in Chapter 9.1.4); 3. We also used a different

technique to quantify CBF- we used ASL to measure CBF, while Braun et al. used water PET; although it has been suggested that ASL can reliably quantify absolute CBF (Ye et al., 2000).

Braun et al. showed that absolute CBF during pre-sleep wake was ~54 ml $100g^{-1}$ min^{-1} that is considerably higher than during post sleep wake ~45 ml $100g^{-1}$ min^{-1}. We have estimated wake CBF at 46.7 ml $100g^{-1}$ min^{-1}, which is very close to their post sleep wake value. Furthermore, they estimated SWS CBF at ~40 ml $100g^{-1}$ min^{-1}, which is virtually the same (39.8 ml $100g^{-1}$ min-1) as the CBF recorded during sleep in our study. The absolute values for grey matter CBF during wake and sleep compared to Braun et al.'s findings suggests that our participants managed to achieve SWS during the sleep scan.

Another study used ASL to quantify global as well as local changes between different brain states (Tushaus et al., 2017). Their reported grey matter pre sleep CBF value was ~43 ml $100g^{-1}$ min^{-1} and ~38 ml $100g^{-1}$ min^{-1} post sleep, which are both lower than in our study (46.7 ml $100g^{-1}$ min^{-1}). They reported a decrease in CBF with sleep initiation and progression (stage 1 and 2), with deep sleep associated with an increase in CBF with respect to light sleep. This finding of an increase in global CBF during SWS does not fit in well with the previous PET literature, where SWS is typically associated with global as well as local reductions (Braun et al. 1997; Maquet et al. 1997; Andersson et al., 1998; Kajimura et al., 1999). However, there are some discrepancies in study design between the studies that might have affected the results. For example, the amount of sleep deprivation was different, e.g., Tushaus et al. used partial sleep deprivation with a maximum 4h sleep, while Braun et al. used 24-54h and we used 24h sleep deprivation + Zolpidem. Furthermore, post sleep wake CBF values would be affected by how long after waking they measured it.

6.7 Conclusion

Absolute as well as regional CBF changes suggest that our participants managed to achieve slow wave sleep in the scanner. However, we need to keep in mind that in Tushaus et al.'s study only light sleep stages were associated with significant CBF reduction compared to pre-sleep wake and not-post sleep wake—which might be a result of using a different sleep protocol.

Chapter 7 Measuring change in interstitial volume fraction with ^{23}Na MRI

7.1 Introduction

In Chapter 1.8 I described the relationship between glymphatic clearance and SWS. One of the principal factors contributing to the increased glymphatic clearance during sleep is an expansion of the interstitial space. In rodent studies, a 30-60% increase in interstitial volume fraction has been reported during SWS, which in turn reduced the resistance to fluid exchange and passage of ISF through the tissue (Xie et al., 2013; Ding et al, 2016). These authors reported that these changes can be at least partly attributed to a reduction in noradrenergic tone (Xie et al., 2013, O'Donnell et al., 2012) during sleep, when the ascending arousal network activity is reduced (AAN). Reduced Locus Coeruleus activity during sleep might therefore be particularly important in inducing changes in interstitial volume, as it is the primary source of noradrenaline in the CNS (Aston-Jones and Waterhouse, 2016; O'Donnell et al., 2012). In Chapter 1.8.1, I presented preclinical studies suggesting a link between neurotransmission, extracellular ion composition, CBF, glymphatic system (as it is tightly linked to interstitial volume) and SWS with astrocytes being an integral part of this link.

Furthermore, I discussed a human MRI study that showed that neural activity related to CBF/CBV anticorrelated with CSF signal measured in the fourth ventricle during sleep (Fultz et al., 2019). This study argued that reduced CBV during SWS allows the influx of CSF into the Virchow-Robin space with less resistance. This study gave indirect evidence of increased external, i.e., fluid movement in perivascular spaces during SWS.

A previous study attempting to measure the changes in interstitial volume associated with internal glymphatic clearance, i.e., fluid flow in the interstitial space, utilized diffusion weighted MRI (Demiral et al., 2019). While some diffusion models might be sensitive to interstitial changes, they cannot fully distinguish between signal originating from intra/ extracellular compartments. Sodium MRI provides a promising way of directly measure changes in the relative size of intra and extracellular compartments with the need for only a few assumptions: e.g., that the measured signal within a voxel is coming from two fluid compartments with constant sodium concentration. These assumptions are credible, as the sodium signal from solid compartment can be considered negligible compared to the fluid compartments and intra/extracellular sodium ion concentrations

are tightly regulated (this assumption might not be applicable for non-healthy participants). Due to the high concentration gradient between intra- and extracellular sodium concentrations, even a small increase in extracellular fluid volume fraction would be associated with a relatively large increase in sodium signal.

7.2 Aims

The aim of this experiment was to investigate the sensitivity of sodium MRI in measuring glymphatic system related volumetric changes in the interstitial fluid compartment during sleep.

7.3 Hypotheses

H1: There will be a global increase in grey matter and whole brain sodium signal during sleep compared to wake

H2: Sodium signal will increase with time asleep during the sleep session, but will not significantly change with time during the wake scan

H3: The sodium increase will be more pronounced in areas that participate in slow wave generation

7.4 Methods

7.4.1 Image processing

The image processing steps for the sodium data are described in detail in Chapter 4.5. To briefly summarise, sodium images were realigned before a mean image was calculated. The mean image served as a reference image for registering the individual images to the high-resolution anatomical image and the signal was normalized to the mean eyes signal. Normalization (spatial) parameters obtained from the segmentation of the anatomical image were applied to the individual sodium images.

7.4.2 Global sodium change

Individual GM and WM tissue probability maps were obtained by segmentation of the T_1 weighted anatomical image (MPRAGE). Normalization parameters obtained from the segmentation were applied to the individual TPMs to wrap the images to MNI space. A group mean GM and WM TPM

were calculated and thresholded at TPM>0.7 to create GM and WM binary masks. A whole brain mask was created by combining the two binary masks. Binary masks were individually applied to the normalized wake sodium images (calculated from 20minutes of acquisition) and sleep (calculated from 40minutes of acquisition). Paired t-test in Matlab was used compare global averages between wake and sleep sessions.

7.4.3 Temporal evolution of sodium signal change

The temporal evolution of global sodium signal was estimated by applying GM, WM and CSF binary masks to the wake and sleep images in high resolution image space ($1mm^3$.) The masks were obtained by thresholding the participant's TPMs, TPM higher than 90% were used for binarization. The mean signal (in MPRAGE space) was calculated for every 5 minutes of acquisition, so for each TPM there were 4 values for the wake and 8 for the sleep scans (per participant). Both wake and sleep sodium values were normalized to the mean wake value (in the same manner as described in Chapter 5.2.4 *Data visualization*) to visualise percentage change with respect to baseline. Significant interaction between the sessions and time (5-minute epochs) was assessed with repeated measures ANOVA. Note, that the sleep scans lasted twice as long as the wake scans, therefore wake (4 epochs) was compared with sleep first and last 20 minutes separately, to test the effect of session at later time points as well.

7.4.4 ROI analysis using predefined ROIs

15 ROIs were selected from the existing literature and from our findings, based on significant decreases in CBF during SWS (Chapter 6.5.4). Masks for the selected areas were extracted from the Mindboggle MNI Atlas (Klein and Tourville, 2012) and were grouped bilaterally in the following way (Mindboggle labels in brackets): 1. Caudate (11, 50); 2. Cingulate Gyrus(1002, 2002, 1010, 2010, 1023, 2023, 1026, 2026); 3. Middle Temporal Gyrus (1015, 2015); 4. Precuneus (1025, 2025); 5. Occipital cortex (1011, 2011); 6. Cerebellum (6, 45); 7. Basal Forebrain (91, 92); 8. Insula (1035, 2035); 9. Frontal cortex (1012, 2012, 1028, 2028, 1014, 2014); 10. Brainstem (16); 11. Thalamus (10, 49); 12. Superior Parietal and Supra Marginal gyrus (1029, 2029, 1031, 2031); 13. Superior Temporal gyrus (1030, 2030); 14. Putamen (12, 51); 15. Pallidum (13, 52). The average sodium MRI signal (normalized to eye-ball signal) was extracted for each of these regions, and paired t-tests used to compare mean normalized signal in the ROIs- wake vs. first 20 minutes of sleep and wake vs. last 20 minutes of sleep, and sleep first 20 vs sleep last 20 minutes. Significance was determined at alpha= 0.05 after FDR correction.

7.4.5 Correlation of sodium change (Exploratory analysis)

I investigated the relationship between temporal evolution of GM sodium signal change and button press response.

Finally, I correlated the mean sodium percentage change with physiological recordings (button press and high frequency power of heart rate variability) and subjective sleep metrics (sleep type, sleep depth and sleep length the night before the wake scan). This analysis was performed only for the ROIs that showed a significant change between sleep and wake.

7.5 Results

7.5.1 Visual inspection of mean sodium signal

Figure 48 shows the mean normalized sodium signal during the wake and sleep scans. At first glance, no obvious differences stand out, although closer inspection revealed that some areas exhibit higher sodium signal during sleep, as marked with arrows on Figure 48**.** These areas include precuneous, posterior and anterior cingulate cortex, frontal cortex, parietal cortex, insula, brainstem, pontine region and thalamus.

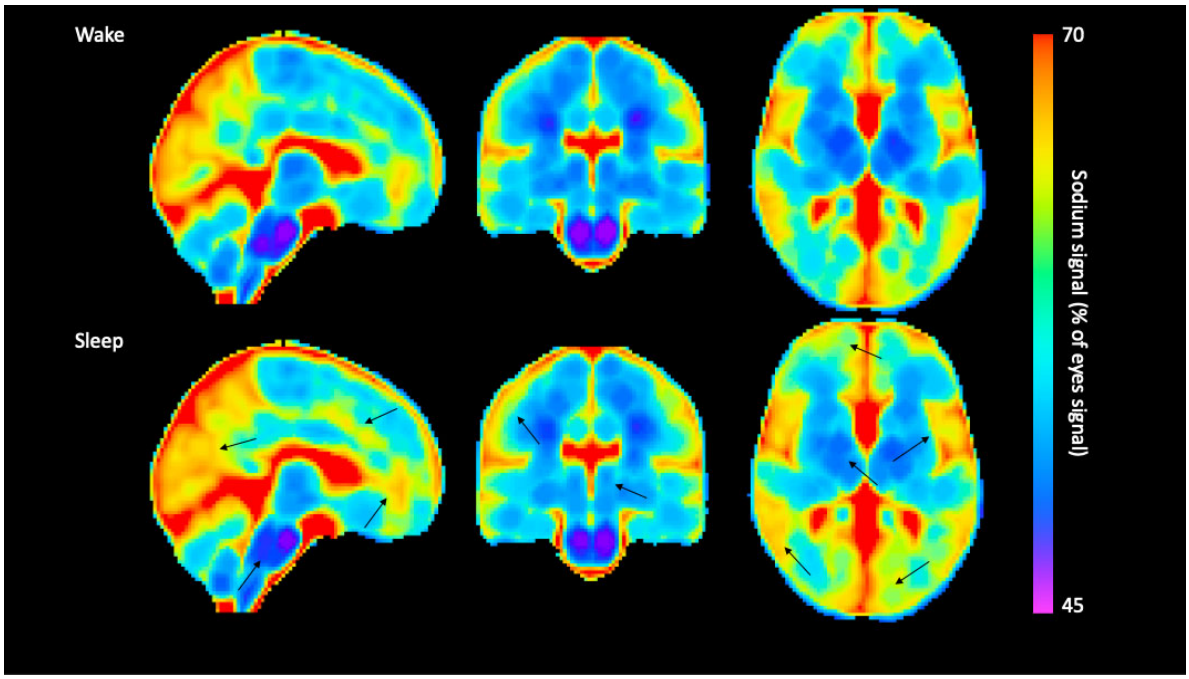

Figure 48: Mean sodium signal during wake and sleep

Illustration of mean normalized sodium signal images (N=21) during wake and sleep scans. The normalized sodium signal value changes from cold (low blood flow) to warm (high blood flow) colours. Slices were positioned at MNI: x= 6 y= -22 z= 4. Black arrows represent brain regions where there is visible increase in sodium signal.

7.5.2 Global sodium change

Figure 49 shows the mean sodium signal (normalized to the eye signal) in grey matter and whole brain. The mean normalized sodium signal during the awake session was 63.7 ± 1.4% and 62.0 ± 1.2% in grey matter and whole brain respectively. The mean normalized sodium signal was significantly higher during the sleep session in both grey matter and whole brain: 64.3 ± 1.7% and 62.6 ± 1.7% (paired t-test, t= 1.828, df=20, one-tailed p= 0.0413 and t= 1.895, df= 20, p= 0.0363 respectively). This a 0.9% change in global sodium signal in grey matter and whole brain.

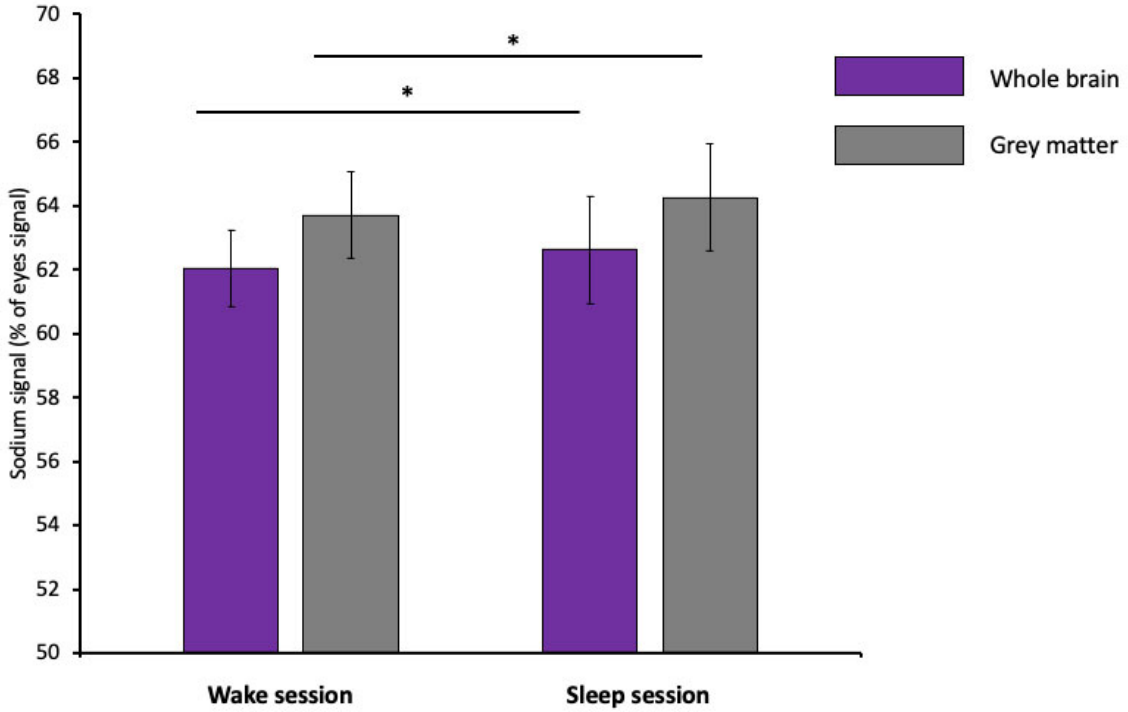

Figure 49: Bar graph of mean global sodium signal values during wake and sleep

Bar plot illustrating mean normalized sodium signal values between the wake and sleep scan in grey matter (grey colour) and whole brain (purple colour). Bars represent normalized sodium signal values (mean ± SD in units of % of eyes' sodium signal). * one-tailed paired t-test $p<0.05$.

7.5.3 Temporal evolution of sodium signal

Next, I investigated how the sodium signal changes with time between the two conditions in GM, WM and CSF. Figure 50 shows the temporal evolution of sodium signal (normalized to the mean awake signal= baseline) in grey matter, that was ~1.3% higher at the beginning (in the first 10 minutes) of the scan during sleep and showed a gradual decrease but always remained higher than awake.

Repeated measure ANOVA comparing wake sodium signal in GM with the first 20 minutes of sleep signal showed a significant effect of session ($F_{(1, 20)} = 5.626$, $p=0.028$). Furthermore, there was a significant effect of time ($F_{(1.423, 28.464)} = 10.996$, $p=0.001$), as Mauchley's test indicated violation of sphericity ($\chi^2(5) = 50.127$, $p < 0.001$) Greenhouse- Geisser (Epsilon= 0.474) correction was used.

Comparison of the wake sodium signal in GM with the last 20 minutes of sleep signal showed that effect of session was no longer statistically significant.

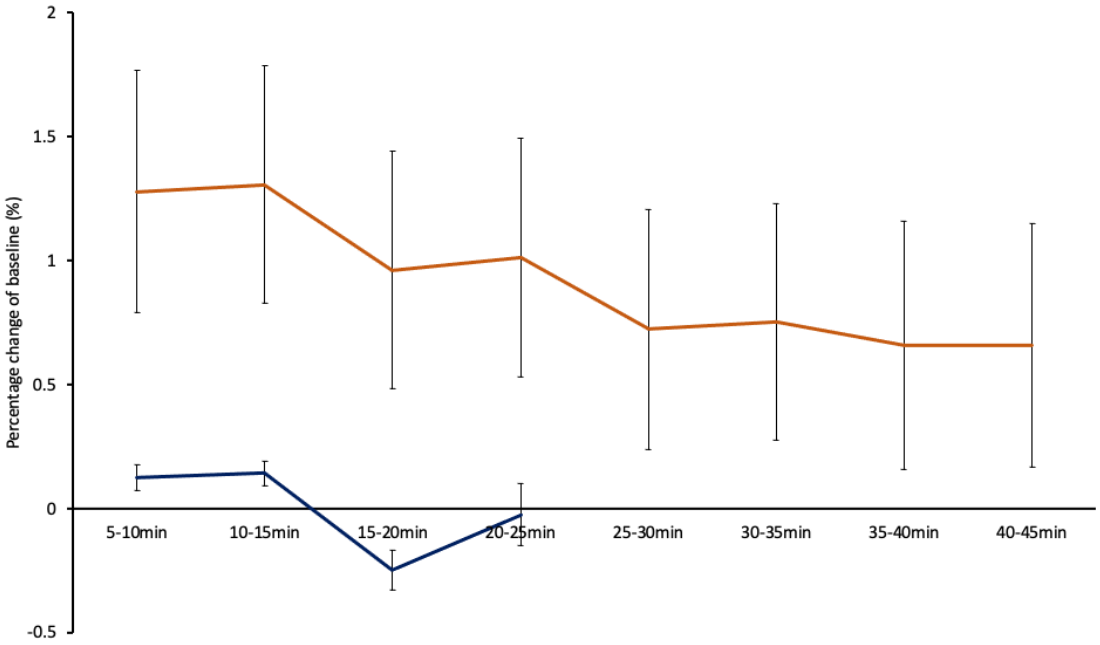

Figure 50: Temporal change in grey matter sodium signal during wake and sleep

Line plot illustrating the mean percentage change of sodium signal during the wake and sleep sessions in GM. Error bars represent SEM.

White matter showed a similar trend, with the highest increase in sodium signal (~1.5% above baseline) at the beginning of the scan and then gradually decreasing to 1% increase compared to baseline at the end of the sleep scan, as displayed on Figure 51.

Repeated measure ANOVA comparing wake sodium signal in WM with the first 20 minutes of sleep sodium signal showed significant effect session ($F_{(1, 20)} = 5.488$, $p=0.03$) and time ($F_{(1.667, 33.341)} = 13.508$, $p<0.001$; Mauchley's test indicated violation of sphericity $\chi^2(5) = 24.561$, $p < 0.001$ and Greenhouse- Geisser (Epsilon= 0.556) correction was used).

Comparison of wake sodium signal in WM with the last 20 minutes of sleep signal showed that effect of session was no longer significant.

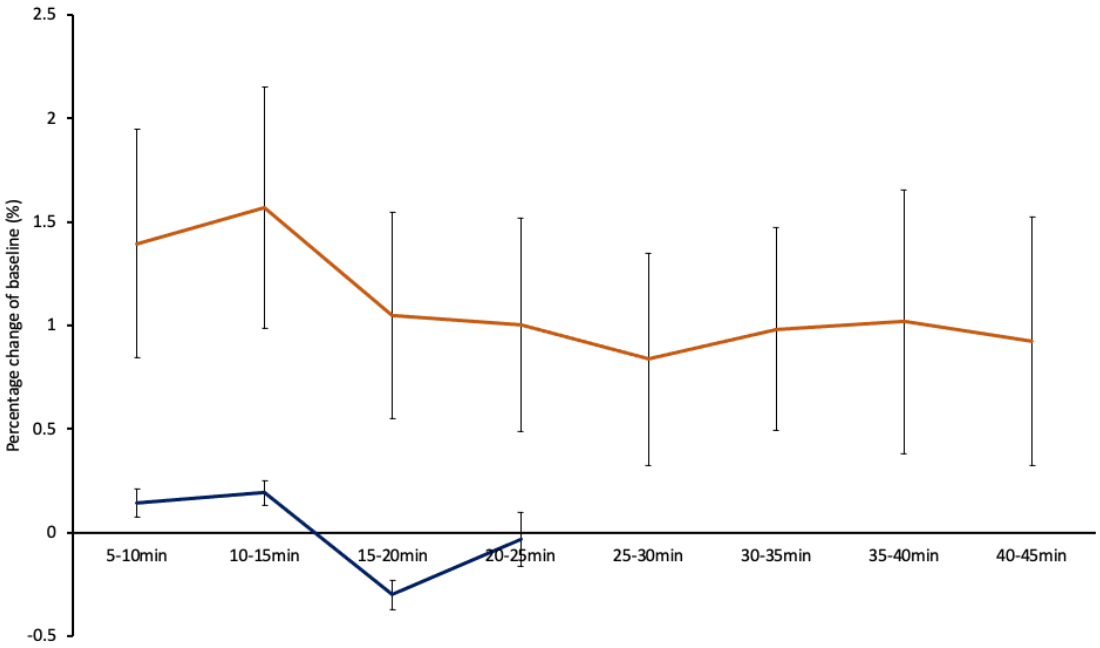

Figure 51: Temporal change in white matter sodium signal during wake and sleep

Line plot illustrating the mean percentage change of sodium signal during wake and sleep sessions in white matter. Error bars represent SEM.

As for GM and WM, CSF sodium signal was higher at the beginning of sleep scan than during awake, it stayed stable (1% increase compared to baseline) for the first 20 minutes before returning to approximately the same value as baseline, as displayed on Figure 52 Repeated measure ANOVA comparing wake sodium signal in CSF with the first 20 minutes of sleep sodium signal indicated a significant effect session ($F_{(1, 20)} = 4.761$, $p=0.041$), which was no longer significant when compared with the last 20 minutes of sleep.

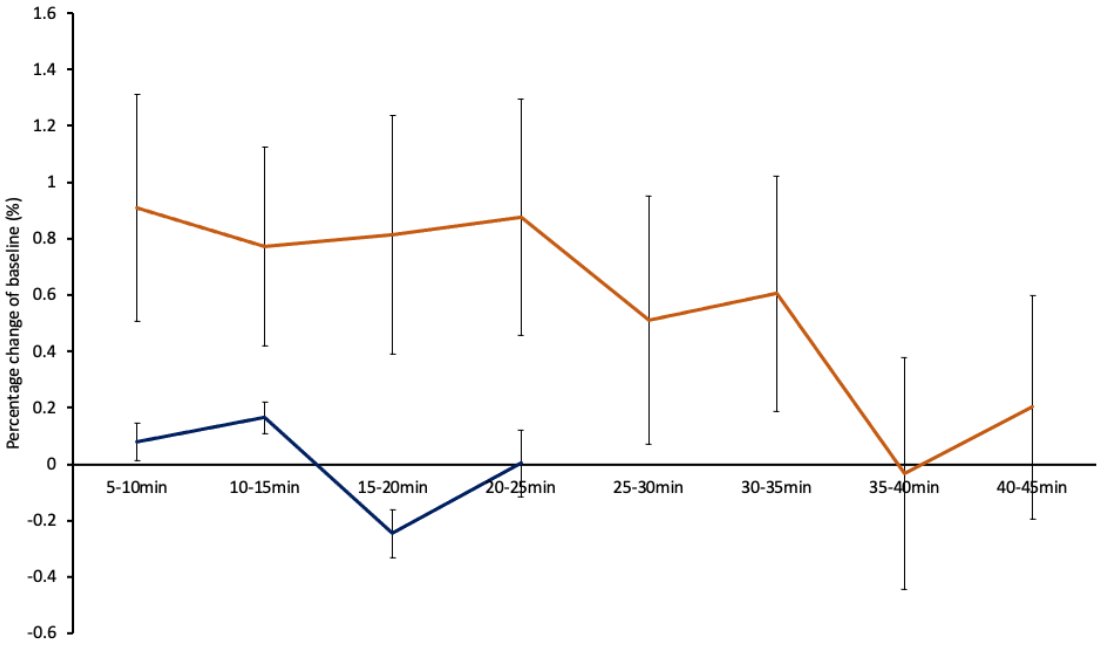

Figure 52: Temporal change in CSF sodium signal during wake and sleep

Line plot illustrating the mean percentage change of sodium signal during wake and sleep sessions in CSF. Error bars represent SEM.

7.5.4 ROI analysis

Mean sodium signal images from the 20 minutes of wake acquisition were compared with the mean images of the first 20 minutes of the sleep acquisition in 15 predefined ROIs. 5 ROIs survived FDR correction and showed a significant increase in mean sodium signal during the first 20 minutes of sleep, these regions are displayed on Figure 53. No significant regions survived FDR correction, when wake was compared to the last 20 minutes of sleep.

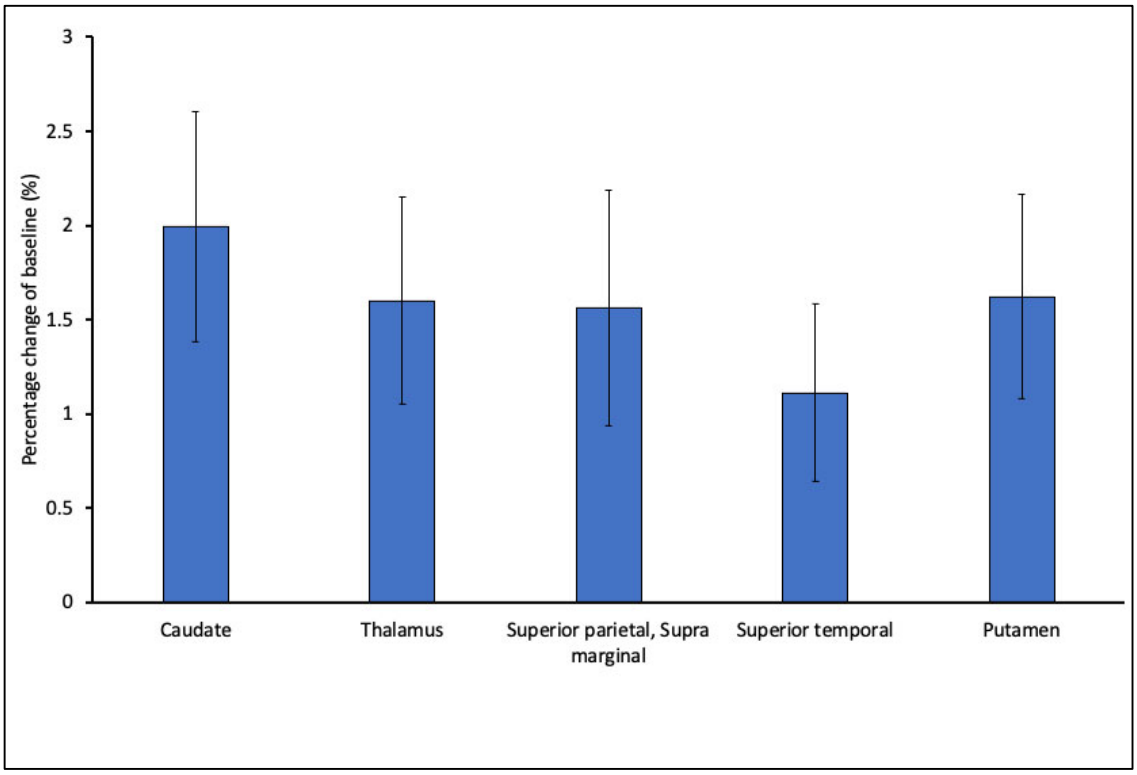

Figure 53: ROIs showing significant increase in sodium signal during sleep

Bar graph illustrating significant ROIs with the mean percentage increase of sodium signal during the first 20 minutes sleep compared to the wake session. Error bars represent SEM.

Mean sodium signal images from the last 20 minutes of sleep acquisition were compared with the mean images of the first 20 minutes of sleep acquisition in 15 predefined ROIs. All but 2 ROIs (Pallidum and Basal forebrain) survived FDR correction and a showed significant decrease in mean sodium signal during the last 20 minutes of sleep, these regions are displayed on Figure 54.

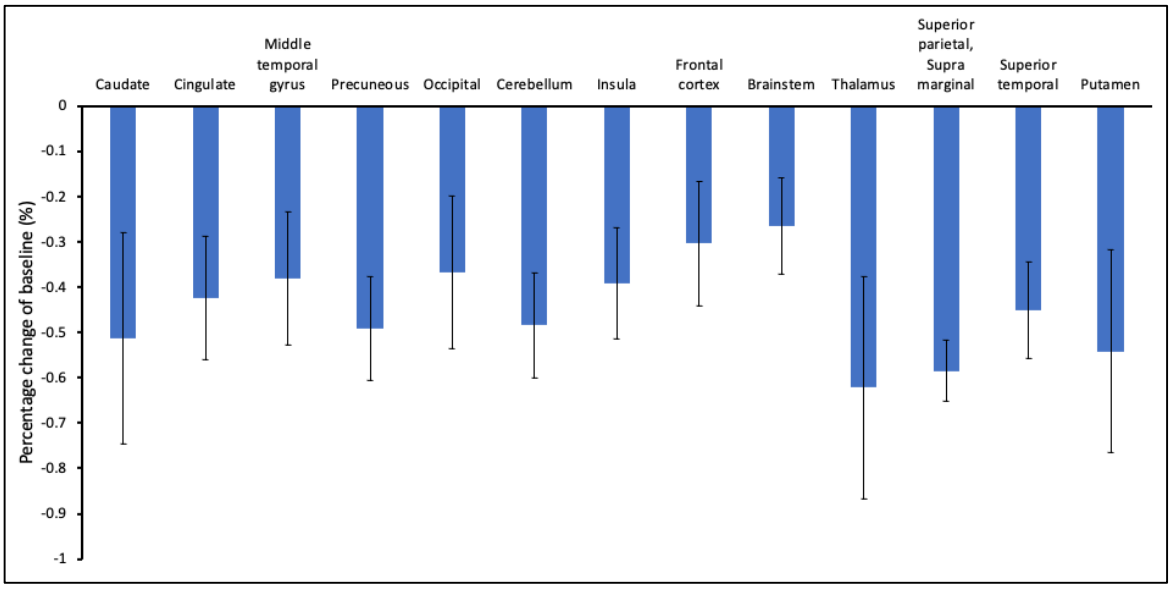

Figure 54: ROIs showing significant decrease in sodium between end and beginning of sleep

Bar chart illustrating significant ROIs with the mean percentage decrease of sodium signal during the last 20 minutes sleep compared to the first 20 minutes of sleep. Error bars represent SEM.

7.5.5 Correlation of sodium change in GM and button press response during sleep

Figure 55 shows the (non-significant) association between the temporal evolution of GM percentage change with button press response (Pearson correlation coefficient: r(19)= 0.7, p= 0.0543).

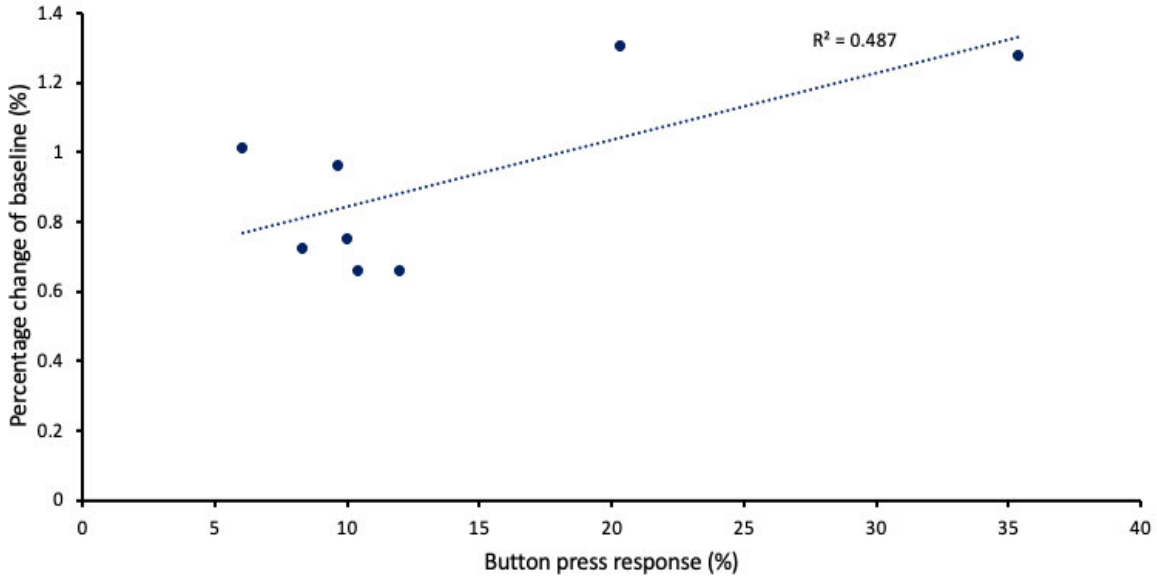

Figure 55: Correlation of temporal evolution GM percentage change with button press response

7.5.6 Correlation of significant ROIs with sleep measures

No significant correlation was observed between any of the significant ROIs and any of the sleep measures.

7.6 Discussion

7.6.1 Key results

Sodium MRI results indicated a brain wide increase in sodium signal during sleep session, which was in line with our hypothesis, i.e., expansion of interstitial space results in an increase in sodium signal. On the other hand, temporal analysis of sodium signal change during sleep indicated that the signal decreases with time, which contradicts our hypothesis, as we expected increase in sodium signal with the time being asleep. Nevertheless, we need to be cautious when interpreting these results because the temporal analysis was compromised by low SNR and potentially by a scanner drift. Analysis comparing the mean images of sleep (first 20 minutes) with wake mean images in 15 pre-defined ROIs (based on the CBF findings) showed significant increase in sleep condition in basal ganglia, thalamus, parietal and temporal lobes, however the increase was not present in the last 20minutes of sleep. Improvements in image processing and quantification are necessary to make a conclusion about sodium MRI's sensitivity to the glymphatic system.

7.6.2 Global change

Visual inspection of the mean wake and sleep sodium signal images suggested an increase in sodium signal in the posterior and anterior cingulate, frontal, and parietal cortices, insula, brainstem, pontine region and thalamus. Interestingly these areas show some overlap with those where we observed significant reductions in CBF (Chapter 6.5.4, Figure 44). As hypothesized sleep resulted in significant global increase in grey matter and whole brain sodium signal. Despite the absolute increase was small, it was significant, which suggests that it was consistent across participants.

7.6.3 Temporal evolution of sodium signal

Next, I went on to investigate the temporal evolution of the sodium signal in GM, WM and CSF with the hypothesis that there will be an increase in sodium signal with time. Sodium signal was significantly higher during the first 20 minutes of sleep than during wake scan. There was no significant effect of session when the last 20 minutes of sleep was compared with wake. In all tissue segments the sodium signal was higher at the beginning of the sleep scan and showed a decrease with time, going against my hypothesis. Before trying to give an alternative explanation to the decrease in sodium signal with sleep, I will focus on the individual tissue segments.

Observing significant changes in CSF sodium signal is difficult to interpret physiologically, as CSF sodium concentration is tightly regulated and linked to blood plasma sodium concentration, where we would not expect a change (Di Terlizzi and Platt, 2006). Therefore, a change in CSF sodium signal might reflect either a change in other tissue compartment as the sodium MRI has a relatively wide point spread function so there would a substantial signal overflow from other tissue compartments (especially form GM), or it might be due to technical issues.

The GM sleep sodium signal showed a stepwise reduction, while the WM sleep signal appeared to plateau. Interestingly, the wake signal followed the same temporal pattern in all tissues, which was unexpected and might arise from technical/processing problems.

It is important to note, that for this dynamic analysis I used single averages of the of the k-space (using the method described in Chapter 2.1.2 Figure 10), which have a very low SNR. For this reason, the signal was normalised using the signal from the eyeballs from the overall mean image.

Therefore, if there was a hardware-induced drift in the signal, the normalisation would not have adjusted for it, and might explain the paradoxical results.

Higher sodium signal at the beginning of the sleep scan that gradually decreases points in the opposite direction as our hypothesis. Figure 55 also shows a (non-significant) positive correlation between button response and sodium change in GM (at different time points). Sodium signal was higher when participants were indicating that they were awake. One possible explanation for a high sodium signal at the beginning of the scan with a decreasing trend could be that the sodium signal is more sensitive to changes in CBF/CBV than to changes in extra/intracellular volume factions. CBF is known to increase with sleep debt (from morning to evening) and further increases after a night of sleep deprivation (Elvsåshagen et al., 2019). In theory, it would be possible that at the beginning of the scan we were measuring an increase in sodium signal due to an increase in CBF, which then gradually decreased with sleep duration (as discussed previously). Note that our sleep CBF measures were always taken approximately 60 minutes after the beginning of the sodium scan, while the sodium data were acquired at the beginning of each session.

However, before jumping to quick conclusions I would like to discuss how blood flow and total sodium signal (and TSC) might be related based on previous findings. TSC is the mean sodium concentration weighted by the volume fraction of the different sodium compartments. We can divide the sodium compartments in brain parenchyma into a high sodium concentration [140mM] compartment that includes blood, CSF in Virchow-Robin space, and extracellular fluid; and a low sodium concentration compartment [12mM] that includes intracellular fluid.

First, let's assume that the change in sodium signal is indeed a reflection of a change in CBF. We know that neural activity is associated with increases in CBF and cerebral blood volume (CBV) (Mandeville et al., 1999), which would in turn result in an overall sodium signal increase (if CBF increase was the only change accompanying neural activity). However, a negative relationship was found between CBV and CSF compartments during neural activation- in an 8ml visual cortex voxel CSF compartment was estimated to be 10% and was reduced by 5% upon visual stimulation (Piechnik et al., 2009). Further evidence for the reciprocal relationship between CBV and CSF compartment comes from the anticorrelation that has been observed between neural activity and CSF-waves during slow wave sleep, which in fact might be due to increased resistance in CSF-flow in the Virchow-Robin space when CBV is increased due to activity (Fultz et al., 2019). A reduction in the CSF compartment during neural stimulation could be explained by the increase in CBV which in turn reduces the Virchow-Robin space volume. This in theory would result in no net sodium signal

change as the change in compartment size should be proportional and they are both high concentration compartments.

This raises the question: If the change that we observe is not from reduction in cell volume or from increase in blood volume, then where is it from? One study looked at TSC change corresponding to finger-tapping task, where participants were asked to continuously carry out a motor task during sodium acquisition (Gandini Wheeler-Kingshott et al., 2018). Using my argument that sodium MRI is sensitive to intra/extracellular volume changes, with constant activation (for 5 min) I would assume either no change or a decrease in TSC at the site of activation, as increased neural activity has been associated with increased glial volume fraction. Glial cells are involved in taking up K^+ that is released to extracellular space when neurons hyperpolarize, and water follows (Ransom, Yamate and Connors, 1985; Walz, 2000). Contradicting my hypothesis, they found increased sodium concentration (~1%) in the contralateral motor cortex, they argued that this increase is not due to blood change (as CSF buffering discussed above) but it is the result of a shift in sodium concentration equilibrium between compartments, potentially by the temporal dynamics of Na^+/K^+ pump and voltage activated sodium channels (Gandini Wheeler-Kingshott et al., 2018).

Sodium change measured during neural activation suggests that sodium MRI signal is more complicated than I previously thought and describing the signal change between two conditions (and/or across time points) as change in relative compartment sizes might be too simplistic.

7.6.4 ROI analysis

Not knowing the exact origin of the sodium signal makes the interpretation of ROI analysis challenging. The significant increase in sodium signal during sleep vs awake was observed in the deep grey matter structures, in the thalamus, caudate and putamen, which have been also implicated in slow wave generation (Steriade, 2003, Lazarus et al., 2013).

ROIs showing a significant decrease in last 20minutes of sleep compared to the first 20minutes, do not show any spatial specificity (13 out of 15 show reduction in sodium signal) and the reduction is rather low ~0.5% which might argue for a scanner drift effect.

7.6.5 Limitations and future improvements

We did not randomize the pulse sequences (to increase the chance of falling asleep in the proton scan, as explained in Chapter 3.10), which could have given some important information about

sodium sensitivity to CBF. If sodium signal is mainly sensitive to CBF then sodium images acquired at the end of the session (~70min) should have lower mean GM sodium signal than wake images.

Diffusion-weighted magnetic resonance spectroscopy (DW MRS) sensitive to glial metabolites could in theory give valuable information about glial cell volume at different time points during sleep (Palombo et al., 2018). This could provide valuable information for understanding dynamic changes observed in the sodium signal during sleep, i.e., if the changes are indeed due to scanner drift.

Another point to consider is that the assumption that there are no sleep related changes in eye sodium concentration with sleep might not be correct, as no one has investigated this, but it is unlikely for reasons described in Chapter 4.5.

Absolute quantification was not possible due to motion issues described in Chapter 4.4. In any future experiment this should be avoided by either using a fixed rack that holds the phantoms, which can be adjusted to participants head size to be in proximity of the head—this would prevent independent phantom movement; or by placing the sodium phantoms around a large calibration phantom with the same electrical property as the human head and acquire phantom images separately from the participant images (Lu et al., 2010).

It is important to reiterate that the eye signal normalized values might still have been affected by motion as well—as the whole image was used in the realignment, meaning that the phantoms (that moved separately from the brain) could still influence how the images were re-aligned. Especially, given that the phantoms had a higher signal relative to the brain signal. This might have biased the SPM re-alignment cost-function and introduced errors. One way to overcome this is by creating a "rough" brain mask that does not include the phantoms then estimate the rigid body transformation vectors from re-alignment of the de-skulled (phantomless) images then apply them to whole images. This would not solve the problems with phantom movement but would reduce the chance of phantom motion affecting the brain realignment. Note, applying the motion parameters to the whole images is necessary because the eyes would not be part of the de-skulled image (when standard SPM segmentation is used).

Potential improvements could also be introduced by combining motion correction and image reconstruction with approaches like Radial Interstices Enable Speedy Low-Volume imaging (RIESLING) (https://github.com/spinicist/riesling). These methods are known to increase the SNR and therefore would lead to a better estimation of realignment parameters and altogether better motion compensation and less blurring. This is work in progress.

Phantom images could also be de-blurred by using a similar approach, i.e. dissecting them out and realigning them independently.

7.7 Conclusion

With our current data we cannot reject or accept the hypothesis of an increase in extracellular volume fraction during sleep. One line of evidence is pointing towards an increase in the interstitial volume, as sodium signal in the parenchyma during sleep is higher than during wake. On the other hand, sodium changes over time did not follow the predicted change, and thus suggests that the overall increase might come from elsewhere. Nevertheless, it would be unwise to make a conclusion based solely on the dynamic analysis, which are intrinsically limited in SNR and the way the images were quantified (by normalization to mean eye signal) makes it susceptible to scanner drift. Furthermore, we should not exclude the possibility that a maximum of 45 minutes of sleep is not enough to induce the expected changes in water compartment size. Further improvements in analysis and experiments are warranted.

Chapter 8 Higher order diffusion analysis and VBM

8.1 Introduction

To my best knowledge, only one published study to date has proposed investigating changes in interstitial volume associated with glymphatic clearance during sleep in humans using diffusion weighted MRI (Demiral et al., 2019). This study utilized diffusion MRI with a range of b-values (b-values: 0, 50, 300, and 1000 s/mm^2) along 3 orthogonal directions. They obtained two ADC measures, by splitting the data into "fast" (b-values: 0, 50, 300) and "slow" (b-values: 300, and 1000 s/mm^2) diffusion components and averaged the x, y and z components, resulting in a measure for "fast" and "slow" isotropic diffusion.

Similar to our study, their sleep protocol included 24h of sleep deprivation and all scanning took place in the morning. However in contrast to our study no sleep-inducing drug was used. In this study, there were no significant changes in either slow or fast ADCs at a global level. However, voxel-wise analysis revealed significant increases in slow ADC of the cerebellum and the temporal lobe and reductions in fast ADC in the thalamus, insula, parahippocampus and striatal regions during sleep.

In addition to dwMRI, this group also acquired T_1-weighted anatomical images for VBM analysis during wake and sleep and found a significant increase in CSF volume during sleep. The increase in CSF was associated with an increase in slow ADC in the dorsal cerebellar cluster. The authors suggested that the increase in slow ADC might be related to increased interstitial space volume and increased glymphatic clearance, however the effects were much smaller than anticipated from animal studies. Furthermore, they suggested that the increase in fast ADC might reflect the change in perfusion that is known to occur during sleep. However, measuring ADC might be too simplistic (Chapter 2.2.2) to uncover glymphatic system related changes: as all water compartments contribute to ADC, using it as an approximation for interstitial volume change might be a biased approach.

Consequently, we hypothesized that acquiring diffusion weighted images with higher b-values in more directions and using higher order diffusion model such as DKI that allows the quantification of non-Gaussian diffusion associated with complex microstructural environment may be more sensitive to changes in interstitial volume during sleep. Previous studies have shown that kurtosis measures are more sensitive to detect changes immediately after ischemic stroke than diffusion

measures derived from DTI (Jenesen et al., 2011; Grinberg et al., 2012; Hui et al., 2012). Ischaemic stroke has also been associated with a decrease in diffusion measures such as MD, AD and RD and an increase in kurtosis parameters. In this study, the increase in kurtosis reported was about twice the magnitude of the reported decrease in diffusion (Jenesen et al., 2011; Hui et al., 2012). During ischaemia the lack of oxygen reduces/stops ATP production, consequently the Na^+/K^+-pump fails. The Na^+/K^+-pump plays a crucial role in cell volume control, and its failure rapidly leads to cell swelling (Simard et al., 2007). It has been hypothesized that cell swelling can act as diffusion dead-space microdomains that increases extracellular space tortuosity, hence the increase in diffusion kurtosis measures (Tao, Tao and Nicholson, 2005). Following this logic, a decrease in cell size (or expansion of interstitial space), as expected with sleep, would lead to a decrease in the kurtosis measures. Although the changes induced by glymphatic flow are not expected to be as dramatic as those induced by stroke.

8.2 Aims

The main aim of this study was to expand on the previous literature presented in the introduction. This work was based on the assumption that using higher b-values (that is more sensitive to microstructural changes, as described in Chapter 2.2.4) could unravel glymphatic system related changes in water diffusivity.

8.3 Hypotheses

H1: Sleep will be associated with an increase in gaussian diffusion measures and a decrease in kurtosis measures

H2: Change in kurtosis will be more pronounced than change in diffusion measures

H3: Sleep related diffusion/kurtosis changes will be more prevalent in areas associated with SWA

H4: There will be global increase in CSF (hypothesis formulated based on Demiral et al.'s findings)

8.4 Methods

8.4.1 Imaging parameters (dwMRI)

dwMRI images were acquired with a 32-channel head coil. The measurement were taken over 2 shells (b = 800 and 2600 s/mm^2), sampled in 32 and 64 directions respectively with single shot, twice-refocused spin echo (Reese et al., 2003) and an echo planar readout. Nine b= 0 s/mm^2 volumes were also acquired. Images were acquired with phase encoding in the anterior to posterior direction, a single b0 (b= 0 s/mm^2) image was also acquired in the posterior to anterior direction to calculate the susceptibility induced off-resonance field to correct the images.

- TR= 4100ms
- TE= 87ms
- Flip angle= 90°
- FOV= 240 x 240mm^2
- Matrix size= 96 x96
- Number of slices= 60
- Slice thickness= 2.5mm
- Multiband factor= 2
- GRAPPA reduction factor= 2

8.4.2 Image pre-processing (dwMRI)

The diffusion weighted images were corrected for motion and eddy current induced distortions using the *eddy* function of the FMRIB Software Library (FSL, version 6.0.1) (Andersson and Sotiropoulos, 2016). The following steps were applied to correct the images:

1. Estimation of susceptibility induced off-resonance field from b0 images acquired in different phase encoding directions
2. Volume-to-volume motion correction: Mutual information-based rigid body registration was used to perform between b-value motion correction that first calculates an average for each b-value and then estimates the motion between the averages relative to the b0 average.

3. Outlier replacement: Subject movement during diffusion encoding can result in signal dropout affecting part of a slice or more commonly the whole slice as shown in Figure 56A. When the volume is rotated back to correct for out of plane rotations, the signal dropout will result in diagonal bands, as shown in Figure 56B. This has a significant effect on any diffusion modelling, but non-Gaussian (kurtosis) measures are particularly sensitive to motion related signal dropout (Sairanen, Leemans and Tax, 2018). Outliers were estimated slice-wise and replaced with the Gaussian Process prediction, which makes two assumptions to predict the diffusion signal: 1. The signal from diffusion weighing along two vectors is more similar when the angle between the two vectors is small than when the angle is large; 2. The signal from two acquisitions along vectors v and -v is identical (Andersson et al., 2016).
4. Slice-to-volume motion correction: One of the assumptions of volume-to-volume correction is that the subject does not move during the acquisition of a single volume that takes in our case 4.1 seconds. This assumption holds up in most of the cases, however we were imaging sleeping participants where involuntary motion is unavoidable. Motion during the acquisition of a single volume leads to signal dropout that results in zig-zag pattern (Figure 56A and B) in the coronal and sagittal plane, when the slices are acquired in an interleaved manner (like in our acquisition). Slice-to-volume correction was achieved by modelling movement as a piecewise continuous function over time (Andersson et al., 2017). Figure 56C shows an example of the final result of the eddy correction.

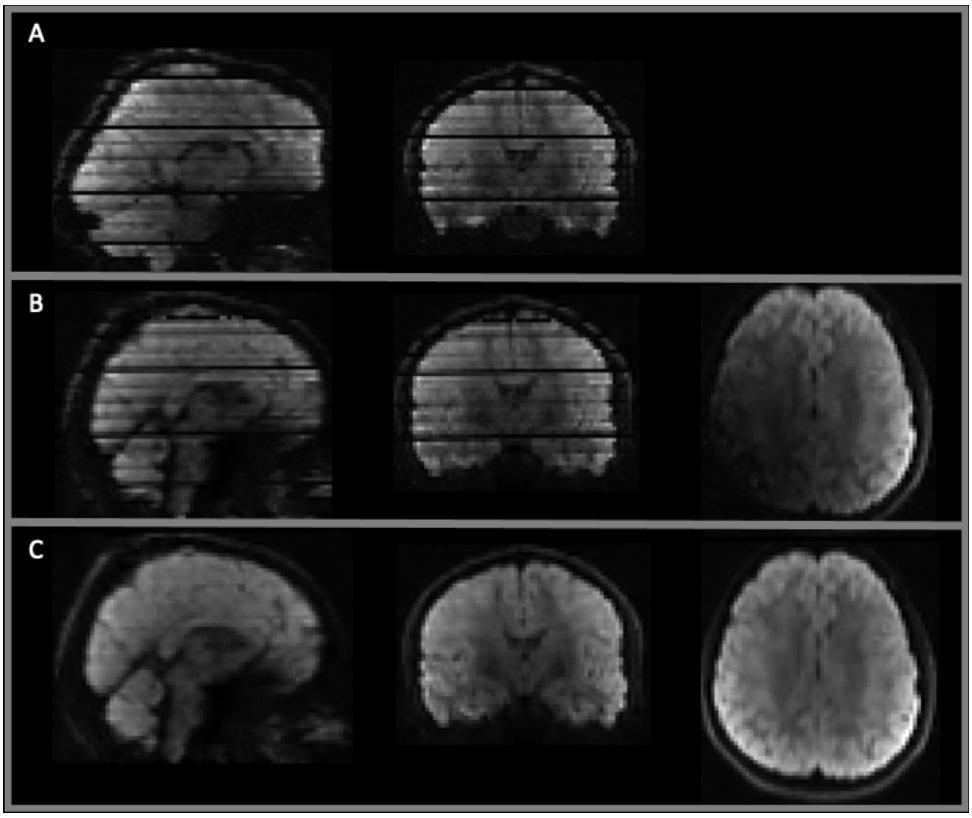

Figure 56: Correction of diffusion weighted images

A: Example of diffusion weighted image without any correction. The signal dropout in the axial slice is so high that it is not visible at this signal windowing. **B:** Image after susceptibility induced off-resonance, volume-to-volume rigid body motion correction and correction for eddy current induced distortions. Diagonal band in the signal can be observed in the axial plane, that is due to correcting for rotation. **C:** Image after all eddy correction steps. Note that the signal drop out was completely recovered and the zig-zag lines in the sagittal and coronal slices have almost completely disappeared.

8.4.3 DKI/DKTI model

3D Gaussian smoothing with a kernel of FWHM=1.25mm was used as suggested by the DKI pioneer Jensen et al. 2005. DKI/DKTI model was fitted with the *DiffusionKurtosisModel* from the DIPY library and produced 4 diffusion images MD, AD, RD and FA, and 3 kurtosis images MK, MKT, and KFA (Garyfallidis et al., 2014). The MKT image was used as a source image to co-register all images to the high resolution T_1-weighted anatomical image, both sessions were registered to the same high resolution anatomical image separately. The normalization parameters obtained from the

segmentation of high-resolution anatomical image were used to wrap the DKI/DKTI images into MNI space. 3D Gaussian smoothing with FWHM= 6mm was applied to the normalized images.

8.4.4 Global analysis (dwMRI)

Global DKI/DKTI measures were obtained by applying GM, WM and CSF binary masks to the wake and sleep images in high resolution space. The masks were obtained by thresholding the participant's tissue probability masks (TPM), TPM higher than 90% was used for binarization. Percentage change of baseline was calculated in the following way: ((sleep-wake)/wake) *100. Paired sample t-test was used to assess statistical significance.

8.4.5 Voxel-wise analysis (dwMRI)

Wake and sleep DKI/DKTI parameters (normalized to MNI space and smoothed FHWM=6mm) were compared using voxel-wise paired sample t-test (SPM12). The statistical significance was determined using cluster size inference with an initial cluster forming threshold of $p< 0.001$, where clusters with FDR-corrected $p<0.05$ were considered significant.

8.4.6 Participant exclusions

5 participants were excluded from the final analysis. Two because they could not sleep during the proton acquisition and 3 because of motion related artifacts, despite the advanced motion correction used in pre-processing. The same participants were also excluded from VBM analysis to allow direct comparisons between diffusion/kurtosis measures and brain tissue volumetric changes.

8.4.7 Imaging parameters (anatomical T_1-weighted)

- TR= 2300ms
- TE= 2.19ms
- TI= 920ms
- Flip angle= 9°
- FOV= 256 x 256 x 256 mm^3
- Resolution= 1mm^3 (isotropic)

8.4.8 Image segmentation (anatomical T_1-weighted)

MPRAGE images for the sleep and wake sessions were processed in SPM12 using field bias correction (light regularisation) to correct non-uniform fields and were then segmented into GM, WM, and CSF sections using tissue probability maps based on the International Consortium of Brain Mapping (ICBM) template for European brains. SPM12's DARTEL tool was used to normalize the tissue segments (TPMs) to the Montreal Neurological Institute (MNI) template with a 1.5×1.5×1.5 mm^3 voxel size and modulated for volumes.

8.4.9 Brain tissue volume- global analysis

Brain tissue volume was determined by integrating the voxel values of each TPM over the whole brain. Significant changes in total tissue volume (GM, WM and CSF) were determined by paired sample t-test analysis using Matlab, $p<0.05$ was considered significant.

8.4.10 Voxel-wise comparison (anatomical T_1-weighted)

All normalized TPM images were smoothed with 8-mm FWHM isotropic Gaussian kernel. Further, details of the processing steps are described in https://www.fil.ion.ucl.ac.uk/~john/misc/VBMclass10.pdf. Statistical comparisons between sleep and wake conditions were performed in SPM using a paired-sample t-test design. Only clusters surviving whole brain FDR correction $\alpha<0.05$ after thresholding at an uncorrected statistical threshold of $p<0.001$ were considered significant.

8.5 Results

8.5.1 Global diffusion changes

Table 4 summarizes global DKI/DKTI parameters estimated during the wake and sleep conditions. No significant changes were observed in the standard diffusion measures, except for a significant increase in GM FA ($t= 2.1551$, $df=15$, $p= 0.024$). However, there were significant differences in both DKI and DKTI measures. Specifically, there was a significant decrease in MK in both GM and WM ($t= 2.8242$, $df=15$, $p= 0.006$ and $t= 2.4926$, $df= 15$, $p= 0.012$ respectively), and in RK GM and WM ($t= 2.8664$, $df= 15$, $p= 0.006$ and $t= 2.6284$, $df= 15$, $p= 0.01$ respectively). Furthermore, there was a

significant decrease in MKT in both GM and WM (t= 2.7006, df= 15, p= 0.008 and t= 1.9951, df= 15, p= 0.032 respectively). Note that the MK and MKT values in GM are virtually the same, while in WM MKT produced lower values. A significant increase in KFA was observed in both the GM and WM (t= 2.4055, df= 15, p= 0.015 and t= 2.2951, df= 15, p= 0.018 respectively). Note that the significant decrease in MK, MKT, and RK were ~1.5% in both GM and WM, while the significant increase in KFA was 8.2% in GM.

	GM			WM		
	Wake	**Sleep**	**% change**	**Wake**	**Sleep**	**% change**
Diffusion measures						
MD(μm^2/ms)	1.042 ± 0.036	1.038 ± 0.033	-0.40 ± 1.88	0.903 ± 0.015	0.899 ± 0.012	-0.36 ± 1.76
AD (μm^2/ms)	1.168 ± 0.036	1.166 ± 0.032	-0.15 ± 1.60	1.283 ± 0.014	1.279 ± 0.015	-0.32 ± 1.59
RD (μm^2/ms)	0.979 ± 0.035	0.973 ± 0.033	-0.55 ± 2.09	0.713 ± 0.018	0.710 ± 0.013	-0.40 ± 1.98
FA	0.124 ± 0.005	0.127 ± 0.005	2.26 ± 4.15 *	0.367 ± 0.011	0.368 ± 0.009	0.29 ± 1.41
Kurtosis measures (DKI)						
MK	0.711 ± 0.014	0.703 ± 0.018	-1.12 ± 1.58 *	0.940 ± 0.027	0.930 ± 0.033	-1.05 ± 1.68 *
AK	0.683 ± 0.012	0.681 ± 0.015	-0.21 ± 1.62	0.760 ± 0.016	0.757 ± 0.016	-0.40 ± 1.36
RK	0.752 ± 0.020	0.740 ± 0.024	-1.63 ± 2.25 *	1.190 ± 0.043	1.173 ± 0.055	-1.41 ± 2.12 *

DKTI						
MKT	0.712 ± 0.014	0.704 ± 0.017	-1.01 ± 1.49 *	0.917 ± 0.024	0.910 ± 0.028	-0.82 ± 1.64 *
KFA	0.198 ± 0.017	0.213 ± 0.021	8.21 ± 13.6 *	0.395 ± 0.015	0.402 ± 0.011	1.87 ± 3.25 *

Table 4: Global diffusion and kurtosis measures

Summary of mean ± SD of global GM (GM TPM>90%) and WM (WM TPM>90%) diffusion and kurtosis measures.

8.5.2 Voxel-wise comparison (dwMRI)

Voxel-wise comparison between wake and sleep conditions revealed significant localised decreases in MK (and MKT), RK and significant increase in KFA.

Mean Kurtosis

Figure 57 shows brain regions after initial cluster forming, from these clusters 4 survived FDR correction. Significant MK clusters and the corresponding percentage change are summarized in Table 5, the largest cluster (size= 1868 voxels) is centred at bilateral posterior and middle cingulate and extends to precuneus, cuneus, and calcarine sulcus. The second largest cluster (size= 674 voxels) is centred in the right middle occipital cortex and runs down to the middle temporal lobe. There is a large cluster (size= 590 voxels) running from the right thalamus through the third ventricle towards the cerebellum and touches onto the midbrain. The fourth significant cluster (size= 182) runs between left thalamus and left superior temporal gyrus.

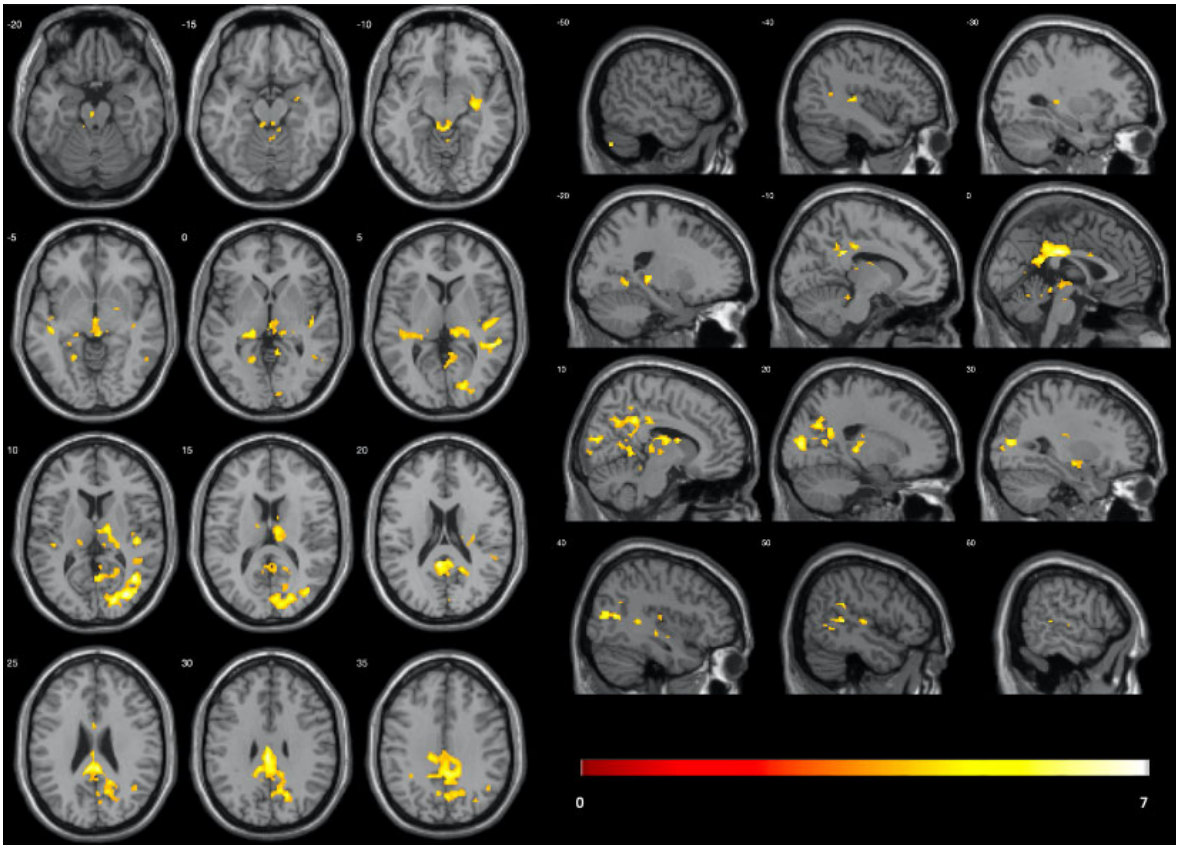

Figure 57: Voxel-wise comparison of mean kurtosis between wake and sleep

Brain regions with significantly reduced MK during sleep. The statistical significance was determined using cluster size inference with an initial cluster forming threshold of $p < 0.001$, where clusters with a corrected FDR of $p < 0.05$ were considered significant. Left side of the image displays axial slices from z= -20 to z= 35 in 5mm increments. Right side displays sagittal slices from x= -50 to x= 60 in 10mm increments. The colour bar represents T-value.

MK: Brain regions	MNI [x y z]	Cluster	L/R	T value	p (FDR-corr) cluster	% Change of baseline
Middle Occipital	[34 -78 10]	674	R	7.244	0.000	-2.2 ± 1.4
Temporal_Mid_R (aal3v1	[42 -62 10]		R	6.7796		
Cuneus_R (aal3v1)	[22 -84 10]		R	6.4942		
Cingulate_Post_L (aal3v1)	[-8 -38 28]	1868	L	7.0755	0.000	-2.7 ± 1.6

Cingulate_Post_L (aal3v1)	[-4 -46 20]		L	6.9685		
Cingulate_Mid_R (aal3v1)	[0 -28 30]		R	6.9386		
Thal_PuI_R (aal3v1)	[16 -26 2]	590	R	5.7438	0.000	-2.9 ± 1.5
Thal_VL_R (aal3v1	[14 -12 12]		R	5.3819		
Vermis_3 (aal3v1)	[2 -36 -10]		R	5.3425		
Thal_VPL_L (aal3v1)	[-20 -28 2]	182	L	5.5387	0.037	-2.8 ± 1.7
Temporal_Sup_L (aal3v1)	[-42 -26 8]		L	4.8973		
Thal_PuA_L (aal3v1)	[-14 -24 10]		L	4.0985		

Table 5: Clusters showing significant reduction in mean kurtosis during sleep

Percentage change was determined for each participant before averaging in the following way: ((mean cluster sleep MK- mean cluster wake MK)/mean cluster wake MK) *100; ± represents SD between participants. The statistical significance was determined using cluster size inference with an initial cluster forming threshold of $p< 0.001$, where clusters with FDR- corrected $p<0.05$ were considered significant. Anatomical information was derived using the xjView toolbox (http://www.alivelearn.net/xjview; based on the WFU_PickAtlas, http://fmri.wfubmc.edu/software/PickAtlas). In the table “aal3v1” denotes Automated Anatomical Labeling.

Mean Kurtosis Tensor

Voxel-wise comparison of MKT images between the two session produces a statistical map identical to the one from MK, hence not displayed here.

Axial Kurtosis

No significant change was observed in AK.

Radial Kurtosis

Figure 58 illustrates areas with a significant decrease in RK, these areas coincide with areas showing a reduction in MK (Figure 57). As for the MK findings, there were four significant clusters in RK that

are summarized in Table 6. The changes in RK overlap very well with those found with MK, suggesting that the changes in MK are mainly driven by the radial component.

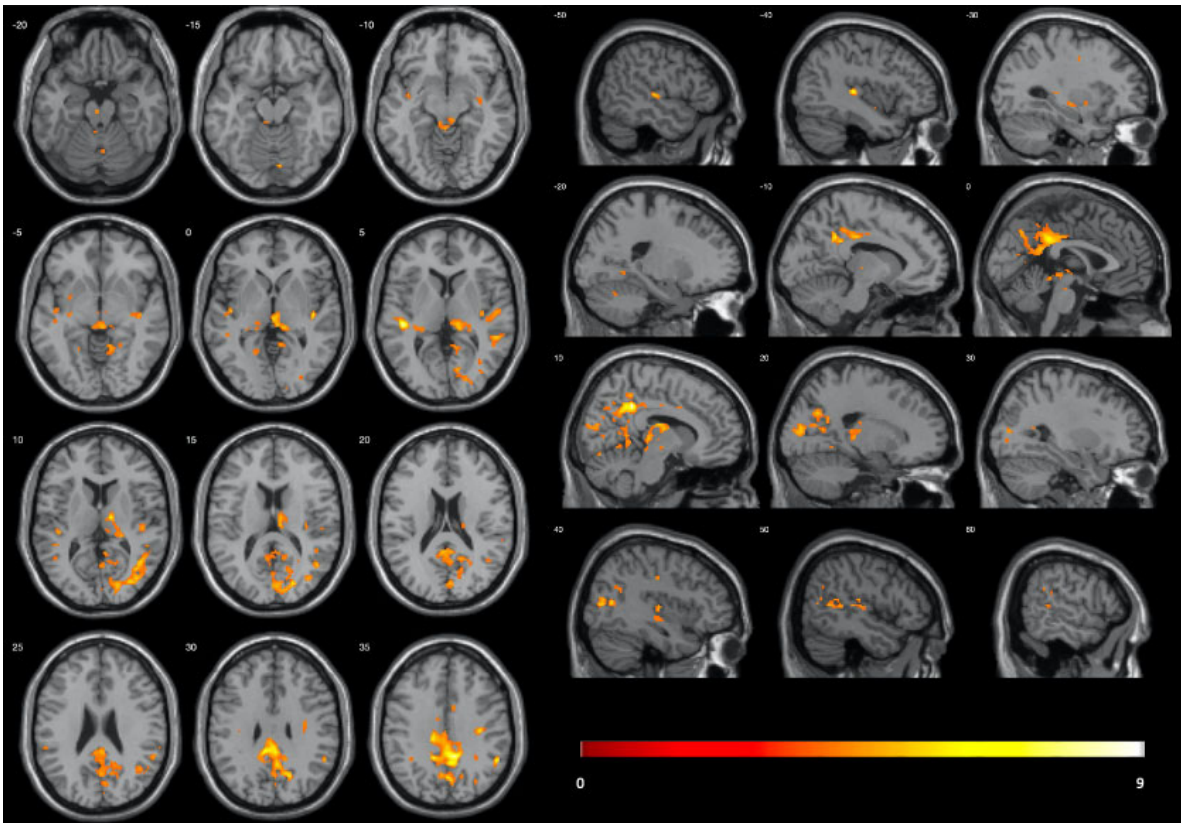

Figure 58: Voxel-wise comparison of radial kurtosis between wake and sleep

Brain regions with significantly reduced RK during sleep. The statistical significance was determined using cluster size inference with an initial cluster forming threshold of $p < 0.001$, where clusters with a corrected FDR of $p < 0.05$ were considered significant. Left side of the image displays axial slices from z= -20 to z= 35 in 5mm increments. Right side displays sagittal slices from x= -50 to x= 60 in 10mm increments. The colour bar represents T-statistics.

RK: Brain regions	MNI [x y z]	Cluster	L/R	T value	p (FDR-corr) cluster	% Change of baseline
Cingulate_Mid_R (aal3v1)	[10 -44 38]	3180	R	9.5425	0.000	-3.0 ± 1.6
Cingulate_Mid_L (aal3v1)	[-12 -46 36]		L	7.2165		

Cingulate_Mid_R (aal3v1)	[4 -42 32]		R	7.1227		
Temporal_Sup_L (aal3v1)	[-44 -26 6]	153	L	8.7197	0.040	-2.3 ± 1.5
Temporal_Sup_L (aal3v1)	[-42 -12 0]		L	5.2141		
Thal_PuM_R (aal3v1)	[14 -28 4]	555	R	6.6219	0.000	-4.1 ± 1.9
Thal_VL_R (aal3v1)	[14 -12 12]		R	6.4304		
Thalamus right	[2 -20 0]		R	5.7345		
Temporal_Sup_R (aal3v1)	[44 -18 0]	200	R	5.8944	0.017	-2.5 ± 1.6
Heschl_R (aal3v1)	[46 -22 10]		R	4.7805		
Temporal_Sup_R (aal3v1)	[54 -14 4]		R	4.7174		

Table 6: Clusters showing significant reduction in radial kurtosis during sleep

Percentage change was determined for each participant before averaging in the following way: ((mean cluster sleep RK- mean cluster wake RK)/mean cluster wake RK) *100; ± represents SD between participants. The statistical significance was determined using cluster size inference with an initial cluster forming threshold of $p< 0.001$, where clusters with FDR- corrected $p<0.05$ were considered significant. Anatomical information was derived using the xjView toolbox (http://www.alivelearn.net/xjview; based on the WFU_PickAtlas, http://fmri.wfubmc.edu/software/PickAtlas). In the table “aal3v1” denotes Automated Anatomical Labeling.

Kurtosis Fractional Anisotropy

Figure 59 illustrates significant clusters with increased KFA, note that the axial slices start from z=-5 (as opposed to Figure 57 and Figure 58, where they start from z= -20) that is because there are no significant clusters bellow this slice. There are 4 clusters that survive FDR correction, summarized in Table 7. The largest significant cluster (size= 742 voxels) passes through the right supramarginal gyrus, right superior temporal gyrus and passes down to the medial temporal gyrus. The second largest significant KFA cluster (size= 720 voxels) is centred around bilateral posterior cingulate gyrus, similarly as the largest MK cluster. The other two clusters are in the left/right cuneus (which is also significant in the MK, RK maps) and left superior temporal gyrus and left insula, except for the latter the KFA clusters seem to roughly coincide with the other significant kurtosis clusters.

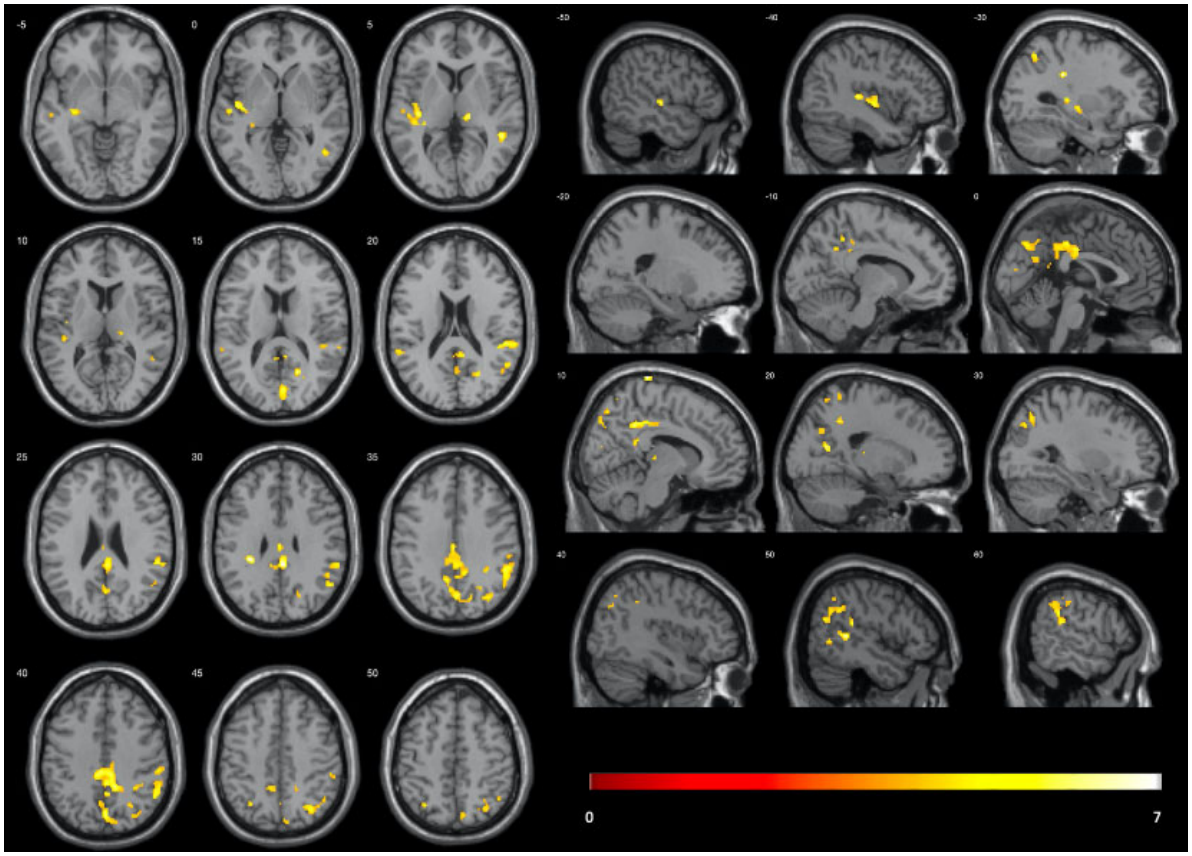

Figure 59: Voxel-wise comparison of kurtosis fractional anisotropy between wake and sleep

Brain regions with significantly increased KFA during sleep. The statistical significance was determined using cluster size inference with an initial cluster forming threshold of $p < 0.001$, where clusters with a corrected FDR of $p < 0.05$ were considered significant. Left side of the image displays axial slices from z= -20 to z= 35 in 5mm increments. Right side displays sagittal slices from x= -50 to x= 60 in 10mm increments. The colour bar represents T-statistics.

KFA: Brain regions	MNI [x y z]	Cluster	L/R	T value	p (FDR-corr) cluster	% Change of baseline
Cingulate_Post_R (aal3v1)	[6 -38 30]	720	R	6.8874	0.000	10.4 ± 6.5
Precuneus_R (aal3v1)	[12 -46 38]		R	6.0198		
Cingulate_Mid_R (aal3v1)	[2 -40 38]		R	5.5913		

Insula_L (aal3v1)	[-36 -20 4]	261	L	6.5552	0.006	10.9 ± 6.6
Temporal_Sup_L (aal3v1)	[-40 -28 8]		L	5.609		
Temporal_Sup_L (aal3v1)	[-50 -18 2]		L	5.4642		
SupraMarginal_R (aal3v1)	[56 -36 24]	742	R	6.3541	0.000	13.8 ± 9.5
SupraMarginal_R (aal3v1)	[52 -46 34]		R	5.5561		
Parietal_Inf_R (aal3v1)	[54 -54 38]		R	5.172		
Precuneus_R (aal3v1)	[2 -74 40]	266	R	5.6311	0.006	14.2 ± 10.8
Precuneus_L (aal3v1)	[-8 -54 36]		L	5.1683		
Parietal_Sup_R (aal3v1)	[12 -74 52]		R	4.9544		

Table 7: Clusters showing significant increase in kurtosis fractional anisotropy during sleep

Percentage change was determined for each participant before averaging in the following way: ((mean cluster KFA- mean cluster wake KFA)/mean cluster wake KFA) *100; ± represents SD between participants. The statistical significance was determined using cluster size inference with an initial cluster forming threshold of $p< 0.001$, where clusters with FDR- corrected $p<0.05$ were considered significant. Anatomical information was derived using the xjView toolbox (http://www.alivelearn.net/xjview; based on the WFU_PickAtlas, http://fmri.wfubmc.edu/software/PickAtlas). In the table “aal3v1” denotes Automated Anatomical Labelling.

8.5.3 Global VBM

There were no significant differences in GM, WM and CSF volumes between wake and sleep scans. The absolute volumes as well as the differences are summarized in Table 8.

Figure 60 illustrates the distribution of mean percentage differences between wake and sleep condition in GM, WM and CSF.

		Wake Session	Sleep Session	Difference	p-two tailed
Brain Volumes	**GM (ml)**	780.4 ± 89.6	776.2 ± 88.1	-4.2 ± 10.8	0.1434
	WM (ml)	456.1 ± 78.4	458.2 ± 74.2	2.0 ± 8.1	0.3301
	CSF (ml)	320.5 ± 63.3	317.8 ± 67.3	-2.7 ± 33.3	0.7476

Table 8: Summary of brain tissue volumes during wake and sleep (Mean ± SD)

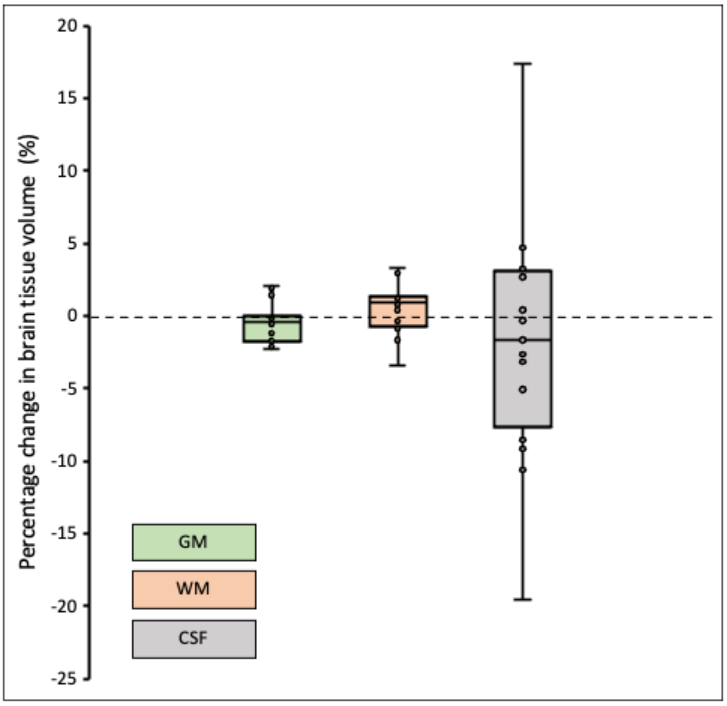

Figure 60: Box plot illustrating brain tissue volume change during sleep

Midline in the box represents the median value; the outer edges of the box represent the 25th and 75th percentiles; the whiskers represent the 5th and 95th percentiles. There was one outlier in the CSF volume change (not shown in this figure) with 26% increase in CSF volume.

8.5.4 Voxel-wise comparison (VBM)

There were no clusters that survived the correction for multiple comparison.

8.6 Discussion

8.6.1 Key results

Diffusion kurtosis analysis indicated global as well as region-wise reduction in kurtosis during sleep, which was driven by reduction in radial kurtosis. A decrease in kurtosis might reflect an increase interstitial space volume fraction, as diffusion becomes more Gaussian when it is less restricted. Significant decrease in kurtosis was observed in brain regions involved in SWA generation (e.g., brainstem, thalamus) and in areas that are particularly active during wake e.g., regions associated with the default mode network. Based on these observations, i.e., increased glymphatic clearance in areas extensively used during wake, it is very tempting to speculate that local homeostatic control sleep (described in Chapter 1.4.2) has evolved to clear metabolites formed during high activity during wake. Interestingly, the changes were more restricted to the posterior parts of the brain.

8.6.2 Global diffusion changes

To my best knowledge we are the first group to investigated diffusion kurtosis during sleep. Diffusion kurtosis is a measure of deviation from a Gaussian diffusion and in biology it has been associated with tissue complexity. We observed significant reductions in MK, MKT and RK in global GM and WM, which was in line with our hypothesis. A decrease in kurtosis means that water diffusion is becoming more Gaussian, which is what one would expect with an increase in the interstitial volume fraction during sleep. We also observed significant increases in KFA in both GM and WM. KFA is mathematically analogous to FA and provides information about anisotropy in kurtosis or in other words gives information about the directionality in non-Gaussian diffusion (Glenn et al., 2015). Understanding the physiological meaning of a significant increase in KFA is rather difficult, especially considering the limited number of studies investigating KFA variations in various conditions. Nevertheless, it is useful to reiterate that the observed changes in MK/MKT are likely explained by changes in the radial component of kurtosis only (as AK did not change), thus implying a change in kurtosis anisotropy.

There were no significant differences in the (Gaussian) diffusion measure, except for FA. We observed an increase in GM FA, which suggests increased directionality in gaussian diffusion. Although, we need to be cautious with this interpretation as FA is estimated from a diffusion tensor model, which is a simplistic representation of diffusion in a complex environment such as GM.

Furthermore, the FA increase was only present on a global level and was not localised as the other kurtosis measures.

8.6.3 Voxel-wise diffusion changes

1st observation: The location of MK (MKT), RK and KFA changes all seem to coincide. The MK (MKT) and RK statistical maps are almost identical in terms of cluster localisation, although RK clusters shows higher statistical significance and higher percentage decrease than MK. This is perhaps unsurprising, as no significant differences were observed in AK. The simplest explanation for the similar statistical maps is that the changes in all significant measures are driven by changes in RK.

2nd observation: There seems to be some symmetry (except for the right occipital and right thalamic clusters) and anatomical continuity in significant clusters. Two large clusters in MK and RK seem to form a continuous path:1. Running from posterior cingulate gyrus to precuneus and down to the cuneus bilaterally; 2. Running from right thalamus, through third ventricle and midbrain to the cerebellum.

3rd observation: Cluster showing significant decrease in kurtosis appear to be functionally linked. Posterior cingulate, precuneus, middle temporal, parietal clusters are key nodes of the default mode network that are metabolically highly active during wake (Raichle et al., 2001). Functionally, the posterior cingulate/precuneus has been associated with attention, memory and perception (Andrews-Hanna, Smallwood and Spreng, 2014). The lower part of the posterior cingulate has been associated with processing concepts associated with self, past and future, while the upper section has been associated with awareness and arousal. Precuneus has also been associated with attentional processing in both visual and sensorimotor domains. These areas, particularly the posterior cingulate cortex and precuneus have been shown to be particularly vulnerable to ischaemia, CO poisoning and are one of the early areas affected by Alzheimer's disease (Raichle et al., 2001; Minoshima et al., 1997; DeVolder, 1990). Moreover, these areas have been consistently shown to be largely deactivated during sleep, anaesthesia induced loss of consciousness, in hypnotic and vegetative states (Braun et al. 1997; Maquet et al. 1997; Andersson et al. 1998; Fiset et al. 1999; Maquet et al. 1999; Laureys et al. 1999). Interestingly, these areas were shown to be significantly affected sleep deprivation, there was a ~1.7% decrease in cortical thickness in these areas after 23h of sleep deprivation (Elvsåshagen et al., 2017). Considering that cortical thickness returns to baseline after recovery sleep (Bernardi et al., 2016), it might be possible that the decrease in kurtosis in these areas was due to the glymphatic system opposing the effects of sleep

deprivation (which makes sense in terms of cortical deactivation/reduced CBF considering the link between SWS, increase in interstitial volume and increased CSF pulses (Fultz et al. 2019)).

Thalamus/brainstem clusters: The thalamus has been showed to been involved in delta rhythm generation via disfacilitation of the cortex (Steriade and Amzica 1998). There is an anatomical connection between brainstem adrenergic, serotonergic and cholinergic neurons and the midline of the thalamus that forms extensive connections the neocortex (Royce et al., 1991; Krout, Belzer and Loewy, 2002; Herrera et al., 2016; Vertes, Hoover and Rodriguez, 2012). The connections between brainstem nuclei and the thalamus are believed to be involved in sleep state switching, medial thalamus acts as a hub for natural sleep initiation (as well as for the initiation of loss of consciousness after anaesthesia) (Saper et al., 2010; Baker et al., 2014; Gent et al., 2018).

8.6.4 Limitations

As with our study design we were unable to decouple the main effect of sleep, sleep deprivation, zolpidem, and their interactions consequently we cannot be certain that the observed changes are just/or if at all due to sleep in the scanner. Nevertheless, we can interpret our results based on previous findings.

The effect of sleep deprivation on ADC and brain tissue volumes was shown to be statistically non-significant by comparing data acquired after a good night sleep and after 24h sleep deprivation (Demiral et al., 2019). However, the authors only looked at Gaussian diffusion, which has been shown to be less sensitive to microstructural changes than kurtosis measures (Jenesen et al., 2011; Grinberg et al., 2012; Hui et al., 2012) and therefore we cannot rule out a main effect of sleep deprivation on DKI-derived indices.

Other studies investigating the effects of sleep deprivation (~24h) with DTI indicated significant reduction in diffusion measures (MD, AD, and RD) in both white and grey matter structures, which were reversed by recovery sleep (Elvsåshagen et al., 2015; Bernardi et al., 2016). The exact origin of MD reduction is unknown, but it has been speculated that it could be due to glial cell swelling due to increased neural activity as astrocytes are actively involved in K^+ uptake (after neural hyperpolarization) (Ransom, Yamate and Connors, 1985). Although there are no studies on the effects of sleep deprivation on DKI, it is conceivable, based on these DTI results, that such effects would be non-negligible or would be in the opposite direction (e.g., increase in MK). However, on the back of sleep deprivation studies that suggest that sleep and sleep deprivation have opposing

effects on fluid dynamics in the brain, we can only speculate that a decrease in the interstitial fluid volume fraction would lead to an increase in MK.

No data on the effects of Zolpidem on diffusion measures are available, therefore it is not possible to exclude that some of our findings might be caused by the drug, or its interaction with sleep deprivation. However, pre-clinical studies have shown that glymphatic system related changes are state dependent (sleep state vs wake/arousal) and not exclusively dependent on natural (as opposed to pharmacologically induced) sleep (Xie et al., 2013; Ding et al., 2016). On the other hand, Zolpidem and other GABA A potentiators are known to affect SWS power spectra, which could in theory affect glymphatic system related changes (Borbély et al., 1985; Dijk et al., 1989; Brunner et al., 1991; Benoit et al., 1994). I will discuss how Zolpidem might have affected our results in Chapter 9.1.4, where I talk about the co-localized changes observed during sleep across the different modalities.

8.6.5 VBM

No significant changes were observed in brain tissue volume neither on global or voxel-wise levels. Considering the large changes in CSF, it is likely that SPM segmentation was affected by motion during image acquisition. One way to control/consider the effect of motion would be to calculate some summary measure from the motion parameters estimated from diffusion/ASL motion correction and use it as a co-variate. Alternatively, other segmentation method could be used such as free surfer and parcellate the brains for ROI comparison.

8.7 Conclusion

Overall, a reduction in radial kurtosis is consistent with our hypothesis, i.e., with a relative increase in the interstitial fluid volume fraction, a water compartment associated with Gaussian diffusion (Assaf and Basser, 2005). The fact that we observe significant changes in kurtosis but not in diffusion measures, suggests that kurtosis is more sensitive to sleep related changes than diffusion. Reductions in kurtosis has been observed in brain areas associated with slow wave generation (thalamus, brainstem), as hypothesized. Moreover, reductions in kurtosis were also observed in default mode network regions, which might be related to an increased glymphatic function during recovery sleep as a result of prolonged activity during wake.

Chapter 9 Main findings and general discussion

In this thesis I showed that a full night of sleep deprivation in combination with 10mg Zolpidem can successfully induce sleep in the scanner. This was reflected by both physiological/behavioural measurements as well as by reduced CBF, which has been previously reported (Hofle et al., 1997). Using ^{23}Na MRI for approximating changes in interstitial volume associated with sleep led to mixed results, as global analysis indicated increase in sodium signal during sleep that is in line with our hypothesis. On the other, temporal signal changes indicated a reduction in sodium signal with sleep, which goes against our hypothesis. It should be remarked that my sodium results are likely to be compromised by low SNR and potentially by a scanner drift. Moreover, quantification (TSC estimation) was not possible due to motion related issues. To reach a conclusion about ^{23}Na MRI's sensitivity to glymphatic function further experiments are warranted. Higher order dwMRI indicated a significant decrease in radial diffusion kurtosis on both global and regional level during sleep. Decrease in kurtosis is in line with our hypothesis, as diffusion becomes more Gaussian when it is less restricted, which is expected with an increase in interstitial volume fraction during sleep. Significant decrease in kurtosis, while no change in "classical" diffusion measures suggests that diffusion kurtosis is more sensitive to microstructural changes associated with sleep than diffusivity.

Next, I will discuss how observed effects across modalities may fit in with the glymphatic system hypothesis. Furthermore, I will discuss the limitations of study design that affected all modalities and make suggestions for future work.

9.1 Localization of sleep related changes across modalities

A link between change neurotransmission, glymphatic system, CBF and SWA has been shown in pre-clinical studies (Xie et al., 2013, Ding et al., 2016, Seigneur et al., 2005) as well as in a human sleep study (Fultz et al., 2019). Simultaneous recording of CBF and EEG in previous studies has shown a significant negative correlation of CBF and SWA that were mostly located in thalamus, brainstem, cerebellum, anterior/medial cingulate, prefrontal cortex, basal ganglia, insula and precuneus (Hofle et al., 1997; Tüshaus et al., 2017; Dang-Vu et al., 2005). Based on the assumption that glymphatic function related interstitial volume change is linked to SWA, areas that exhibit "more" SWA (and reduced CBF) during sleep would also show changes in our proposed glymphatic measures, i.e., increased sodium signal and reduced kurtosis.

We observed the most prominent CBF reduction in anterior and posterior cingulate, orbitofrontal cortex, precuneus, cuneus, insula, basal ganglia, temporal and parietal cortices. Visual inspection (Figure 48) of sodium data revealed increases in sodium signal included precuneus, posterior and anterior cingulate cortex, frontal cortex, parietal cortex, insula, brainstem, pontine region, and the thalamus. Although, ROI analysis only indicated significant increase in basal ganglia, thalamus, parietal and temporal lobes in the first 20 minutes of sleep compared to wake. Significant reduction in diffusion kurtosis were observed in posterior cingulate/precuneus, thalamus, temporal, occipital and putamen (although only a small portion of the significant cluster is touching onto the putamen).

The most consistent changes across modalities were observed in the midbrain/brainstem, thalamus, posterior cingulate/precuneus, basal ganglia, temporal cortex.

9.1.1 Brainstem and thalamus

The connection between brainstem and thalamus are particularly interesting for sleep generation. Brainstem is the centre of arousal promoting neurotransmitters, which have also been shown to modulate CBF as well as interstitial volume fraction (Moruzzi and Magoun, 1949; Sherpa et al., 2016; Seigneur et al., 2005; Xie et al., 2013, Ding et al., 2016). The activity of mesencephalic reticular formation and cholinergic reticular nuclei decreases at sleep initiation and stays low during SWS that in fact induces thalamic nuclei disfacilitation (Steriade et al., 1993). Aminergic (serotonergic and catecholaminergic) nuclei also display synchronous tonic firing with long periods of hyperpolarization and reduced CBF (Steriade and McCarley 1990), and the reduction in firing and CBF in these structures are associated with sleep rhythm generation. Hence, reduced brainstem activity (as indicated by ASL results) might be a driver for changes observed in the thalamus across modalities. As sleep deepens thalamic neurons become progressively more hyperpolarized and the thalamic delta rhythm spreads to the cortex and disfacilitates it (Steriade and Amzica 1998).

9.1.2 Basal ganglia

Basal ganglia have been associated with sleep regulation (Lazarus et al., 2013). Lesions to the putamen and caudate nucleus resulted in decreased wakefulness and fragmentation of sleep-wake behaviour, while lesions to the nucleus accumbens resulted in increased wakefulness and reduced the duration of NREM sleep (Qiu et al., 2010). Evidence for striatal influence on sleep-wake regulation in humans comes from Huntington's disease, which is characterized by severe striatal impairment (Ross and Shoulson, 2009). There is an association between striatal atrophy in

Huntington's disease and reduction is SWS, however it is not entirely clear whether the impairment in sleep-wake regulation is not a non-specific consequence of the disease (Wiegand et al., 1991).

9.1.3 Posterior cingulate/ precuneus

Posterior cingulate/ precuneus as well as parts of the temporal are part of the default mode network, which show particularly high activity during rest (Raichle et al., 2001). Based on the local control of sleep homeostasis these areas might "need" more rest after sleep deprivation hence we see significant reduction in CBF and increased glymphatic activity (as indicated by significant reduction in kurtosis and non-significant increase in sodium signal). It should be remarked, that after sleep deprivation there is increased anterior SWA (Achermann, Finelli and Borbély, 2001). This raises the question: Why did we not observe significant changes in kurtosis or sodium in anterior brain regions if they indeed reflect increase in interstitial volume fraction due to SWS? Furthermore, it questions my assumption that CBF change can be used as an approximation for SWA, because significant reduction in CBF is not restricted to posterior regions.

9.1.4 Posterior preference in glymphatic measures

We observed a brain wide reduction in CBF, while changes in glymphatic measures were restricted to the posterior regions of the brain, which might be a result of Zolpidem. One study investigated the combined effect of 40h sleep deprivation and 20mg Zolpidem on EEG activity (Landolt et al., 2000) and on CBF (Finelli et al., 2000) simultaneously. Zolpidem reduced SWA after sleep deprivation and changed the spatial distribution of EEG spectra, there was posterior shift NREM power. The authors suggested that the posterior shift might be linked to receptor binding of Zolpidem, which was shown to have higher affinity in fronto-parietal structures in rats (Ruano et al., 1993), and GABA A receptor density that shows an antero-posterior gradient in primate cortex (Dennis et al., 1988). Based on these findings, Zolpidem might have reduced SWA associated with recovery sleep in the anterior areas more than in the posterior. Furthermore, they showed that while Zolpidem had a significant effect on EEG spectra after sleep deprivation, which did not have obvious CBF correlates by water PET (Finelli et al., 2000; Landolt et al. 2000). Thus, it might be possible that Zolpidem affected diffusion measures more than it did CBF measures. Although, simultaneous measurements of EEG and diffusion is necessary to assess how kurtosis changes with EEG spectra. Alternatively, measuring diffusion during sleep after sleep deprivation without the use of Zolpidem could shed light whether the posterior preference is driven the posterior shift in EEG power due to Zolpidem.

9.2 Study limitations

9.2.1 Limitations of facility

Our facility lacked a sleep laboratory, thus we could not observe participants' sleep behaviour prior to scanning and had to rely on their compliance. Moreover, we could not scan at night when circadian drive for sleep is the highest (Borbély, 2016), which could have further increased the chance of falling asleep and achieving deep sleep in the scanner.

9.2.2 Absence of EEG recordings

Glymphatic clearance and the associated change in interstitial volume fraction has been linked to slow wave activity. In order to measure SWA in the scanner, one must acquire simultaneous EEG. In our study this was not possible due to the nature of pulse sequences used. There have been no safety evaluations of using MR compatible EEG with our sodium pulse sequence, furthermore, using EEG with the diffusion poses the possibility of overheating and burning the participant (as previously reported in Demiral et al., 2019). We were aware of not having EEG recording during scan would make data interpretation more difficult. Thus, we planned an experiment with the same sleep protocol, but in a dummy scanner (without magnetic field, but with all the associated noises/vibrations) where we planned to measure EEG activity. This would have allowed us to approximate what stage of sleep can participants achieve in the scanner with our sleep protocol and the variability in EEG activity between participants. Most importantly we wanted to correlate sleep measures (that we also measured in the real scan) with the EEG activity to see which measure/combination of measures are the best at predicting sleep stage. Despite of the studies that looked at correlations between HR variability, respiration, behavioural responses with EEG activity they are not fully or if at all applicable to our study because of the unique nature of our experiment (sleep deprivation + Zolpidem+ non sleep conducive environment). Unfortunately, we could not carry out this experiment because of the COVID19 pandemic.

9.2.3 Circadian variations across participants

While all scanning sessions took place at the same time of the day, it is still likely that there were circadian variations across participants due to different bedtimes and due to different scanning days.

To make sure that participants are in the same circadian state, their sleep midpoint should be estimated from actimetry (e.g., recorded over 7 days) and scanning times adjusted to the individual's sleep midpoint (e.g., each scan taking place 6h after the participant's estimated sleep midpoint). Moreover, scanning days should be controlled, i.e., always scan either beginning of the week or end of the week. Individuals tend to "catch up" on sleep during the weekend, hence participants might be more tired towards the end of the week compared to the beginning of the week. This can further introduce unwanted variation in the data.

Controlling scanning time according to the participant's sleep midpoint and scan at the same time of the week could minimise unwanted variation in the data.

9.2.4 Absence of control scans

To disentangle the main effect of these factors and their interactions, additional control experiments would have needed to be conducted: sleep scan without sleep deprivation or Zolpidem; wake scan after sleep deprivation; sleep scan after sleep deprivation; wake scan after Zolpidem; sleep scan after Zolpidem and wake scan after sleep deprivation and Zolpidem. Consequently, in order to acquire a full dataset from 20 participants, we would have needed at least 160 scans, but probably more due to high chance of not achieving sleep or wake when needed. This was not viable considering the high chance of participant dropout and costs of the scans for which this project did not have budget. Although, we were planning to investigate the main effect of Zolpidem, i.e., scanning participants after night of sleep and asking them to stay awake after giving them Zolpidem. This would have been interesting, because as the effect of sleep deprivation on CBF and diffusion has been reported before, the effect of Zolpidem was only investigated for CBF during sleep after sleep deprivation. Unfortunately, this was not possible because of the COVID19 pandemic. Furthermore, we were planning to invite back participants who could sleep well in the scanner to repeat the sleep session without the use of Zolpidem. However, this was not possible for the same reason.

9.2.5 Microsleep during wake scan

3 participants during sodium and 2 during proton scan reported some sleep during the wake session. Although, they reported very brief periods of sleep and it was not confirmed by button response. Consequently, it is likely that participants experienced episodes of microsleep, which

have been extensively reported during resting state fMRI studies. One study looking at the effect of microsleep (defined as eyelid closure longer than 4s) on BOLD fMRI activity, found that microsleep episodes were associated with reduction in respiration and heart rate that affected BOLD signal and resting state functional connectivity (Soon et al., 2021). They found a lower within-network connectivity in default and attention networks during microsleep episodes that was comparable with the contrast between sleep deprived and rested awake participants (Yeo, Tandi and Chee, 2015). It is possible that our results were affected by microsleep, however if anything it would reduce the effects observed in sleep and not increase it.

9.3 Study conclusion and future perspectives

The aim of my PhD was to test two non-invasive MRI techniques with potential sensitivity for glymphatic system related changes, i.e., expansion of interstitial volume during sleep. While one line of evidence (global increase in sodium signal) suggested that ^{23}Na MRI might be sensitive to the internal glymphatic system, temporal signal change suggested that the increase in sodium signal might have other origins and it is likely to be compromised by technical issues. In future studies looking at change in sodium signal during sleep, one should focus on reducing participant/calibration phantom motion and improve image processing to reach a conclusion about ^{23}Na MRI's sensitivity to the glymphatic system.

Acquiring higher order diffusion weighted images with high b-values in many directions that allows for modelling kurtosis proved to be a promising technique for imaging glymphatic system related changes during sleep. Future studies should focus on verifying diffusion kurtosis measures against more established techniques for measuring glymphatic function, e.g., distribution of fluorescent dye in brain parenchyma in anaesthetized animals.

Diffusion kurtosis imaging (and potentially ^{23}Na MRI) could provide information about correct functioning of internal glymphatic system, which should be tested in elderly participants with and without neurodegenerative disorders. I would expect increased kurtosis in patients with neurodegenerative disorders compared to age matched controls, because of neuroinflammation which has been associated with astrogliosis and activated microglia that reduces interstitial volume (Webers, Heneka and Gleeson, 2019). Moreover, I would expect reduced decrease in kurtosis in response to sleep in patients with dementia due to the increased sleep disturbances and compromised sleep architecture reported in dementia (Kinnunen, Vikhanova and Livingston, 2017). Although achieving sleep in the scanner for patients with dementia and for elderly participants

would be extremely difficult. Consequently, in order to study the glymphatic system in humans with dementia, it is extremely important to find other interventions (possibly drugs targeting the noradrenergic system) to activate the glymphatic system. Agonists for the glymphatic system could help us to gain better understanding of neurodegeneration in humans in addition they might also be effective in treating dementia.

Appendix A- PSQI

Name:_____ Date: _____

Pittsburgh Sleep Quality Index (PSQI)

Instructions: The following questions relate to your usual sleep habits during the past month only. Your answers should indicate the most accurate reply for the majority of days and nights in the past month. **Please answer all questions.**

1. During the past month, what time have you usually gone to bed at night? _____
2. During the past month, how long (in minutes) has it usually taken you to fall asleep each night? _____
3. During the past month, what time have you usually gotten up in the morning? _____
4. During the past month, how many hours of actual sleep did you get at night? (This may be different than the number of hours you spent in bed.) _____

5. During the past month, how often have you had trouble sleeping because you…	Not during the past month	Less than once a week	Once or twice a week	Three or more times a week
a. Cannot get to sleep within 30 minutes				
b. Wake up in the middle of the night or early morning				
c. Have to get up to use the bathroom				
d. Cannot breathe comfortably				
e. Cough or snore loudly				
f. Feel too cold				
g. Feel too hot				
h. Have bad dreams				
i. Have pain				
j. Other reason(s), please describe:				
6. During the past month, how often have you taken medicine to help you sleep (prescribed or "over the counter")?				
7. During the past month, how often have you had trouble staying awake while driving, eating meals, or engaging in social activity?				
	No problem at all	Only a very slight problem	Somewhat of a problem	A very big problem
8. During the past month, how much of a problem has it been for you to keep up enough enthusiasm to get things done?				
	Very good	Fairly good	Fairly bad	Very bad
9. During the past month, how would you rate your sleep quality overall?				

Scoring the PSQI

The order of the PSQI items has been modified from the original order in order to fit the first 9 items (which are the only items that contribute to the total score) on a single page. Item 10, which is the second page of the scale, does not contribute to the PSQI score.

In scoring the PSQI, seven component scores are derived, each scored 0 (no difficulty) to 3 (severe difficulty). The component scores are summed to produce a global score (range 0 to 21). Higher scores indicate worse sleep quality.

Component 1: Subjective sleep quality—question 9

Response to Q9	Component 1 score
Very good	0
Fairly good	1
Fairly bad	2
Very bad	3

Component 1 score:_____

Component 2: Sleep latency—questions 2 and 5a

Response to Q2	Component 2/Q2 subscore
≤ 15 minutes	0
16-30 minutes	1
31-60 minutes	2
> 60 minutes	3

Response to Q5a	Component 2/Q5a subscore
Not during past month	0
Less than once a week	1
Once or twice a week	2
Three or more times a week	3

Sum of Q2 and Q5a subscores	Component 2 score
0	0
1-2	1
3-4	2
5-6	3

Component 2 score:_____

Component 3: Sleep duration—question 4

Response to Q4	Component 3 score
> 7 hours	0
6-7 hours	1
5-6 hours	2
< 5 hours	3

Component 3 score:_____

Component 4: Sleep efficiency—questions 1, 3, and 4

Sleep efficiency = (# hours slept/# hours in bed) X 100%

hours slept—question 4

hours in bed—calculated from responses to questions 1 and 3

Sleep efficiency	Component 4 score
> 85%	0
75-84%	1
65-74%	2
< 65%	3

Component 4 score:_____

Appendix B- Actigraphy clinicians report example

Bed time	Getup time	Time in bed (h:m:s)	Total Sleep Time (h:m:s)	Onset Latency (minutes)	Sleep Efficiency (%)	WASO (minutes)	# Awakenings
12:22:30 AM	8:01:45 AM	7:39:15	6:37:00	5.25	86.45	26.75	29
10:26:15 PM	6:38:00 AM	8:11:45	7:50:00	1.25	95.58	20.25	30
12:24:00 AM	7:30:15 AM	7:06:15	6:29:30	6.5	91.38	15.25	28

Example of Actiware "Clinician's report": Bed time- when the subject got in bed (rest interval start time); Getup time- this corresponds to the rest interval end time; Time in bed- the time between the bed time and get up time; Total Sleep Time- subject was in bed and met the criteria of sleep by the algorithm; Onset Latency- time between bed time and when the algorithm detected that subject fell asleep; Sleep efficiency- how much of the rest interval was scored as sleep; WASO (Wake after sleep onset)- is the time that the subject stayed awake after the fell asleep; # Awakenings- how many awakenings there were during sleep

Appendix C- KSS

Karolinska sleepiness scale

Please, indicate your sleepiness during the 5 minutes before this rating through circling the appropriate description

1=extremely alert

2=very alert

3=alert

4=rather alert

5=neither alert nor sleepy

6=some signs of sleepiness

7=sleepy, but no effort to keep awake

8=sleepy, some effort to keep awake

9=very sleepy, great effort to keep awake, fighting sleep

Appendix D- Subjective sleep questionnaires

These questions apply to the **first part of the scan** (before you were moved).

1. **Did you fall asleep at any point of the scan?**

   Yes No

2. **Tick the option that most describes your sleep in the scanner:**

   - ☐ I didn't fall asleep
   - ☐ I fell asleep, but woke up and couldn't fall asleep again
   - ☐ I kept falling asleep and waking up
   - ☐ Once I fell asleep, I didn't wake up until the researchers woke me up

If you didn't sleep at all:

How sleepy did you feel during the scan?

Not sleepy at all — Very sleepy

If you did sleep (even for a little while):

Indicate approximately when you fell asleep

Beginning of the scan — End of the scan

How long did you sleep during the scan?

No sleep at all — Slept through the whole scan

How deep did you sleep?

Very light sleep — Deep sleep

Did you dream?

Yes No

These questions apply to the **second part of the scan** (before you were moved out of the scanner the second time at the end of the experiment).

3. **Did you fall asleep at any point of the scan?**

Yes No

4. **Tick the option that most describes your sleep in the scanner:**

- ☐ I didn't fall asleep
- ☐ I fell asleep, but woke up and couldn't fall asleep again
- ☐ I kept falling asleep and waking up
- ☐ Once I fell asleep, I didn't wake up until the researchers woke me up

If you didn't sleep at all:

How sleepy did you feel during the scan?

Not sleepy at all Very sleepy

If you did sleep (even for a little while):

Indicate approximately when you fell asleep

Beginning of the scan End of the scan

How long did you sleep during the scan?

No sleep at all Slept through the whole scan

How deep did you sleep?

Very light sleep Deep sleep

Did you dream?

Yes No

List of references

Absinta, M., Ha, S., Nair, G., Sati, P., Luciano, N., Palisoc, M., Louveau, A., Zaghloul, K., Pittaluga, S., Kipnis, J. and Reich, D. (2017). Human and nonhuman primate meninges harbor lymphatic vessels that can be visualized noninvasively by MRI. eLife, 6.

Achermann, P. and Borbély, A., 1997. Low-frequency (<1Hz) oscillations in the human sleep electroencephalogram. Neuroscience, 81(1), pp.213-222.

Achermann, P., Finelli, L. and Borbély, A., 2001. Unihemispheric enhancement of delta power in human frontal sleep EEG by prolonged wakefulness. Brain Research, 913(2), pp.220-223.

Ahn, S. and Prince, E. (2013). Basic Vascular Neuroanatomy of the Brain and Spine: What the General Interventional Radiologist Needs to Know. Seminars in Interventional Radiology, 30(03), pp.234-239.

Akselrod, S., Gordon, D., Ubel, F., Shannon, D., Berger, A. and Cohen, R., 1981. Power spectrum analysis of heart rate fluctuation: a quantitative probe of beat-to-beat cardiovascular control. Science, 213(4504), pp.220-222.

Alba-Ferrara, L. and de Erausquin, G., 2013. What does anisotropy measure? Insights from increased and decreased anisotropy in selective fiber tracts in schizophrenia. Frontiers in Integrative Neuroscience, 7.

Albargothy, N., Johnston, D., MacGregor-Sharp, M., Weller, R., Verma, A., Hawkes, C. and Carare, R., 2018. Convective influx/glymphatic system: tracers injected into the CSF enter and leave the

brain along separate periarterial basement membrane pathways. Acta Neuropathologica, 136(1), pp.139-152.

Allen, M. and Crowell, M., 1989. Patterns of Autonomic Response During Laboratory Stressors. Psychophysiology, 26(5), pp.603-614.

Alsop, D. and Detre, J., 1996. Reduced Transit-Time Sensitivity in Noninvasive Magnetic Resonance Imaging of Human Cerebral Blood Flow. Journal of Cerebral Blood Flow & Metabolism, 16(6), pp.1236-1249.

Alsop, D., Detre, J., Golay, X., Günther, M., Hendrikse, J., Hernandez-Garcia, L., Lu, H., MacIntosh, B., Parkes, L., Smits, M., van Osch, M., Wang, D., Wong, E. and Zaharchuk, G., 2014. Recommended implementation of arterial spin-labeled perfusion MRI for clinical applications: A consensus of the ISMRM perfusion study group and the European consortium for ASL in dementia. Magnetic Resonance in Medicine, 73(1), pp. 102- 116.

Alsop, D., Detre, J., Golay, X., Günther, M., Hendrikse, J., Hernandez-Garcia, L., Lu, H., MacIntosh, B., Parkes, L., Smits, M., van Osch, M., Wang, D., Wong, E. and Zaharchuk, G., 2014. Recommended implementation of arterial spin-labeled perfusion MRI for clinical applications: A consensus of the ISMRM perfusion study group and the European consortium for ASL in dementia. Magnetic Resonance in Medicine, 73(1), pp.102-116.

Amzica, F. and Steriade, M., 1997. Cellular substrates and laminar profile of sleep K-complex. Neuroscience, 82(3), pp.671-686.

Andersson, J. and Sotiropoulos, S., 2016. An integrated approach to correction for off-resonance effects and subject movement in diffusion MR imaging. NeuroImage, 125, pp.1063-1078.

Andersson, J., Graham, M., Drobnjak, I., Zhang, H., Filippini, N. and Bastiani, M., 2017. Towards a comprehensive framework for movement and distortion correction of diffusion MR images: Within volume movement. NeuroImage, 152, pp.450-466.

Andersson, J., Graham, M., Zsoldos, E. and Sotiropoulos, S., 2016. Incorporating outlier detection and replacement into a non-parametric framework for movement and distortion correction of diffusion MR images. NeuroImage, 141, pp.556-572.

Andersson, J., Onoe, H., Hetta, J., Lidström, K., Valind, S., Lilja, A., Sundin, A., Fasth, K., Westerberg, G., Broman, J., Watanabe, Y. and Långström, B., 1998. Brain Networks Affected by Synchronized Sleep Visualized by Positron Emission Tomography. Journal of Cerebral Blood Flow & Metabolism, 18(7), pp.701-715.

Andrade, T., Zangrossi, H. and Graeff, F., 2013. The median raphe nucleus in anxiety revisited. Journal of Psychopharmacology, 27(12), pp.1107-1115.

Andrews-Hanna, J., Smallwood, J. and Spreng, R., 2014. The default network and self-generated thought: component processes, dynamic control, and clinical relevance. Annals of the New York Academy of Sciences, 1316(1), pp.29-52.

Ansseau, M., Pitchot, W., Hansenne, M. and Moreno, A., 1992. Psychotic reactions to zolpidem. The Lancet, 339(8796), pp.809.

Arab, A., Wojna-Pelczar, A., Khairnar, A., Szabó, N. and Ruda-Kucerova, J., 2018. Principles of diffusion kurtosis imaging and its role in early diagnosis of neurodegenerative disorders. Brain Research Bulletin, 139, pp.91-98.

Arbel-Ornath, M., Hudry, E., Eikermann-Haerter, K., Hou, S., Gregory, J., Zhao, L., Betensky, R., Frosch, M., Greenberg, S. and Bacskai, B., 2013. Interstitial fluid drainage is impaired in ischemic stroke and Alzheimer's disease mouse models. Acta Neuropathologica, 126(3), pp.353-364.

Armstrong, L., 2007. Assessing Hydration Status: The Elusive Gold Standard. Journal of the American College of Nutrition, 26(sup5), pp.575S-584S.

Aserinsky, E. and Kleitman, N., 1953. Regularly Occurring Periods of Eye Motility, and Concomitant Phenomena, During Sleep. Science, 118(3062), pp.273-274.

Ashburner, J., 2007. A fast diffeomorphic image registration algorithm. NeuroImage, 38(1), pp.95-113.

Asllani, I., Borogovac, A. and Brown, T., 2008. Regression algorithm correcting for partial volume effects in arterial spin labeling MRI. Magnetic Resonance in Medicine, 60(6), pp.1362-1371.

Aspelund, A., Antila, S., Proulx, S., Karlsen, T., Karaman, S., Detmar, M., Wiig, H. and Alitalo, K., 2015. A dural lymphatic vascular system that drains brain interstitial fluid and macromolecules. The Journal of Experimental Medicine, 212(7), pp.991-999.

Assaf, Y. and Basser, P., 2005. Composite hindered and restricted model of diffusion (CHARMED) MR imaging of the human brain. NeuroImage, 27(1), pp.48-58.

Aston-Jones, G. and Waterhouse, B., 2016. Locus coeruleus: From global projection system to adaptive regulation of behavior. Brain Research, 1645, pp.75-78.

Baker, R., Gent, T., Yang, Q., Parker, S., Vyssotski, A., Wisden, W., Brickley, S. and Franks, N., 2014. Altered Activity in the Central Medial Thalamus Precedes Changes in the Neocortex during Transitions into Both Sleep and Propofol Anesthesia. Journal of Neuroscience, 34(40), pp.13326-13335.

Barakat, R. and Redzic, Z. (2015). The Role of Activated Microglia and Resident Macrophages in the Neurovascular Unit during Cerebral Ischemia: Is the Jury Still Out?. Medical Principles and Practice, 25(1), pp.3-14.

Basser, P. and Pierpaoli, C., 1996. Microstructural and Physiological Features of Tissues Elucidated by Quantitative-Diffusion-Tensor MRI. Journal of Magnetic Resonance, Series B, 111(3), pp.209-219.

Basser, P., Mattiello, J. and Lebihan, D., 1994. Estimation of the Effective Self-Diffusion Tensor from the NMR Spin Echo. Journal of Magnetic Resonance, Series B, 103(3), pp.247-254.

Benington, J. and Craig Heller, H., 1995. Restoration of brain energy metabolism as the function of sleep. Progress in Neurobiology, 45(4), pp.347-360.

Benjamini, Y. and Hochberg, Y., 1995. Controlling the False Discovery Rate: A Practical and Powerful Approach to Multiple Testing. Journal of the Royal Statistical Society: Series B (Methodological), 57(1), pp.289-300.

Benoit, O., Bouard, G., Payan, C., Borderies, P. and Prado, J. 1994. Effect of a single dose (10 mg) of zolpidem on visual and spectral analysis of sleep in young poor sleepers. Psychopharmacology, 116(3), pp.297-303.

Benveniste, H., Lee, H., Ding, F., Sun, Q., Al-Bizri, E., Makaryus, R., Probst, S., Nedergaard, M., Stein, E. and Lu, H. (2017). Anesthesia with Dexmedetomidine and Low-dose Isoflurane Increases Solute Transport via the Glymphatic Pathway in Rat Brain When Compared with High-dose Isoflurane. Anesthesiology, 127(6), pp.976-988.

Bernardi, G., Cecchetti, L., Siclari, F., Buchmann, A., Yu, X., Handjaras, G., Bellesi, M., Ricciardi, E., Kecskemeti, S., Riedner, B., Alexander, A., Benca, R., Ghilardi, M., Pietrini, P., Cirelli, C. and Tononi, G., 2016. Sleep reverts changes in human gray and white matter caused by wake-dependent training. NeuroImage, 129, pp.367-377.

Berridge, C. and Waterhouse, B. (2003). The locus coeruleus–noradrenergic system: modulation of behavioral state and state-dependent cognitive processes. Brain Research Reviews, 42(1), pp.33-84.

Blake, H., Gerard, R. and Kleitman, N., 1939. Factors influencing brain potentials during sleep. Journal of Neurophysiology, 2(1), pp.48-60.

Boada, F., Shen, G., Chang, S. and Thulborn, K., 1997. Spectrally weighted twisted projection imaging: ReducingT2 signal attenuation effects in fast three-dimensional sodium imaging. Magnetic Resonance in Medicine, 38(6), pp.1022-1028.

Bojarskaite, L., Bjørnstad, D., Pettersen, K., Cunen, C., Hermansen, G., Åbjørsbråten, K., Chambers, A., Sprengel, R., Vervaeke, K., Tang, W., Enger, R. and Nagelhus, E., 2020. Astrocytic Ca2+ signaling is reduced during sleep and is involved in the regulation of slow wave sleep. Nature Communications, 11(1).

Borbély, A. A., Mattmann, P., Loepfe, M., Strauch, I. and Lehmann, D., 1985, Effect of benzodiazepine hypnotics on all-night sleep EEG spectra. Human Neurobiology, 4, pp189-194.

Borbély, A., Daan, S., Wirz-Justice, A. and Deboer, T. (2016). The two-process model of sleep regulation: a reappraisal. Journal of Sleep Research, 25(2), pp.131-143.

Borogovac, A. and Asllani, I., 2012. Erratum to "Arterial Spin Labeling (ASL) fMRI: Advantages, Theoretical Constrains and Experimental Challenges in Neurosciences". International Journal of Biomedical Imaging, 2012, pp.1-1.

Brant-Zawadzki, M., Gillan, G. and Nitz, W., 1992. MP RAGE: a three-dimensional, T1-weighted, gradient-echo sequence--initial experience in the brain. Radiology, 182(3), pp.769-775.

Braun, A., 1997. Regional cerebral blood flow throughout the sleep-wake cycle. An H2(15)O PET study. Brain, 120(7), pp.1173-1197.

Brunner, D., Dijk, D., Münch, M. and Borbély, A., 1991. Effect of zolpidem on sleep and sleep EEG spectra in healthy young men. Psychopharmacology, 104(1), pp.1-5.

Buchsbaum, M., 2001. Positron Emission Tomography with Deoxyglucose-F18 Imaging of Sleep. Neuropsychopharmacology, 25(5), pp.S50-S56.

Burgess, H., Kleiman, J. and Trinder, J., 1999. Cardiac activity during sleep onset. Psychophysiology, 36(3), pp.298-306.

Burgess, H., Trinder, J., Kim, Y. and Luke, D., 1997. Sleep and circadian influences on cardiac autonomic nervous system activity. American Journal of Physiology-Heart and Circulatory Physiology, 273(4), pp.H1761-H1768.

Buysse, D.J., Reynolds 3rd, C.F., Monk, T.H., Berman, S.R., Kupfer, D.J., 1989. The Pittsburgh Sleep Quality Index: a new instrument for psychiatric practice and research. Psychiatr. Res. 28, 193–213.

Buzsáki, G., 1998. Memory consolidation during sleep: a neurophysiological perspective. Journal of Sleep Research, 7(S1), pp.17-23.

Cavallero, C., Cicogna, P., Natale, V., Occhionero, M. and Zito, A., 1992. Slow Wave Sleep Dreaming. Sleep, 15(6), pp.562-566.

Chappell, M., Groves, A., MacIntosh, B., Donahue, M., Jezzard, P. and Woolrich, M., 2011. Partial volume correction of multiple inversion time arterial spin labeling MRI data. Magnetic Resonance in Medicine, 65(4), pp.1173-1183.

Cirelli, C. and Tononi, G., 2008. Is Sleep Essential?. PLoS Biology, 6(8), pp. 1605- 1611

Cirelli, C., Gutierrez, C. and Tononi, G., 2004. Extensive and Divergent Effects of Sleep and Wakefulness on Brain Gene Expression. Neuron, 41(1), pp.35-43.

Coe, J., 1969. Postmortem Chemistries on Human Vitreous Humor. American Journal of Clinical Pathology, 51(6), pp.741-750.

Colrain, I., Trinder, J., Fraser, G. and Wilson, G., 1987. Ventilation during sleep onset. Journal of Applied Physiology, 63(5), pp.2067-2074.

Czervionke, L., Czervionke, J., Daniels, D. and Haughton, V. (1988). Characteristic features of MR truncation artifacts. American Journal of Roentgenology, 151(6), pp.1219-1228.

Da Mesquita, S., Louveau, A., Vaccari, A., Smirnov, I., Cornelison, R., Kingsmore, K., Contarino, C., Onengut-Gumuscu, S., Farber, E., Raper, D., Viar, K., Powell, R., Baker, W., Dabhi, N., Bai, R., Cao, R., Hu, S., Rich, S., Munson, J., Lopes, M., Overall, C., Acton, S. and Kipnis, J., 2018. Functional aspects of meningeal lymphatics in ageing and Alzheimer's disease. Nature, 560(7717), pp.185-191.

Da Mesquita, S., Papadopoulos, Z., Dykstra, T., Brase, L., Farias, F., Wall, M., Jiang, H., Kodira, C.,de Lima, K., Herz, J., Louveau, A., Goldman, D., Salvador, A., Onengut-Gumuscu, S., Farber, E.,Dabhi, N., Kennedy, T., Milam, M., Baker, W., Smirnov, I., Rich, S., Benitez, B., Karch, C., Perrin, R.,Farlow, M., Chhatwal, J., Holtzman, D., Cruchaga, C., Harari, O. and Kipnis, J., 2021. Meningeal lymphatics affect microglia responses and anti-Aβ immunotherapy. Nature, 593(7858), pp.255-260.

Dai, W., Garcia, D., de Bazelaire, C. and Alsop, D., 2008. Continuous flow-driven inversion for arterial spin labeling using pulsed radio frequency and gradient fields. Magnetic Resonance in Medicine, 60(6), pp.1488-1497.

Dang-Vu, T., Desseilles, M., Laureys, S., Degueldre, C., Perrin, F., Phillips, C., Maquet, P. and Peigneux, P., 2005. Cerebral correlates of delta waves during non-REM sleep revisited. NeuroImage, 28(1), pp.14-21.

Dang-Vu, T., Desseilles, M., Petit, D., Mazza, S., Montplaisir, J. and Maquet, P., 2007. Neuroimaging in sleep medicine. Sleep Medicine, 8(4), pp.349-372.

Dement, W. and Kleitman, N., 1957. The relation of eye movements during sleep to dream activity: An objective method for the study of dreaming. Journal of Experimental Psychology, 53(5), pp.339-346.

Demiral, Ş., Tomasi, D., Sarlls, J., Lee, H., Wiers, C., Zehra, A., Srivastava, T., Ke, K., Shokri-Kojori, E., Freeman, C., Lindgren, E., Ramirez, V., Miller, G., Bandettini, P., Horovitz, S., Wang, G., Benveniste, H. and Volkow, N. (2019). Apparent diffusion coefficient changes in human brain during sleep – Does it inform on the existence of a glymphatic system?. NeuroImage, 185, pp.263-273.

Dennis, T., Dubois, A., Benavides, J. and Scatton, B., 1988. Distribution of central ω1 (Benzodiazepine1) and ω2 (Benzodiazepine2) receptor subtypes in the monkey and human brain. An autoradiographic study with [3H]flunitrazepam and the ω1 selective ligand [3H]zolpidem. Journal of Pharmacology and Experimental Therapeutics, 247, pp. 309-322.

DeVolder, A., 1990. Brain Glucose Metabolism in Postanoxic Syndrome. Archives of Neurology, 47(2), pp.197.

Di Terlizzi, R. and Platt, S., 2006. The function, composition and analysis of cerebrospinal fluid in companion animals: Part I – Function and composition. The Veterinary Journal, 172(3), pp.422-431.

Dijk, D., Beersma, D., Daan, S. and van den Hoofdakker, R., 1989. Effects of seganserin, a 5-HT2 antagonist, and temazepam on human sleeps stages and EEG power spectra. European Journal of Pharmacology, 171(2-3), pp.207-218.

Dijk, D., Brunner, D. and Borbely, A., 1990. Time course of EEG power density during long sleep in humans. American Journal of Physiology-Regulatory, Integrative and Comparative Physiology, 258(3), pp.R650-R661.

Ding, F., O'Donnell, J., Xu, Q., Kang, N., Goldman, N. and Nedergaard, M., 2016. Changes in the composition of brain interstitial ions control the sleep-wake cycle. Science, 352(6285), pp.550-555.

Douglas, N., White, D., Pickett, C., Weil, J. and Zwillich, C., 1982. Respiration during sleep in normal man. Thorax, 37(11), pp.840-844.

Edlow, B., Takahashi, E., Wu, O., Benner, T., Dai, G., Bu, L., Grant, P., Greer, D., Greenberg, S., Kinney, H. and Folkerth, R., 2012. Neuroanatomic Connectivity of the Human Ascending Arousal System Critical to Consciousness and Its Disorders. Journal of Neuropathology & Experimental Neurology, 71(6), pp.531-546.

Eide, P. and Ringstad, G. (2015). MRI with intrathecal MRI gadolinium contrast medium administration: a possible method to assess glymphatic function in human brain. Acta Radiologica Short Reports, 4(11).

Eide, P., Vatnehol, S., Emblem, K. and Ringstad, G. (2018). Magnetic resonance imaging provides evidence of glymphatic drainage from human brain to cervical lymph nodes. Scientific Reports, 8(1).

Einstein, A., 1905. Über die von der molekularkinetischen Theorie der Wärme geforderte Bewegung von in ruhenden Flüssigkeiten suspendierten Teilchen. Annalen der Physik, 322(8), pp.549-560.

Elvsåshagen, T., Mutsaerts, H., Zak, N., Norbom, L., Quraishi, S., Pedersen, P., Malt, U., Westlye, L., van Someren, E., Bjørnerud, A. and Groote, I., 2019. Cerebral blood flow changes after a day of wake, sleep, and sleep deprivation. NeuroImage, 186, pp.497-509.

Elvsåshagen, T., Norbom, L., Pedersen, P., Quraishi, S., Bjørnerud, A., Malt, U., Groote, I. and Westlye, L., 2015. Widespread Changes in White Matter Microstructure after a Day of Waking and Sleep Deprivation. PLOS ONE, 10(5).

Elvsåshagen, T., Zak, N., Norbom, L., Pedersen, P., Quraishi, S., Bjørnerud, A., Alnæs, D., Doan, N., Malt, U., Groote, I. and Westlye, L., 2017. Evidence for cortical structural plasticity in humans after a day of waking and sleep deprivation. NeuroImage, 156, pp.214-223.

Faro, S., Mohamed, F., Helpern, J., Jensen, J., Thulborn, K., Atkinson, I., Sair, H. and Mikulis, D., 2013. From standardization to quantification: beyond biomarkers towards bioscales as neuro MR imaging surrogates of clinical endpoints. Hot Topics in Functional Neuroradiology. American Journal of Neuroradiology, 34(12), pp.2241-2249.

Feldman, H., Yeatman, J., Lee, E., Barde, L. and Gaman-Bean, S., 2010. Diffusion Tensor Imaging: A Review for Pediatric Researchers and Clinicians. Journal of Developmental & Behavioral Pediatrics, 31(4), pp.346-356.

Finelli, L., Landolt, H., Buck, A., Roth, C., Berthold, T., Borbély, A. and Achermann, P., 2000. Functional neuroanatomy of human sleep states after zolpidem and placebo: A H215O-PET study. Journal of Sleep Research, 9(2), pp.161-173.

Fiset, P., Paus, T., Daloze, T., Plourde, G., Meuret, P., Bonhomme, V., Hajj-Ali, N., Backman, S. and Evans, A., 1999. Brain Mechanisms of Propofol-Induced Loss of Consciousness in Humans: a Positron Emission Tomographic Study. The Journal of Neuroscience, 19(13), pp.5506-5513.

Flanigan WF., 1972 Behavioral states and electroencephalograms of reptiles. In: Chase MH (ed.).The Sleeping Brain. Los Angeles: UCLA Brain Information Service/Brain Research Institute

Fleysher, L., Oesingmann, N., Brown, R., Sodickson, D., Wiggins, G. and Inglese, M., 2012. Noninvasive quantification of intracellular sodium in human brain using ultrahigh-field MRI. NMR in Biomedicine, 26(1), pp.9-19.

Foulkes, W., 1962. Dream reports from different stages of sleep. The Journal of Abnormal and Social Psychology, 65(1), pp.14-25.

Frank, L., 2001. Anisotropy in high angular resolution diffusion-weighted MRI. Magnetic Resonance in Medicine, 45(6), pp.935-939.

Frank, M., 2012. Erasing Synapses in Sleep: Is It Time to Be SHY?. Neural Plasticity, 2012, pp.1-15.

Friston, K., Williams, S., Howard, R., Frackowiak, R. and Turner, R., 1996. Movement-Related effects in fMRI time-series. Magnetic Resonance in Medicine, 35(3), pp.346-355.

Fujisawa, S. and Buzsáki, G., 2011. A 4 Hz Oscillation Adaptively Synchronizes Prefrontal, VTA, and Hippocampal Activities. Neuron, 72(1), pp.153-165.

Fultz, N., Bonmassar, G., Setsompop, K., Stickgold, R., Rosen, B., Polimeni, J. and Lewis, L., 2019. Coupled electrophysiological, hemodynamic, and cerebrospinal fluid oscillations in human sleep. Science, 366(6465), pp.628-631.

Gaberel, T., Gakuba, C., Goulay, R., De Lizarrondo, S., Hanouz, J., Emery, E., Touze, E., Vivien, D. and Gauberti, M. (2014). Impaired Glymphatic Perfusion After Strokes Revealed by Contrast-Enhanced MRI. Stroke, 45(10), pp.3092-3096.

Gandini Wheeler-Kingshott, C., Riemer, F., Palesi, F., Ricciardi, A., Castellazzi, G., Golay, X., Prados, F., Solanky, B. and D'Angelo, E., 2018. Challenges and Perspectives of Quantitative Functional Sodium Imaging (fNaI). Frontiers in Neuroscience, 12.

Gao, Y., Zhang, Y., Wong, C., Wu, P., Zhang, Z., Gao, J., Qiu, D. and Huang, B., 2012. Diffusion abnormalities in temporal lobes of children with temporal lobe epilepsy: a preliminary diffusional kurtosis imaging study and comparison with diffusion tensor imaging. NMR in Biomedicine, 25(12), pp.1369-1377.

Garyfallidis, E., Brett, M., Amirbekian, B., Rokem, A., van der Walt, S., Descoteaux, M. and Nimmo-Smith, I., 2014. Dipy, a library for the analysis of diffusion MRI data. Frontiers in Neuroinformatics, 8.

Gast, L., Gerhalter, T., Hensel, B., Uder, M. and Nagel, A., 2018. Double quantum filtered 23Na MRI with magic angle excitation of human skeletal muscle in the presence of B 0 and B 1 inhomogeneities. NMR in Biomedicine, 31(12), p.e4010.

Gent, T., Bandarabadi, M., Herrera, C. and Adamantidis, A., 2018. Thalamic dual control of sleep and wakefulness. Nature Neuroscience, 21(7), pp.974-984.

Glenn, G., Helpern, J., Tabesh, A. and Jensen, J., 2015. Quantitative assessment of diffusional kurtosis anisotropy. NMR in Biomedicine, 28(4), pp.448-459.

Golay, X., Hendrikse, J. and Lim, T., 2004. Perfusion Imaging Using Arterial Spin Labeling. Topics in Magnetic Resonance Imaging, 15(1), pp.10-27.

Grinberg, F., Ciobanu, L., Farrher, E. and Shah, N., 2012. Diffusion kurtosis imaging and log-normal distribution function imaging enhance the visualisation of lesions in animal stroke models. NMR in Biomedicine, 25(11), pp.1295-1304.

Gudbjartsson, H. and Patz, S., 1995. The rician distribution of noisy mri data. Magnetic Resonance in Medicine, 34(6), pp.910-914.

Gutierrez, G., Williams, J., Alrehaili, G., McLean, A., Pirouz, R., Amdur, R., Jain, V., Ahari, J., Bawa, A. and Kimbro, S., 2016. Respiratory rate variability in sleeping adults without obstructive sleep apnea. Physiological Reports, 4(17).

Hablitz, L., Vinitsky, H., Sun, Q., Stæger, F., Sigurdsson, B., Mortensen, K., Lilius, T. and Nedergaard, M., 2019. Increased glymphatic influx is correlated with high EEG delta power and low heart rate in mice under anesthesia. Science Advances, 5(2).

Hansen, B., 2019. An Introduction to Kurtosis Fractional Anisotropy. American Journal of Neuroradiology.

Hansen, B., Lund, T., Sangill, R. and Jespersen, S., 2013. Experimentally and computationally fast method for estimation of a mean kurtosis. Magnetic Resonance in Medicine, 69(6), pp.1754-1760.

Hatfield, B., Spalding, T., Maria, D., Porges, S., Potts, J., Byrne, E., Brody, E. and Mahon, A., 1998. Respiratory sinus arrhythmia during exercise in aerobically trained and untrained men. Medicine &amp Science in Sports &amp Exercise, 30(2), pp.206-214.

Hayano, J. and Yuda, E., 2019. Pitfalls of assessment of autonomic function by heart rate variability. Journal of Physiological Anthropology, 38(1).

Health.gov. 2021. Sleep - Healthy People 2030 | health.gov. [online] Available at: <https://health.gov/healthypeople/objectives-and-data/browse-objectives/sleep> [Accessed 23 June 2021].

Herrera, C., Cadavieco, M., Jego, S., Ponomarenko, A., Korotkova, T. and Adamantidis, A., 2016. Hypothalamic feedforward inhibition of thalamocortical network controls arousal and consciousness. Nature Neuroscience, 19(2), pp.290-298.

Hobson, J., 1989. Sleep. New York: Scientific American Library.

Hofle, N., Paus, T., Reutens, D., Fiset, P., Gotman, J., Evans, A. and Jones, B., 1997. Regional Cerebral Blood Flow Changes as a Function of Delta and Spindle Activity during Slow Wave Sleep in Humans. The Journal of Neuroscience, 17(12), pp.4800-4808.

Holth, J., Fritschi, S., Wang, C., Pedersen, N., Cirrito, J., Mahan, T., Finn, M., Manis, M., Geerling, J., Fuller, P., Lucey, B. and Holtzman, D., 2019. The sleep-wake cycle regulates brain interstitial fluid tau in mice and CSF tau in humans. Science, 363(6429), pp.880-884.

Holz RW, Fisher SK., 1999. Synaptic Transmission. In: Siegel GJ, Agranoff BW, Albers RW, et al., editors. Basic Neurochemistry: Molecular, Cellular and Medical Aspects. 6th edition. Philadelphia: Lippincott-Raven.

Hoy, A., Koay, C., Kecskemeti, S. and Alexander, A. (2014). Optimization of a free water elimination two-compartment model for diffusion tensor imaging. NeuroImage, 103, pp.323-333.

Hoyer, S., 1994. Age as Risk Factor for Sporadic Dementia of the Alzheimer Type?. Annals of the New York Academy of Sciences, 719(1 The Aging Clo), pp.248-256.

Huber, E., Henriques, R., Owen, J., Rokem, A. and Yeatman, J., 2019. Applying microstructural models to understand the role of white matter in cognitive development. Developmental Cognitive Neuroscience, 36, p.100624.

Huhn, K., Engelhorn, T., Linker, R. and Nagel, A., 2019. Potential of Sodium MRI as a Biomarker for Neurodegeneration and Neuroinflammation in Multiple Sclerosis. Frontiers in Neurology, 10.

Hui, E., Fieremans, E., Jensen, J., Tabesh, A., Feng, W., Bonilha, L., Spampinato, M., Adams, R. and Helpern, J., 2012. Stroke Assessment With Diffusional Kurtosis Imaging. Stroke, 43(11), pp.2968-2973.

Hussain, M., Stobbe, R., Bhagat, Y., Emery, D., Butcher, K., Manawadu, D., Rizvi, N., Maheshwari, P., Scozzafava, J., Shuaib, A. and Beaulieu, C., 2009. Sodium imaging intensity increases with time after human ischemic stroke. Annals of Neurology, 66(1), pp.55-62.

Iliff, J. and Nedergaard, M., 2013. Is There a Cerebral Lymphatic System?. Stroke, 44(6, Supplement 1), pp.S93-S95.

Iliff, J., Chen, M., Plog, B., Zeppenfeld, D., Soltero, M., Yang, L., Singh, I., Deane, R. and Nedergaard, M., 2014. Impairment of Glymphatic Pathway Function Promotes Tau Pathology after Traumatic Brain Injury. The Journal of Neuroscience, 34(49), pp.16180-16193.

Iliff, J., Wang, M., Liao, Y., Plogg, B., Peng, W., Gundersen, G., Benveniste, H., Vates, G., Deane, R., Goldman, S., Nagelhus, E. and Nedergaard, M., 2012. A Paravascular Pathway Facilitates CSF Flow Through the Brain Parenchyma and the Clearance of Interstitial Solutes, Including Amyloid. Science Translational Medicine, 4(147).

Iliff, J., Wang, M., Zeppenfeld, D., Venkataraman, A., Plog, B., Liao, Y., Deane, R. and Nedergaard, M. 2013b. Cerebral Arterial Pulsation Drives Paravascular CSF-Interstitial Fluid Exchange in the Murine Brain. Journal of Neuroscience, 33(46), pp.18190-18199.

Inagaki, T., Miyaoka, T., Tsuji, S., Inami, Y., Nishida, A. and Horiguchi, J., 2010. Adverse Reactions to Zolpidem. The Primary Care Companion to The Journal of Clinical Psychiatry.

Jensen, J. and Helpern, J., 2010. MRI quantification of non-Gaussian water diffusion by kurtosis analysis. NMR in Biomedicine, 23(7), pp.698-710.

Jensen, J., Falangola, M., Hu, C., Tabesh, A., Rapalino, O., Lo, C. and Helpern, J., 2011. Preliminary observations of increased diffusional kurtosis in human brain following recent cerebral infarction. NMR in Biomedicine, 24(5), pp.452-457.

Jensen, J., Helpern, J., Ramani, A., Lu, H. and Kaczynski, K., 2005. Diffusional kurtosis imaging: The quantification of non-gaussian water diffusion by means of magnetic resonance imaging. Magnetic Resonance in Medicine, 53(6), pp.1432-1440.

Jessen, N., Munk, A., Lundgaard, I. and Nedergaard, M., 2015. The Glymphatic System: A Beginner's Guide. Neurochemical Research, 40(12), pp.2583-2599.

Ji, D. and Wilson, M., 2006. Coordinated memory replay in the visual cortex and hippocampus during sleep. Nature Neuroscience, 10(1), pp.100-107.

Johanson, C., Duncan, J., Klinge, P., Brinker, T., Stopa, E. and Silverberg, G., 2008. Multiplicity of cerebrospinal fluid functions: New challenges in health and disease. Cerebrospinal Fluid Research, 5(1), p.10.

Jones, D. and Basser, P., 2004. "Squashing peanuts and smashing pumpkins": How noise distorts diffusion-weighted MR data. Magnetic Resonance in Medicine, 52(5), pp.979-993.

Jones, D., Knösche, T. and Turner, R., 2013. White matter integrity, fiber count, and other fallacies: The do's and don'ts of diffusion MRI. NeuroImage, 73, pp.239-254.

Jorgensen, P., Håkansson, K. and Karlish, S., 2003. Structure and Mechanism of Na,K-ATPase: Functional Sites and Their Interactions. Annual Review of Physiology, 65(1), pp.817-849.

Ju, Y., Ooms, S., Sutphen, C., Macauley, S., Zangrilli, M., Jerome, G., Fagan, A., Mignot, E., Zempel, J., Claassen, J. and Holtzman, D., 2017. Slow wave sleep disruption increases cerebrospinal fluid amyloid-β levels. Brain, 140(8), pp.2104-2111.

Kajimura, N., Uchiyama, M., Takayama, Y., Uchida, S., Uema, T., Kato, M., Sekimoto, M., Watanabe, T., Nakajima, T., Horikoshi, S., Ogawa, K., Nishikawa, M., Hiroki, M., Kudo, Y., Matsuda, H., Okawa, M. and Takahashi, K., 1999. Activity of Midbrain Reticular Formation and Neocortex during the Progression of Human Non-Rapid Eye Movement Sleep. The Journal of Neuroscience, 19(22), pp.10065-10073.

Kattler, H., Dijk, D. and Borbély, A., 1994. Effect of unilateral somatosensory stimulation prior to sleep on the sleep EEG in humans. Journal of Sleep Research, 3(3), pp.159-164.

Kemp-Harper, R., Brown, S., Hughes, C., Peter Styles and Wimperis, S., 1997. 23Na NMR methods for selective observation of sodium ions in ordered environments. Progress in Nuclear Magnetic Resonance Spectroscopy, 30(3-4), pp.157-181.

Kinnunen, K., Vikhanova, A. and Livingston, G., 2017. The management of sleep disorders in dementia. *Current Opinion in Psychiatry*, 30(6), pp.491-497.

Kirby, D. and Verrier, R., 1989. Differential effects of sleep stage on coronary hemodynamic function during stenosis. Physiology & Behavior, 45(5), pp.1017-1020.

Klein, A. and Tourville, J., 2012. 101 Labeled Brain Images and a Consistent Human Cortical Labeling Protocol. Frontiers in Neuroscience, 6.

Konstandin, S. and Nagel, A., 2013. Measurement techniques for magnetic resonance imaging of fast relaxing nuclei. Magnetic Resonance Materials in Physics, Biology and Medicine, 27(1), pp.5-19.

Krieger, J., Maglasiu, N., Sforza, E. and Kurtz, D., 1990. Breathing During Sleep in Normal Middle-Aged Subjects. Sleep,.

Kristiansen, K. and Courtois, G., 1949. Rhythmic electrical activity from isolated cerebral cortex. Electroencephalography and Clinical Neurophysiology, 1(1-4), pp.265-272.

Krout, K., Belzer, R. and Loewy, A., 2002. Brainstem projections to midline and intralaminar thalamic nuclei of the rat. The Journal of Comparative Neurology, 448(1), pp.53-101.

Kryger, M., Roth, T. and Dement, W., 2016. Normal human sleep: an overview. In: Principles and Practice of Sleep Medicine. Philadelphia: Elsevier Health Sciences.

Landolt, H. and Borbély, A., 2001. Age-dependent changes in sleep EEG topography. Clinical Neurophysiology, 112(2), pp.369-377.

Landolt, H., Finelli, L., Roth, C., Buck, A., Achermann, P. and Borbély, A., 2000. Zolpidem and sleep deprivation: Different effect on EEG power spectra. Journal of Sleep Research, 9(2), pp.175-183.

Langtry, H. and Benfield, P., 1990. Zolpidem. A review of its pharmacodynamic and pharmacokinetic properties and therapeutic potential, Drugs, 40(2), pp.291-313.

Laureys, S., Goldman, S., Phillips, C., Van Bogaert, P., Aerts, J., Luxen, A., Franck, G. and Maquet, P., 1999. Impaired Effective Cortical Connectivity in Vegetative State: Preliminary Investigation Using PET. NeuroImage, 9(4), pp.377-382.

Lazarus, M., Chen, J., Urade, Y. and Huang, Z., 2013. Role of the basal ganglia in the control of sleep and wakefulness. Current Opinion in Neurobiology, 23(5), pp.780-785.

Le Bihan, D., 2013. Apparent Diffusion Coefficient and Beyond: What Diffusion MR Imaging Can Tell Us about Tissue Structure. Radiology, 268(2), pp.318-322.

Le Bihan, D., 2019. What can we see with IVIM MRI?. NeuroImage, 187, pp.56-67.

Le Bihan, D., Breton, E., Lallemand, D., Grenier, P., Cabanis, E. and Laval-Jeantet, M., 1986. MR imaging of intravoxel incoherent motions: application to diffusion and perfusion in neurologic disorders. Radiology, 161(2), pp.401-407.

Lee, S. and Dan, Y., 2012. Neuromodulation of Brain States. Neuron, 76(1), pp.209-222.

Liao, S. and Padera, T. (2013). Lymphatic Function and Immune Regulation in Health and Disease. Lymphatic Research and Biology, 11(3), pp.136-143.

Lim, M., Gerstner, J. and Holtzman, D., 2014. The sleep–wake cycle and Alzheimer's disease: what do we know?. Neurodegenerative Disease Management, 4(5), pp.351-362.

Louveau, A., Herz, J., Alme, M., Salvador, A., Dong, M., Viar, K., Herod, S., Knopp, J., Setliff, J., Lupi, A., Da Mesquita, S., Frost, E., Gaultier, A., Harris, T., Cao, R., Hu, S., Lukens, J., Smirnov, I., Overall, C., Oliver, G. and Kipnis, J., 2018. CNS lymphatic drainage and neuroinflammation are regulated by meningeal lymphatic vasculature. Nature Neuroscience, 21(10), pp.1380-1391.

Louveau, A., Smirnov, I., Keyes, T., Eccles, J., Rouhani, S., Peske, J., Derecki, N., Castle, D., Mandell, J., Lee, K., Harris, T. and Kipnis, J. (2015). Structural and functional features of central nervous system lymphatic vessels. Nature, 523(7560), pp.337-341.

Lu, A., Atkinson, I., Claiborne, T., Damen, F. and Thulborn, K., 2010. Quantitative sodium imaging with a flexible twisted projection pulse sequence. Magnetic Resonance in Medicine, 63(6), pp.1583-1593.

Lucey, B., McCullough, A., Landsness, E., Toedebusch, C., McLeland, J., Zaza, A., Fagan, A., McCue, L., Xiong, C., Morris, J., Benzinger, T. and Holtzman, D., 2019. Reduced non–rapid eye movement sleep is associated with tau pathology in early Alzheimer's disease. Science Translational Medicine, 11(474).

Luyster, F., Strollo, P., Zee, P. and Walsh, J. (2012). Sleep: A Health Imperative. Sleep, 35(6), pp.727-734.

Lyamin, O., Pavlova, I., Kosenko, P., Mukhametov, L. and Siegel, J., 2012. Regional differences in cortical electroencephalogram (EEG) slow wave activity and interhemispheric EEG asymmetry in the fur seal. Journal of Sleep Research, 21(6), pp.603-611.

Mackiewicz, M., Shockley, K., Romer, M., Galante, R., Zimmerman, J., Naidoo, N., Baldwin, D., Jensen, S., Churchill, G. and Pack, A., 2007. Macromolecule biosynthesis: a key function of sleep. Physiological Genomics, 31(3), pp.441-457.

Madelin, G. and Regatte, R., 2013. Biomedical applications of sodium MRI in vivo. Journal of Magnetic Resonance Imaging, 38(3), pp.511-529.

Madelin, G., Babb, J., Xia, D. and Regatte, R., 2015. Repeatability of Quantitative Sodium Magnetic Resonance Imaging for Estimating Pseudo-Intracellular Sodium Concentration and Pseudo-Extracellular Volume Fraction in Brain at 3 T. PLOS ONE, 10(3).

Maiter, A., Riemer, F., Allinson, K., Zaccagna, F., Crispin-Ortuzar, M., Gehrung, M., McLean, M., Priest, A., Grist, J., Matys, T., Graves, M. and Gallagher, F., 2021. Investigating the relationship between diffusion kurtosis tensor imaging (DKTI) and histology within the normal human brain. Scientific Reports, 11(1).

Mander, B., Marks, S., Vogel, J., Rao, V., Lu, B., Saletin, J., Ancoli-Israel, S., Jagust, W. and Walker, M., 2015. β-amyloid disrupts human NREM slow waves and related hippocampus-dependent memory consolidation. Nature Neuroscience, 18(7), pp.1051-1057.

Mander, B., Rao, V., Lu, B., Saletin, J., Lindquist, J., Ancoli-Israel, S., Jagust, W. and Walker, M., 2013. Prefrontal atrophy, disrupted NREM slow waves and impaired hippocampal-dependent memory in aging. Nature Neuroscience, 16(3), pp.357-364.

Mandeville, J., Marota, J., Ayata, C., Zaharchuk, G., Moskowitz, M., Rosen, B. and Weisskoff, R., 1999. Evidence of a Cerebrovascular Postarteriole Windkessel with Delayed Compliance. Journal of Cerebral Blood Flow & Metabolism, 19(6), pp.679-689.

Maquet, 2000. Functional neuroimaging of normal human sleep by positron emission tomography. Journal of Sleep Research, 9(3), pp.207-231.

Maquet, P., Degueldre, C., Delfiore, G., Aerts, J., Péters, J., Luxen, A. and Franck, G., 1997. Functional Neuroanatomy of Human Slow Wave Sleep. The Journal of Neuroscience, 17(8), pp.2807-2812.

Maquet, P., Dive, D., Salmon, E., Sadzot, B., Franco, G., Poirrier, R., von Frenckell, R. and Franck, G., 1990. Cerebral glucose utilization during sleep-wake cycle in man determined by positron emission tomography and [18F]2-fluoro-2-deoxy-d-glucose method. Brain Research, 513(1), pp.136-143.

Maquet, P., Faymonville, M., Degueldre, C., Delfiore, G., Franck, G., Luxen, A. and Lamy, M., 1999. Functional neuroanatomy of hypnotic state. Biological Psychiatry, 45(3), pp.327-333.

Massimini, M., Huber, R., Ferrarelli, F., Hill, S. & Tononi, G, 2004. The Sleep Slow Oscillation as a Traveling Wave. Journal of Neuroscience, 24(31), pp.6862-6870.

McLaughlin, P. S., & McLaughlin, B. G. (1987). Chemical analysis of bovine and porcine vitreous humors: correlation of normal values with serum chemical values and changes with time and temperature. American journal of veterinary research, 48(3), 467–473.

Mellon, E., Pilkinton, D., Clark, C., Elliott, M., Witschey, W., Borthakur, A. and Reddy, R., 2009. Sodium MR Imaging Detection of Mild Alzheimer Disease: Preliminary Study. American Journal of Neuroradiology, 30(5), pp.978-984.

Meyers, S., Tam, R., Lee, J., Kolind, S., Vavasour, I., Mackie, E., Zhao, Y., Laule, C., Mädler, B., Li, D., MacKay, A. and Traboulsee, A., 2016. Does hydration status affect MRI measures of brain volume or water content?. Journal of Magnetic Resonance Imaging, 44(2), pp.296-304.

Minoshima, S., Giordani, B., Berent, S., Frey, K., Foster, N. and Kuhl, D., 1997. Metabolic reduction in the posterior cingulate cortex in very early Alzheimer's disease. Annals of Neurology, 42(1), pp.85-94.

Mori, S. and Tournier, J., 2014. Introduction to Diffusion Tensor Imaging; Chapter 5 Mathematics of Diffusion Tensor Imaging. 2nd ed. Burlington: Elsevier, pp.33-37.

Moruzzi, G. and Magoun, H., 1949. Brain stem reticular formation and activation of the EEG. Electroencephalography and Clinical Neurophysiology, 1(1-4), pp.455-473.

Moseley, M., Kucharczyk, J., Asgari, H. and Norman, D., 1991. Anisotropy in diffusion-weighted MRI. Magnetic Resonance in Medicine, 19(2), pp.321-326.

Mukhametov, L., Supin, A. and Polyakova, I., 1977. Interhemispheric asymmetry of the electroencephalographic sleep patterns in dolphins. Brain Research, 134(3), pp.581-584.

Najdenovska, E., Alemán-Gómez, Y., Battistella, G., Descoteaux, M., Hagmann, P., Jacquemont, S., Maeder, P., Thiran, J., Fornari, E. and Bach Cuadra, M., 2018. In-vivo probabilistic atlas of human thalamic nuclei based on diffusion- weighted magnetic resonance imaging. Scientific Data, 5(1).

Nakamura, K., Brown, R., Narayanan, S., Collins, D. and Arnold, D., 2015. Diurnal fluctuations in brain volume: Statistical analyses of MRI from large populations. NeuroImage, 118, pp.126-132.

Nedergaard, M. and Goldman, S., 2020. Glymphatic failure as a final common pathway to dementia. Science, 370(6512), pp.50-56.

Nilsson, C., Lindvall-Axelsson, M. and Owman, C., 1992. Neuroendocrine regulatory mechanisms in the choroid plexus-cerebrospinal fluid system. Brain Research Reviews, 17(2), pp.109-138.

Nilsson, C., Stahlberg, F., Thomsen, C., Henriksen, O., Herning, M. and Owman, C., 1992. Circadian variation in human cerebrospinal fluid production measured by magnetic resonance imaging. American Journal of Physiology-Regulatory, Integrative and Comparative Physiology, 262(1), pp.R20-R24.

Nofzinger, E., Buysse, D., Miewald, J., Meltzer, C., Price, J., Sembrat, R., Ombao, H., Reynolds, C., Monk, T., Hall, M., Kupfer, D. and Moore, R., 2002. Human regional cerebral glucose metabolism during non-rapid eye movement sleep in relation to waking. Brain, 125(5), pp.1105-1115.

Novikov, D., Veraart, J., Jelescu, I. and Fieremans, E., 2018. Rotationally-invariant mapping of scalar and orientational metrics of neuronal microstructure with diffusion MRI. NeuroImage, 174, pp.518-538.

O'Donnell, J., Zeppenfeld, D., McConnell, E., Pena, S. and Nedergaard, M., 2012. Norepinephrine: A Neuromodulator That Boosts the Function of Multiple Cell Types to Optimize CNS Performance. Neurochemical Research, 37(11), pp.2496-2512.

Ogilvie, R., 2001. The process of falling asleep. Sleep Medicine Reviews, 5(3), pp.247-270.

Palombo, M., Shemesh, N., Ronen, I. and Valette, J., 2018. Insights into brain microstructure from in vivo DW-MRS. NeuroImage, 182, pp.97-116.

Peever, J. and Fuller, P., 2017. The Biology of REM Sleep. Current Biology, 27(22), pp.R1237-R1248.

Peng, W., Achariyar, T., Li, B., Liao, Y., Mestre, H., Hitomi, E., Regan, S., Kasper, T., Peng, S., Ding, F., Benveniste, H., Nedergaard, M. and Deane, R., 2016. Suppression of glymphatic fluid transport in a mouse model of Alzheimer's disease. Neurobiology of Disease, 93, pp.215-225.

Penzel, T., Kantelhardt, J., Lo, C., Voigt, K. and Vogelmeier, C., 2003. Dynamics of Heart Rate and Sleep Stages in Normals and Patients with Sleep Apnea. Neuropsychopharmacology, 28(S1), pp.S48-S53.

Piechnik, S., Evans, J., Bary, L., Wise, R. and Jezzard, P., 2009. Functional changes in CSF volume estimated using measurement of waterT2relaxation. Magnetic Resonance in Medicine, 61(3), pp.579-586.

Pigarev, I., Nothdurft, H. and Kastner, S., 1997. Evidence for asynchronous development of sleep in cortical areas. NeuroReport, 8(11), pp.2557-2560.

Pipe, J., Zwart, N., Aboussouan, E., Robison, R., Devaraj, A. and Johnson, K. (2011). A new design and rationale for 3D orthogonally oversampled k-space trajectories. Magnetic Resonance in Medicine, 66(5), pp.1303-1311.

Plog, B., Dashnaw, M., Hitomi, E., Peng, W., Liao, Y., Lou, N., Deane, R. and Nedergaard, M., 2015. Biomarkers of Traumatic Injury Are Transported from Brain to Blood via the Glymphatic System. The Journal of Neuroscience, 35(2), pp.518-526.

Pollay, M., 2010. The function and structure of the cerebrospinal fluid outflow system. Cerebrospinal Fluid Research, 7(1).

Priest, R., Terzano, M., Parrino, L. and Boyer, P., 1997. Efficacy of zolpidem in insomnia. European Psychiatry, 12(S1), pp.4S-14S.

Prince, M et al (2014) Dementia UK: Update Second Edition report produced by King's College London and the London School of Economics for the Alzheimer's Society

Qiu, M., Vetrivelan, R., Fuller, P. and Lu, J. (2010). Basal ganglia control of sleep-wake behavior and cortical activation. European Journal of Neuroscience, 31(3), pp.499-507.

Raichle, M., MacLeod, A., Snyder, A., Powers, W., Gusnard, D. and Shulman, G., 2001. A default mode of brain function. Proceedings of the National Academy of Sciences, 98(2), pp.676-682.

Ramar, K., Malhotra, R., Carden, K., Martin, J., Abbasi-Feinberg, F., Aurora, R., Kapur, V., Olson, E., Rosen, C., Rowley, J., Shelgikar, A. and Trotti, L., 2021. Sleep is essential to health: an American Academy of Sleep Medicine position statement. Journal of Clinical Sleep Medicine,.

Ransom, B., Yamate, C. and Connors, B., 1985. Activity-dependent shrinkage of extracellular space in rat optic nerve: a developmental study. The Journal of Neuroscience, 5(2), pp.532-535.

Rechtschaffen, A. and Bergmann, B., 2002. Sleep Deprivation in the Rat: An Update of the 1989 Paper. Sleep, 25(1), pp.18-24.

Reese, T., Heid, O., Weisskoff, R. and Wedeen, V., 2003. Reduction of eddy-current-induced distortion in diffusion MRI using a twice-refocused spin echo. Magnetic Resonance in Medicine, 49(1), pp.177-182.

Reetz, K., Romanzetti, S., Dogan, I., Saß, C., Werner, C., Schiefer, J., Schulz, J. and Shah, N., 2012. Increased brain tissue sodium concentration in Huntington's Disease — A sodium imaging study at 4T. NeuroImage, 63(1), pp.517-524.

Reeves, C., Galang, E., Padalia, R., Tran, N. and Padalia, D., 2017. Intrathecal Injection of Gadobutrol: A Tale of Caution. Journal of Pain & Palliative Care Pharmacotherapy, 31(2), pp.139-143.

Reimund, E., 1994. The free radical flux theory of sleep. Medical Hypotheses, 43(4), pp.231-233.

Ringstad, G., Vatnehol, S. and Eide, P. (2017). Glymphatic MRI in idiopathic normal pressure hydrocephalus. Brain, 140(10), pp.2691-2705.

Rooney, W. and Springer, C., 1991. A comprehensive approach to the analysis and interpretation of the resonances of spins 3/2 from living systems. NMR in Biomedicine, 4(5), pp.209-226.

Rose, A. and Valdes, R., 1994. Understanding the sodium pump and its relevance to disease. Clinical Chemistry, 40(9), pp.1674-1685.

Ross, C. and Shoulson, I., 2009. Huntington disease: pathogenesis, biomarkers, and approaches to experimental therapeutics. Parkinsonism & Related Disorders, 15, pp.S135-S138.

Royce, G., Bromley, S. and Gracco, C., 1991. Subcortical projections to the centromedian and parafascicular thalamic nuclei in the cat. The Journal of Comparative Neurology, 306(1), pp.129-155.

Ruano, D., Benavides, J., Machado, A. and Vitorica, J., 1993. Regional differences in the enhancement by GABA of [3H]zolpidem binding to ω1 sites in rat brain membranes and sections. Brain Research, 600(1), pp.134-140.

Sairanen, V., Leemans, A. and Tax, C., 2018. Fast and accurate Slicewise OutLIer Detection (SOLID) with informed model estimation for diffusion MRI data. NeuroImage, 181, pp.331-346.

Sakakibara, M., Takeuchi, S. and Hayano, J., 1994. Effect of relaxation training on cardiac parasympathetic tone. Psychophysiology, 31(3), pp.223-228.

Saladin, KS (2018). "Chapter 14 - The Brain and Cranial Nerves". Anatomy and Physiology: The Unity of Form and Function (8th ed.). New York: McGraw-Hill. The Reticular Formation, pp. 518-519

Saper, C., Fuller, P., Pedersen, N., Lu, J. and Scammell, T., 2010. Sleep State Switching. Neuron, 68(6), pp.1023-1042.

Saper, C., Scammell, T. and Lu, J., 2005. Hypothalamic regulation of sleep and circadian rhythms. Nature, 437(7063), pp.1257-1263.

Sbardella, E., Tona, F., Petsas, N. and Pantano, P., 2013. DTI Measurements in Multiple Sclerosis: Evaluation of Brain Damage and Clinical Implications. Multiple Sclerosis International, 2013, pp.1-11.

Scharf, M., Naidoo, N., Zimmerman, J. and Pack, A., 2008. The energy hypothesis of sleep revisited. Progress in Neurobiology, 86(3), pp.264-280.

Sebag, J., 1989. The vitreous. Structure, function, and pathobiology. New York: Springer-Verlag.

Seigneur, J., Kroeger, D., Nita, D. and Amzica, F., 2005. Cholinergic Action on Cortical Glial Cells In Vivo. Cerebral Cortex, 16(5), pp.655-668.

Shaffer, F. and Ginsberg, J., 2017. An Overview of Heart Rate Variability Metrics and Norms. Frontiers in Public Health, 5.

Shaw, P., Tononi, G., Greenspan, R. and Robinson, D., 2002. Stress response genes protect against lethal effects of sleep deprivation in Drosophila. Nature, 417(6886), pp.287-291.

Sherpa, A., Xiao, F., Joseph, N., Aoki, C. and Hrabetova, S., 2016. Activation of β-adrenergic receptors in rat visual cortex expands astrocytic processes and reduces extracellular space volume. Synapse, 70(8), pp.307-316.

Shokri-Kojori, E., Wang, G., Wiers, C., Demiral, S., Guo, M., Kim, S., Lindgren, E., Ramirez, V., Zehra, A., Freeman, C., Miller, G., Manza, P., Srivastava, T., De Santi, S., Tomasi, D., Benveniste, H. and Volkow, N., 2018. β-Amyloid accumulation in the human brain after one night of sleep deprivation. Proceedings of the National Academy of Sciences, 115(17), pp.4483-4488.

Simard, J., Kent, T., Chen, M., Tarasov, K. and Gerzanich, V., 2007. Brain oedema in focal ischaemia: molecular pathophysiology and theoretical implications. The Lancet Neurology, 6(3), pp.258-268.

Singh, G. and Loona, N., 2013. Zolpidem-induced hallucinations: A brief case report from the indian subcontinent. Indian Journal of Psychological Medicine, 35(2), p.212.

Soon, C., Vinogradova, K., Ong, J., Calhoun, V., Liu, T., Zhou, J., Ng, K. and Chee, M., 2021. Respiratory, cardiac, EEG, BOLD signals and functional connectivity over multiple microsleep episodes. NeuroImage, 237, p.118129.

Soto, C. and Pritzkow, S., 2018. Protein misfolding, aggregation, and conformational strains in neurodegenerative diseases. Nature Neuroscience, 21(10), pp.1332-1340.

Stephenson, R., Chu, K. and Lee, J., 2007. Prolonged deprivation of sleep-like rest raises metabolic rate in the Pacific beetle cockroach, Diploptera punctata (Eschscholtz). Journal of Experimental Biology, 210(14), pp.2540-2547.

Steriade, M. and McCarley, R. W. Brainstem Control of Wakefulness and Sleep. Plenum Press, New York, 1990

Steriade, M., & Amzica, F., 1998. Coalescence of sleep rhythms and their chronology in corticothalamic networks. Sleep research online : SRO, 1(1), pp.1–10.

Steriade, M., 2003. The corticothalamic system in sleep. Frontiers in Bioscience, 8(4), pp.d878-899.

Steriade, M., Contreras, D., Curro Dossi, R. and Nunez, A., 1993. The slow (< 1 Hz) oscillation in reticular thalamic and thalamocortical neurons: scenario of sleep rhythm generation in interacting thalamic and neocortical networks. The Journal of Neuroscience, 13(8), pp.3284-3299.

Sterman, M. and Clemente, C., 1962. Forebrain inhibitory mechanisms: Sleep patterns induced by basal forebrain stimulation in the behaving cat. Experimental Neurology, 6(2), pp.103-117.

Streitbürger, D., Möller, H., Tittgemeyer, M., Hund-Georgiadis, M., Schroeter, M. and Mueller, K., 2012. Investigating Structural Brain Changes of Dehydration Using Voxel-Based Morphometry. PLoS ONE, 7(8).

Szczepankiewicz, F., van Westen, D., Englund, E., Westin, C., Ståhlberg, F., Lätt, J., Sundgren, P. and Nilsson, M., 2016. The link between diffusion MRI and tumor heterogeneity: Mapping cell eccentricity and density by diffusional variance decomposition (DIVIDE). NeuroImage, 142, pp.522-532.

T. Goetz, A. Arslan, W. Wisden, P. Wulff, 2007. GABA A receptors: structure and function in the basal ganglia, Progress in Brain Research, Elsevier, vol (160), pp. 21-41

Tabernero, C., 2000. Fatal familial insomnia: clinical, neuropathological, and genetic description of a Spanish family. Journal of Neurology, Neurosurgery & Psychiatry, 68(6), pp.774-777.

Tao, A., Tao, L. and Nicholson, C., 2005. Cell cavities increase tortuosity in brain extracellular space. Journal of Theoretical Biology, 234(4), pp.525-536.

Thomas, C., Sadeghi, N., Nayak, A., Trefler, A., Sarlls, J., Baker, C. and Pierpaoli, C. (2018). Impact of time-of-day on diffusivity measures of brain tissue derived from diffusion tensor imaging. NeuroImage, 173, pp.25-34.

Thulborn, K., 2018. Quantitative sodium MR imaging: A review of its evolving role in medicine. NeuroImage, 168, pp.250-268.

Thulborn, K., Gindin, T., Davis, D. and Erb, P., 1999. Comprehensive MR Imaging Protocol for Stroke Management: Tissue Sodium Concentration as a Measure of Tissue Viability in Nonhuman Primate Studies and in Clinical Studies. Radiology, 213(1), pp.156-166.

Thulborn, K., Lui, E., Guntin, J., Jamil, S., Sun, Z., Claiborne, T. and Atkinson, I., 2016. Quantitative sodium MRI of the human brain at 9.4 T provides assessment of tissue sodium concentration and cell volume fraction during normal aging. NMR in Biomedicine, 29(2), pp.137-143.

Tononi, G. and Cirelli, C. (2014). Sleep and the Price of Plasticity: From Synaptic and Cellular Homeostasis to Memory Consolidation and Integration. Neuron, 81(1), pp.12-34.

Tracy, R. and Tracy, L., 1974. Reports of Mental Activity from Sleep Stages 2 and 4. Perceptual and Motor Skills, 38(2), pp.647-648.

Trefler, A., Sadeghi, N., Thomas, A., Pierpaoli, C., Baker, C. and Thomas, C., 2016. Impact of time-of-day on brain morphometric measures derived from T1-weighted magnetic resonance imaging. NeuroImage, 133, pp.41-52.

Trinder, J., Whitworth, F., Kay, A. and Wilkin, P., 1992. Respiratory instability during sleep onset. Journal of Applied Physiology, 73(6), pp.2462-2469.

Tüshaus, L., Omlin, X., Tuura, R., Federspiel, A., Luechinger, R., Staempfli, P., Koenig, T. and Achermann, P., 2017. In human non-REM sleep, more slow-wave activity leads to less blood flow in the prefrontal cortex. Scientific Reports, 7(1).

Tuura, R., Volk, C., Callaghan, F., Jaramillo, V. and Huber, R., 2021. Sleep-related and diurnal effects on brain diffusivity and cerebrospinal fluid flow. NeuroImage, 241.

Vanoli, E., Adamson, P., Ba-Lin, Pinna, G., Lazzara, R. and Orr, W., 1995. Heart Rate Variability During Specific Sleep Stages. Circulation, 91(7), pp.1918-1922.

Vertes, R., Hoover, W. and Rodriguez, J., 2012. Projections of the central medial nucleus of the thalamus in the rat: Node in cortical, striatal and limbic forebrain circuitry. Neuroscience, 219, pp.120-136.

Viens, M., De Koninck, J., Van den Bergen, H., Audet, R. and Christ, G., 1988. A refined switch-activated time monitor for the measurement of sleep-onset latency. Behaviour Research and Therapy, 26(3), pp.271-273.

Vyazovskiy, V. and Harris, K., 2013. Sleep and the single neuron: the role of global slow oscillations in individual cell rest. Nature Reviews Neuroscience, 14(6), pp.443-451.

Walz, W., 2000. Role of astrocytes in the clearance of excess extracellular potassium. Neurochemistry International, 36(4-5), pp.291-300.

Wang, C. and Holtzman, D., 2019. Bidirectional relationship between sleep and Alzheimer's disease: role of amyloid, tau, and other factors. Neuropsychopharmacology, 45(1), pp.104-120.

Webers, A., Heneka, M. and Gleeson, P., 2019. The role of innate immune responses and neuroinflammation in amyloid accumulation and progression of Alzheimer's disease. Immunology & Cell Biology, 98(1), pp.28-41.

Wennberg, R., 2010. Intracranial cortical localization of the human K-complex. Clinical Neurophysiology, 121(8), pp.1176-1186.

Werth, E., Achermann, P. and Borbély, A., 1996b. Brain topography of the human sleep EEG. NeuroReport, 8(1), pp.123-127.

Werth, E., Dijk, D., Achermann, P. and Borbely, A., 1996a. Dynamics of the sleep EEG after an early evening nap: experimental data and simulations. American Journal of Physiology-Regulatory, Integrative and Comparative Physiology, 271(3), pp.R501-R510.

Wheeler-Kingshott, C. and Cercignani, M., 2009. About "axial" and "radial" diffusivities. Magnetic Resonance in Medicine, 61(5), pp.1255-1260.

Whitwell, J., 2009. Voxel-Based Morphometry: An Automated Technique for Assessing Structural Changes in the Brain. Journal of Neuroscience, 29(31), pp.9661-9664.

Wickens, C., Hutchins, S., Laux, L. and Sebok, A., 2015. The Impact of Sleep Disruption on Complex Cognitive Tasks. Human Factors: The Journal of the Human Factors and Ergonomics Society, 57(6), pp.930-946.

Wiegand, M., Möller, A., Schreiber, W., Lauer, C. and Krieg, J., 1991. Brain morphology and sleep EEG in patients with Huntington's disease. European Archives of Psychiatry and Clinical Neuroscience, 240(3), pp.148-152.

Wilkie, I. W., & Bellamy, J. E. (1982). Estimation of antemortem serum electrolytes and urea concentrations from vitreous humor collected postmortem. Canadian journal of comparative medicine : Revue canadienne de medecine comparee, 46(2), pp146–149.

Wolff, S. and Balaban, R., 1989. Magnetization transfer contrast (MTC) and tissue water proton relaxationin vivo. Magnetic Resonance in Medicine, 10(1), pp.135-144.

Wong, E., Buxton, R. and Frank, L., 1998. A theoretical and experimental comparison of continuous and pulsed arterial spin labeling techniques for quantitative perfusion imaging. Magnetic Resonance in Medicine, 40(3), pp.348-355.

Wu, W., Fernández-Seara, M., Detre, J., Wehrli, F. and Wang, J., 2007. A theoretical and experimental investigation of the tagging efficiency of pseudocontinuous arterial spin labeling. Magnetic Resonance in Medicine, 58(5), pp.1020-1027.

Xie, L., Kang, H., Xu, Q., Chen, M., Liao, Y., Thiyagarajan, M., O'Donnell, J., Christensen, D., Nicholson, C., Iliff, J., Takano, T., Deane, R. and Nedergaard, M. (2013). Sleep Drives Metabolite Clearance from the Adult Brain. Science, 342(6156), pp.373-377.

Yamada, S., Miyazaki, M., Yamashita, Y., Ouyang, C., Yui, M., Nakahashi, M., Shimizu, S., Aoki, I., Morohoshi, Y. and McComb, J. (2013). Influence of respiration on cerebrospinal fluid movement using magnetic resonance spin labeling. Fluids and Barriers of the CNS, 10(1), p.36.

Ye, F., Berman, K., Ellmore, T., Esposito, G., van Horn, J., Yang, Y., Duyn, J., Smith, A., Frank, J., Weinberger, D. and McLaughlin, A., 2000. H215O PET validation of steady-state arterial spin tagging cerebral blood flow measurements in humans. Magnetic Resonance in Medicine, 44(3), pp.450-456.

Yeo, B., Tandi, J. and Chee, M., 2015. Functional connectivity during rested wakefulness predicts vulnerability to sleep deprivation. NeuroImage, 111, pp.147-158.

Yoo, S., Hu, P., Gujar, N., Jolesz, F. and Walker, M., 2007. A deficit in the ability to form new human memories without sleep. Nature Neuroscience, 10(3), pp.385-392.

Žemaityte, D., Varoneckas, G., Plauška, K. and Kaukenas, J., 1986. Components of the heart rhythm power spectrum in wakefulness and individual sleep stages. International Journal of Psychophysiology, 4(2), pp.129-141.

Zhang, H., Schneider, T., Wheeler-Kingshott, C. and Alexander, D., 2012. NODDI: Practical in vivo neurite orientation dispersion and density imaging of the human brain. NeuroImage, 61(4), pp.1000-1016.

Zhou, Y., Cai, J., Zhang, W., Gong, X., Yan, S., Zhang, K., Luo, Z., Sun, J., Jiang, Q. and Lou, M., 2020. Impairment of the Glymphatic Pathway and Putative Meningeal Lymphatic Vessels in the Aging Human. Annals of Neurology, 87(3), pp.357-369.

Zhuo J., Gullapalli R.P. (2020) Diffusion Kurtosis Imaging. In: Mannil M., Winklhofer SX. (eds) Neuroimaging Techniques in Clinical Practice. Springer

Zimmerman, J., Naidoo, N., Raizen, D. and Pack, A. (2008). Conservation of sleep: insights from non-mammalian model systems. Trends in Neurosciences, 31(7), pp.371- 376.

Zwart, N., Johnson, K. and Pipe, J., 2011. Efficient sample density estimation by combining gridding and an optimized kernel. Magnetic Resonance in Medicine, 67(3), pp.701-710.